# Interactions between catalysts and oxygen carriers in chemical looping processes


**Alexander Robert Paul Harrison**

Department of Chemical Engineering and Biotechnology
University of Cambridge

This dissertation is submitted for the degree of
*Doctor of Philosophy*

Emmanuel College August 2024

*To the happy few!*

# Declaration

This thesis is the result of my own work and includes nothing which is the outcome of work done in collaboration except as declared in the preface and specified in the text. It is not substantially the same as any work that has already been submitted, or, is being concurrently submitted, for any degree, diploma or other qualification at the University of Cambridge or any other University or similar institution except as declared in the preface and specified in the text. It does not exceed the prescribed word limit for the relevant Degree Committee.

Sections of work from this Dissertation have been published, as listed below:

- Harrison, A. R. P., Kwong, K. Y., Zheng, Y., Balkrishna, A., Dyson, A., & Marek, E. J. (2023). Kinetic and Thermodynamic Enhancement of Low-Temperature Oxygen Release from Strontium Ferrite Perovskites Modified with Ag and $CeO_2$. *Energy & Fuels*, *37*(13), 9487–9499. ***(Included in Chapter 3)***

- Harrison, A. R. P. & Marek, E. J. (2022). Selective formation of propan-1-ol from propylene *via* a chemical looping approach. *Reaction Chemistry & Engineering*, *7*, 2534–2549. ***(Included in Chapter 6)***

Research performed during the period of doctoral study, but outside of the scope of this Dissertation, has also been published, in:

- Gebers, J. C., Harrison, A. R. P., & Marek, E. J. (2022). How does the oxidation and reduction time affect the chemical looping epoxidation of ethylene? *Discover Chemical Engineering*, *2*(1), 4.

- Kwong, K. Y., Harrison, A. R. P., Gebers, J. C., Dennis, J. S., & Marek, E. J. (2022). Chemical Looping Combustion of a Biomass Char in $Fe_2O_3$-, CuO-, and $SrFeO_{3-\delta}$-Based Oxygen Carriers. *Energy & Fuels*, *36*(17), 9437–9449.

Alexander Robert Paul Harrison

August 2024

# Abstract

This Dissertation considers the fundamentals and applications of materials composed of a metal catalyst supported on a reactive metal oxide, applied for chemical looping processes, using $Ag/SrFeO_{3-\delta}$ as a model system. In chemical looping processes, lattice oxygen is provided from a metal oxide (termed the oxygen carrier) to generate purified oxygen, or, to react with a reducing gas (*e.g.* a hydrocarbon) to form oxygenated products, in the absence of gaseous oxygen. The oxygen carrier is then re-oxidised in air, in a separate step.

Chemical looping has been investigated for a variety of selective oxidation reactions, either with the metal oxide oxygen carrier acting as both an oxygen reservoir and a catalyst for selective oxidation, or, by preparing particles composed of a metal catalyst supported on an oxygen carrier. During reduction, oxygen is transported from the lattice of the metal oxide to the surface of the metal catalyst. However, the interactions between the catalyst and the oxygen carrier, and the pathways taken by oxygen, are poorly understood, and hence form the subject of this Dissertation.

To understand the influence of Ag on oxygen availability from $SrFeO_{3-\delta}$, kinetic studies were performed by measuring the rate of oxygen release and re-uptake from $SrFeO_{3-\delta}$ with and without Ag (15 wt%) by reducing and oxidising the material in $N_2$ and $O_2$ ($pO_2$ = 0.21 or 0.05 atm) in a packed bed. The presence of Ag increased the amount of oxygen released *per* redox cycle by more than three-fold at 500°C. From thermogravimetric experiments, interactions between Ag and $SrFeO_{3-\delta}$ were shown to influence the thermodynamics of the material, with Ag increasing the concentration of oxygen vacancies at equilibrium, and hence lowering the oxygen stoichiometry under all investigated oxygen partial pressures ($pO_2 = 10^{-5}$-0.21 atm).

Characterisation studies under simulated reaction conditions were performed to understand the changes in bulk and surface properties of $Ag/SrFeO_{3-\delta}$ during chemical looping. *In-situ* X-ray diffraction under 5 vol% $H_2$ showed that the presence of Ag allowed phase transformation of perovskite $SrFeO_{3-\delta}$ to brownmillerite $SrFeO_{2.5}$ at 300°C, as compared to 500°C for bare $SrFeO_{3-\delta}$. Near-ambient pressure X-ray

photoelectron spectroscopy measurements under reduction and oxidation showed that oxygen removal from Ag/$SrFeO_{3-\delta}$ was enhanced by the formation of reactive Ag-$O_x$ surface species. Pathways for oxygen transport from the $SrFeO_{3-\delta}$ to the surface of Ag were proposed, based on *in-situ* Raman spectroscopy and $H_2$-TPR measurements.

To further understand the mechanisms of oxygen transport in Ag/$SrFeO_{3-\delta}$, samples were prepared incorporating a layer of $Na_2CO_3$, either covering the surface of the particles, or in between the Ag nanoparticles and the $SrFeO_{3-\delta}$ support. The Ag-$Na_2CO_3$-$SrFeO_{3-\delta}$ materials were applied for a selective oxidation reaction, epoxidation of ethylene, demonstrating that an exposed Ag surface was necessary for reaction. The sample with an internal layer of $Na_2CO_3$ showed improved selectivity towards ethylene oxide during chemical looping epoxidation, as the carbonate layer mitigated complete combustion at the surface of $SrFeO_{3-\delta}$.

Lastly, a series of Ag/$SrFeO_{3-\delta}$-based materials, modified with Cl and, or, Au, were investigated for the oxidation of propylene in a chemical looping mode. The materials containing Cl and Au showed unexpected selectivity towards propan-1-ol, with mechanisms proposed based on the reactions of possible intermediate products.

In summary, this Dissertation demonstrates how the addition of metal catalysts to oxygen carriers can both enhance availability of lattice oxygen, and enable selective oxidation processes operated in a chemical looping mode. The interactions between the catalyst and oxygen carrier play a key role in determining kinetic and thermodynamic properties of the combined material. In particular, the transport of oxygen from the oxygen carrier to form reactive surface species greatly enhances reactivity under reducing and oxidising conditions. Hence, the work in this Dissertation expands the theoretical understanding regarding the behaviour of oxygen carriers during redox reactions, and opens new avenues to design materials for chemical looping processes.

# Acknowledgements

I would like to thank my supervisor, Dr Ewa Marek, for her support, enthusiasm, and patience throughout the course of my doctoral study, and in particular for her guidance in cultivating good habits for clear scientific writing. I would also like to thank my advisor, Professor Stuart Scott, for his pellucid insights on my work, and for providing access to his laboratory. I am also grateful for interesting and productive conversations regarding my research with Professor Allan Hayhurst, Professor John Dennis, Professor Alexei Lapkin, and Professor Patrick Barrie.

This project was made possible by a doctoral training scholarship from the EPSRC and the Cambridge School of Technology Vice-Chancellor's award, by grants for instrument access from the Henry Royce Institute, and funding for research and conference travel from the Royal Society of Chemistry, the Cambridge Philosophical Society, and Emmanuel College, for all of which I am very grateful.

I wish to thank my colleagues and friends in the Energy Reactions and Carriers Group (née Combustion), and the Energy Group, for their practical, intellectual, and moral support over the course of my Ph.D. work, namely Dr Zach Bond, Dr Sam Gabra, Dr Kenny Kwong, Dr Michael Sargent, Dr Yaoyao Zheng, Dr Santi Sukma, George Fulham, Paula Mendoza-Moreno, Joe Gebers, Abu Kasim, Raymond Chen, Aki Fujinawa, Tracy Wang, and Dr Thodoris Papalas. I am also thankful to the group alumni, for providing a model to emulate. I would like to thank my IIB project students, Abhishek Balkrishna, Alice Dyson, Hari Prasad, and Jake Stokes, for teaching me a great deal about research that I would not have learnt otherwise. I would also like to thank the technicians for their assistance in constructing the rigs used in my experiments, including Chris Bawden, Phil Salway, Josh Easy, and Dr Simon Butler.

The experiments reported in this dissertation would not have been possible without assistance from many people across several departments. I would like to thank Dr Chris Truscott, James Steele, and Cheng Liu for their assistance collecting and processing XRD measurements, Dr Carmen Fernandez-Posada and Dr Shaoliang Guan for conducting XPS measurements, Dr Nigel Howard for conducting ICP-AES analysis,

and Dr Heather Greer, Simon Griggs and Dr Richard Langford for their assistance with electron microscopy. I also wish to express my special gratitude to Dr Simon Fairclough for his invaluable support in conducting the *in-situ* TEM measurements, and for his assistance in analysing the data thereof. I would also like to thank Dr Richard Görke for sharing his code for the calculation of kinetic parameters, and Amy Xu for her assistance in generating simulated electron diffraction patterns.

I am very grateful to Dr Beth Willneff and Dr Andrew Britton of the University of Leeds for the use of their NAP-XPS instrument, and for their expertise in helping conduct the experiments and interpret the results. I would also like to thank Dr Felix Donat, Alexander Oing, and Professor Christoph Müller (and everyone else in the LESE group) of ETH Zürich for hosting me in their laboratory, helping me conduct *in-situ* XRD and Raman spectroscopy experiments, and for helpful advice regarding the synthesis and characterisation of $Na_2CO_3$-$SrFeO_{3-\delta}$ materials.

Lastly, I would like to thank Andrew Harrison and Professor Hilary Rogers, and Anna Stephenson, for their advice and support with many aspects of this project, and much else besides.

# Table of contents

# List of figures

# List of tables

# Nomenclature

### Roman Symbols

| | |
|---|---|
| $A_{MT}$ | Area available for mass transfer ($m^2$) |
| $c$ | Concentration (ppm) |
| $C_{bal}$ | Average carbon balance (-) |
| $\mathscr{D}$ | Diffusivity ($m^2 s^{-1}$) |
| $d_{3,2}$ | Sauter mean diameter (nm) |
| Đ | Dispersion (-) |
| $h$ | Planck Constant (J s) |
| $I$ | Intensity (-) |
| $J$ | Molar flux (mol $m^{-2}$ $s^{-1}$) |
| $K$ | Shape factor in Scherrer equation (-) |
| $k$ | First-order rate constant (mol $s^{-1}$ $m^{-3}$ $Pa^{-1}$) |
| $k_{M,g}$ | External mass transfer coefficient (m $s^{-1}$) |
| $k'$ | First-order rate constant, corrected for internal mass transfer (mol $s^{-1}$ $m^{-3}$ $Pa^{-1}$) |
| $L$ | Length of packed bed (m) |
| $m$ | Mass (g) |
| $M_r$ | Molar mass (g $mol^{-1}$) |
| $\dot{n}$ | Molar flowrate (mol $s^{-1}$) |

| | |
|---|---|
| $n$ | Number of moles (mol) |
| $P$ | Pressure (Pa) |
| $pO_2$ | Partial pressure of oxygen (Pa) |
| $q$ | Volumetric flowrate (mL $min^{-1}$) |
| $R$ | Molar gas constant (J $mol^{-1}K^{-1}$) |
| $r$ | Specific rate of oxygen release or uptake ($mol_{O_2}$ $s^{-1}$ $g^{-1}$) |
| $R^2$ | Coefficient of determination (-) |
| $\bar{S}$ | Average selectivity (-) |
| $T$ | Temperature (K) |
| $t$ | Sample thickness (nm) |
| $t_{start}$ | Start time of each chemical looping reduction step (s) |
| $t_{end}$ | End time of each chemical looping reduction step (s) |
| $t_{dead}$ | Reactor dead time (s) |
| $T_{onset}$ | Onset temperature of reaction (°C) |
| $v$ | Superficial velocity (m $s^{-1}$) |
| $V_p$ | Volume of packed bed ($m^3$) |
| $\bar{X}$ | Average conversion (-) |
| $x_{O_2}$ | Mole fraction of oxygen (-) |
| $\bar{Y}$ | Average percentage yield (-) |
| $y_i$ | Mole fraction of component $i$ (-) |
| $z$ | Distance along packed bed (m) |

**Dimensionless Groups**

| | |
|---|---|
| $\phi$ | Thiele modulus |

$Re$ Reynolds number

$Sc$ Schmidt number

$Sh$ Sherwood number

**Greek Symbols**

$\varepsilon$ Voidage of packed bed (-)

$\eta_{eff}$ Effectiveness factor (-)

$\beta$ Peak full width at half maximum (radians)

$\kappa$ Thermal conductivity (W $m^{-1}K^{-1}$)

$\lambda$ Wavelength (nm)

$\lambda_{fp}$ Electron mean free path (nm)

$\lambda_m$ Mass fraction (-)

$\nu$ X-ray frequency ($s^{-1}$)

$\phi_{spec}$ XPS instrument work function (J)

$\rho$ Density (g $cm^{-3}$)

$\tau_{cryst}$ Mean crystallite size (nm)

$\tau_{mix}$ First-order mixing time (s)

$\Phi$ Oxygen solubility (-)

$\tau_p$ Pore tortuosity (-)

**Acronyms and Abbreviations**

AA Allyl alcohol, $C_3H_6O$

Ala Alanine, $C_3H_7NO_2$

BF Bright field

BM Brownmillerite

BSE Back-scattered electron

$C_{adv}$ Adventitious carbon

CLAS Chemical looping air separation

CLC Chemical looping combustion

CL Chemical looping

CLE Chemical looping epoxidation

CLOU Chemical looping with oxygen uncoupling

CLR Chemical looping reforming

EDS Energy dispersive X-ray spectroscopy

EELS Electron energy loss spectroscopy

EO Ethylene oxide, $C_2H_4O$

PO Propylene oxide, $C_3H_6O$

FID Flame-ionisation detector

FTIR Fourier-transform infrared

GC Gas chromatography

HAADF High-angle annular dark field

ICP-AES Inductively coupled plasma atomic emission spectroscopy

ICSD Inorganic Crystal Structure Database

I.D. Internal diameter (mm)

MFC Mass-flow controller

MS Mass spectrometry or Mass spectrometer

MvK Mars-van Krevelen

NAP-XPS Near-ambient pressure X-ray photoelectron spectroscopy

NCO Sodium carbonate, $Na_2CO_3$

OC Oxygen carrier

O.D. External diameter (mm)

OMC Oxametallacycle

PV Perovskite

RCF Relative centrifugal force

SAED Selected area electron diffraction

SEM Scanning electron microscopy

SE Secondary electron

SFO Strontium ferrite, $SrFeO_{3-\delta}$

STEM Scanning transmission electron microscopy

TCD Thermal-conductivity detector

TEM Transmission electron microscopy

TGA Thermogravimetric analysis or Thermogravimetric analyser

TPR Temperature-programmed reduction

UEGO Universal exhaust gas oxygen sensor

VPP Vanadium pyrophosphate, $VO_xPO_4$

XPS X-ray photoelectron spectroscopy

XRD X-ray diffraction

# Chapter 1

# Introduction

## 1.1 Chemical looping technologies

### 1.1.1 Industrial chemical looping processes

Chemical looping processes are a class of reactions whereby a metal oxide (termed an 'oxygen carrier') is reduced and oxidised in a cyclic mode, releasing and absorbing oxygen from the crystal lattice of the material. Chemical looping can be applied to produce purified oxygen gas, or to provide oxygen to a chemical reaction. The first chemical looping process applied at industrial scale was the Brin process (Jensen, 2009) for the production of purified oxygen *via* chemical looping air separation (CLAS), patented in 1886. In the Brin process, barium oxides are applied as the oxygen carrier, undergoing the reversible reaction shown in Eq. 1.1.

$$\mathrm{BaO_2} \rightleftharpoons \mathrm{BaO} + \frac{1}{2}\mathrm{O_2} \tag{1.1}$$

The process is split into two distinct steps: in the reduction step, barium peroxide ($\mathrm{BaO_2}$) decomposes at elevated temperature under vacuum, to release pure oxygen, then, in the oxidation step, the reduced barium oxide (BaO) is exposed to air to regenerate the peroxide by reacting with oxygen, thereby closing the chemical loop, as illustrated in Fig. 1.1. The separate oxidation and reduction steps can be achieved either by alternating the feed to a single reactor vessel, or, through the use of circulating fluidised beds (Moghtaderi, 2010; Pröll *et al.*, 2009), with transfer of solid material from a reduction reactor to an oxidation reactor, and *vice-versa*.

The barium oxide materials used are susceptible to carbonation by reaction with $\mathrm{CO_2}$ to form inert $\mathrm{BaCO_3}$. Hence, the Brin process requires an initial purification step

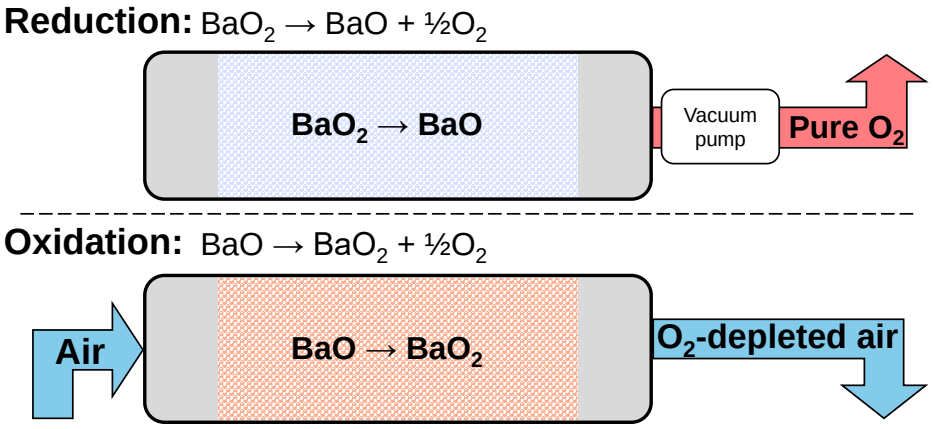


Fig. 1.1 Schematic diagram of the Brin process for the production of oxygen by chemical looping air separation (CLAS).

to remove the $CO_2$ from the air used in the oxidation step, and allow the oxygen carrier to be recycled indefinitely. The Brin process for oxygen production was supplanted by cryogenic distillation of air around 1906 (Jensen, 2009), however, development of novel materials, less vulnerable to carbonation in air, has renewed research interest in CLAS processes for air separation and oxy-fuel combustion (Moghtaderi, 2010; Shah *et al.*, 2013). Recent research into CLAS processes has investigated multi-metallic oxides, such as $SrFeO_{3-\delta}$-derived oxides with perovskite structure (Görke *et al.*, 2020), or brownmillerite $Ca_2MnAlO_{5+\delta}$ (Tian *et al.*, 2022b). From medium-scale experiments (1 kg oxygen carrier) and process simulation, the energy consumption of a CLAS system using $Sr_{0.8}Ca_{0.2}Fe_{1-x}Co_x$ ($x = 0.1$ or 0.6) oxygen carriers with heat supplied to the reduction step using steam was estimated to be *c.* 135-183 kWh $t_{O_2}^{-1}$ for producing >95vol% $O_2$ (Cai *et al.*, 2022; Krzystowczyk *et al.*, 2021). The authors also identified further opportunities for improving the process efficiency by integrating low-grade waste heat to supply energy to the endothermic reduction step, reducing theoretical consumption to *c.* 110 kWh $t_{O_2}^{-1}$ (Cai *et al.*, 2024; Krzystowczyk *et al.*, 2021). By comparison, the energy consumption of industrial cryogenic air separation processes for producing 95-99vol% purity $O_2$ is around 200-260 kWh $t_{O_2}^{-1}$ (Banaszkiewicz *et al.*, 2015; Pfaff and Kather, 2009), based on reported energy demand of existing installed units.

In addition to CLAS processes, chemical looping has been applied for the combustion (CLC) of hydrocarbon fuels (Mattisson, 2013), and for hydrogen generation *via* the 'steam-iron' process (Hacker *et al.*, 2000; Messerschmitt, 1908), both summarised in Fig. 1.2. In both processes, the oxygen carrier is reduced by reaction with a carbonaceous fuel (*e.g.* natural gas, coal, or biomass), then, is either reoxidised exothermically in air

to release energy for power generation, or, in the steam-iron process, is reoxidised by $H_2O$ to generate a pure stream of $H_2$. After removing water from the exhaust stream of the reduction reactor by condensation, both processes generate an almost-pure stream of carbon dioxide as a product without dilution in nitrogen, suitable for sequestration without further purification (Winayu *et al.*, 2023).

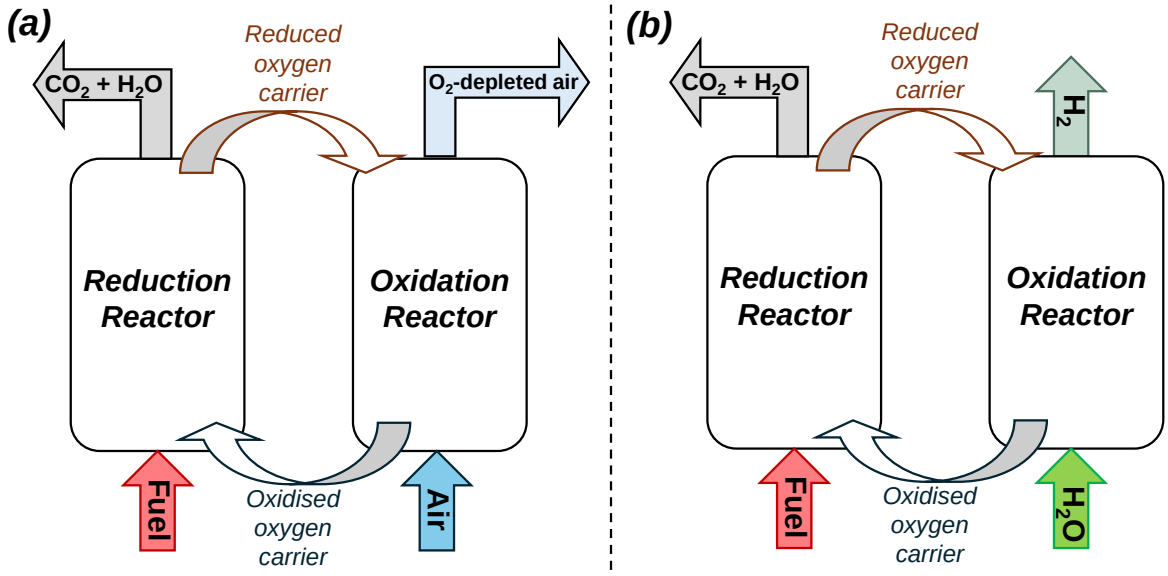


Fig. 1.2 Simplified schematic diagrams showing the **(a)** chemical looping combustion process for energy generation and **(b)** steam-iron process for the production of hydrogen. Here, the systems are shown as interconnected circulated fluidised beds with transfer of solid material between reactors, allowing for continuous operation.

### 1.1.2 Chemical looping catalysis

The processes described in Section 1.1 apply chemical looping for non-selective reactions, *i.e.* production of oxygen or hydrogen, or complete combustion of carbonaceous fuels. However, recent research has considered applying chemical looping for selective oxidation, as reviewed by Zhu *et al.* (2020) and Sun *et al.* (2023). Selective oxidation *via* chemical looping proceeds in a similar manner to CLC as shown in Fig. 1.2a; however, rather than the fuel undergoing complete combustion to form $CO_2$ and $H_2O$, the hydrocarbon undergoes partial oxidation to form a specific product. Selective oxidation *via* chemical looping has the advantage that the hydrocarbon and the air remain separate at all times, as opposed in conventional oxidation processes with a gaseous oxidising agent, where reactions can be limited by safety considerations to

avoid an explosive atmosphere forming inside the reactor (Gebers and Marek, 2024). Furthermore, through tailoring the oxygen carrier to the reaction, the effective $pO_2$ of the oxygen carrier (*i.e.* the partial pressure of oxygen which would be in equilibrium with the solid material at a certain temperature) can be adjusted to optimise for selective oxidation (Sun *et al.*, 2023; Wang *et al.*, 2022a), as discussed in more detail in Section 1.2.

The first chemical looping catalytic process to be applied industrially to produce an oxygenate product was the oxidation of n-butane to maleic anhydride in a plant constructed by DuPont. Supported vanadium pyrophosphate (VPP, $VO_xPO_4$) was used as the oxygen carrier in a circulating fluidised bed arrangement (Contractor, 1999; Patience and Bockrath, 2010). During the chemical looping process, the vanadium ion in the VPP material was present in both the $V^{4+}$ and $V^{5+}$ oxidation states. Hence, in the reduction reactor, a fraction of the $V^{5+}$ ions were reduced to $V^{4+}$, allowing the release of oxygen from the VPP material to partially oxidise the n-butane to maleic anhydride. The partially reduced VPP material was then re-oxidised in air, to convert a fraction of $V^{4+}$ ions to $V^{5+}$ and close the chemical loop. However, over repeated cycles, long-term degradation of the oxygen carriers as a result of particle attrition in the fluidised beds, and incomplete re-oxidation in air resulting in a decrease in available oxygen *per* cycle, lead to the process being discontinued in 2005 (Joshi *et al.*, 2021).

Nevertheless, given the potential advantages for process safety and intensification, the principle of applying chemical looping for selective oxidation has been investigated for a variety of selective oxidation reactions, including oxidation of propane to acrylic acid over $MoVSbO_x$ (Godefroy *et al.*, 2010), partial oxidation of methane to produce syngas over Ni-based oxygen carriers (Luo *et al.*, 2018), and epoxidation of ethylene to ethylene oxide (Chan *et al.*, 2018b) over a silver catalyst supported on a $SrFeO_{3-\delta}$ oxygen carrier ($Ag/SrFeO_{3-\delta}$). Chemical looping can also be applied in oxidative dehydrogenation (CL-ODH) reactions where hydrogen is selectively combusted to convert alkanes to alkenes (Chan *et al.*, 2018a; Mishanin *et al.*, 2017; Neal *et al.*, 2016) or alcohols to aldehydes (Gebers *et al.*, 2023; Joshi *et al.*, 2024), or, in oxidative coupling reactions to convert $C_1$ (Damasceno *et al.*, 2022) or $C_3$ (Fattore, 1975b) molecules to $C_2$ and $C_6$ products respectively.

Chemical looping principles have also been applied for reactions beyond oxidation, for example, using lattice nitrogen in metal imides or nitrides to produce ammonia in a cyclic process. In chemical looping ammonia production, a nitrogen carrier (*e.g.* barium imide, BaNH) reacts with hydrogen to form ammonia and a metal hydride (*e.g.* barium

hydride, $BaH_2$), which can then react with gaseous nitrogen to close the chemical loop (Gao *et al.*, 2018). Wang and Shen (2022) and Zhang *et al.* (2024) provide an overview of recent developments in materials for chemical looping ammonia production, however, the technology remains in its infancy, with limited theoretical understanding of the behaviour of the nitrogen carriers during reduction and nitrogenation.

## 1.2 Reactions of oxygen carriers

During chemical looping processes, the means by which lattice oxygen is provided to the reaction depends strongly on the oxygen carrier, with different metal oxides undergoing reduction *via* distinct mechanisms under equivalent process conditions. For reaction between an oxygen carrier and a gaseous reducing agent, the reducing agent can adsorb at the surface of the metal oxide and react with lattice oxygen, termed 'direct reduction' (Imtiaz *et al.*, 2013; Liu *et al.*, 2024). However, at sufficiently high temperatures (typically $\geq$750°C), some metal oxides such as CuO and $Mn_2O_3$ can thermally decompose, to form $Cu_2O$ and $Mn_3O_4$ respectively, releasing oxygen gas, in a process termed 'chemical looping with oxygen uncoupling' (CLOU) (Mattisson, 2013; Mattisson *et al.*, 2009). Oxygen carriers able to react *via* CLOU have also been applied for the chemical looping combustion of solid fuels, as the uncoupled oxygen can react heterogeneously with particles of coal or biomass without the need to gasify the fuel prior to reaction (Imtiaz *et al.*, 2013; Mattisson *et al.*, 2009). For a given metal oxide able to react *via* CLOU, the ratio of direct reduction to oxygen uncoupling depends on the reaction temperature and the reducing gas applied (Chuang *et al.*, 2009; Imtiaz *et al.*, 2013).

The differences in reaction mechanism between three oxygen carriers ($Fe_2O_3$, CuO, and $SrFeO_3$) undergoing reduction by reaction with CO at 750°C are illustrated in Fig. 1.3 (Kwong *et al.*, 2022). In Fig. 1.3a, CO reacts with lattice oxygen in haematite ($Fe_2O_3$) by direct reduction only, with the iron oxide undergoing a phase transition to form magnetite ($Fe_3O_4$) without the release of gaseous oxygen. Contrastingly, Fig. 1.3b shows the reduction of copper oxide, an oxygen carrier commonly applied for CLOU combustion processes (Imtiaz *et al.*, 2013). In addition to direct reaction between CuO and CO (Chuang *et al.*, 2009; Liu *et al.*, 2024), the cupric oxide (CuO) phase can thermally decompose to cuprous oxide ($Cu_2O$), with uncoupling of gaseous oxygen, which then reacts homogeneously with CO in the gas phase. For $SrFeO_3$, shown in Fig. 1.3c, strontium ferrite can also release oxygen *via* a similar oxygen uncoupling

reaction to CuO, however, the oxygen carrier does not undergo a phase transition: rather, $O_2$ is released by forming oxygen vacancies in the perovskite crystal lattice. The resulting non-stoichiometry in the strontium ferrite is denoted by the term $\delta$ in the chemical formula $SrFeO_{3-\delta}$. Strontium ferrite is also notable for being able to uncouple oxygen at relatively low temperatures (*c.* 400°C) as compared to *e.g.* CuO (Marek *et al.*, 2018a).

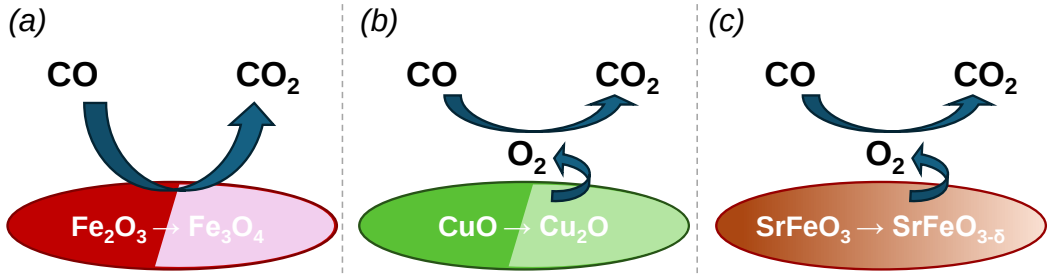


Fig. 1.3 Schematic showing behaviours of different oxygen carriers during reduction by CO at 750°C: **(a)** direct reduction of $Fe_2O_3$ by reaction between the reducing gas and the solid oxygen carrier, inducing a phase change from haematite ($Fe_2O_3$) to magnetite ($Fe_3O_4$), **(b)** oxygen uncoupling (CLOU) from the phase transition of cupric oxide (CuO) to cuprous oxide ($Cu_2O$) **(c)** oxygen uncoupling (CLOU) *via* formation of oxygen vacancies in non-stoichiometric strontium ferrite ($SrFeO_{3-\delta}$).

The thermodynamic differences between stoichiometric oxygen carriers, such as $Fe_2O_3$ and CuO, and non-stoichiometric oxygen carriers, such as $SrFeO_{3-\delta}$, are illustrated in Fig. 1.4. In Fig. 1.4a, a generic stoichiometric oxide $MeO_2$ undergoes a phase transition to form $MeO$ at well defined partial oxygen pressure and temperature ($pO_2$-$T$) conditions, described by the phase boundary line. Contrastingly, Fig. 1.4b shows the phase diagram of a non-stoichiometric oxide, $MeO_{2-\delta}$, where the oxygen non-stoichiometry $\delta$ varies continuously as a function of $pO_2$-$T$ without a well-defined phase boundary (Patrakeev *et al.*, 2011). At any given composition, the non-stoichiometric oxide has two thermodynamic degrees of freedom, $T$ and $pO_2$ (Metcalfe *et al.*, 2019; Panlener *et al.*, 1975).

Hence, if the stoichiometric oxide were to be applied for a CLAS process, the temperature and $pO_2$ conditions in the reduction and oxidation steps must be located on either side of the phase boundary, such that changing the conditions between steps results in the release or uptake of oxygen. By contrast, for the non-stoichometric oxide at any given $pO_2$-$T$ condition, increasing temperature or decreasing oxygen partial pressure would result in a small amount of oxygen gas uncoupling from the material (or *vice-versa* with oxygen uptake if temperature were decreased or $pO_2$ increased),

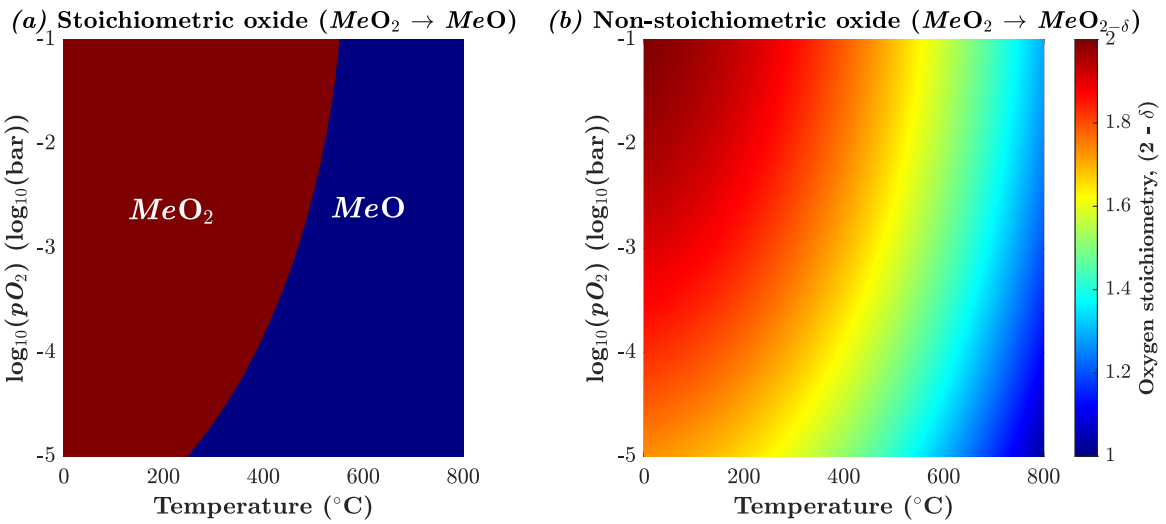


Fig. 1.4 Representative phase diagrams for a generic metal oxide, $MeO_2$, showing **(a)** a distinct phase transition with well-defined oxygen stoichiometry, or **(b)** variable oxygen non-stoichiometry $MeO_{2-\delta}$ as a function of temperature and oxygen partial pressure.

albeit potentially very slowly if the system were kinetically limited. Equivalently, for a non-stoichiometric oxide exposed to a reducing agent at a constant temperature, the equilibrium $pO_2$ of the material will decrease continuously as $\delta$ increases. Certain metal oxides, including strontium ferrite, show both stoichiometric and non-stoichiometric behaviour in different regions of $pO_2$-$T$ conditions (Starkov *et al.*, 2014), discussed in further detail in Section 1.4.

The properties of non-stoichiometric oxygen carriers can be exploited to improve chemical looping processes. For example, continuous variation in $pO_2$ of a $La_{0.6}Sr_{0.4}FeO_{3-\delta}$ oxygen carrier along the length of a packed bed reactor, applied for the water gas shift reaction ($CO + H_2O \rightleftharpoons CO_2 + H_2$) in a chemical looping mode, allows for operation arbitrarily close to thermodynamic equilibrium at each point along the bed (Metcalfe *et al.*, 2019). Given the strong non-linearity of $pO_2$-$T$-$\delta$ relationships for many non-stoichiometric oxides, a relatively large number of measurements are required to characterise the overall behaviour of novel oxides (Wilson *et al.*, 2023). Hence, relatively few oxides (*e.g.* $CeO_{2-\delta}$ (Panlener *et al.*, 1975) and $SrFeO_{3-\delta}$ (Görke *et al.*, 2020)) have comprehensive $pO_2$-$T$-$\delta$ measurements available in literature, despite recent innovations in data sampling to decrease the number of experimental measurements required to find regions of $pO_2$-$T$ conditions where $\delta$ changes rapidly (Wilson and Muhich, 2024).

As described in Section 1.1.2, chemical looping catalysis has been applied for a variety of different oxidation reactions, using the metal oxide as both a catalyst and an oxygen carrier. In principle, any conventional oxidation reaction which proceeds *via* a Mars-van Krevelen (MvK) mechanism, whereby lattice oxygen from an oxide catalyst participates in the reaction and is then regenerated by gaseous oxygen (Doornkamp and Ponec, 2000; Mars and van Krevelen, 1954), can be adapted for chemical looping operation (Zhu *et al.*, 2020), provided the metal oxide forms a stable reduced phase. For example, oxidative dehydrogenation of ethane to ethylene over a $MoVNbTeO_x$ catalyst proceeds *via* a Mars-van Krevelen mechanism (Chen *et al.*, 2023), with oxygen supplied to the reaction from the oxide lattice. Hence, by alternating the feed to the catalyst bed between ethane and air, the reaction can be performed in a chemical looping mode (Gabra, 2022; Mishanin *et al.*, 2017), as shown in Fig. 1.5a.

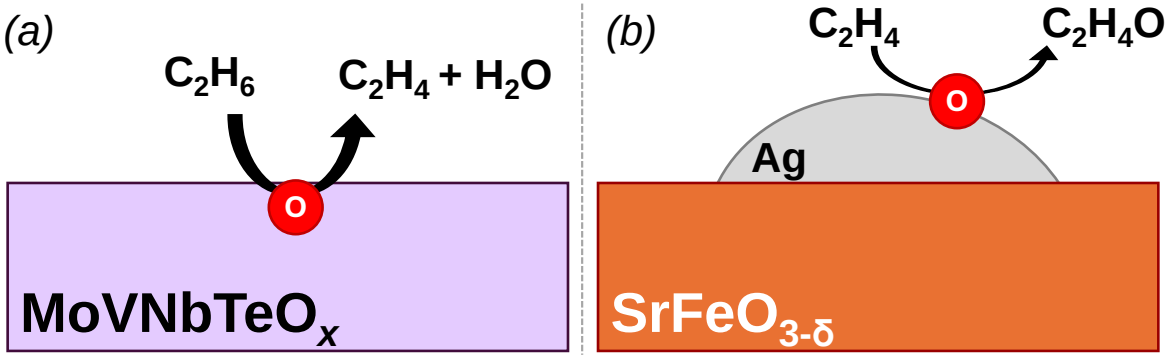


Fig. 1.5 Two mechanisms of oxygen carrier reduction in chemical looping catalysis: **(a)** oxidative dehydrogenation by reaction of ethane with lattice oxygen in $MoVNbTeO_x$, **(b)** oxidation of ethylene to form ethylene oxide by reaction with $O_a$ adatoms on an Ag catalyst, provided by the $SrFeO_{3-\delta}$ oxygen carrier.

Furthermore, reactions which do not proceed *via* a MvK mechanism can be adapted for chemical looping by combining a metal catalyst with a metal oxide oxygen carrier, whereby the oxygen carrier donates oxygen to the active sites at the metal surface. An example of chemical looping using a material composed of a metal catalyst supported on a metal oxide oxygen carrier is shown in Fig. 1.5b. In the chemical looping epoxidation of ethylene, oxygen is transported from the lattice of the $SrFeO_{3-\delta}$ oxygen carrier to the surface of the metallic Ag catalyst, forming $O_a$ adatoms, which are the active species for epoxidation (Chan *et al.*, 2018b). However, the interactions between the Ag and the $SrFeO_{3-\delta}$, and the mechanisms by which lattice oxygen is transported to the metal surface, are poorly understood. Understanding the reactive behaviour of modified $Ag/SrFeO_{3-\delta}$ materials is one of the key aims of this Dissertation.

## 1.3 Improving the activity of perovskite oxygen carriers

Criteria for candidate oxygen carriers include rapid kinetics of oxygen uptake and release at low temperature, minimal degradation over repeated redox cycles, high gravimetric oxygen capacity, and a wide operating range of $pO_2$-$T$ conditions (de Vos *et al.*, 2020; Kwong *et al.*, 2022; Zhu *et al.*, 2020). As discussed in Section 1.1, a class of materials of interest for chemical looping processes, including CLAS and chemical looping catalysis, are non-stoichiometric oxides with perovskite structure (He *et al.*, 2009; Krishnamurthy *et al.*, 2008), in particular, $SrFeO_{3-\delta}$ (Bulfin *et al.*, 2019; Lau *et al.*, 2017). Strontium ferrite-based oxygen carriers are able to release and uptake oxygen by forming oxygen vacancies at relatively low operating temperatures ($\leq$650°C), (Marek *et al.*, 2018a) with minimal degradation in oxygen capacity over repeated cycles of oxidation and reduction (Krzystowczyk *et al.*, 2021), albeit with inferior oxygen capacity to stoichiometric oxygen carriers such as CuO (Kwong *et al.*, 2022). Furthermore, by partial substitution of Sr or Fe with other elements, $SrFeO_{3-\delta}$ can be tuned to operate at different $pO_2$ conditions, by altering the $pO_2$-$\delta$-$T$ characteristics of the material (Wang *et al.*, 2022a).

Particles of $SrFeO_{3-\delta}$ can be produced *via* straightforward solid-state methods from oxide and carbonate precursors (Liu *et al.*, 2022b; Marek *et al.*, 2018a) and have demonstrated stable CLAS performance with fast kinetics of oxygen release over up to 1000 redox cycles in air and $N_2$ (Görke *et al.*, 2020). However, kinetics for the oxidation of $SrFeO_{3-\delta}$ in air have not yet been reported.

A benefit of perovskite oxygen carriers, in particular, $SrFeO_{3-\delta}$, is their tuneability using relatively simple methods, *e.g.* by introducing bulk (Marek *et al.*, 2020; Tian *et al.*, 2022a), structural (Liu, 2021), or surface (Wang *et al.*, 2021) dopants. The addition of noble metals to perovskites (Ag, Pd, Pt), in addition to acting as catalysts for oxidation reactions, has been shown to aid oxygen release at lower temperatures than those for unmodified perovskites (Beppu *et al.*, 2018, 2017; Cheng *et al.*, 2024; Wang *et al.*, 2021). The enhancement of oxygen release from the presence of noble metals on the perovskite surface is possibly caused by donation of electrons from the metal to the perovskite reducing the energy barrier for the transport of oxygen ions (Wang *et al.*, 2021) and, or by the metal catalysing the reaction of $O_{lattice}$ ions to form gaseous $O_2$ molecules and oxygen vacancies in the crystal lattice (Kovalev *et al.*, 2021; Leo *et al.*, 2009).

The impregnation of $SrFeO_{3-\delta}$ with particles of Ag or $CeO_2$ has been exploited in chemical looping catalytic systems for selective oxidation reactions (Gebers *et al.*, 2023; Marek *et al.*, 2020) leading to more active oxygen carriers as compared to unmodified $SrFeO_{3-\delta}$. Metal oxides, such as $CeO_2$ (Marek *et al.*, 2020; Tian *et al.*, 2022a) CaO (Wang *et al.*, 2022b) or $FeO_x$ (Dueso *et al.*, 2015; Neagu *et al.*, 2020) introduced to the bulk of particles of oxygen carriers can also improve the rate of oxygen release from the perovskite. Furthermore, the partial substitution of Sr and Fe with other elements to influence the specific oxygen capacity, and the minimum temperature required for detectable oxygen release, has been widely investigated (Vieten *et al.*, 2019; Wang *et al.*, 2022a). For example, the partial substitution of Sr with Ce, giving $Sr_{1-x}Ce_xFeO_{3-\delta}$, facilitates the ionic conductivity of $O^{2-}$ through the crystal lattice, possibly by partial reduction of $Ce^{4+}$ to $Ce^{3+}$. However, the effects of each modification method on the intrinsic kinetics of oxygen release and reuptake from $SrFeO_{3-\delta}$ have not been studied systematically.

As discussed in Section 1.2, the stoichiometry of perovskite materials at thermodynamic equilibrium, which determines the maximum oxygen capacity and chemical driving force for oxygen release, is a function of temperature and oxygen partial pressure. The effects of partial substitution of Sr in $SrFeO_{3-\delta}$ on the thermodynamic properties of the material have been investigated in experimental and theoretical studies (Bush *et al.*, 2021; Krzystowczyk *et al.*, 2020; Vieten *et al.*, 2017). For example, Krzystowczyk *et al.* (2020) found that at low temperatures ($\leq$600°C), partial substitution of Sr with Ba or Y increased the concentration of oxygen vacancies at equilibrium, whereas doping with K or La resulted in a slight decrease. Similarly, Vieten *et al.* (2017) found that substitution of Sr with Mn increased the concentration of oxygen vacancies, with the extent of increase becoming greater at higher temperatures (up to 1200°C). However, the effect of interactions between a perovskite oxygen carrier and another phase (*e.g.* Ag or $CeO_2$) on the oxygen stoichiometry of $SrFeO_{3-\delta}$ at equilibrium is not well understood.

## 1.4 Probing the redox behaviour of $SrFeO_{3-\delta}$

From *in-situ* X-ray diffraction (XRD) measurements and packed-bed reactor studies, the reduction and oxidation of strontium ferrite has been shown to proceed *via* three distinct regimes. For 'shallow' reduction of $SrFeO_{3-\delta}$ (where $0.5 > \delta > 0$), vacancies form in the perovskite structure as oxygen uncouples from the surface of the material, or reacts

with a reducing gas (Marek *et al.*, 2018a; Reller, 1993). During reduction, the oxygen stoichiometry of $SrFeO_{3-\delta}$ changes pseudo-continuously as oxygen is removed (Chizhik and Nemudry, 2018; Metcalfe *et al.*, 2019). Partially reduced phases of the general form $Sr_nFe_nO_{3n-1}$ (where $n$ = 2, 4, 8) form stable orthorhombic and tetragonal crystal structures with ordered oxygen vacancies (Hodges *et al.*, 2000), where intermediate compositions of $SrFeO_{3-\delta}$ are equivalent to solid-state solutions of the different phases in appropriate combinations to achieve the overall oxygen stoichiometry (Schmidt and Campbell, 2002). However, the intermediate phases are difficult to distinguish from cubic perovskite by laboratory XRD (Marek *et al.*, 2018a), requiring instead synchrotron radiation or neutron diffraction for detailed phase refinement (Hodges *et al.*, 2000; Schmidt and Campbell, 2002).

Furthermore, below oxygen stoichiometries of (3 - $\delta$) = 2.52, reduction is relatively slow, down to $SrFeO_{2.5}$ (Starkov *et al.*, 2014). At a composition of $SrFeO_{2.5}$, the strontium ferrite undergoes a topotactic phase transition (*i.e.* preserving relative crystal orientation) from perovskite to brownmillerite structure (Hodges *et al.*, 2000; Xing *et al.*, 2019). Formation of hyper-stoichiometric $SrFeO_{2.5+\delta}$ brownmillerite has also been observed from high-temperature XRD analysis (Mizusaki *et al.*, 1992) and *in-situ* transmission electron microscopy (TEM) studies (Batuk *et al.*, 2023; Xing *et al.*, 2022) of reduction and oxidation, as a transient intermediate phase during reduction of $SrFeO_{3-\delta}$ to $SrFeO_{2.5}$, or *vice-versa*.

Under inert and mildly reducing atmospheres, $SrFeO_{2.5}$ undergoes further reduction very slowly (Starkov *et al.*, 2014). Under stronger reducing atmospheres (*e.g.* $H_2$ at >800°C), the brownmillerite $SrFeO_{2.5}$ phase decomposes into Sr-rich phases with Ruddlesden-Popper structure ($Sr_{n+1}Fe_nO_{3n+1}$) (Savinskaya *et al.*, 2008), iron rich phases including $Sr_4Fe_6O_{13}$ and $SrFe_{12}O_{19}$ (Fossdal *et al.*, 2004; Kleveland *et al.*, 2000), and metallic Fe (Savinskaya *et al.*, 2008). The final products of deep reduction of $SrFeO_{3-\delta}$ under $H_2$ at 900°C were reported by Marek *et al.* (2018a) as SrO and Fe, which re-oxidised reversibly in air to re-form the original perovskite phase, or under $CO_2$ to form the brownmillerite phase.

As discussed in Section 1.3, the presence of Ag nanoparticles at the surface of $SrFeO_{3-\delta}$ aids the transport of oxygen by withdrawing electron density from the perovskite, aiding the formation of oxygen vacancies (Lee *et al.*, 2021; Wang *et al.*, 2021), and, or, by catalysing reactions between oxygen surface species to facilitate formation and dissociation of $O_2$ (Kovalev *et al.*, 2021; Leo *et al.*, 2009; Majewski and Dhir, 2018). Additionally, from *in-situ* Raman spectroscopy studies of oxidation of

hydrocarbons over $CeO_{2-\delta}$ materials with and without Ag catalysts, the addition of Ag altered the distribution of oxygen surface species ($O^-$, $O_2^{2-}$, and $O_2^-$) available for reaction (Grabchenko *et al.*, 2019; Lee *et al.*, 2021, 2019; Wang *et al.*, 2017), and changed the reaction mechanism from a Mars-Van Krevelen mechanism (direct reaction between the hydrocarbon with $CeO_2$ lattice oxygen) to Langmuir-Hinshelwood (reaction between the hydrocarbon and $O_a$ adatoms at the Ag surface) (Wang *et al.*, 2023). However, the pathways taken by oxygen from the bulk of the $SrFeO_{3-\delta}$ to form surface species adsorbed on Ag, which then react with molecules in the gas phase, have yet to be determined.

## 1.5 Structured oxygen carriers

In chemical looping processes for selective oxidation of hydrocarbons, selectivity towards the desired product can be limited by direct reaction between the hydrocarbon and the oxygen carrier, to form $CO_2$ and $H_2O$ (Gao *et al.*, 2016). Hence, synthesis of structured oxygen carriers with a protective layer has been applied in chemical looping oxidative dehydration of alkanes (CL-ODH), where, for example, ethane is passed over an oxygen carrier at high temperature to produce ethylene and water (Neal *et al.*, 2016). The protective layer limits direct combustion of the alkane with lattice oxygen in the oxygen carrier (Liu *et al.*, 2022a), while allowing oxygen species to diffuse from the oxygen carrier through the layer to the surface of the particle, and react with the alkane to selectively combust hydrogen and form an alkene.

In a typical scheme, a metal salt with a melting point lower than the intended reaction temperature is impregnated onto an oxygen carrier, for example, 10 wt% $Li_2CO_3$ on $La_{1-x}Sr_xFeO_{3-\delta}$ (Gao *et al.*, 2020), for CL-ODH at 700-800°C. Then, under reaction conditions, the metal salt melts to form a layer over the oxygen carrier, wetting the surface of the particle. The combinations of oxygen carriers and molten salts applied for CL-ODH were recently reviewed by Liu and Li (2023), with the molten salt layers classified into one of two categories: 'inert' molten salts, which acted solely as a diffusion barrier to prevent the alkane reaching the surface of the oxygen carrier (*e.g.* $Na_2WO_4$), and 'active' salts which selectively permitted the transport of specific oxygen species selective for the oxidation reaction (*e.g.* $Li_2CO_3$, which favoured transport of peroxide species, selective for ODH, and inhibited the transport of non-selective atomic oxygen). However, in order to achieve surface wetting, the reaction temperature must exceed

the melting point of the salt (Gao *et al.*, 2022), generally around 700°C for molten carbonates.

Luongo *et al.* (2022) applied a different approach to produce structured oxygen carriers for selective oxidation at relatively lower temperatures (≤500°C). Particles of a $Sr_{0.8}Ca_{0.2}FeO_{3-\delta}$ oxygen carrier were impregnated with 10 wt% $NaNO_3$, and then calcined in ambient air at 500°C, causing the nitrate to melt, wetting the surface of the oxygen carrier. The calcination temperature was sufficient to induce decomposition of the nitrate to sodium oxide, which reacted with atmospheric $CO_2$ to form a solid layer of $Na_2CO_3$ at the surface of the material. The $Na_2CO_3/Sr_{0.8}Ca_{0.2}FeO_{3-\delta}$ material was arranged in a packed bed reactor, in series with a bed of a catalyst selective for oxidative dehydrogenation of ethane, $MoVNbTeO_x$ (Chen *et al.*, 2023), with a schematic of the arrangement shown in Fig. 1.6a.

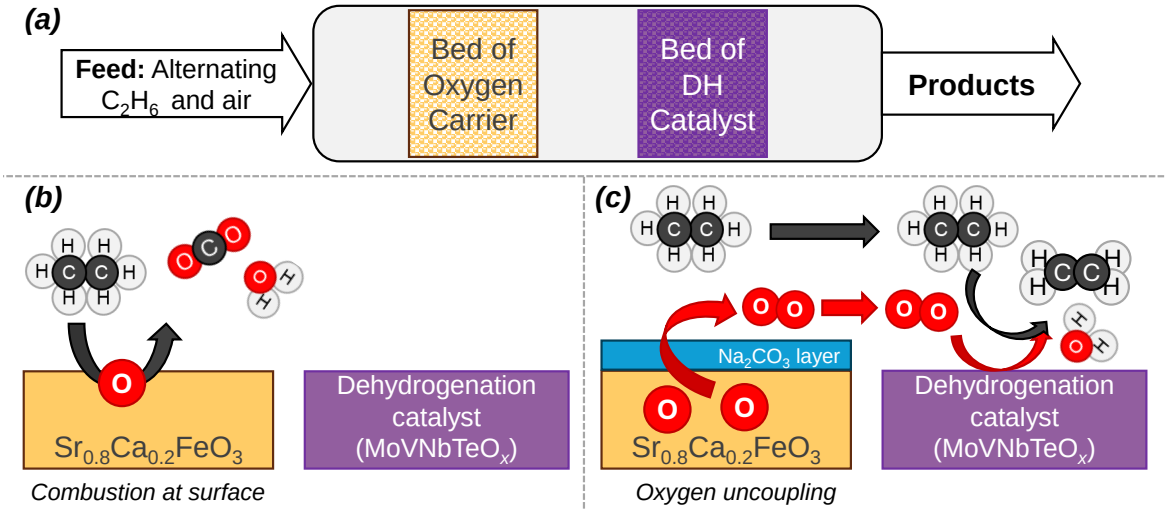


Fig. 1.6 Schematic of chemical looping oxidative dehydrogenation (CL-ODH): **(a)** Overall reactor arrangement, with consecutive beds of **(b)** $Sr_{0.8}Ca_{0.2}FeO_{3-\delta}$ or **(c)** $Na_2CO_3/Sr_{0.8}Ca_{0.2}FeO_{3-\delta}$, and $MoVNbTeO_x$, showing the mechanisms described by Luongo *et al.* (2022). In each case, the reactions during the reduction step under flowing ethane are shown.

Chemical looping cycles of feeding ethane and air alternately were applied over the layered bed at 500°C (well below the melting point of $Na_2CO_3$, 851°C). Without the protective layer of $Na_2CO_3$, the ethane partially combusted over the $Sr_{0.8}Ca_{0.2}FeO_{3-\delta}$ oxygen carrier, with poor performance for selective dehydrogenation (<20% yield of ethylene), shown in Fig. 1.6b. In the absence of the $MoVNbTeO_x$ catalyst, no oxidative dehydrogenation occurred, but $O_2$ gas was detected in the outlet stream, as a result of oxygen uncoupling from the oxygen carrier. From isotope tagging experiments,

producing samples of $Sr_{0.8}Ca_{0.2}Fe^{18}O_{3-\delta}$, the transport of oxygen from the oxygen carrier through the $Na_2CO_3$ layer was found to be feasible under reaction conditions, with the solid carbonate layer likely behaving in a manner analogous to the 'inert' molten salt layers described by Liu and Li (2023). Therefore, Luongo *et al.* (2022) concluded that the selective CL-ODH reaction proceeded *via* the scheme shown in Fig. 1.6c, with the $Na_2CO_3/Sr_{0.8}Ca_{0.2}FeO_{3-\delta}$ material undergoing CLAS cycles to provide $O_2$ gas to the reaction stream, allowing oxidative dehydrogenation of ethane over the bed of $MoVNbTeO_x$ catalyst.

However, the applicability of solid protective carbonate layers for other selective oxidation reactions, and in particular, for oxygen carriers incorporating metal catalysts, remain underexplored. Furthermore, the three-way interactions between the oxygen carrier, the protective carbonate layer, and a metal catalyst impregnated onto the surface of the material, are unknown.

## 1.6 Selective oxidation of propylene *via* chemical looping

As discussed in Section 1.1.2, chemical looping processes have been investigated for the selective conversion of propylene to value-added products. Gan *et al.* (2024) investigated chemical looping ammoxidation (co-feeding ammonia during reduction to form a product containing nitrogen) of propylene over commercial $BiMoO_x$ catalysts to form acrylonitrile, with chemical looping outperforming steady-state operation in terms of time-averaged product yield.

Processes for the chemical looping oxidation of propylene have proven more elusive. Chemical looping over unsupported $PdO_x$ produced propylene oxide (PO) at up to 28% selectivity during the first cycle, with acrolein and propanal forming *via* isomerisation of PO at 38% and 33% selectivity respectively (Dibenedetto *et al.*, 2008). However, overall conversion of propylene was low, at around 0.4%, and the $PdO_x$ oxygen carriers used did not show a consistent product distribution over multiple redox cycles, with 98% selectivity towards acrolein at 0.01% propylene conversion for the second and subsequent cycles. The broad distribution of oxygenate products was ascribed to the ability of Pd to act as a catalyst for hydrogen transfer reactions, which aid isomerisation of PO to other oxygenates. In contrast, near 100% selectivity for PO was achieved using unsupported $V_2O_5$ as an oxygen carrier, but at very low (0.03%) conversion

of propylene. The use of $V_2O_5$ supported on $SiO_2$ or $\gamma$-$Al_2O_3$ allowed for a modest improvement in the conversion of propylene, up to 0.1%, at 70% selectivity towards PO over a single reduction step. Fattore (1975a,b) investigated $Bi_2O_3$–$MoO_3$ and $Fe_2SbO_x$ for oxidation of propylene in the absence of gaseous oxygen, finding that acrolein was the dominant $C_3$ oxygenate product over $MoO_3$, 2 $Bi_2O_3$·$MoO_3$, and $Fe_2SbO_x$, and that oxidative coupling to form $C_6$ molecules (hexadiene or benzene) was favoured over $Bi_2O_3$ and $Sb_2O_4$. However, no PO was detected over any of the oxygen carriers investigated, nor were the reactions repeated over multiple redox cycles.

Silver-based catalysts on metal oxide supports, as applied for chemical looping epoxidation of ethylene, have been widely investigated for selective oxidation of propylene (Teržan *et al.*, 2020) under conventional oxidation conditions (*i.e.* not chemical looping), but have generally shown relatively poor selectivity towards $C_3$ oxygenates. For propylene reacting with oxygen over Ag, the $\gamma$-carbon atom in propylene preferentially reacts with atoms of oxygen adsorbed at the Ag surface, $O_a$, to form $CO_2$ *via* complete combustion. The complete combustion reaction can be partially suppressed by the addition of chloride species, either on the surface of the catalyst or in the feed gas (Charisteidis and Triantafyllidis, 2020; Lu and Zuo, 1999; Seubsai and Senkan, 2011) but at the penalty of decreased propylene conversion. Selectivity towards $C_3$ oxygenates *via* oxidation of propylene is further limited by isomerisation reactions. Kulkarni *et al.* (2012) investigated the reactions of PO over Ag surfaces under aerobic and anaerobic conditions, finding that propylene oxide can undergo H-transfer reactions to form a broad distribution of products, including propanal, acetone, allyl alcohol, and acrolein.

The use of Ag–Au bimetallic catalysts in selective oxidation reactions has been investigated by Geenen *et al.* (1982), where increasing the proportion of Au to Ag reduced the extent of complete combustion, with acrolein as the favoured oxygenate product. The increase in selectivity towards acrolein was attributed to the catalysts having isolated Ag sites (*i.e.* the separation between the catalyst's active sites greatly exceeded the size of propylene molecules), which inhibit the dissociation of molecular oxygen from forming two neighbouring $O_a$–Ag species. Therefore, the favoured surface species was adsorbed molecular $(O_2)_a$ (Geenen *et al.*, 1982; Rojluechai *et al.*, 2007), selective towards acrolein.

Chemical looping processes using Ag/$SrFeO_{3-\delta}$ have been shown to be effective for chemical looping epoxidation of ethylene (Chan *et al.*, 2018b; Damba *et al.*, 2024), however, such materials have not yet been applied for selective oxidation of propylene.

Furthermore, the effect of adding catalytic promoters (Cl and Au) to the Ag/$SrFeO_{3-\delta}$ on the reaction mechanism during chemical looping is unknown.

## 1.7 Objectives and structure of this Dissertation

Strontium ferrite has been identified as a suitable oxygen carrier for various chemical looping processes at the laboratory scale, with the addition of Ag as a catalyst enabling applications for the selective oxidation of hydrocarbons. The primary research objectives of this Dissertation are to understand how modifying $SrFeO_{3-\delta}$ with additional elements affects the reactive properties of the oxygen carrier, and to understand the mechanisms by which lattice oxygen from the oxygen carrier becomes available for reaction at the active catalytic sites on Ag. Specifically, the aims of this Dissertation are:

- To understand the influence of bulk, surface, and structural dopants on the thermodynamic properties and kinetics of oxygen uncoupling and re-oxidation for $SrFeO_{3-\delta}$.
- To apply *in-situ* characterisation in order to understand the bulk and surface reactions over the course of each chemical looping cycle, and the pathways taken by oxygen from the $SrFeO_{3-\delta}$ lattice to the surface of Ag.
- To assess the reactive properties of structured Ag/$SrFeO_{3-\delta}$ materials incorporating a protective carbonate layer, applied for selective oxidation reactions, and to determine whether an exposed Ag surface, and, or, contact between the Ag catalyst and the $SrFeO_{3-\delta}$ oxygen carrier, is necessary for reaction.
- To investigate the chemical looping oxidation of propylene over Ag/$SrFeO_{3-\delta}$-based materials modified with Cl and, or Au.

The methods applied in this Dissertation to prepare and characterise oxygen carriers, and descriptions of the reactors used in experiments, are given in Chapter 2.

In Chapter 3, a series of $SrFeO_{3-\delta}$ oxygen carriers modified with Ag and $CeO_2$ at the surface, bulk, and in the structure, were prepared. The effects of each modification method on the rate of oxygen release and re-uptake in a CLAS system were investigated, and kinetic parameters estimated for reduction and oxidation. The influence of Ag on the thermodynamic properties of $SrFeO_{3-\delta}$ was characterised by thermogravimetric analysis.

In Chapter 4, *in-situ* characterisation techniques (X-ray diffraction, transmission electron mictroscopy, X-ray photoelectron spectroscopy, and Raman spectroscopy) were applied to deduce the bulk and surface changes in $SrFeO_{3-\delta}$ and $Ag/SrFeO_{3-\delta}$ over the course of each chemical looping cycle. Reduction in hydrogen and oxidation in air were used as model reactions, in order to understand the interactions between the Ag catalyst and the $SrFeO_{3-\delta}$ support, and the mechanisms by which lattice oxygen from the $SrFeO_{3-\delta}$ was transported to the surface of Ag.

In Chapter 5, a series of structured $Ag\text{-}Na_2CO_3\text{-}SrFeO_{3-\delta}$ materials were prepared in order to understand the applicability of protective carbonate layers in materials for chemical looping oxidation incorporating metal catalysts. The materials were applied for epoxidation of ethylene as a model selective oxidation reaction operated in a chemical looping mode.

In Chapter 6, $Ag/SrFeO_{3-\delta}$ modified with Cl and Au was investigated for the chemical looping oxidation of propylene. The reaction mechanisms at the surface of the modified catalysts to form various oxygenated $C_3$ products were considered.

Lastly, Chapter 7 discusses the overall conclusions arrived at from the work in this Dissertation, and presents suggestions for future research. Further experimental measurements and supporting data for each Chapter are provided in the Appendices.

# Chapter 2

# Experimental methods

This Chapter discusses the experimental methods used in this Dissertation, including synthesis of materials (Section 2.1), descriptions of characterisation techniques used (Section 2.2), and the design and operation of packed bed reactors used in experiments (Section 2.3). Further experimental details specific to a particular section of work are included in subsequent Chapters where relevant.

## 2.1 Preparation of oxygen carriers

### 2.1.1 Solid-state synthesis

The oxygen carrier used in experimental work was the mixed metal oxide strontium ferrite ($SrFeO_{3-\delta}$, with synthesised material referred to as SFO for brevity). Particles of SFO were prepared using a solid-state method adapted from Marek *et al.* (2018a), with a typical batch size of 0.5 mol SFO (95.7 g of product). Stoichiometric quantities of strontium carbonate ($SrCO_3$, Sigma Aldrich, $\geq$98%) and iron (III) oxide ($\alpha$-$Fe_2O_3$, Honeywell Fluka, $\geq$99%) were added to a 250 mL stainless steel grinding jar with 10-13 stainless steel balls (O.D. 20 mm), and mixed with 75 mL ethanol (Fisher Scientific, 99.8%) to form a homogeneous paste. The mixture was then milled using a ball mill (Pulverisette 6, Fritsch) with 2 min of milling at 600 rpm, followed by 20 min of cooling in ambient air, repeated 15 times. The resulting mixture was dried at 50°C in air for 24 h, then crushed and seived to $\leq$355 $\mu$m. The particles were then calcined at 1000°C for 12 to 22 h in a muffle furnace under static air, either in a single step, or in multiple steps with intermediate cooling to room temperature, to form coarse, dark grey particles. No differences in physical or chemical properties were observed between

batches of SFO produced with differing calcination conditions. Each batch of strontium ferrite prepared was verified to have a phase purity of at least 95 wt% perovskite $SrFeO_{3-\delta}$ by X-ray diffraction, as described in Section 2.2.1. The main impurity phases detected included Ruddlesden-Popper $Sr_3Fe_2O_7$, and unreacted $SrCO_3$ (up to *c.* 2 wt% each). For all subsequent calculations, the presence of impurity phases was neglected, with the phase purity of the SFO starting material assumed to be 100 wt% perovskite $SrFeO_{3-\delta}$. Therefore, properties estimated on a mass basis (*e.g.* rates of reaction, and oxygen capacity) represent a lower bound estimate, as the true mass of $SrFeO_{3-\delta}$ used in experiments was slightly lower than the assumed mass used for analysis.

### 2.1.2 Surface-modified oxygen carriers

Modified oxygen carriers were prepared with silver deposited on the surface of SFO by incipient wetness impregnation, to achieve a uniform dispersion of Ag nanoparticles (Marek and García-Calvo Conde, 2021). A precursor solution containing Ag was prepared by dissolving $AgNO_3$ (Alfa Aesar, >99.8%) in deionised water. The concentration of the $AgNO_3$ solution was adjusted to achieve the desired nominal Ag loading (generally 10 wt% or 15 wt%). The resulting solution was added dropwise to particles of SFO (sieved to 180-355 $\mu$m), with manual mixing using a spatula until all liquid was absorbed. The particles were dried at 120°C for 12 h, then calcined at 650°C for 5 h in static air to decompose the $AgNO_3$, forming metallic Ag and gaseous nitrogen oxides. Samples of SFO impregnated with Ag were designated Ag/SFO.

To prepare particles of SFO with AgCl deposited at the surface, the addition of $AgNO_3$ was followed by the addition of hydrochloric acid (37wt%, VWR), added dropwise with manual mixing, followed by drying and calcination as for Ag/SFO. A 50 mol% excess of HCl was added with respect to Ag, to ensure all Ag present reacted to form AgCl.

Particles of SFO modified with $CeO_2$ at the surface were prepared by incipient wetness impregnation of $Ce(NO_3)_3{\cdot}6H_2O$ (Acros Organics, 99.5%) dissolved in deionised water. Saturated $Ce(NO_3)_3$ solution was added to SFO until the particles coalesced (corresponding to maximum liquid volume for incipient wetness impregnation), giving a nominal loading of 9.3wt%. The impregnated particles were dried at 120°C for 12 h, then calcined at 650°C for 5 h in static air.

Oxygen carriers modified with sodium carbonate were prepared using a method adapted from Luongo *et al.* (2022), illustrated in Fig. 2.1. Sodium nitrate ($NaNO_3$, Aldrich, 99%) was dissolved in deionised water, with the nitrate mass chosen to give a

nominal final loading of 10 wt% sodium carbonate. The precursor solution was then added to SFO dropwise with mixing, dried for 12 h at 120°C, and calcined at 700°C for 5 h to ensure complete decomposition of the nitrate (Bond and Jacobs, 1966). During calcination, the impregnated nitrate melted at 308°C, wetting the surface of the particle of SFO (Luongo *et al.*, 2022). Then, at >600°C, the nitrate decomposed and reacted with atmospheric $CO_2$ in ambient air, to form a solid layer of the sodium carbonate, covering the surface of SFO. Materials modified with both Ag and $Na_2CO_3$ were prepared by sequential impregnation and calcination, described in further detail in Chapter 5.

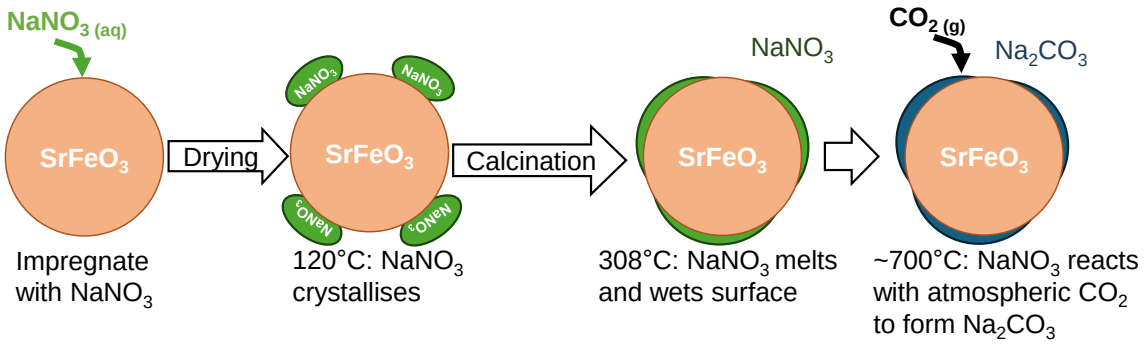


Fig. 2.1 Schematic diagram showing steps in impregnation of SFO with an alkali metal nitrate to form a sodium carbonate layer.

Samples of SFO were modified with gold using two preparation methods. Gold-containing samples with chloride ions present in the final material were prepared using a method adapted from Suo *et al.* (2008). A batch of precursor solution containing Au was prepared by dissolving $AuCl_3$ (Alfa Aesar, >99.8%) in deionised water (0.65 g $mL^{-1}$). Then, the solution was adjusted to pH 7-8 by adding NaOH solution (Fisher Scientific, 10% w/v) dropwise to form the $[AuCl(OH)_3]^-$ ion in solution. The gold precursor solution was added dropwise to SFO, then dried for 12 h at 120°C and calcined for 5 h at 650-700°C. For materials modified with both Ag and Au, the SFO was impregnated with both Ag and Au precursor solution, then dried and calcined. During impregnation, the $AgNO_3$ reacted with the $AuCl_3$ solution to form AgCl, Au, and AgAu on the surface of the calcined material. The target Ag-Au ratio was adjusted by varying the volumes of each solution added, described in further detail in Chapter 6.

To prepare SFO modified with Au without the presence of chloride in the final material, a ligand complexation method was used, adapted from Murayama *et al.* (2017). In a typical batch, 1.82 mmol $\beta$-alanine (Acros Organics, 99%) was dissolved in 2 mL NaOH solution (Fisher Scientific, 1.25 M), with 3 mL ethanol (Fisher Scientific,

99.8vol%) then added. A separate solution was prepared by adding 1 mL $HAuCl_4$ solution (Acros Organics, ACS Reagent, 0.227 M) to 4 mL ethanol. The two solutions were mixed, and cooled at -18°C for approximately 12 h, to form a pale orange precipitate. The precipitate was separated by centrifugation at 528 RCF for 10 min with cooling to 4°C, then washed with 70 vol% ethanol (*i.e.* the concentration of ethanol in the supernatant). The solids were dried overnight in a dessicator to form a dark Au-($\beta$-alanine) solid, which was insoluble in 70 vol% ethanol but soluble in water. The Au-($\beta$-alanine) was dissolved in deionised water, and added dropwise to particles of SFO. To prepare mixed Ag/Au-L/$SrFeO_{3-\delta}$ materials, $AgNO_3$ solution was then added dropwise, and the material dried for 12 h at 120°C and calcined for 5 h at 650°C.

### 2.1.3 Bulk-modified oxygen carriers

Strontium ferrite with $CeO_2$ mixed into the bulk was prepared by mixing 0.025 mol $CeO_2$ with 0.5 mol $SrCO_3$ and 0.25 mol $Fe_2O_3$, for a target loading of 5.0 mol% $CeO_2$ (4.3 wt%). The material was then ball-milled with ethanol, dried, and calcined, as described in Section 2.1.1. The $CeO_2$ powder was prepared by heating $Ce(NO_3)_3{\cdot}6H_2O$ to 500°C at a rate of 1°C $min^{-1}$ in air to induce thermal decomposition, holding for 4 h, then slowly cooling to room temperature (Marek *et al.*, 2020). Partial substitution of strontium with cerium to form produce $Sr_{0.95}Ce_{0.05}FeO_{3-\delta}$ was performed by mixing 0.025 mol $CeO_2$ with 0.475 mol $SrCO_3$ and 0.25 mol $Fe_2O_3$. The sample was ball-milled and dried, then calcined in air at a higher temperature of 1200°C in two steps of 4 and 18 h respectively (Markov *et al.*, 2020). After initial calcination, the material produced was not active for redox reactions, potentially as a result of incomplete reoxidation during rapid cooling in air to room temperature after calcination, or incomplete incorporation of Ce into the perovskite structure (Markov *et al.*, 2020). To activate the material, the material was deeply reduced to aid incorporation of $Ce^{3+}$ into the strontium ferrite structure and to remove any residual $CeO_2$ (Marek and García-Calvo Conde, 2021), then, slowly cooled in air to ensure the material reoxidised (Marek *et al.*, 2018b). The particles of synthesised $Sr_{0.95}Ce_{0.05}FeO_{3-\delta}$ were reduced for 1.5 h in flowing 5 vol% $H_2$ (certified at 4.87 vol%, balance $N_2$, Air Liquide) at 700°C in a quartz reactor tube, using an electric tube furnace for heating. The material was then removed from the reactor, and reoxidised by heating the sample to 650°C in air in a muffle furnace, holding for 30 min, and cooling to room temperature at a ramp rate of -2°C $min^{-1}$. The Ce was confirmed to remain in the perovskite structure by X-ray diffraction, as described in Chapter 3, and the activated material was able to cyclically

release and uptake oxygen in redox reactions. However, the exact mechanisms by which the procedure of deep reduction followed by gradual oxidation helps activate oxygen carrier materials are not fully understood (Marek *et al.*, 2018b).

The samples prepared and used in experiments in each Chapter are summarised in Table 2.1.

Table 2.1 Summary of samples prepared in each Chapter, and preparation methods used

| **Chapter** | **Description of samples** |
|---|---|
| 3 | SFO modified with $CeO_2$ at surface (9.3 wt%);<br>Bulk modification of SFO with $CeO_2$ (4.3 wt%);<br>Structural doping of SFO with Ce (5 mol%);<br>SFO modified with Ag at surface (15 wt%) |
| 4 | SFO modified with Ag at surface (10 wt% and 15 wt%) |
| 5 | SFO impregnated with Ag (10wt%) and $Na_2CO_3$ (10 wt%) |
| 6 | SFO modified with Ag, AgCl, and Au (2.5-10 wt%) |

| **Chapter** | **Preparation method(s) used** |
|---|---|
| 3 | Incipient wetness impregnation ($Ce(NO_3)_3{\cdot}6H_2O$ or $AgNO_3$);<br>Solid-state ball milling ($CeO_2$) |
| 4 | Incipient wetness impregnation ($AgNO_3$) |
| 5 | Incipient wetness impregnation ($AgNO_3$ and $NaNO_3$) |
| 6 | Incipient wetness impregnation ($AgNO_3$ and, or $AgCl_3$);<br>Treatment with HCl;<br>Impregnation with Au-($\beta$-ala) complex |

## 2.2 Characterisation of prepared materials

### 2.2.1 X-ray diffraction (XRD)

The phase composition of samples produced by solid state synthesis was determined using powder X-ray diffraction (XRD). Samples were prepared by dispersing a thin layer of particles onto a glass cover slip coated with silicone grease, then, the sample was introduced into the diffractometer instrument, using Cu-K$\alpha$ radiation at 40 kV voltage and 40 mA current to collect diffraction patterns. Two different models of diffractometer instrument (Bruker D8 Discover or Malvern Panalytical Empyrean) were used to collect the XRD measurements reported in this Dissertation. The phase composition of the samples was estimated by Rietveld or Pawley refinement, using Profex (Doebelin and Kleeberg, 2015) and TOPAS v5 (Coelho, 2018) software. Phases were fitted based on reference structures from the Inorganic Crystal Structure Database (ICSD) (Belsky *et al.*, 2002), with ICSD collection codes for phases used given in Appendix A, Table A.1. In a typical measurement, diffraction patterns were collected over the angular range $2\theta$ = 5-80° with a step size of 0.05° and a step time of 2 s, with a typical scan time of approximately 50 min. Measurements at low Bragg angles ($2\theta < 20°$) gave a large, broad background peak, as a result of diffraction from the amorphous grease used to affix the sample to the cover slip.

Diffraction patterns at above-ambient temperature under varied gas environments were collected by mounting the powder sample in a gas-tight furnace with a rotating sample stage (Anton Paar, XRK 900). Gases (compressed air, $N_2$, or 5 vol% $H_2$ in $N_2$, all BOC) were passed through the sealed sample chamber at a flowrate of 200 mL min$^{-1}$, set using calibrated rotameters. For *in-situ* measurements, to mitigate changes in the composition of samples over the course of each scan as a result of reaction, shorter scan times were used, with an angular range of $2\theta$ = 20-70°, giving an overall scan time of approximately 20 min. Some of the *in-situ* XRD measurements reported in this Dissertation were performed by Dr Chris Truscott (Yusuf Hamied Department of Chemistry, University of Cambridge).

The mean crystallite size of materials impregnated onto SFO was estimated from XRD patterns using Eq. 2.1 (Scherrer, 1918), where $\tau$ is the mean crystallite size (nm), $K$ is a dimensionless shape factor (taken to be approximately $K = 0.9$), $\lambda$ is the X-ray wavelength (0.15406 nm for Cu-K$\alpha$ radiation), $\beta$ is the full width at half maximum of a given peak in the diffraction pattern (radians), and $\theta$ is the Bragg angle of the peak centre (radians).

$$\tau_{cryst} = \frac{K\lambda}{\beta cos(\theta)} \tag{2.1}$$

### 2.2.2 Thermogravimetric analysis (TGA)

Thermogravimetric analysis (TGA) of samples was performed using a Metter Toledo TGA/DSC 1 or TGA/DSC 3+ analyser with a horizontally oriented microbalance. Reactive gases were delivered over the sample *via* a capillary tube (shown in Fig. 2.2), with the flow rate of each gas set to 50 mL $min^{-1}$. An alumina crucible was loaded with 20–50 mg of particulate sample and placed on the balance pan. The temperature program, comprising ramping steps at defined temperature ramp rates, and hold steps at given temperature setpoints, was set using StarE software. Delivery of reactive gas was controlled using computer controlled solenoid valves to switch between gases (all gases used in the TGA instruments were BOC, 99.99+%). The chamber and balance were continuously purged with protective flows of $N_2$, each with a flow rate of 50 mL $min^{-1}$, for a total flow of 150 mL $min^{-1}$ through the TGA sample chamber. For experiments using samples of SFO-based materials, samples were cleaned by heating in air to 800-900°C, then cooling to room temperature at 10°C $min^{-1}$ to remove any carbonate impurities (Marek *et al.*, 2018a).

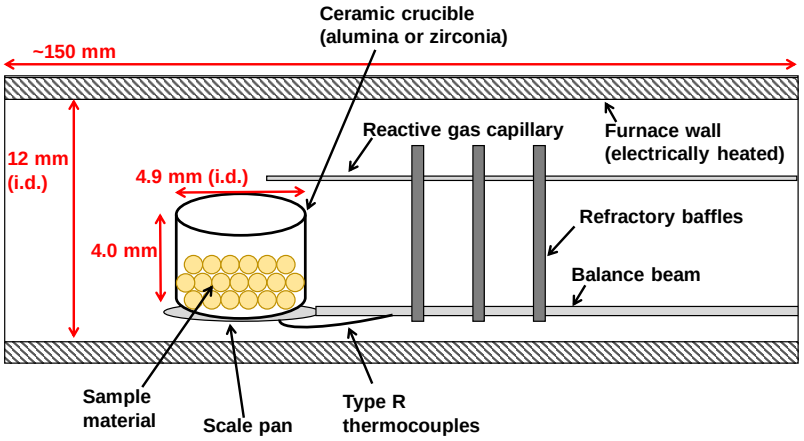


Fig. 2.2 Schematic diagram showing internal components of TGA furnace. Not to scale.

In Chapters 3 and 5, a temperature ramp in the TGA was used to determine the onset temperature at which samples undergoing reduction began to lose mass, $T_{onset}$, found using the `findchangepts` function in MATLAB. When temperature in the TGA

furnace was changed, the change in buoyancy of gases flowing around the balance beam resulted in apparent changes in sample mass, even in the absence of any reaction of the solids. To correct for the mass change induced by changes in buoyancy, for all TGA experiments, a blank run was generated by performing the experimental procedure using an empty sample crucible, then, the mass change associated with the blank was subtracted from subsequent measurements of samples. The difference between raw TGA output, and corrected mass with blank subtraction, is shown in Fig. 2.3a.

Furthermore, during a temperature ramp at a constant heating rate, the onset temperature for a gas-solid reaction (equivalently described as the first temperature where $\frac{d^2m}{dT^2} = 0$, where $m$ is the sample mass and $T$ is the sample temperature) is related to both the apparent activation energy of the reaction, and the heating rate used (Criado and Ortega, 1986; Vyazovkin, 2020). Hence, the effect of varying ramp rate is shown in Fig. 2.3b, where a sample of Ag/$SrFeO_{3-\delta}$ was heated from 50-900°C at rates of 2.5, 5, 10, and 20 °C $min^{-1}$, with $N_2$ as the reactive gas. A *c.* 35°C range in apparent onset temperatures was observed, with faster ramp rates showing higher values of $T_{onset}$. Hence, to ensure measurements of different samples were comparable to one another, a ramp rate of 10°C $min^{-1}$ was used for all temperature ramp experiments in the TGA.

Additional factors in TGA experiments can affect rate of mass loss, including flow patterns of gas around the sample depending on the TGA arrangement, diffusion limitations within the sample, and thermal dissipation within the sample, discussed in detail by Steiner *et al.* (2024). Given the difficulties in using TGA to access the kinetically controlled regime of reactions, TGA measurements were not used to quantify kinetic parameters; instead, to assess reaction kinetics, experiments in a packed bed with well-defined gas flow were performed, as described in Section 2.3.1.

In Chapter 3, experiments were performed in the TGA to determine the equilibrium non-stoichiometry (3 - $\delta$) of SFO based materials, by bringing the materials to equilibrium under varied temperature and partial oxygen pressure ($pO_2$) conditions. For each gas composition of interest, a target $pO_2$ was achieved by blending compressed air (taken to have nominal $pO_2 = 0.21$ atm), and $N_2$ (rated at nominal $pO_2 = 10^{-5}$ atm) from gas cylinders. As a result of mixing between the reactive gas and the purge and protective gases, the concentration of the reactive gas at the sample crucible was expected to be diluted, with dilution factors between 1/3 and 2/3 reported in literature (Hu *et al.*, 2016; Marek *et al.*, 2018a) for the experimental arrangement used here. Furthermore, after switching the gases supplied to the TGA furnace chamber, variation

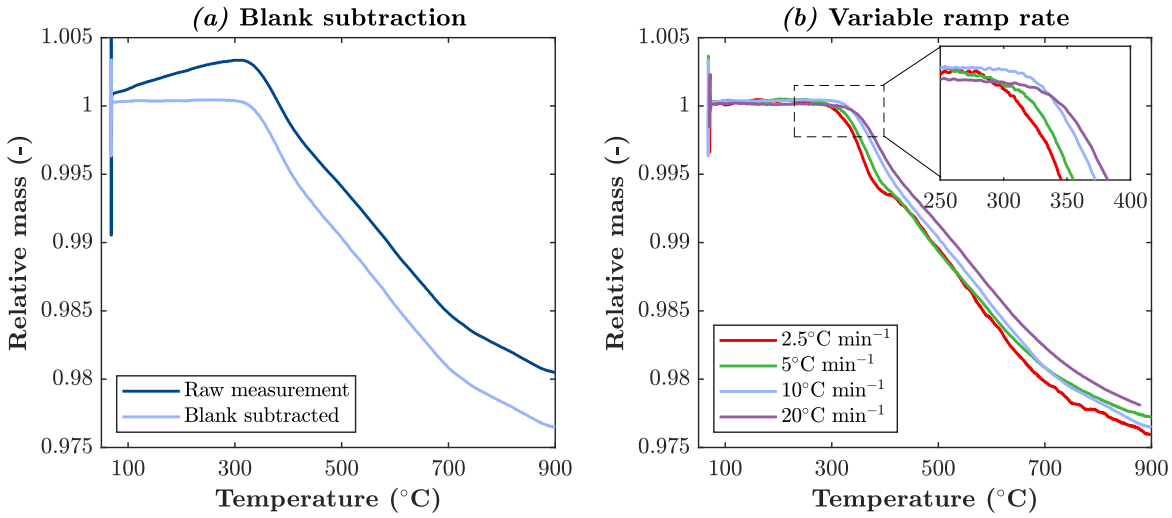


Fig. 2.3 **(a)** Comparison between raw and blank-subtracted measurements during reduction of $Ag/SrFeO_{3-\delta}$ between 50-900°C in $N_2$ at a ramp rate of 10°C $min^{-1}$ and **(b)** differences in apparent onset of reduction with ramp rate varied between 2.5-20°C $min^{-1}$. Inset in **(b)** shows zoomed section to highlight onset temperature of reaction.

in $pO_2$ within the chamber was expected, as a result of imperfect mixing of gases (Steiner *et al.*, 2024).

Hence, in order to achieve accurately known $pO_2$ conditions at the sample for quantitative analysis of equilibrium properties, the blended gas at known $pO_2$ was passed through the purge and protective gas channels as well as through to the reactive gas capillary. The TGA system was purged with the blended gas for 2-4 h before experiments, to ensure all gas within the instrument was at a known, uniform value of $pO_2$. The required ratios of air and $N_2$ flow rates were set using rotameters, with the total flow to the TGA instrument kept at 150 mL $min^{-1}$ for all experiments.

The experiment started by ramping the temperature to a set-point in the range of 500–600°C, followed by a 3 h isothermal hold to allow the investigated sample to reach equilibrium with the flowing gas. The nominal $pO_2$ at the outlet of the TGA was verified using an ABB EL3020 analyser fitted with a Magnos 206 paramagnetic oxygen sensor (ABB Ltd.), with representative measurements of $pO_2$ in the TGA outlet gas over the course of an experiment shown in Appendix A, Fig. A.2.

### 2.2.3 Temperature programmed reduction ($H_2$-TPR)

Temperature programmed reduction in $H_2$ ($H_2$-TPR) was performed to assess the reactive properties of SFO-based materials in a reducing environment, and identify the temperatures required for removal of oxygen species at the surface of each sample (Pirola *et al.*, 2018). The $H_2$-TPR experiments were conducted using a purpose-built rig, with a schematic shown in Fig. 2.4. A sample of material (*c.* 30-50 mg) was placed in a quartz U-tube reactor, and secured using glass wool (Thermo Scientific). The U-tube was connected to the rig using Swagelok Ultra-Torr fittings, and inserted into the tube furnace, with a K-type thermocouple placed in the centre of the bed of active material.

To clean any adsorbed carbonaceous species or water from the surface of the material, air (99.99%, BOC) was passed over the sample at 50 mL $min^{-1}$ for 2 h at 650°C. The sample was then cooled to room temperature in air, then, the feed to the reactor was changed to 5 vol% $H_2$ in $N_2$ (99.99%, BOC). The reactor outlet was passed over a bed of crushed A3 molecular sieves (3 Å pore size, Acros Organics), and cooled to *c.* 2°C using a Peltier cooler, to remove any moisture generated by the reaction of the solid sample with $H_2$. The dried gas was then passed to a thermal conductivity detector (TCD, Valco Instruments Co. Inc.) to measure the difference in thermal conductivity between the outlet stream and a reference stream of 50 mL $min^{-1}$ He (99.99+%, BOC).

The voltage output from the TCD was calibrated with respect to 5 vol% $H_2$ in $N_2$, and pure $N_2$, allowing the hydrogen concentration in the outlet stream to be estimated by assuming a linear response from the TCD. The system was allowed to stabilise for *c.* 5 min with flowing 5 vol% $H_2$ in $N_2$ at room temperature, then, the furnace set-point temperature was ramped to 700°C at 5°C $min^{-1}$, with the temperature at the thermocouple in the centre of the bed recorded using a data logger (PicoLog TC-08, Pico Technology). The dead time in the system was estimated to be $t_{dead} = 16.0 \pm 0.5$ s by alternating feeds of 5 vol% $H_2$ in $N_2$ and $N_2$ to the reactor, and measuring the time taken for the TCD signal to change by 1%.

To determine the mixing time for the system, the glass U-tube was assumed to be well-described as a single continuous stirred-tank reactor (CSTR). Then, by modelling the sensor response after a gas switch as a first-order decay, the first-order mixing time was estimated to be $\tau_{mix} = 10.1 \pm 0.1$ s. Hence, the output signals from the TCD and temperature logger were corrected for dead time and mixing time, in order to synchronise the estimated sample temperature and TCD signal.

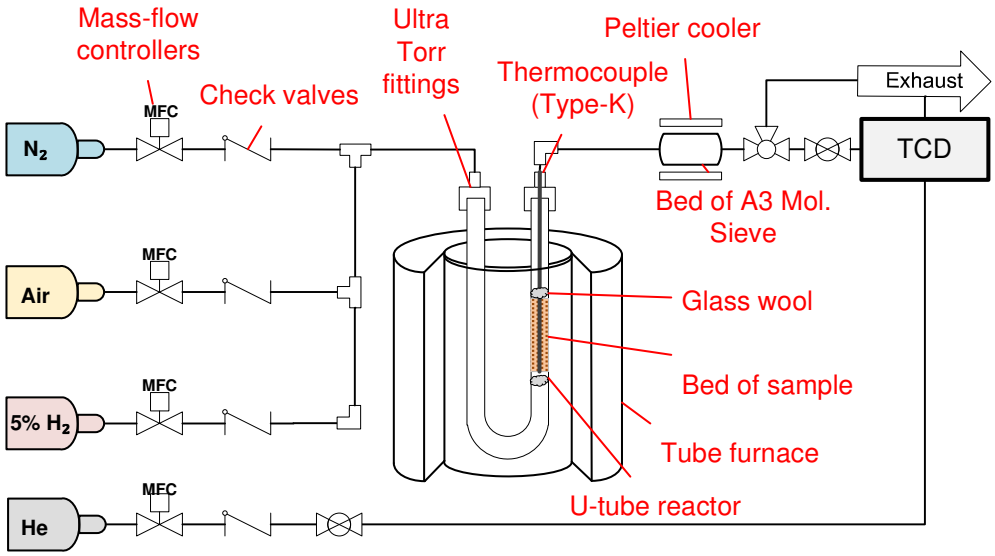


Fig. 2.4 Schematic diagram showing main components in rig used for $H_2$-TPR. Not drawn to scale; some pipework and fittings have been omitted for clarity.

### 2.2.4 Inductively coupled plasma atomic emission spectroscopy (ICP-AES)

To determine the elemental composition of synthesised materials, inductively coupled plasma atomic emission spectroscopy (ICP-AES) was performed. Briefly, a small sample (*c.* 2 mg) of solid material was dissolved in 5 mL nitric acid (67%, TraceMetal$^{TM}$, Fisher Scientific), then diluted to 10 mL volume using deionised water, and then a 0.5 mL sample of the resulting solution was further diluted 20-fold to 10 mL. The resulting solution was analysed for each element of interest using a Thermo Fisher Scientific ICAP7400 DuO instrument, calibrating the instrument response against a dilution series of known concentrations. Sample preparation, and measurements using ICP-AES, were performed by Dr Nigel Howard (Yusuf Hamied Department of Chemistry, University of Cambridge).

### 2.2.5 Transmission electron microscopy (TEM)

Transmission electron microscopy (TEM) measurements at room temperature were collected using a Thermo Fisher Talos F200X G2, operated at 200 kV accelerating voltage. Scanning transmission electron microscopy bright field (STEM-BF) and high-angle annular dark field (STEM-HAADF) images were collected in parallel, alongside energy dispersive X-ray spectra (EDS). Samples were crushed to a fine powder and

suspended in propan-2-ol (Fisher Scientific, 99%). A drop of the suspension was then deposited onto a holey carbon grid (53 $\mu$m, EM Resolutions), and inserted into the TEM instrument. The sample chamber was evacuated to $10^{-8}$ mbar total pressure, corresponding to an oxygen partial pressure of approximately $pO_2 = 2.1 \times 10^{-7}$ Pa.

Sample preparation, and collection of TEM measurements at room temperature reported in this Dissertation, was performed by Dr Heather Greer (Yusuf Hamied Department of Chemistry, University of Cambridge).

### TEM measurements with *in-situ* heating

Measurements using TEM at elevated temperatures (up to 700°C) were performed using a Thermo Fisher Spectra 300 instrument operating at 300 kV accelerating voltage. Samples were prepared for *in-situ* TEM analysis by manually crushing particles of synthesised material in an agate mortar. The resulting powder was then suspended in chloroform (Sigma Aldrich, >99%), and a drop of the resulting suspension was deposited onto a heating chip (DENSSolutions Wildfire), then dried for 45 min at 50°C on a hotplate. Adhesion of the crushed material to the heating chip was verified using an optical microscope, shown in Fig. 2.5. The chip was mounted in a sample holder and inserted into the TEM instrument, then, the sample temperature was increased to a given set-point value using DENSSolutions Impulse software, and allowed to settle for 5 min before collecting measurements. Selected area electron diffraction (SAED) patterns were collected at each point on the sample using a MerlinEM direct electron detector (Quantum Detectors), alongside EDS and electron energy loss spectra (EELS). Simulated SAED patterns were generated using SingleCrystal® (CrystalMaker Software).

The choice of solvent used to deposit the crushed sample onto the heating chip had a marked impact on the quality of TEM images. Initial attempts at sample preparation using propan-2-ol (Fisher Scientific, 99%) or acetone (Fisher Scientific, 99%) were unsuccessful, as the solvent resulted in excessive carbon deposition onto the sample, giving poor image resolution, whereas hexane (Sigma Aldrich, >99%) resulted in poor adhesion of crushed material to the heating chip.

The TEM measurements at elevated temperatures reported in this Dissertation were performed by Dr Simon Fairclough (Department of Materials Science and Metallurgy, University of Cambridge).

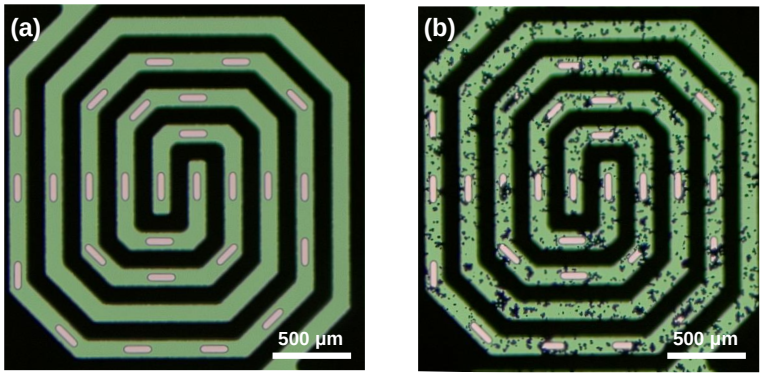


Fig. 2.5 Optical microscope images of the DENS Wildfire heating chip, **(a)** before and **(b)** after loading with crushed sample. Heating was provided by current supplied though wire coil (shown in black), with TEM images taken of particles suspended over oval holes (shown in white).

### Energy dispersive X-ray spectroscopy (EDS)

Energy dispersive X-ray spectroscopy (EDS) is a electron microscopy technique used to quantify the elemental composition of a solid sample. When exposed to incident electrons from the electron beam, atoms within the sample become excited, releasing X-rays at characteristic wavelengths, corresponding to the energies of specific electronic transitions within the sample material (Hodoroaba, 2020). A representative EDS spectrum over the X-ray energy range 0-15 keV for a sample of Ag/SFO is shown in Fig. 2.6, with peaks corresponding to electronic transitions in Ag, Fe, Sr and O indicated, as well as residual C and Cu present in the sample as a result of the preparation method.

Elemental composition was determined from EDS measurements by calculating the area between the peak and the baseline for each electronic transition, normalised according to the Cliff-Lorimer response factors for each element with respect to Si (Cliff and Lorimer, 1975; Sheridan, 1989). The EDS spectra were collected during TEM imaging using a SuperX EDS detector, with maps showing the distribution of elements of interest generated using the Hyperspy Python package (Pena *et al.*, 2017; Peña *et al.*, 2022) or Velox software (Thermo Fisher Scientific).

### Electron energy loss spectroscopy (EELS)

Electron energy loss spectroscopy (EELS) is a TEM technique which can be used to estimate the oxidation state of transition metals in a sample (Tan *et al.*, 2012). The

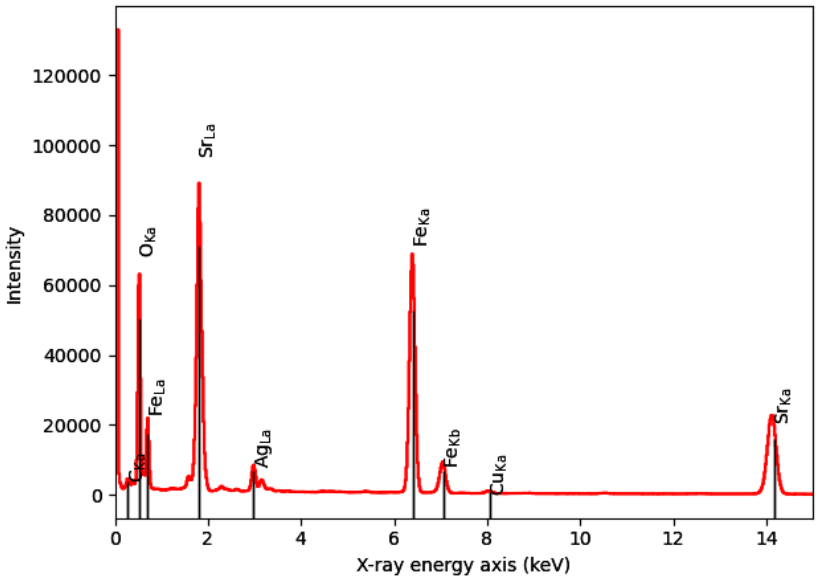


Fig. 2.6 Representative EDS spectrum for Ag/SFO, with labelled peaks corresponding to elemental transitions of interest.

majority of electrons incident on a thin sample pass through without interacting with the material - however, a small fraction of the electrons undergo inelastic scattering, losing energy (Hofer *et al.*, 2016). The energy loss during inelastic scattering corresponds to a specific electronic transition of an element in the sample, hence, by analysing the relative intensity of peaks in the EELS spectrum at characteristic energies, the local chemical environment can be estimated.

A Gatan Continuum EELS detector was used to collect EELS spectra in parallel with TEM images and EDS measurements. The resulting EELS spectra were processed and analysed using the Hyperspy Python package (Peña *et al.*, 2022). For a given EELS scan, low-loss (energy loss range -61-550 eV, shown in Fig. 2.7a) and high-loss (energy loss range 240-850 eV, shown in Fig. 2.7b) spectral measurements were collected in parallel.

Instrument calibration was performed by setting the position of the peak with maximum intensity in the low-loss spectrum to 0 eV, corresponding to transmitted electrons with no energy loss. The mean number of scattering events *per* incident electron is described by the dimensionless group $\frac{t}{\lambda_{fp}}$, corresponding to the ratio of sample thickness (nm) to electron mean free path (nm), estimated from Eq. 2.2 (Malis *et al.*, 1988), where $I_0$ is the area of the zero-loss peak, and $I_{tot}$ is the total area of the low-loss EELS spectrum. The values of $\frac{t}{\lambda_{fp}}$ estimated at each point on the samples of $SrFeO_{3-\delta}$ and $Ag/SrFeO_{3-\delta}$ used in EELS analysis are shown in Fig. 2.8.

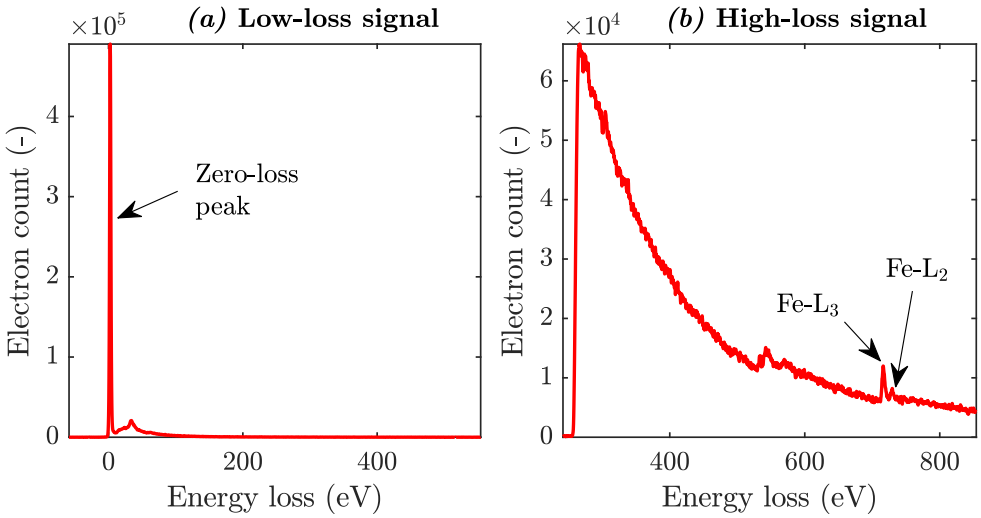


Fig. 2.7 **(a)** Low-loss and **(b)** High-loss EELS spectra for $Ag/SrFeO_{3-\delta}$, with peaks of interest indicated.

$$\frac{t}{\lambda_{fp}} = -ln\left(\frac{I_0}{I_{tot}}\right) \tag{2.2}$$

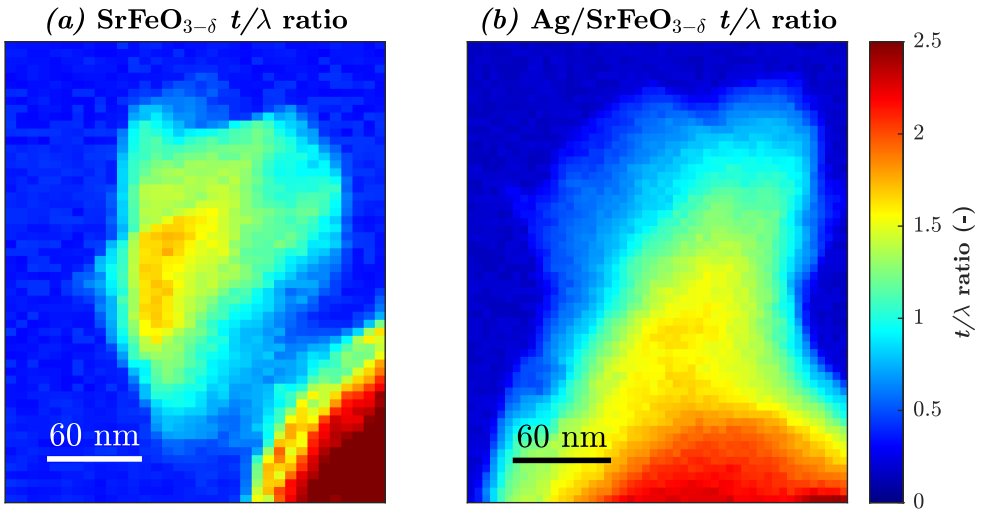


Fig. 2.8 Maps of $\frac{t}{\lambda_{fp}}$ ratio for **(a)** $SrFeO_{3-\delta}$ and **(b)** $Ag/SrFeO_{3-\delta}$, determined from Eq. 2.2 for each point on the samples.

Electron mean free path in EELS approximately scales according to the relationship $\lambda_{fp} \propto \rho^{-0.3}$, where $\rho$ is the material density (Iakoubovskii *et al.*, 2008). Taking the density of $SrFeO_3$ as 5.57 g cm$^{-3}$ (Villars and Cenzual, 2012), the electron mean free

path was estimated to be $\lambda_{fp} = 132.5$ nm by extrapolating experimental measurements reported by Iakoubovskii *et al.* (2008). Hence, the thicknesses at each point on the samples were estimated from the EELS signals, as described in Chapter 4.

For thick sections of each particle ($t > 250$ nm), plural electronic scattering (*i.e.* incident electrons undergoing multiple scattering events *per* electron), and low signal intensity as a result of attenuation through the solid resulted in poor quality EELS signals, and hence were excluded from subsequent calculations. To mitigate any further influence of plural scattering on the EELS signal, Fourier ratio deconvolution (Wang *et al.*, 2009) was applied between the low-loss and high-loss spectra using Hyperspy software, and a power-law background was fitted to the high-loss spectra.

### Determination of local oxidation state from EELS measurements

From the EELS measurements, the local oxidation state of Fe in $SrFeO_{3-\delta}$ was estimated from the intensity of the Fe-$L_3$ and Fe-$L_2$ peaks, corresponding to excitation of the Fe $2p_{3/2}$ and Fe $2p_{1/2}$ electrons respectively to the Fe 3d energy level (Garvie *et al.*, 1994). Baseline correction was performed by fitting a double-arctan function (Van Aken and Liebscher, 2002) of the form given in Eq. 2.3 to the EELS spectrum over the energy range 703.0-735.0 eV.

$$\begin{aligned} f(\Delta E) = h_0 + \frac{h_1}{\pi}\left(arctan\left(\frac{\pi}{w_1}\cdot(\Delta E - E_1)\right) + \frac{\pi}{2}\right) \\ + \frac{h_2}{\pi}\left(arctan\left(\frac{\pi}{w_2}\cdot(\Delta E - E_2)\right) + \frac{\pi}{2}\right) \end{aligned} \tag{2.3}$$

The inflection points of each arctan function were fixed at $E_1 = 713.0$ eV and $E_2 = 726.0$ eV, and widths fixed at $w_1 = w_2 = 1.0$ eV. The parameters $h_0$, $h_1$, and $h_2$, corresponding to the asymptotes of each arctan function, were then fitted to the experimental measurements. To evaluate the intensity of the $L_3$ and $L_2$ peaks, the area between the measured values and the fitted baseline, over an integration window of width 2 eV centred on the peak maximum, was found by numerical integration (Tan *et al.*, 2012; Van Aken and Liebscher, 2002). A representative EELS spectrum for Ag/SFO is shown in Fig. 2.9.

For oxides of Fe, the local oxidation state of Fe ions is correlated to the ratio of areas of the Fe-$L_3$ and Fe-$L_2$ peaks ($\frac{I_{L_3}}{I_{L_2}}$), provided the materials contain Fe in two oxidation states only (*i.e.* $Fe^{4+}$ and $Fe^{3+}$, or $Fe^{2+}$ and $Fe^{3+}$) (Tan *et al.*, 2012). Van Aken and Liebscher (2002) report the area ratios between the Fe-$L_3$:Fe-$L_2$ in EELS signals for mixed iron oxides with known $Fe^{3+}$ fraction ($\frac{Fe^{3+}}{\Sigma Fe}$), shown in Fig. 2.10.

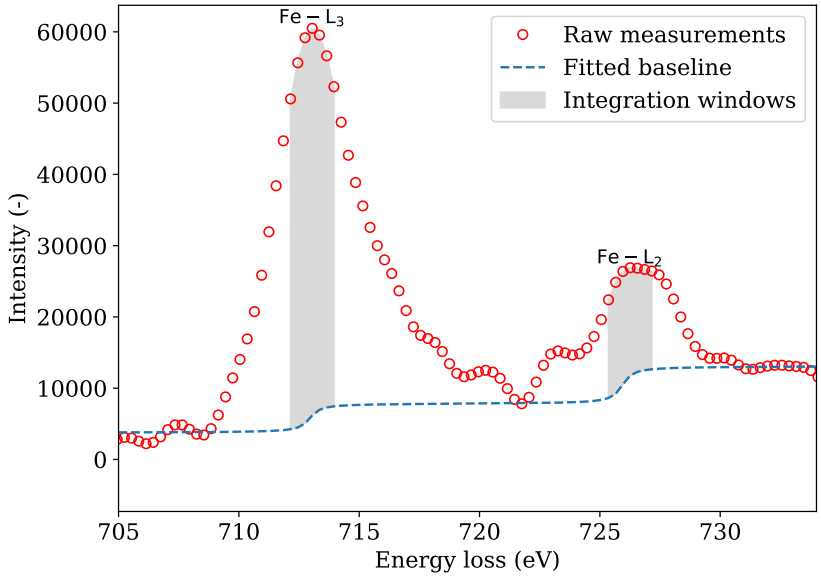


Fig. 2.9 Section of EELS spectrum showing Fe-$L_3$ and Fe-$L_2$ peaks, with fitted double arctan baseline and white line integration windows shown.

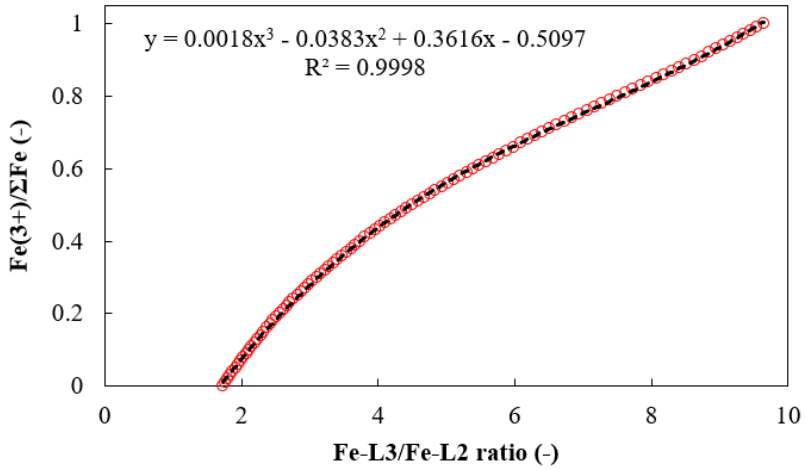


Fig. 2.10 Relationship between $\frac{I_{L_3}}{I_{L_2}}$ and $Fe^{3+}$ as a fraction of total Fe present ($\frac{Fe^{3+}}{\Sigma Fe}$) reported by Van Aken and Liebscher (2002) (red circles), with a third order polynomial function fitted (dashed black line).

By fitting a polynomial curve to the reported experimental measurements to extrapolate oxidation state from measured $\frac{I_{L_3}}{I_{L_2}}$, a map of the local oxidation state of iron in a sample can be estimated from EELS measurements (Lopez-Adams *et al.*, 2022). Assuming that iron is only present in $SrFeO_{3-\delta}$ and $Ag/SrFeO_{3-\delta}$ in the oxidation states $Fe^{4+}$ and $Fe^{3+}$ (Zhou and Goodenough, 2005), the $\frac{L_3}{L_2}$ intensity ratio was estimated for each point on the samples. In order to satisfy charge neutrality for $SrFeO_{3-\delta}$, assuming the strontium and oxygen are present as $Sr^{2+}$ and $O^{2-}$ ions respectively, the overall charge balance is given by Eq. 2.4.

$$1 \times 2 + \frac{Fe^{3+}}{\Sigma Fe} \times 3 + \left(1 - \frac{Fe^{3+}}{\Sigma Fe}\right) \times 4 + (3 - \delta) \times -2 = 0 \tag{2.4}$$

Hence, rearranging Eq. 2.4, the implied local oxygen stoichiometry of $SrFeO_{3-\delta}$ at each point on the samples was estimated from Eq. 2.5.

$$(3 - \delta) = 3 - \frac{1}{2} \times \frac{Fe^{3+}}{\Sigma Fe} \tag{2.5}$$

### 2.2.6 Scanning electron microscopy (SEM)

Scanning electron microscopy (SEM) images were taken using a Tescan Mira3 FEG-SEM microscope with an accelerating voltage of 5-15 kV, and secondary electron (SE) and back-scattered electron (BSE) detectors in parallel. Samples were prepared using a plasma sputterer to deposit a thin surface coating of Pt (*c.* 10-20 nm) over the sample, to mitigate the effect of surface charging. EDS spectra were collected using an Oxford Instruments Aztec Energy X-maxN 80 EDS, with elemental composition estimated as described in Section 2.2.5 using AZtec software (Oxford Instruments). The size distributions of particles deposited on the surface of SFO were estimated using ImageJ software (Rueden *et al.*, 2017) by manually measuring particles from SEM images.

### 2.2.7 X-ray photoelectron spectroscopy (XPS)

X-ray photoelectron spectroscopy (XPS) is a technique used to measure the chemical environments at the surface of solid materials, with penetration depth into the sample of the order 10 nm (Stevie and Donley, 2020). In XPS, a solid sample is illuminated with X-rays of known energy to induce photoemission, where the energy from a photon incident on the sample ionises the surface of the material, releasing an electron. By measuring the spectrum of kinetic energies of the electrons emitted from the sample,

the binding energies of the electrons in the sample can be estimated according to Eq. 2.6, where $h$ is the Planck constant (J s), $\nu$ is the frequency of incident X-rays ($s^{-1}$), BE is the binding energy of electrons in the sample (J), KE is the kinetic energy of electrons emitted from the sample (J), and $\phi_{spec}$ is an instrument work function (J), taken to be a constant.

$$h\nu = BE + KE + \phi_{spec} \tag{2.6}$$

Peaks in the spectrum of binding energies detected by XPS correspond to the release of electrons from specific elements in the sample, with multiple different electrons detected from some given elements (*e.g.* peaks at BE values in the range 130-136 eV correspond to electrons from Sr3d orbitals, and peaks at 265-275 eV correspond to electrons from Sr3p orbitals). Hence, from the energy range of peaks detected in the XPS spectrum, the elements present in the sample, and the number of distinct chemical environments for each element present, can be estimated.

*Ex-situ* XPS measurements were performed under high vacuum (*c.* $10^{-8}$ mbar) using a ThermoFisher Scientific Escalab 250Xi spectrometer, using a monochromated Al-K$\alpha$ X-ray source (1486.7 eV), with 20 eV detector scan pass energy. Analysis of XPS measurements was performed using CasaXPS software (Fairley *et al.*, 2021), with a Shirley type background fitted to all regions (Shirley, 1972).

Given XPS analysis relies on photoemission of electrons from the surface of the sample, the surfaces of electrically insulating samples develop a net positive charge over the course of measurements. The surface becoming charged results in an apparent shift in binding energy for electrons emitted from the sample, separate from any differences in chemical environment. To compensate for the charging effect, an electron 'flood-gun' was used in parallel with the X-ray source, to bombard the surface of the sample with low energy electrons in order to mitigate build-up of positive charge (Evans, 2022; Greczynski and Hultman, 2020). However, the use of a flood-gun resulted in an unknown fixed offset in measured binding energies, hence, the energy scale of each measurement wass calibrated relative to a chemical species at known binding energy, which was not expected to change significantly between different samples (Biesinger, 2022; Greczynski and Hultman, 2020).

The energy scales of each scan reported in Chapters 4 and 5 were calibrated relative to the C1s peak at 284.8 eV (Biesinger, 2022), corresponding to adsorbed aliphatic carbon onto the sample from exposure to trace hydrocarbon impurities in air ($C_{adv}$).

For measurements investigating the chemical state of Au described in Chapter 6, the energy scale was set by external calibration with respect to a Au foil standard in electrical contact with the samples (Alfa Aesar, 99.9975+%), by setting the binding energy of the $Au4f_{7/2}$ peak to 84.00 eV (Seah *et al.*, 1998). For samples where the Au external standard was used to calibrate the energy scale, the position of the $C_{adv}$ was found to shift to *c.* 284.5 eV (with an example for $Ag/SrFeO_{3-\delta}$ shown in Fig. 2.11), just within the reported maximum uncertainty range of 284.8±0.3 eV (Biesinger, 2022; Miller *et al.*, 2002), possibly as a result of the flood gun inducing a slight difference in energy shift between samples.

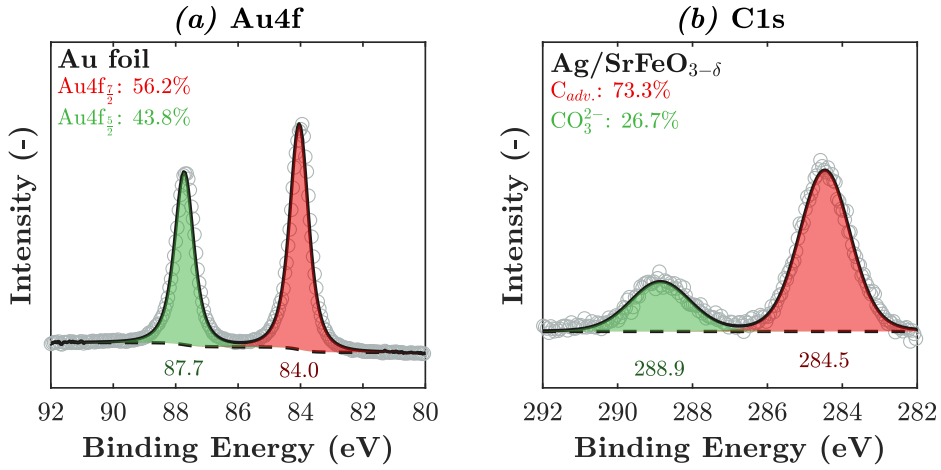


Fig. 2.11 Sections of XPS spectra showing **(a)** position of Au $4f_{7/2}$ set to 84.00 eV as measured from an external foil standard, and **(b)** corresponding C1s spectrum of a sample of $Ag/SrFeO_{3-\delta}$, showing a slightly lower than expected binding energy for $C_{adv}$, and carbonate impurities. Percentage areas estimated for each peak are given, corresponding to the approximate proportion (at%) of each species at the surface.

Descriptions of peak fitting parameters, and assignment to specific chemical environments are given in the relevant Chapters. *Ex-situ* XPS measurements were performed by Dr Carmen Fernandez-Posada and Dr Shaoliang Guan (both Maxwell Centre, University of Cambridge).

### Near-ambient pressure XPS (NAP-XPS)

In order to measure the changes in surface composition during reaction, near-ambient pressure (NAP-XPS) measurements were performed. Under NAP-XPS conditions, the total pressure in the sample chamber operates at *c.* 5 mbar under a controlled gas environment, with simultaneous heating of the sample to induce surface reactions.

The NAP-XPS measurements were performed using a SPECS EnviroESCA NAP-XPS spectrometer, with results and peak assignments reported in Chapter 4. Gases (5 vol% $H_2$ in $N_2$, $N_2$, or compressed air, all BOC, 99.99+%) were supplied using mass flow controllers, with composition in the sample chamber measured using a mass spectrometer (MS, MKS e-Vision 2).

The presence of gaseous molecules in between the surface of the sample, and the electron detector, decreases the mean free path of photoelectrons emitted from the sample (Cushman *et al.*, 2017). Hence, to achieve adequate signal intensity, the samples under investigation were pelletised, with photoelectrons collected *via* a sampling cone positioned close to the surface of the sample. The sample pellets were mounted on a ceramic sample stage, with temperature controlled between 25-430°C by varying the current supplied through a resistive heating coil inside the stage. Prior to NAP-XPS measurements, samples were cleaned of carbonate species adsorbed at the surface by heating to 650°C in air for 5 h. The samples were then stored in an Ar-filled glovebox, and transferred to the NAP-XPS instrument immediately before collecting measurements. Any residual carbonate remaining on the sample, detected from measurements of the C1s spectra, desorbed upon heating to temperatures above 177°C.

Energy calibration was performed relative to the adventitious carbon C1s peak at 284.8 eV, with the caveat that for measurements at high temperatures (>300°C) under oxidising conditions, the signal intensity of the $C_{adv}$ peak was low, as a result of the carbon desorbing. For NAP-XPS measurements without a clear $C_{adv}$ peak, measurements were calibrated relative to the central position of the Sr $3p_{3/2}$ peak, at 268.4 eV, which was found not to shift significantly (<0.25 eV) with respect to the $C_{adv}$ peak in spectra where both were visible, under variable temperatures and gas atmospheres. Under NAP-XPS conditions, the use of a flood gun for charge compensation was not required, as photoionisation of gaseous molecules by the X-ray source neutralised the overall surface charge, termed environmental charge compensation (Dietrich *et al.*, 2019; Salmeron and Schlögl, 2008).

Measurements using NAP-XPS were performed by Dr Beth Willneff and Dr Andrew Britton (School of Design and School of Chemical and Process Engineering respectively, University of Leeds, with instrument access provided by the Henry Royce Institute).

### 2.2.8 Raman spectroscopy

Raman spectroscopy is an optical spectroscopy technique used to characterise crystalline materials (Orlando *et al.*, 2021) or absorbed surface species (Wang *et al.*, 1999) by measuring the shift in wavelength in scattered light when the sample is excited by a laser. The penetration depth of the laser into the sample is of the order 1-10 $\mu$m (Adar *et al.*, 2010).

*Ex-situ* Raman spectra were collected using a Horiba Jobin-Yvon LabRAM HR instrument, equipped with an Olympus BX41 microscope with 50x magnification objective lens, and a green (532 nm) laser to excite the sample. Prior to measurements, the instrument was calibrated with respect to a Si thin film standard, with a strong Raman band at 520.5 $cm^{-1}$. As the quality of the Raman signal depended strongly on the surface of the sample being exactly aligned with the focal plane of the microscope, powder samples were compressed into a flat pellet prior to measurements. The spot size of Raman measurements at 50x magnification was determined to be *c.* 20 $\mu$m, by measuring the area of beam damage on a light-sensitive sample of $Ag_2CO_3$ (Sigma-Aldrich, 99%), shown in Appendix A, Fig. A.1.

In a typical experiment, Raman spectra were collected over the wavenumber range 150-1800 $cm^{-1}$ at a laser power of 0.5 mW and 15 s acquisition time, with each measurement repeated five times and averaged to improve the signal quality. For characterisation of a given sample using Raman spectroscopy, five points on the sample were scanned, then normalised to the maximum detected signal intensity and averaged.

*In-situ* Raman spectroscopy was performed using a Thermo Scientific DXR 2 Raman spectrometer, fitted with a Linkam CCR1000 heated stage. Gases (compressed air, $N_2$, or 5vol% $H_2$ in $N_2$, all Carbagas, 99.99+%) were supplied to the stage at a total flowrate of 35 mL $min^{-1}$, set using mass-flow controllers. For measurements at elevated temperature (200-350°C), the set-point of the heated stage was set to the target temperature with a nominal ramp rate of 10°C $min^{-1}$, and allowed to settle for 5-10 min prior to collecting Raman spectra.

The *in-situ* Raman spectroscopy experiments were performed at the Department of Mechanical and Process Engineering, ETH Zürich, with some assistance in collecting measurements from Dr Felix Donat and Mr Alexander Oing.

## 2.3 Experiments in packed bed reactors

### 2.3.1 Packed bed micro-reactor for kinetic experiments

To determine the kinetics of oxygen uncoupling from SFO-based materials, as described in Chapter 3, a small scale packed bed reactor (total bed mass $\leq$1 g) was assembled, with a schematic shown in Fig. 2.12.

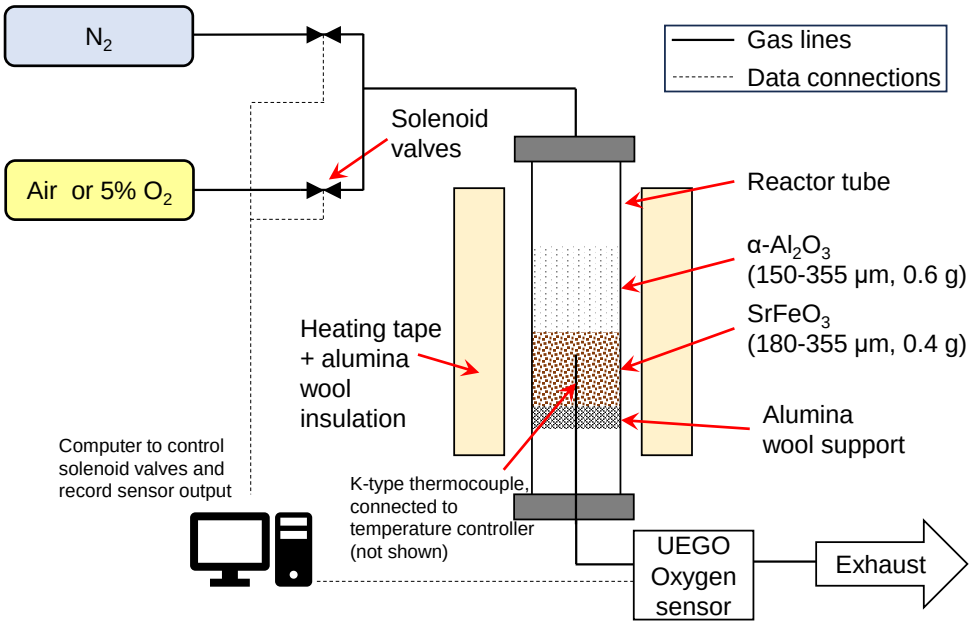


Fig. 2.12 Schematic diagram of packed bed micro-reactor used in experiments (Not to scale).

The reactor was constructed from a stainless steel tube with an internal diameter of 4.8 mm and a length of 8.0 cm. The packed bed, composed of a preheating section of 0.60 g of $\alpha$-$Al_2O_3$, (150–355 $\mu$m, Boud Minerals), and an active bed of 0.40 g of the SFO-based oxygen carrier (180–355 $\mu$m), was placed inside the reactor and secured using alumina wool. The feed to the reactor was controlled using two solenoid flipper valves (Bürkert Type 6124-2/2 way) connected to air and $N_2$ cylinders (both BOC, >99.998%). The flow rate of gases to the reactor was controlled using an orifice place (I.D. 0.025"). Flow through the reactor was set to 750 mL $min^{-1}$ (NTP) by adjusting the inlet pressure upstream of the orifice plate and checking the flow rate with an Agilent ADM digital flowmeter.

The reactor tube was heated using a high-temperature heating tape (Briskheat TBIH102), controlled with a K-type thermocouple (O.D. 1.5 mm) placed at the center

of the packed bed. The oxygen content of the outlet gas was measured using a Bosch 4.9 LSU wideband universal exhaust gas sensor (UEGO) connected to a control unit (Cambustion Ltd.). Oxygen partial pressure was measured at a nominal sample rate of 50 $s^{-1}$, giving a temporal resolution of 20 ms. Experiments were carried out over the temperature range of 450–600°C, performing redox cycles, with each cycle comprising 30 s oxidation in air, followed by 30 s reduction in $N_2$. Given only the initial rate of reduction, when the material was the furthest from equilibrium, was used to determine kinetic parameters, 30 s reduction cycles were adequate for packed bed experiments, as opposed to longer reduction steps (45 min) used in TGA experiments.

The dead time of the reactor, $t_{dead}$, defined as the time interval between sending an electronic signal to the solenoid valves to change feed gas from air to nitrogen, and the smoothed sensor voltage decreasing to 95% of the initial value, was estimated to be $0.17 \pm 0.01$ s for an inert bed of 1.00 g of $\alpha$-$Al_2O_3$. The $t_{dead}$ value was subtracted from the nominal start time of reduction or oxidation to account for the lag between the opening of a solenoid valve and the gas arriving at the oxygen sensor. To account for gas mixing and dispersion within the reactor, a blank run was generated by switching between air and $N_2$ over an inert bed of 1.00 g of $\alpha$-$Al_2O_3$, again subtracting the $t_{dead}$ to ensure all runs were in sync with the timing of the opening of the solenoid valves. The blank run was then subtracted from measurements with active material, compensating for dispersion and mixing within the bed during experiments with SFO-based materials. A comparison between the blank run and the measurement for an active bed is shown in Fig. 2.13.

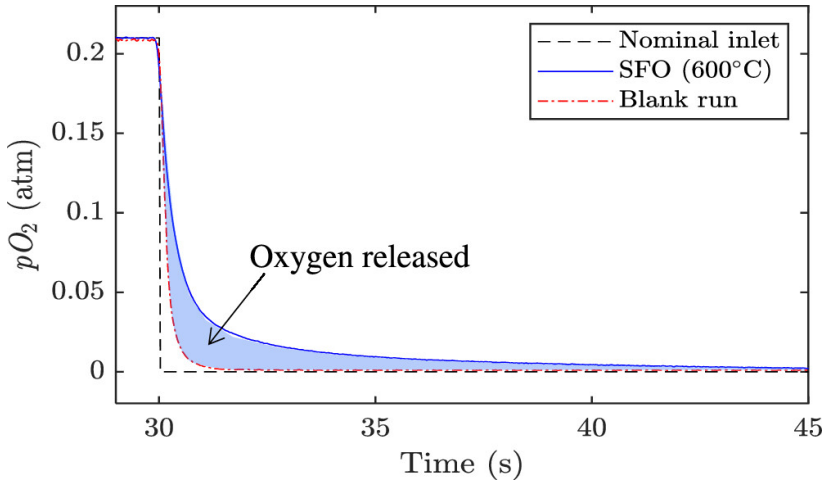


Fig. 2.13 Comparison between the blank run, reduction of SFO at 600°C, and the nominal inlet feed with the lag time subtracted. Oxygen released from SFO is determined from the area between the SFO and blank curves (shaded area).

### 2.3.2 Packed bed reactors for selective oxidation experiments

Experiments concerning the oxidation of hydrocarbons in a chemical looping mode, described in Chapters 5 and 6, were performed in a separate packed-bed reactor. A schematic of the reactor arrangements used is shown in Fig. 2.14.

A bed of active particles, composed of a metal catalyst impregnated onto SFO (1.50-2.00 g, 180–300 $\mu$m) was placed in a quartz tube, in between two layers of SiC (Alfa Aesar, 241-559 $\mu$m) with 2.00 g of SiC below and 3.00 g of SiC above the bed of active particles. The bed was assembled in a quartz reactor tube (200 or 560 mm length, I.D. 8 mm), with a sintered disk supporting the bed 75 or 255 mm from the tube base respectively for the shorter and longer tubes. The reactor was secured using Swagelok Ultra-Torr vacuum fittings with fluorocarbon FKM O-rings, and wrapped with a heating tape (LewVac, 200 W), or placed in the isothermal region of a electric tubular furnace (Carbolite). A thermocouple (K- or N-type), positioned in the centre of the active material, was used to control the setpoint temperature. The reactor was heated under air flow for 2 h prior to experiments, to ensure the setpoint temperature was achieved throughout the bed, and to remove adsorbed carbonate and hydroxide species from the surface of SFO (Marek and García-Calvo Conde, 2021).

Some of the chemical looping oxidation experiments described in Chapter 5 were performed by Mr Joseph Gebers (Department of Chemical Engineering and Biotechnology, University of Cambridge), using a rig described in Gebers and Marek (2024),

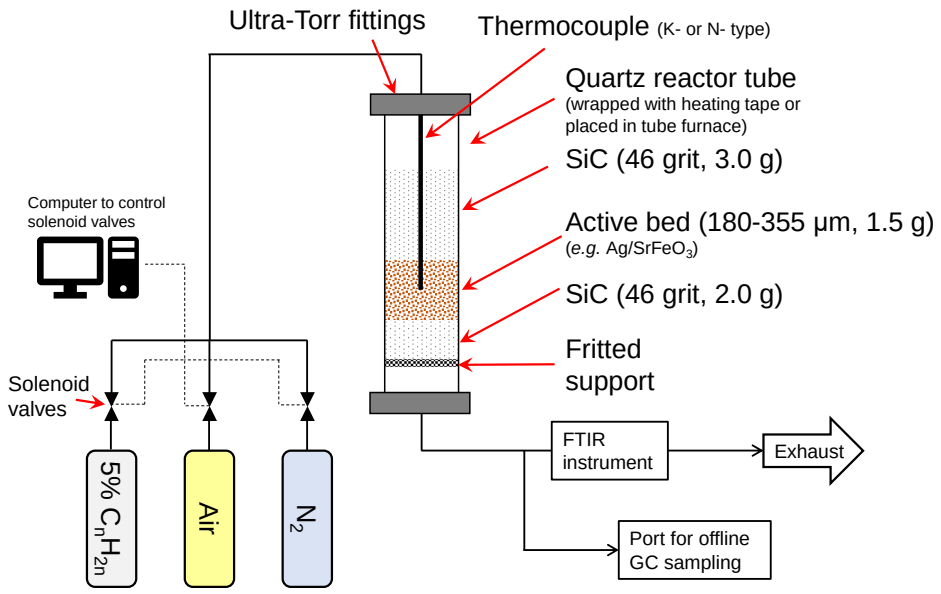


Fig. 2.14 Schematic of packed bed reactor used in chemical looping oxidation experiments (Not to scale).

with the packed bed assembled in a stainless steel tube (I.D. 15 mm) and supported by a plug of quartz wool, with heating provided by an electric tube furnace.

Oxidation products from chemical looping experiments described in Chapter 5 were measured using a Fourier-transform infrared (FTIR) analyser (MKS Instruments, Multigas 2030), equipped with a HgCdTe detector cooled with liquid $N_2$. Before each experiment, the detector was cooled for 2 h, and dry air was passed through the FTIR chamber to purge any residual moisture. The exhaust gas from the packed bed reactor described in Section 2.3.2 was passed through the FTIR detection chamber, scanning the wavenumber range 600-3500 $cm^{-1}$ at a frequency of 0.25 Hz. From the characteristic infrared absorption peaks of different molecules of interest, the concentrations of ethylene, ethylene oxide, CO, $CO_2$, and $H_2O$ were estimated using MKS MG2000 software. Measurements using FTIR, and analysis to estimate gas concentrations, were performed by Mr Joseph Gebers (Department of Chemical Engineering and Biotechnology, University of Cambridge).

### 2.3.3 Gas chromatography (GC)

For experiments described in Chapter 6, product composition was determined using gas chromatography (GC). The gas from the reactor outlet was sampled manually using a gas syringe, withdrawing a 10 mL sample immediately after the reactor tube. Samples

were collected 45 s after the start of each reduction step. The gas composition was measured with an Agilent 7890A gas-chromatograph, using parallel Agilent PoraBOND-Q and Hayesep-Q/MolSieve 13A columns, connected to a flame-ionisation detector (FID) and a thermal-conductivity detector (TCD), respectively. The internal configuration of the GC instrument, showing the separate gas channels to each detector, is described in greater detail by Hubble (2018). The FID channel was used to quantify propylene, propylene oxide (PO), propanal, acetone, propan-1-ol, propan-2-ol, and allyl alcohol (AA), and the TCD channel was used to quantify $CO_2$. No CO, or other carbon-containing products, were detected above 5 ppm. The GC instrument was calibrated using two gas mixtures: (1) 1000 ppm propylene/1000 ppm propylene oxide/balance $N_2$; (2) 1000 ppm $CO_2$/balance $N_2$; both BOC. From measurements of calibration gas mixtures, the accuracy of the FID detection system was estimated to be within ±10% of the true value based on variability of results collected by measuring samples of known compositions. The detection threshold was 1–2 ppm for $C_3$ components containing oxygen. The accuracy of the TCD was estimated to be ±4% of the true value, with a detection threshold of 10 ppm $CO_2$.

To generate low concentration (*c.* 1000 ppm) vapour mixtures of $C_3$ analytes for calibration and catalytic experiments, an Owlstone V-OVG vapour generator was used. A 2.5-3 g sample of liquid analyte was loaded into a stainless steel diffusion tube (acetone: VWR, 99%; propan-1-ol: Sigma Aldrich, 99+%; propan-2-ol, VWR, 99%; propanal: Acros Organics, 99+%; allyl alcohol: Sigma Aldrich, 99+%), and weighed before starting measurements. The tube was then inserted into the heated chamber of the vapour generator, with $N_2$ purge flow set to 220 mL $min^{-1}$. For calibration purposes, 10 mL samples of vapour were taken from the outlet gas stream and injected into the GC inlet, and simultaneously the diffusion tube was removed and weighed. The average vapour concentration was then calculated using Eq. 2.7

$$c = 10^{12} \cdot \frac{RT}{P} \cdot \frac{1}{qM_r} \cdot \frac{dm}{dt} \tag{2.7}$$

where $c$ is the concentration of the analyte in the vapour (ppm), $R$ is the molar gas constant (J $mol^{-1}$ $K^{-1}$), $T$ is the chamber temperature (K), $P$ is the chamber pressure (Pa), $q$ is the nitrogen flowrate (mL $min^{-1}$), $M_r$ is the molar mass of the analyte (g $mol^{-1}$), and $\frac{dm}{dt}$ is the rate of change of sample mass (g $min^{-1}$). For catalytic experiments, the outlet gas from the vapour generator was connected to the reactor inlet,

without removing the diffusion tube over the course of the experiment. Measurements of the mass of the sample tube containing the analyte over time are shown in Fig. A.3.

Retention times for each component during GC measurements were consistent to within ±0.05 min for all measurements, shown in Fig. 2.15.

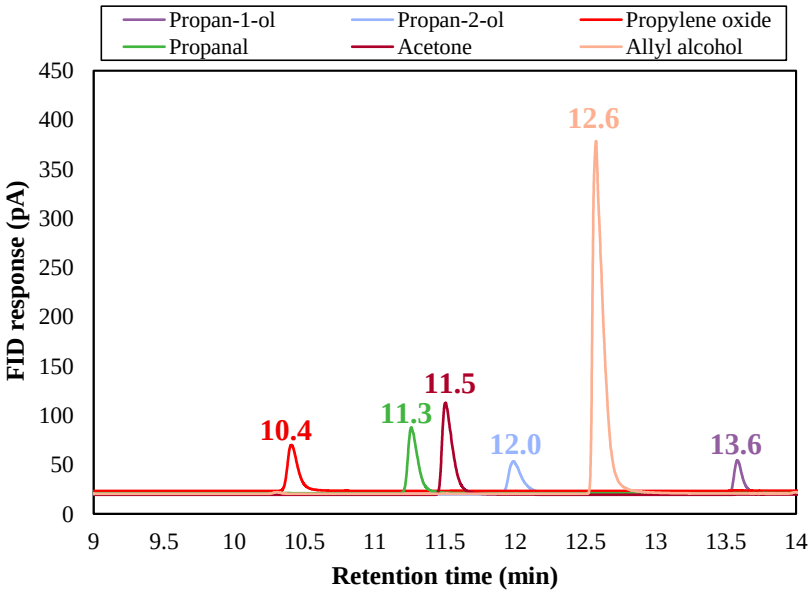


Fig. 2.15 Signal from FID showing average retention times of $C_3$ oxygenates in PoraBOND-Q GC column (arbitrary vapour-phase concentrations used).

# Chapter 3

# Kinetic and thermodynamic enhancement of oxygen uncoupling from modified strontium ferrite perovskites

This Chapter considers the reactive behaviour of strontium ferrite-based oxygen carriers, modified with Ag and $CeO_2$. Sections from this Chapter have been published in Harrison *et al.* (2023), with all sections reproduced in this Dissertation comprising solely my own work.

## 3.1 Introduction

Perovskite oxygen carriers, including $SrFeO_{3-\delta}$, have been investigated for applications including chemical looping air separation (CLAS) (Bulfin *et al.*, 2019; Dou *et al.*, 2020). Various strategies have been developed to improve the oxygen capacity, and rates of oxygen release and reuptake, including partial substitution of Sr or Fe with other elements (Wang *et al.*, 2022a), and addition of metal or metal oxide materials in the bulk or at the surface of the oxygen carrier (Marek *et al.*, 2020; Wang *et al.*, 2021).

In this Chapter, several methods of manipulating oxygen release from $SrFeO_{3-\delta}$ were investigated, using Ag, Ce, and $CeO_2$ as additives. The main research objective was to assess whether the introduction of these three dopants affected the kinetics of reduction and oxidation during CLAS and, or, influenced the maximum oxygen

availability from $SrFeO_{3-\delta}$ at equilibrium under given $pO_2$ conditions. Three methods of engineering $SrFeO_{3-\delta}$ were investigated: (1) introducing Ag or $CeO_2$ to the surface of $SrFeO_{3-\delta}$ *via* surface impregnation, (2) doping $CeO_2$ into the bulk of $SrFeO_{3-\delta}$, thus forming a two-phase composite of the two oxides, and (3) substituting 5 mol% Sr with Ce through structural doping, to produce $Sr_{0.95}Ce_{0.05}FeO_{3-\delta}$. The materials prepared were then investigated *via* thermogravimetric analysis (TGA), and gas cycling experiments in a packed bed reactor to determine the effects of each modification method on the temperature of oxygen release and the apparent kinetics of oxygen release and reuptake in a CLAS system.

## 3.2 Experimental

Particles of $SrFeO_{3-\delta}$ were prepared by ball-milling of $SrCO_3$ and $Fe_2O_3$, followed by drying and calcination, as described in Section 2.1.1. Particles of $SrFeO_{3-\delta}$ were sieved, with the size fraction 180-355 $\mu$m used for subsequent sythesis and experiments. The sample of $SrFeO_{3-\delta}$ without further modification was designated SFO.

Samples modified with $CeO_2$ were prepared by incipient wetness impregnation and solid-state synthesis, with the procedures described in Sections 2.1.2 and 2.1.3. The sample of strontium ferrite impregnated with $CeO_2$ was designated $CeO_2$/SFO, with nominal target loading 9.3 wt% $CeO_2$. Two samples prepared by solid-state synthesis, with $CeO_2$ mixed into the bulk, or partially substituting Sr in $SrFeO_3$, were designated $(CeO_2)_{ss}$SFO and SCeFO respectively. The sample of $(CeO_2)_{ss}$SFO was prepared with a nominal loading of 4.3 wt% $CeO_2$ (5 mol%), and the sample of SCeFO was prepared with composition $Sr_{0.95}Ce_{0.05}FeO_{3-\delta}$.

Prior to use in experiments, the sample of SCeFO was activated by deep reduction in $H_2$, followed by slow oxidation in air, as described in Section 2.1.1. A sample of $SrFeO_{3-\delta}$ impregnated with Ag was prepared using the method described in Section 2.1.2, with nominal loading 15 wt% Ag, designated Ag/SFO. The nominal loadings of $CeO_2$ and Ag were verified by ICP-AES, as described in Section 2.2.4. The samples prepared, with nominal and measured loadings of $CeO_2$ and Ag, and abbreviations used hereafter, are summarized in Table 3.1.

Materials were characterised using X-ray diffraction (XRD), with XRD patterns collected at ambient temperature using a Bruker D8 Discover diffractometer, as described in Section 2.2.1. Phase compositions were estimated using Profex software (Doebelin and Kleeberg, 2015), using reference patterns from the ICSD database (Belsky

Table 3.1 Summary of samples prepared, abbreviations used, and loadings of Ag or $CeO_2$ as determined from ICP-AES measurements

| Sample | Abbreviated name | Target loading | Measured loading |
|---|---|---|---|
| Strontium ferrite, $SrFeO_{3-\delta}$ | SFO | - | - |
| Ceria-impregnated strontium ferrite | $CeO_2$/SFO | 9.3wt% $CeO_2$ | 10.6wt% $CeO_2$ |
| Strontium ferrite with ceria in bulk | $(CeO_2)_{ss}$SFO | 4.3wt% $CeO_2$ | 2.5wt% $CeO_2$ |
| Ce-doped strontium ferrite, $Sr_{0.95}Ce_{0.05}FeO_{3-\delta}$ | SCeFO | - | - |
| Ag-impregnated strontium ferrite | Ag/SFO | 15.0wt% Ag | 12.7wt% Ag |

*et al.*, 2002) given in Appendix A, Table A.1. Scanning electron microscopy (SEM) images were collected using a Tescan MIRA3 FEG-SEM, as described in Section 2.2.6.

Thermogravimetric analysis (TGA) experiments were performed using a Mettler Toledo TGA/DSC 1 analyser as described in Section 2.2.2. Prior to all TGA measurements, the sample was heated in air from 50 to 900°C at 10°C $min^{-1}$, then cooled to 50°C, in order to remove adsorbed surface contaminants from exposure to laboratory air.

Experiments in a packed bed reactor were performed to determine the kinetics of oxygen uncoupling and re-absorption for the prepared materials, with a description of the reactor used given in Section 2.3.1. The reactor was operated between 450-600°C, with the feed alternated between $N_2$ and air, and the $pO_2$ of the outlet gas measured using a UEGO oxygen sensor. From the maximum and minimum values of $pO_2$ measured at the start of each step immediately after a change in feed, the kinetic parameters of reduction and oxidation were estimated, with the methodology described in Section 3.3.1.

The reoxidation of $SrFeO_{3-\delta}$-based oxygen carrier (OC) materials in air at >500°C was previously shown to be very fast, making attempts to assess kinetic parameters difficult (Görke *et al.*, 2020). Additionally, here, during reoxidation in air, the exothermic reaction resulted in a considerable increase in the bed temperature, noticeably above the controller set-point (up to 15°C for the most active samples). To limit the temperature increase and the extent of $O_2$ consumption, the mass of sample in the bed was decreased from 0.4 to 0.1 g, and the redox procedure was changed from 30 to 120 s of reduction in $N_2$ at 475–600°C, followed by 120 s reoxidation in 5.05 vol% $O_2$ (balance $N_2$, BOC).

## 3.3 Theory

### 3.3.1 Derivation of rate expression

Kinetics of oxygen release and uptake were estimated from packed bed experiments using the methodology described by Görke *et al.* (2020).

The instantaneous specific rate of oxygen release ($r$, $\mathrm{mol}_{O_2}\ \mathrm{s}^{-1}\ \mathrm{g}_{OC}^{-1}$) from the materials under investigation was estimated using Eqs. 3.1 and 3.2:

$$r = \frac{x_{O_2,out}\dot{n}_{tot}}{m_{OC}} \tag{3.1}$$

$$\dot{n}_{tot} = \frac{\dot{n}_{N_2}}{(1 - x_{O_2,out})} \tag{3.2}$$

where $x_{O_2,out}$ is the mole fraction of oxygen measured in the exhaust stream, $\dot{n}_{tot}$ is the total molar flow rate of gas out of the reactor (mol $\mathrm{s}^{-1}$), $\dot{n}_{N_2}$ is the molar flow rate of $N_2$ at the inlet of the reactor (658 $\mu$mol $\mathrm{s}^{-1}$, measured at room temperature and assumed to be constant for all experiments), and $m_{OC}$ is the mass of the sample under investigation (g).

The total amount of oxygen released or taken up by the material over each reduction or oxidation cycle was then estimated by integrating the instantaneous rate over the cycle duration. Instantaneously after the gas switch from air to $N_2$, the material was assumed to be in a fully oxidized state (*i.e.* zero conversion), and the greatest $pO_2$ in the outlet gas resulting from oxygen release from the material was observed. Therefore, the maximum value of $pO_2$ after gas switching was used to estimate the apparent rate constant for reaction, $k$.

Hence, immediately after the feed to the bed is changed, the reactor is assumed to be well-approximated as being in a pseudo-steady state, with no gradient in oxygen non-stoichiometry of $SrFeO_{3-\delta}$ along the length of the bed (*i.e.* at t = 0, $\delta = \delta_0$ everywhere). Then, assuming that the reactions shown in Eq. 3.3 can be approximated as first-order with respect to $O_2$ (Chizhik *et al.*, 2022; Görke *et al.*, 2020; Xu *et al.*, 2018), balancing oxygen over the reactor yields Eq. 3.4.

$$SrFeO_{3-\delta_0} \rightleftharpoons SrFeO_{3-\delta} + \frac{\delta - \delta_0}{2} O_2 \tag{3.3}$$

$$\frac{\partial x_{O_2} v}{\partial z} = -kRT(x_{O_2} - x_{O_2,eq}(\delta_0)) \tag{3.4}$$

where $x_{O_2}$ is the mole fraction of oxygen at a point along the bed, $x_{O_2,eq}$ is the mole fraction of oxygen that would be in equilibrium with the solid material, $v$ is the superficial gas velocity through the bed (m $s^{-1}$), $z$ is the distance along the bed (m), $k$ is the first-order rate constant (mol $s^{-1}$ $m^{-3}$ $Pa^{-1}$), $T$ is the reaction temperature (K), and $R$ is the molar gas constant (kJ $mol^{-1}$ $K^{-1}$). The superficial velocity can then be related to the constant molar flux of inert $N_2$, $J_{N_2}$ (mol $m^{-2}$ $s^{-1}$) using Eq. 3.5, where $P$ is the total pressure in the reactor, taken as *c.* 101 kPa.

$$J_{N_2} = v\frac{P}{RT}(1 - x_{O_2}) \Rightarrow v = \frac{J_{N_2}RT}{P(1 - x_{O_2})} \tag{3.5}$$

Combining Eqs. 3.4 and 3.5 and integrating over the length of the bed, $L$ (m), yields Eq. 3.6

$$-\frac{P}{J_{N_2}}k\int_0^L dz = \int_{x_{O_2,in}}^{x_{O_2,out}} \frac{dx_{O_2}}{(1 - x_{O_2})^2 \cdot (x_{O_2} - x_{O_2,eq}(\delta_0))} \tag{3.6}$$

In the case of a switch in feed gas from air to nitrogen, the value of $x_{O_2,in}$,in was taken to be $10^{-5}$ (*i.e.* using the nominal purity of the $N_2$ provided from the certified gas cylinder as 99.999 vol%), the value of $x_{O_2,eq}$ was taken to be 0.21 from the material reaching equilibrium with air, and the value of $x_{O_2,out}$ was estimated by finding the maximum value of $x_{O_2}$ from the UEGO signal. The integral on the right-hand side of Eq. 3.6 has an analytical solution, shown in Eq. 3.7, yielding the first-order rate constant, $k$.

$$k = -\frac{J_{N_2}}{LP}\left[\frac{(x_{O_2}-1)\cdot ln(|x_{O_2}-x_{O_2,eq}(\delta_0)|)-ln(|x_{O_2}-1|)\cdot x_{O_2}+ln(|x_{O_2}-1|)+x_{O_2,eq}(\delta_0)-1}{(x_{O_2,eq}(\delta_0)-1)^2\cdot(x_{O_2}-1)}\right]_{x_{O_2,in}}^{x_{O_2,out}} \tag{3.7}$$

The apparent rate constant for re-oxidation of SFO was determined by evaluating Eq. 3.7 using $x_{O_2,in} = 0.0505$ (*i.e.* the mole fraction of oxygen in the supplied gas from the cylinder), $x_{O_2,eq} = 10^{-5}$, and $x_{O_2,out}$ = (0.0505 - $|x_{UEGO}|$), where $x_{UEGO}$ is the maximum negative deviation measured using the UEGO oxygen sensor with respect to the blank curve recorded over an inert bed.

The variation of the rate constant, $k$, with temperature was described using the Arrhenius law (Eqs. 3.8 and 3.9), where $E_a$ is the apparent activation energy (kJ $mol^{-1}$), and $A$ is a pre-exponential factor ($mol_{O_2}$ $s^{-1}$ $m^3$ $Pa^{-1}$).

$$k = A \cdot exp\left(-\frac{E_a}{RT}\right) \tag{3.8}$$

$$ln(k) = ln(A) - \frac{E_a}{R} \cdot \frac{1}{T} \tag{3.9}$$

To characterise the influence of random errors from experimental measurements on kinetic parameters, values of $E_a$ and $A$ were estimated by fitting Eq. 3.8 directly to the experimentally determined values of $k$ using nonlinear regression, and by separately fitting Eq. 3.9 to the experimentally determined values of $k$ using linear regression. A statistically significant difference between the two regression methods would indicate that the resulting values of $E_a$ and $A$ were significantly affected by the experimental arrangement and, hence, might not accurately reflect the intrinsic kinetics of oxygen release (Barrie, 2011a,b).

### 3.3.2 Limitations on rate of reaction

During experiments in a packed bed reactor, the measured rate of release of oxygen might be limited by (1) external mass transport between the surface of the particles of the oxygen carrier (OC) material and the flowing gas stream, (2) internal mass transport within the pores of particles of OC materials, (3) thermodynamic equilibrium.

#### External mass transfer limitation

To confirm that the experimental arrangement used to estimate kinetics of oxygen release and uptake would not be limited by external mass transfer from the solids to the gas phase, the maximum rate of mass transport from the surface of the OC particles to the gas stream was estimated. Assuming that the rate of oxygen transport is approximately constant across a thin packed bed at the start of the reduction step, the rate of oxygen transport can be assessed according to Eq. 3.10, where $k_{M,g}$ is the external mass transfer coefficient (m $s^{-1}$), $A_{MT}$ is the area of particles available for mass transfer ($m^2$), $V_p$ is the volume of the packed bed ($m^3$), $\varepsilon$ is the bed voidage (taken as *c.* 0.4) and $\rho_s$ is the density of the OC material (kg $m^{-3}$).

$$r = \frac{k_{M,g} A_{MT}}{\rho_s V_p (1-\varepsilon)} \frac{P}{RT} (x_{O_2} - x_{O_2,eq}) \tag{3.10}$$

The mass transfer coefficient was then estimated from the correlation of Wakao and Funazkri (1978), given in Eq. 3.11, where $Sh$ is the Sherwood number, $Sc$ is the Schmidt number for the gas phase, and $Re$ is the Reynolds number.

$$Sh = 2 + 1.1 Sc^{0.33} Re^{0.6} \tag{3.11}$$

To evaluate $Sh$ and $Re$, the characteristic length $d_c$ (m) was used, given by 3.12, where $\langle d_p \rangle$ is the geometric mean of the range of particle sizes used in the packed bad (*i.e.* $\langle d_p \rangle = \sqrt{180 \times 300} = 253$ $\mu$m for the packed beds of particles used here.)

$$d_c = \langle d_p \rangle \cdot \left( \frac{\varepsilon}{1 - \varepsilon} \right) \tag{3.12}$$

**Internal mass transfer limitation**

At high rates of reaction, the observed rate of oxygen release from the OCs may be limited by internal mass transfer (*i.e.* diffusion within pores of the OC particles). Internal diffusion is characterised by the Thiele modulus, $\phi$ , given for a first-order reversible reaction in Bischoff (1967) as Eq. 3.13, where $k_v$ is the rate constant for reactions ($s^{-1}$), $\mathscr{D}_{eff}$ is the effective diffusivity of oxygen within the pores ($m^2 s^{-1}$), $L$ is a characteristic length (m), $c_{O_2,eq}$ is the concentration of oxygen in equilibrium with the OC material (mol $m^{-3}$), and $c_{O_2,bulk}$ is the bulk concentration of oxygen in the gas phase (mol $m^{-3}$).

The function $g(c)$ describes the dependence of the reaction rate on oxygen concentration, given here for a first order reversible reaction by Eqs. 3.14 and 3.15:

$$\phi^2 = \frac{k_v L^2 g(c)}{2 \int_{c_{O_2,eq}}^{c_{O_2,bulk}} \mathscr{D}_{eff} g(c) dc} \tag{3.13}$$

$$g(c) = c_{O_2,eq} - c_{O_2,local} \tag{3.14}$$

$$r_{v,obs} = k_v g(c) \eta_{eff} \tag{3.15}$$

$$\eta_{eff} = \frac{3}{\phi^2} \left( \phi coth(\phi) - 1 \right) \tag{3.16}$$

where $c_{O_2,local}$ is the concentration of oxygen at the surface of the particle (mol $m^{-3}$), $\eta_{eff}$ is an effectiveness factor (-), and $r_{v,obs}$ is the observed rate of reaction *per* particle

in the packed bed (mol $s^{-1}$ $m^{-3}$). Positive values of $r_{v,obs}$ correspond to oxygen release, and negative values of $r_{v,obs}$ correspond to oxygen uptake. The dependence of effectiveness factor on $\phi$ for a first-order reversible reaction is shown in Eq. 3.16 (Bohn, 2010).

In the case where the influence of external mass transport of gas away from the surface of the particle is negligible, as assumed here, $c_{O_2,local} \approx c_{O_2,bulk}$, where $c_{O_2,bulk}$ is the overall concentration of oxygen in the bulk gas stream. Effective diffusivity of oxygen within the pores of the solids is then given by Eq. 3.17, where $\mathscr{D}_m$ is the molecular diffusivity of oxygen in nitrogen ($m^2$ $s^{-1}$), estimated using Chapman-Enskog theory (Poling *et al.*, 2001), $\varepsilon_p$ is the porosity of the OC materials, and $\tau_p$ is the pore tortuosity (taken as $\tau_p = 2$). Porosity was estimated from Eq. 3.18, where $\rho_s$ is the density of particles of SFO ($\rho_s = 2490$ kg $m^{-3}$, measured by weighing a bed of particles of known volume), and $\rho_{SrFeO_3}$ is the density of non-porous $SrFeO_3$, taken to be $\rho_{SrFeO_3}$ = 5570 kg $m^{-3}$ from the Springer Materials database (Villars and Cenzual, 2012).

$$\mathscr{D}_{eff} = \frac{\varepsilon_p}{\tau_p} \cdot \mathscr{D}_m \tag{3.17}$$

$$\varepsilon_p = 1 - \frac{\rho_s}{\rho_{SrFeO_3}} \tag{3.18}$$

The rate of reaction *per* particle was estimated from the measured overall rate of reaction measured over the entire bed volume, $r$ (mol $s^{-1}$ $m^{-3}$) using Eq. 3.19.

$$r_{v,obs} = r \cdot \frac{\pi \langle d_p \rangle^3}{6V(1-\varepsilon)} \tag{3.19}$$

For each observed initial rate of reaction from experiments in the packed-bed, values of $\phi$, $k_v$ ,and $\eta_{eff}$ were found by solving Eqs. 3.13, 3.14, 3.15, and 3.16, taking $\eta_{eff} = 1$ as an initial guess, then iterating until $k_v$, $\phi$ and $\eta_{eff}$ converged. Internal mass transfer limitation may be neglected if the criterion $\phi^2 < 0.603$ is satisfied (Vannice, 2005), corresponding to $\eta_{eff} > 0.977$. Hence, for each temperature investigated, the critical rate of reaction such that $\phi^2 = 0.603$ was estimated (*i.e.* the threshold for internal mass transfer limiting the observed rate of reaction significantly), shown in Section 3.4.3. For measurements where $\phi^2 > 0.603$, the estimated values of rate constant $k$ from Eq. 3.7 were divided by the effectiveness factor (Eq. 3.20), estimated iteratively using Eq. 3.16, to give an adjusted value of the rate constant accounting for internal mass transfer, $k'$.

$$k' = \frac{k}{\eta_{eff}} \tag{3.20}$$

**Equilibrium limitation**

Rate of oxygen release can also be limited by thermodynamic equilibrium, as described by Görke *et al.* (2020), where at a certain point in the bed, the value of $x_{O_2} \rightarrow x_{O_2,eq}(\delta)$. The extent of equilibrium limitation is described by the ratio $\frac{kRTL}{v}$, *i.e.* the ratio of the speed of the reaction front through the packed bed to the superficial velocity of gas. If the speed of the reaction front is much slower than the velocity of the incoming gas, the solids at each point along the length of the packed bed will not reach equilibrium with the local concentration of oxygen before the gas is carried away. However, for an arbitrarily high rate constant or very slow gas velocity, the packed bed will rapidly reach equilibrium with the local concentration of oxygen at each point along the bed, terminating the reaction and resulting in an under-estimate of intrinsic kinetics.

Therefore, if $\frac{kRTL}{v} \ll 1$, no significant profile in $\delta$ develops along the bed, if $\frac{kRTL}{v} \approx 1$ a profile develops but remains away from equilibrium, and as $\frac{kRTL}{v} \rightarrow \infty$, the value of $x_{O_2} \rightarrow x_{O_2,eq}(\delta)$ and the bed becomes strongly limited by equilibrium.

## 3.4 Results

### 3.4.1 Characterisation of materials

**X-ray diffraction measurements**

X-ray diffraction patterns for the as-prepared OC materials are shown in Fig. 3.1, with estimated phase compositions given in Table 3.2, and for spent OC materials after 250 redox cycles in the temperature range 500-600°C in Fig. 3.2. From the XRD measurements, the particles of SFO contained >95wt% perovskite $SrFeO_3$ phase, with some Ruddlesden-Popper $Sr_3Fe_2O_7$, or unreacted $SrCO_3$, also present. The samples of $(CeO_2)_{ss}$SFO and $CeO_2$/SFO, produced by solid-state ball milling and wet impregnation respectively, comprised two distinct phases of $SrFeO_3$ and $CeO_2$ as previously reported (Marek *et al.*, 2020). The estimated loading of $CeO_2$ in $(CeO_2)_{ss}$SFO from both XRD refinement (Table 3.2), and ICP measurements (Table 3.1), was substantially lower than the target value, indicating a possible error in the preparation, with the achieved $CeO_2$ content of 2.6 wt% rather than the target 4.3 wt%. The XRD pattern for SCeFO

showed no discernible $CeO_2$ peaks, indicating that the Ce was incorporated into the perovskite structure, rather than forming a separate phase. Instead, a characteristic shift in the $SrFeO_3$ peak at $2\theta = 47.0°$ is shown in Fig. 3.3, in agreement with previous results for SCeFO (Deganello *et al.*, 2006). The XRD results for Ag/SFO contained additional peaks corresponding to metallic silver, with an estimated Ag loading of 14.5 wt%, in line with the expected value, 15 wt%.

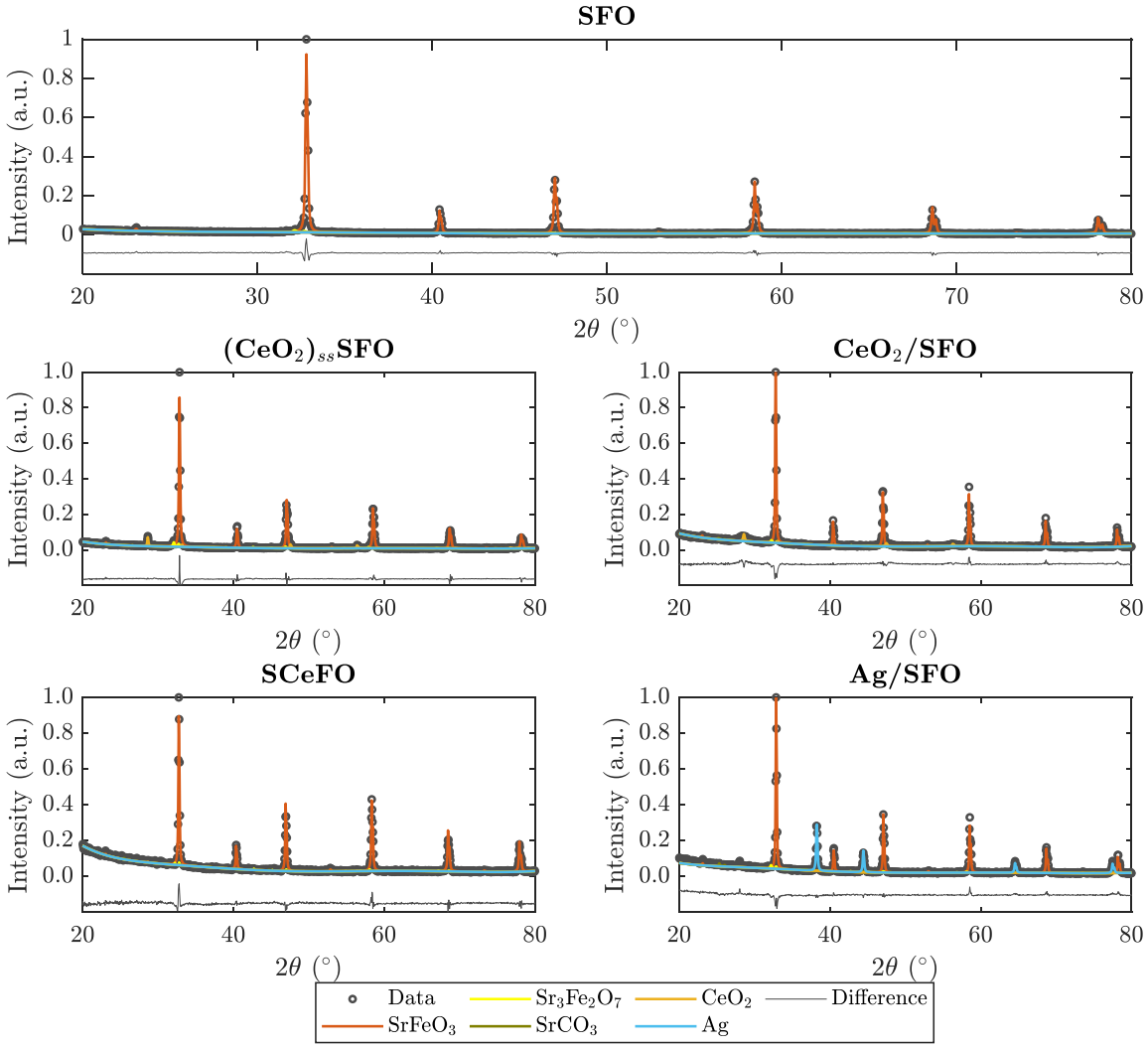


Fig. 3.1 XRD patterns for synthesised materials. Points indicate experimental measurements, lines indicate fitted peaks from reference patterns. XRD patterns were collected for the SCeFO sample after activation in $H_2$ and reoxidation (see Section 2.1.1 of the main Dissertation)

Table 3.2 Estimated phase composition of synthesised samples from XRD. Fractions of SrO and $\alpha$-$Fe_2O_3$ were negligible (<0.1 wt%) for all samples.

| Sample | $SrFeO_3$ (wt%) | $Sr_3Fe_2O_7$ (wt%) | $SrCO_3$ (wt%) | $CeO_2$ (wt%) | Ag (wt%) |
|---|---|---|---|---|---|
| SFO | 96.0 | 3.4 | 0.5 | - | - |
| $CeO_2$/SFO | 91.0 | 3.0 | 2.0 | 3.3 | - |
| $(CeO_2)_{ss}$SFO | 90.0 | 5.9 | 0.9 | 2.8 | - |
| SCeFO | 95.0 | 1.4 | 1.4 | 0.4 | - |
| Ag/SFO | 80.8 | 2.8 | 1.9 | - | 14.5 |

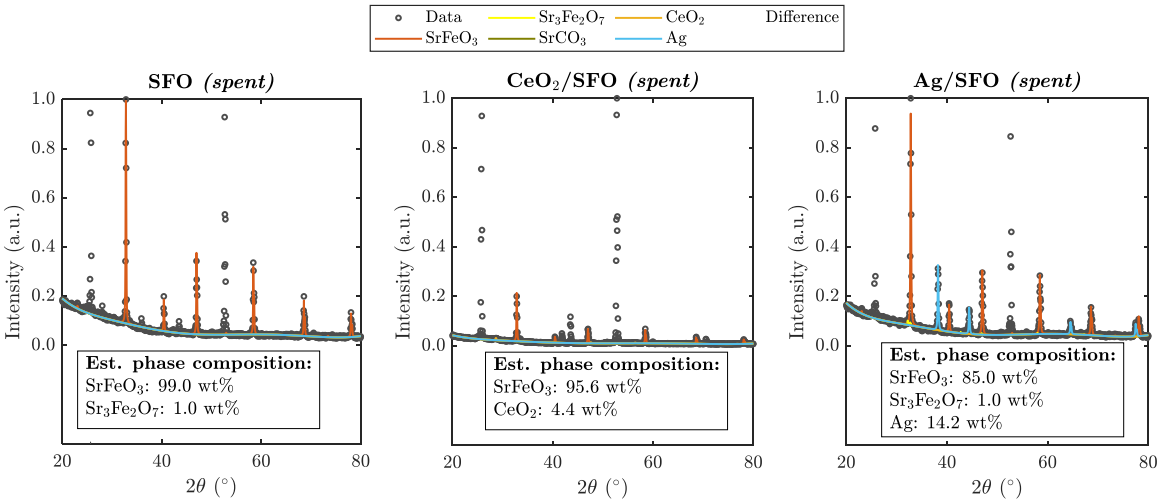


Fig. 3.2 XRD patterns of spent samples of SFO, CeO2/SFO, and Ag/SFO, showing the material remains predominantly in the perovskite phase. Unfitted peaks are ascribed to $Al_2O_3$ used as an inert packing material for experiments in the packed-bed reactor. Estimated compositions were determined by Rietveld refinement, neglecting the mass fraction of $Al_2O_3$

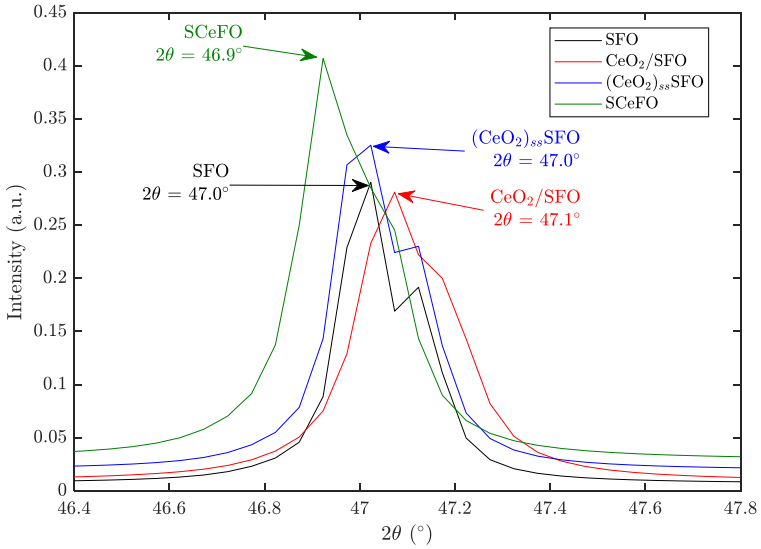


Fig. 3.3 Shift in $SrFeO_3$ peak between samples with un-doped perovskite (SFO, $CeO_2$/SFO, $(CeO_2)_{ss}$SFO), and the sample with Ce incorporated into the perovskite structure (SCeFO) after activation in $H_2$ and reoxidation (see Section 2.1.1 of the main Dissertation)

Crystallite size of Ag and $CeO_2$ in the prepared materials was estimated from XRD measurements, using the Scherrer equation (Eq. 2.1). Estimated values are given in Table 3.3, with no change in Ag crystallite size when comparing Ag/SFO before and after redox cycling, but with spent $CeO_2$/SFO showing an increase in mean $CeO_2$ crystallite size after 250 redox cycles.

Table 3.3 Estimated crystallite sizes of Ag or $CeO_2$ for Ag/SFO, $CeO_2$/SFO and $(CeO_2)_{ss}$SFO from XRD peak broadening. 'Spent' samples refer to samples removed from the packed bed reactor after 250 redox cycles over the temperature range 500-600°C.

| Sample | $CeO_2$ crystallite size (nm) | Ag crystallite size (nm) |
|---|---|---|
| $CeO_2$/SFO (as-prepared) | 6.5 ± 1.0 | - |
| $CeO_2$/SFO (spent) | 11.5 ± 1.2 | - |
| $(CeO_2)_{ss}$SFO | 38.8 ± 11.5 | - |
| Ag/SFO (as-prepared) | - | 39.4 ± 8.8 |
| Ag/SFO (spent) | - | 40.4 ± 18.1 |

### Scanning electron microscopy measurements

Figures 3.4a and 3.4b show SEM micrographs of Ag/SFO material before and after 250 redox cycles, with little visible change in surface morphology. From EDS mapping, shown in Fig. 3.4c, iron and strontium were evenly distributed over the sample, with discrete particles of Ag visible. From measurements of visible Ag particles at the surface of SFO, the size distribution of Ag is given in Fig. 3.4d. Average particle size of Ag somewhat increased during redox cycling (62.2 ± 20.9 nm before cycling, 95.6 ± 29.9 nm after cycling), suggesting that Ag started to agglomerate over 250 cycles.

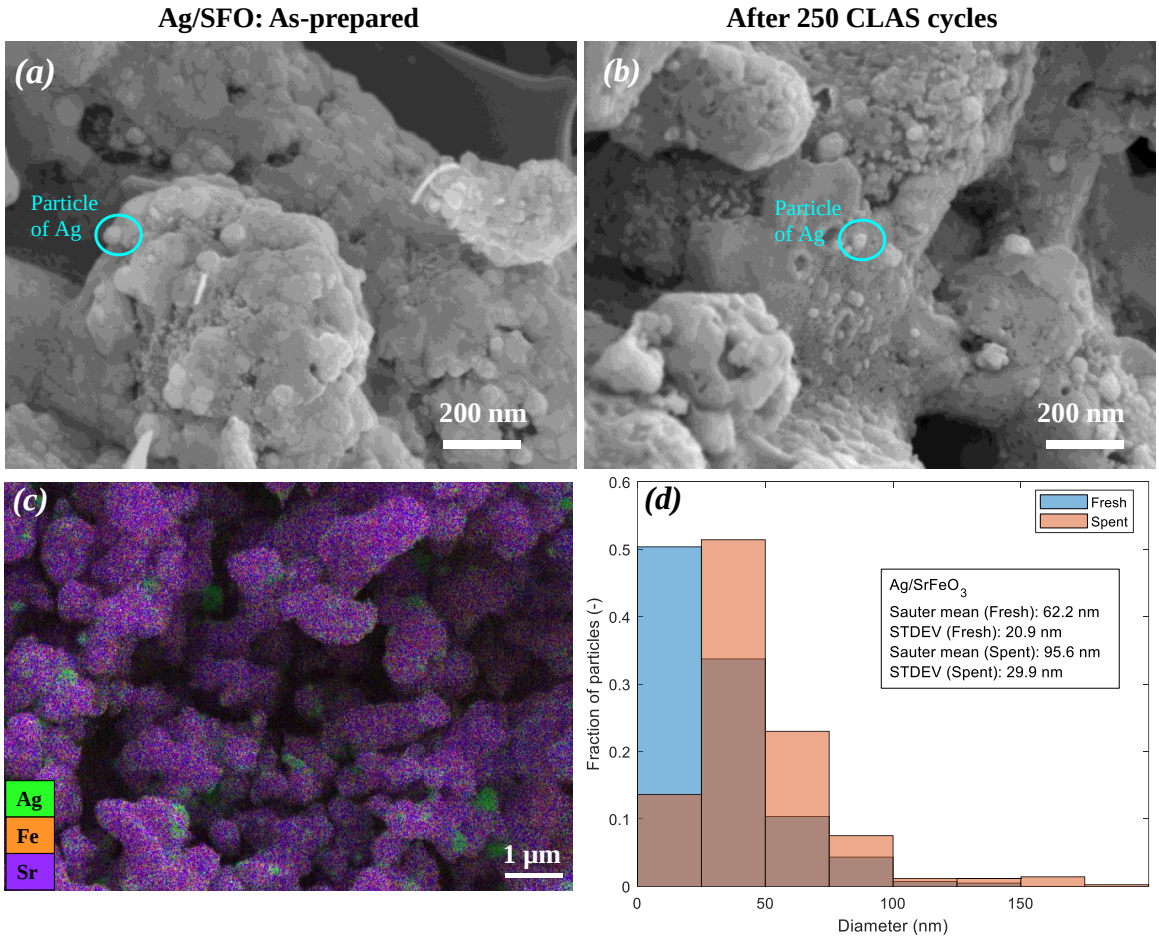


Fig. 3.4 SEM images of Ag/SFO material **(a)** as-prepared, with particles of Ag highlighted and **(b)** after 250 redox cycles in the temperature range 500-600°C, **(c)** EDS map showing distribution of Ag, Fe, and Sr at the surface of spent Ag/SFO, and **(d)** histogram showing particle size distribution of Ag on Ag/SFO, for as-prepared sample (blue bars, 415 particles) and spent sample after 250 cycles over the temperature range 500-600°C (orange bars, 426 particles).

The OC materials containing Ce, $CeO_2$/SFO and $(CeO_2)_{ss}$SFOshowed similar surface morphology to Ag/SFO (Figs. 3.5 and 3.6), whereas the sample of SCeFO (Fig. 3.7) was significantly less porous. The low porosity of SCeFO was likely caused by calcination at a higher temperature than the other samples, 1200°C rather than 1000°C, which was applied to ensure incorporation of Ce into the perovskite structure.

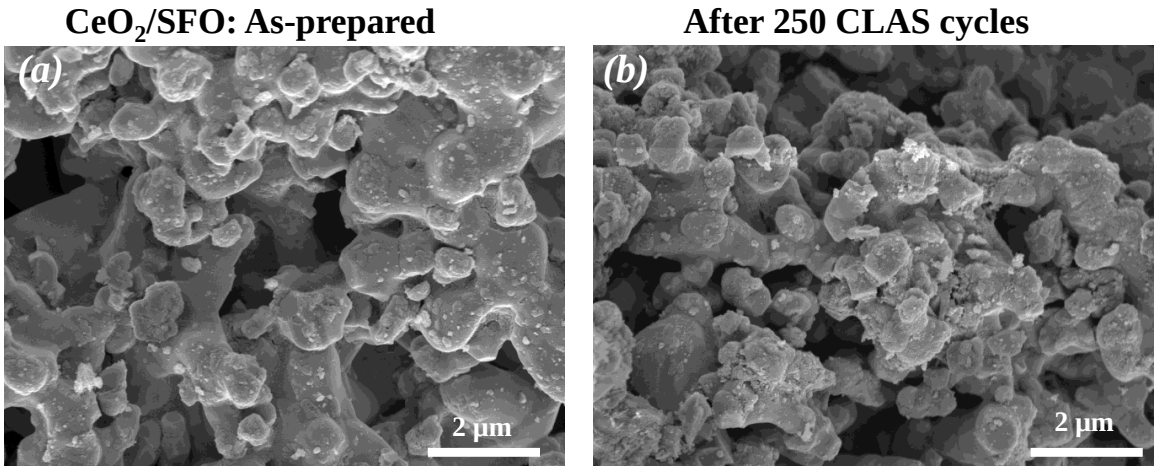


Fig. 3.5 SEM images of $CeO_2$/SFO material **(a)** as-prepared and **(b)** after 250 redox cycles in the temperature range 500-600°C.

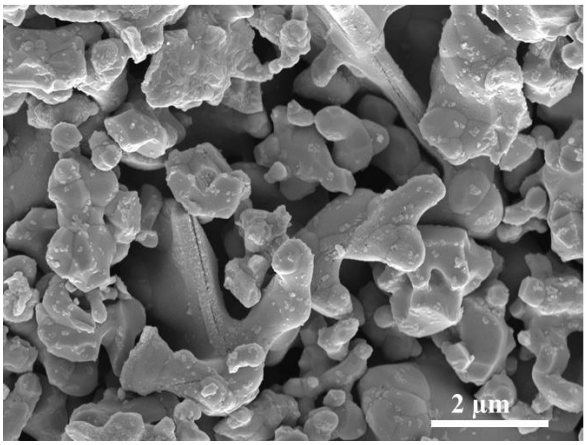


Fig. 3.6 SEM images of as prepared $(CeO_2)_{ss}$SFO.

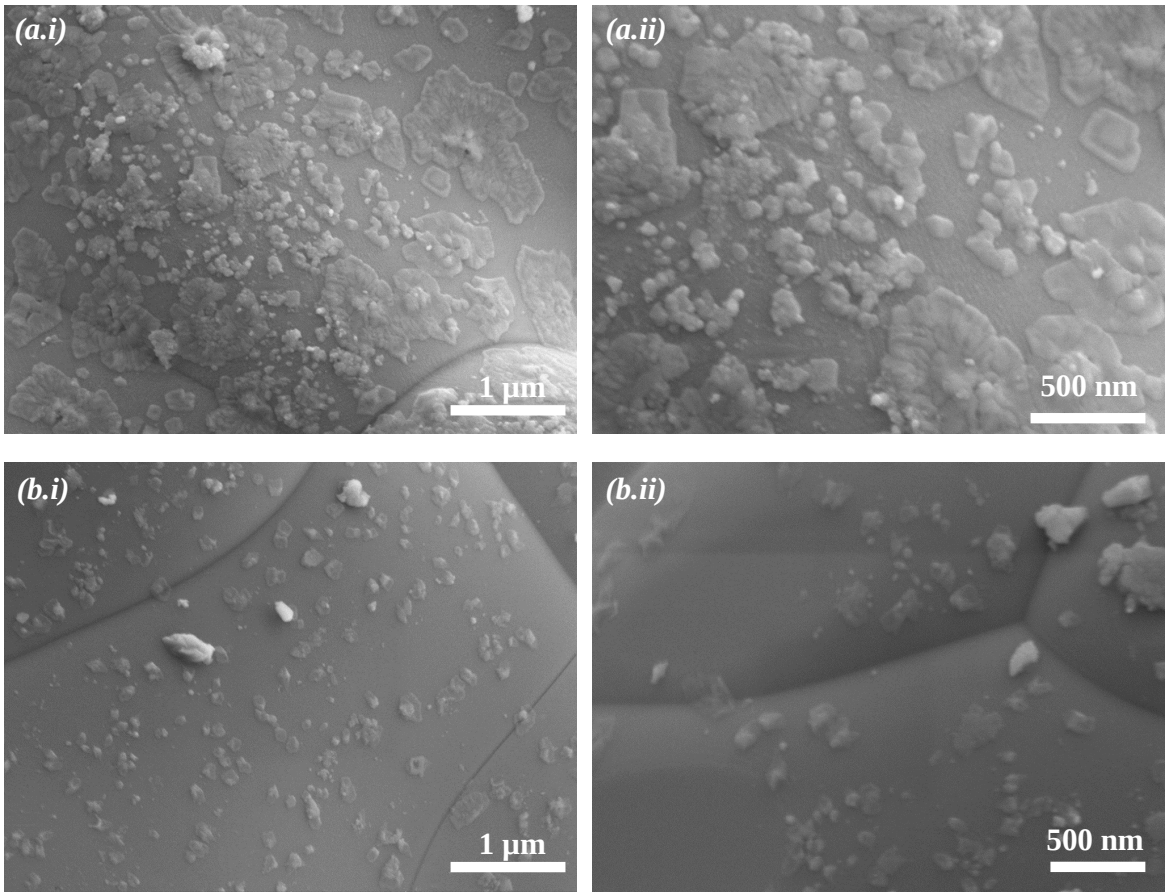


Fig. 3.7 **(a)** SEM image of SCeFO used in redox experiments, *i.e.* after calcination at 1200°C and activation in $H_2$, **(b)** SEM image of fresh SCeFO after calcination at 1200°C but before activation in $H_2$.

### 3.4.2 Thermogravimetric analysis

To determine the initial values of (3 - $\delta$) in the prepared $SrFeO_{3-\delta}$ materials, samples were reduced in 5 vol% $H_2$ in the TGA, shown in Figs. 3.8a and 3.8b. Initial stoichiometry of the $SrFeO_{3-\delta}$ perovskite was estimated from the change in gradient associated with the reduction of $SrFeO_{2.5}$ (Marek *et al.*, 2018a; Starkov *et al.*, 2014) using Eqs. 3.21 and 3.22, where $m_{BM}$ is the relative mass at the change in gradient (as shown on Fig. 3.8), (3 - $\delta_0$) is the initial oxygen stoichiometry, $M_r(BM)$ is the molar mass of brownmillerite $SrFeO_{2.5}$ (183.465 g $mol^{-1}$), and $\lambda_m$ is the mass fraction of inert components (*i.e.* wt% of Ag).

$$M_r(SrFeO_{3-\delta_0}) = M_r(BM) \cdot \frac{1-\lambda_m}{m_{BM}\lambda_m} \tag{3.21}$$

$$(3-\delta_0) = \frac{M_r(SrFeO_{3-\delta_0}) - M_r(Sr) - M_r(Fe)}{M_r(O)} \tag{3.22}$$

For Ag/SFO, the first sharp change in gradient during reduction at *c.* 350°C was assumed to correspond to a decrease in rate of reduction at $SrFeO_{2.52}$, as reported by Starkov *et al.* (2014) for SFO, whereas the second change in gradient at around 510°C was taken to correspond to the brownmillerite stoichiometry $SrFeO_{2.5}$. For unmodified SFO, no clear change in gradient at $SrFeO_{2.52}$ was observed, possibly because of the relatively high temperature ramp rate (10°C $min^{-1}$) used here.

From Eq. 3.22, the estimated initial stoichiometry values over three repeat measurements of the as-prepared SFO and Ag/SFO materials were (3 - $\delta_0$) = 2.82 ± 0.03 and 2.83 ± 0.01 respectively, within the expected range of 2.80-2.85 for $SrFeO_{3-\delta}$ prepared in air (Marek *et al.*, 2018a). Although the difference in the initial content of oxygen for SFO and Ag/SFO were within experimental uncertainty, the Ag/SFO showed a substantially larger change in mass at low temperatures than SFO, reducing to $SrFeO_{2.52}$ at around 350°C, as shown in Fig. 3.8b. The behaviour of SFO and Ag/SFO reduced in $H_2$ atmospheres is discussed in greater detail in Chapter 4.

To confirm that $SrFeO_{2.5}$ stoichiometry was achieved for reduction of Ag/SFO, a sample of Ag/SFO was heated to 500°C under 5 vol% $H_2$ flow in the TGA, then rapidly quenched (25°C $min^{-1}$ cooling rate) to room temperature in $N_2$ and characterised *via* XRD (shown in Fig. 3.8c), confirming that brownmillerite $SrFeO_{2.5}$ was the main phase present. For samples containing $CeO_2$, partial reduction of $CeO_2$ in $H_2$ during heating up to 900°C meant the point at which perovskite $SrFeO_{3-\delta}$ underwent phase transition to brownmillerite $SrFeO_{2.5}$ could not be determined readily. Hence, for

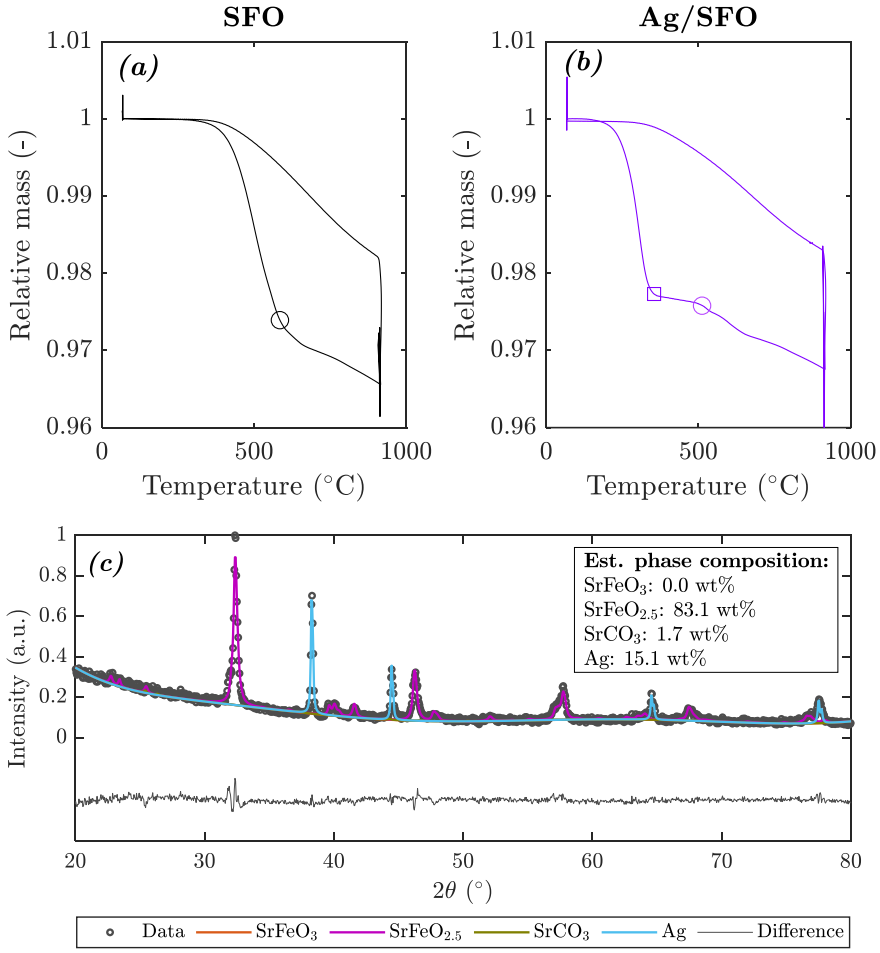


Fig. 3.8 Reduction and oxidation in 5 vol% $H_2$ and air respectively of **(a)** SFO and **(b)** Ag/SFO, and **(c)** XRD pattern of Ag/SFO heated to 500°C in 5vol% $H_2$, then rapidly quenched, with estimated phase composition from Rietveld refinement. The 2nd of three redox cycles is shown for both samples, with circles indicating the change in gradient associated with $SrFeO_{2.5}$ stoichiometry. For Ag/SFO, the point on the reduction curve corresponding to an estimated stoichiometry of $SrFeO_{2.52}$ is indicated by a square.

subsequent calculations, the initial stoichiometry for samples $CeO_2$/SFO, $(CeO_2)_{ss}$SFO, and SCeFO was assumed to be 2.82, as for SFO.

The reduction and oxidation behavior of the prepared materials was determined *via* temperature-programmed reduction in $N_2$ and oxidation in air (shown in Fig. 3.9a for SFO, and in Appendix B, Fig. B.1 for all other samples).

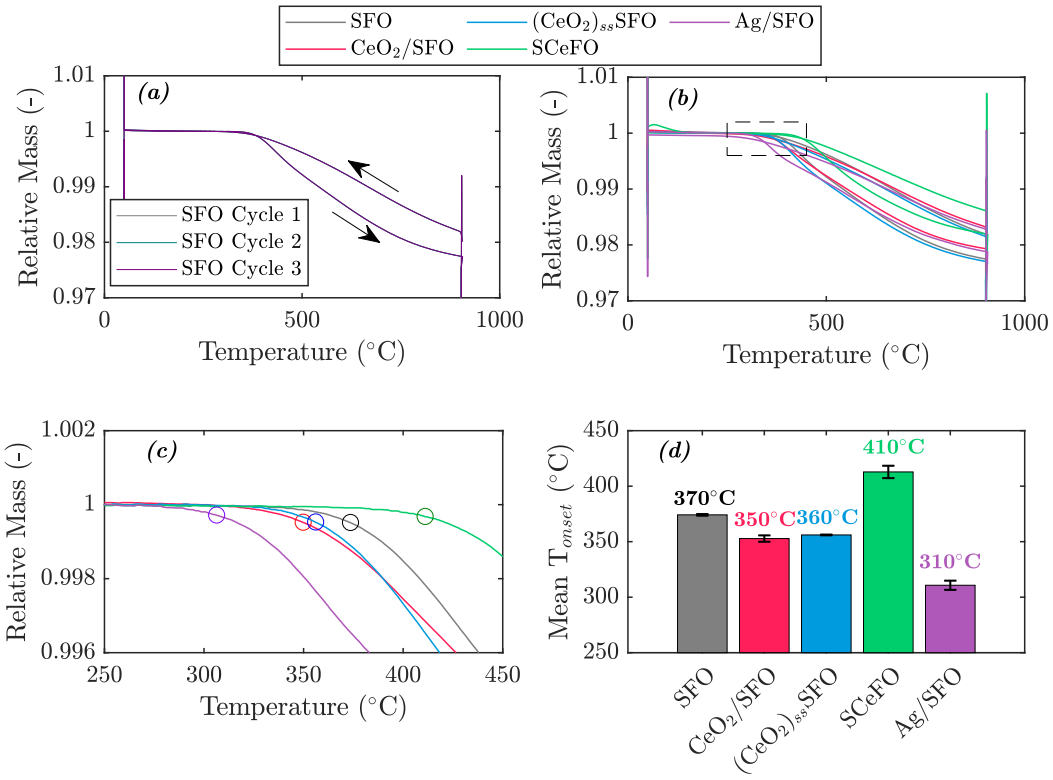


Fig. 3.9 **(a)** Three reduction–oxidation cycles for SFO, showing consistent mass change over each cycle; **(b)** comparison of the second redox cycle for SFO, $CeO_2$/SFO, $(CeO_2)_{ss}$SFO, SCeFO, and Ag/SFO; **(c)** details from the reduction step in **(b)** (dashed box), showing $T_{onset}$ (indicated by circled points) for each sample; and **(d)** mean value of $T_{onset}$ for each sample over three reduction-oxidation cycles (error bars show standard deviation over three cycles). Masses were normalized with respect to the mass at the start of TPR cycles.

All samples showed a consistent mass change over the three cycles, indicating that the initial oxygen non-stoichiometry of $SrFeO_{3-\delta}$ fully regenerated after reoxidation. Particles of $CeO_2$ were also analyzed using temperature cycling in $N_2$ and air; however, the results given Appendix B, Fig. B.2 showed that $CeO_2$ on its own was practically inactive. Given that oxygen release from $CeO_2$ was negligible during temperature cycling, differences in oxygen release between the samples of SFO, $CeO_2$/SFO, and

$(CeO_2)_{ss}$SFO were ascribed solely to the interaction between $SrFeO_{3-\delta}$ and $CeO_2$ (Cooper *et al.*, 2015; Panlener *et al.*, 1975).

For each sample, the starting temperature of reduction in $N_2$, $T_{onset}$, was estimated using MATLAB function `findchangepts` by identifying the point with the greatest change in gradient in mass loss (Fig. 3.9b,c). Impregnation with Ag on the surface of SFO was found to have the largest influence on $T_{onset}$ of the samples investigated, showing a decrease of 60 ± 4°C, as compared to SFO (Fig. 3.9d). A lower $T_{onset}$ was consistent with previous studies investigating the release of oxygen from Ag/$SrFeO_{3-\delta}$ heated in air (Marek and García-Calvo Conde, 2021).

Addition of $CeO_2$ on the surface or in the bulk of SFO lowered the $T_{onset}$ by around 20 ± 3°C and 10 ± 0.3°C for $CeO_2$/SFO and $(CeO_2)_{ss}$SFO, respectively. The decrease in $T_{onset}$ for $(CeO_2)_{ss}$SFO and $CeO_2$/SFO was consistent with the previous findings of Marek *et al.* (2020), who reported a decrease in $T_{onset}$ for $(CeO_2)_{ss}$SFO and $CeO_2$/SFO when reduced in $H_2$. The mass curve during temperature cycling for SCeFO showed a higher $T_{onset}$ and less total oxygen release at 900°C than the unmodified sample of SFO, suggesting that the structural modification by partial substitution of Sr with 5 at% Ce might inhibit oxygen release from the perovskite lattice.

Isothermal TGA measurements over the temperature range 400-600°C, shown in Fig. 3.10, demonstrated that as well as changing $T_{onset}$, modification of SFO with $CeO_2$ and Ag affected the rate of oxygen release. At 400°C, SFO, $CeO_2$/SFO, and $(CeO_2)_{ss}$SFO all released oxygen relatively slowly with decreasing rate of release, reaching a plateau after around 40 min. The Ag/SFO material reduced rapidly at 400°C in $N_2$, reaching 95% of the final mass change within around 15 min. Contrastingly, SCeFO reduced at the slowest rate; given that 400°C was below the estimated $T_{onset}$ for SCeFO, the minimal oxygen release was unsurprising.

At higher temperatures (≥500°C), the differences between samples gradually diminished, with results for SFO and $(CeO_2)_{ss}$SFO almost overlapping at 500 and 600°C (shown in Fig. 3.10b,c). The curves corresponding to the mass change for Ag/SFO, $CeO_2$/SFO, and SCeFO also overlapped at 600°C (shown in Figure 3.10c), with similar total mass change and rate of oxygen release. For all samples, the rate of reoxidation in air was much faster than the rate of the preceding reduction. At 400°C, Ag/SFO fully reoxidised within 1.5 min; SFO, $CeO_2$/SFO, and $(CeO_2)_{ss}$SFO required about 3 min, and SCeFO, the slowest sample, required 13 min. However, when the temperature was increased (≥500°C), all samples reoxidised rapidly, in less than 1 min.

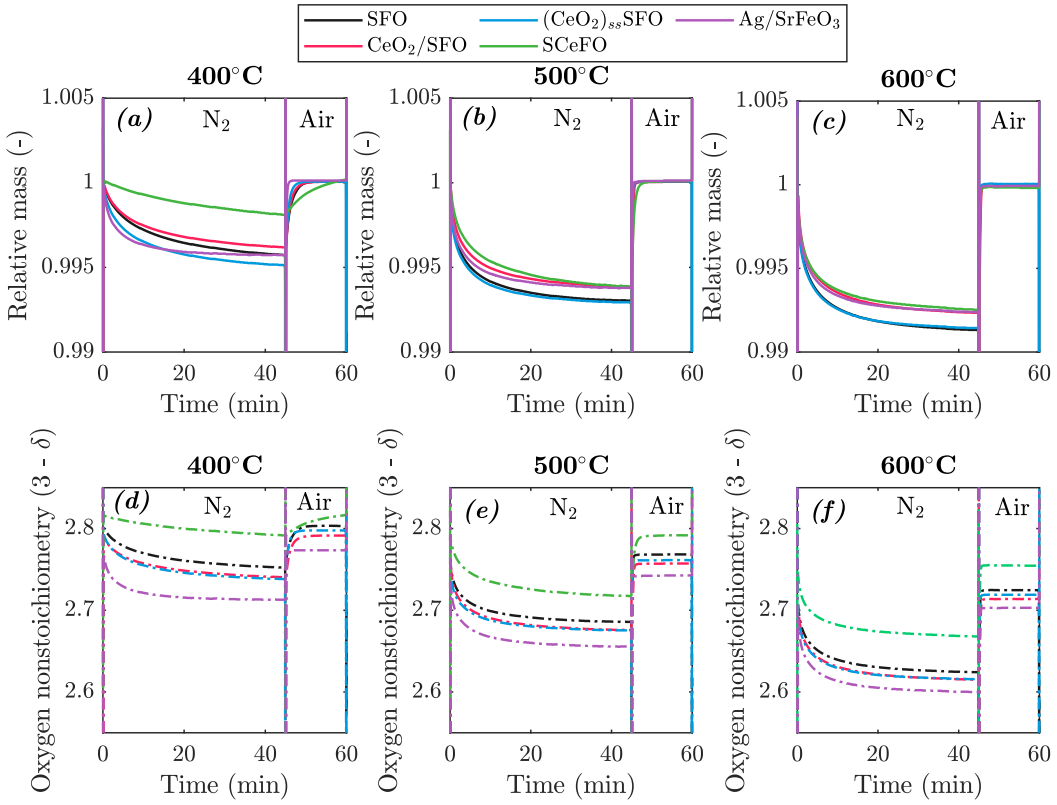


Fig. 3.10 Isothermal gas cycling over SFO, $CeO_2$/SFO, $(CeO_2)_{ss}$SFO, SCeFO, and Ag/SFO at 400-600°C, with vertical lines indicating gas switching between $N_2$ and air. The second of the three redox cycles is shown for all samples and temperatures. Masses were normalized with respect to mass of sample in equilibrium with air at each temperature. Solid lines indicate relative mass **(a–c)**, and dash-dot lines indicate estimated oxygen stoichiometry **(d–f)**.

Figures 3.10d–f present the change in oxygen nonstoichiometry of $SrFeO_{3-\delta}$, *i.e.* $(3-\delta)$, during the isothermal redox cycle. Calculations assumed that the mass of $CeO_2$ in $CeO_2$/SFO and $(CeO_2)_{ss}$SFO (taken from ICP measurements reported in Table 3.1) did not change over time, as $CeO_2$ was not active during reduction in $N_2$, as shown in Appendix B, Fig. B.2.

The final oxygen nonstoichiometry during reduction of all samples over the temperature range of 400–600°C (shown in Fig. 3.10) exhibited the same trend as $T_{onset}$, with the extent of reduction following the order Ag/SFO > $(CeO_2)_{ss}$SFO ≈ $CeO_2$/SFO > SFO > SCeFO. The findings from the isothermal experiments were therefore consistent with the observation from temperature cycling that Ag enhanced the oxygen release from $SrFeO_{3-\delta}$ to the greatest extent, with $CeO_2$ showing a small enhancement, and structurally doped Ce inhibiting the oxygen release, as compared to $SrFeO_{3-\delta}$.

Equilibrium oxygen nonstoichiometry, $(3-\delta_{eq})$, for SFO and Ag/SFO at varied temperatures and $pO_2$ values, was estimated from TGA measurements of the material exposed to a given target $pO_2$ for 3 h at 25°C increments over the range of 500-600°C, with the results presented in Fig. 3.11. Curves showing $\delta_{eq}$ as a function of $T$ for $SrFeO_{3-\delta}$ at $pO_2 = 0.21$ and $10^{-5}$ atm were plotted for comparison using reference thermodynamic data for $SrFeO_{3-\delta}$ from Preis (2017), generated using FactSage 8.2 software (Bale *et al.*, 2016). Raw TGA curves used to generate Fig. 3.11 are also given in Appendix B, Fig. B.3.

The resulting values of $(3-\delta_{eq})$ for SFO estimated here show reasonable agreement with published values of $(3-\delta_{eq})$ for high $pO_2$ values, as shown in Fig. 3.12. At $pO_2 \leq 0.075$ atm, the values of $(3-\delta_{eq})$ obtained here were consistently higher than those reported from TGA measurements by Ikeda *et al.* (2016) and Krzystowczyk *et al.* (2020) but lower than the TGA results from Görke *et al.* (2020) and Vieten *et al.* (2017). Additionally, Starkov *et al.* (2014) estimated the $pO_2$-$T$-$\delta_{eq}$ characteristics for $SrFeO_{3-\delta}$ by measuring the total uptake and release of oxygen from a packed bed of SFO, giving somewhat higher values of $(3-\delta_{eq})$ at all temperatures than those reported here, apart from at $pO_2 = 10^{-5}$ atm, where their estimated value of $(3-\delta_{eq})$ was around 2.5 (*i.e.* indicating phase transition to brownmillerite $SrFeO_{2.5}$) under all temperatures investigated.

Comparing the obtained values for $(3-\delta_{eq})$ for SFO and Ag/SFO in Figure 3.11, in most cases, Ag/SFO equilibrated at lower $(3-\delta_{eq})$ than SFO, with a difference becoming more pronounced at lower values of $pO_2$ (<0.15 atm). Hence, the presence

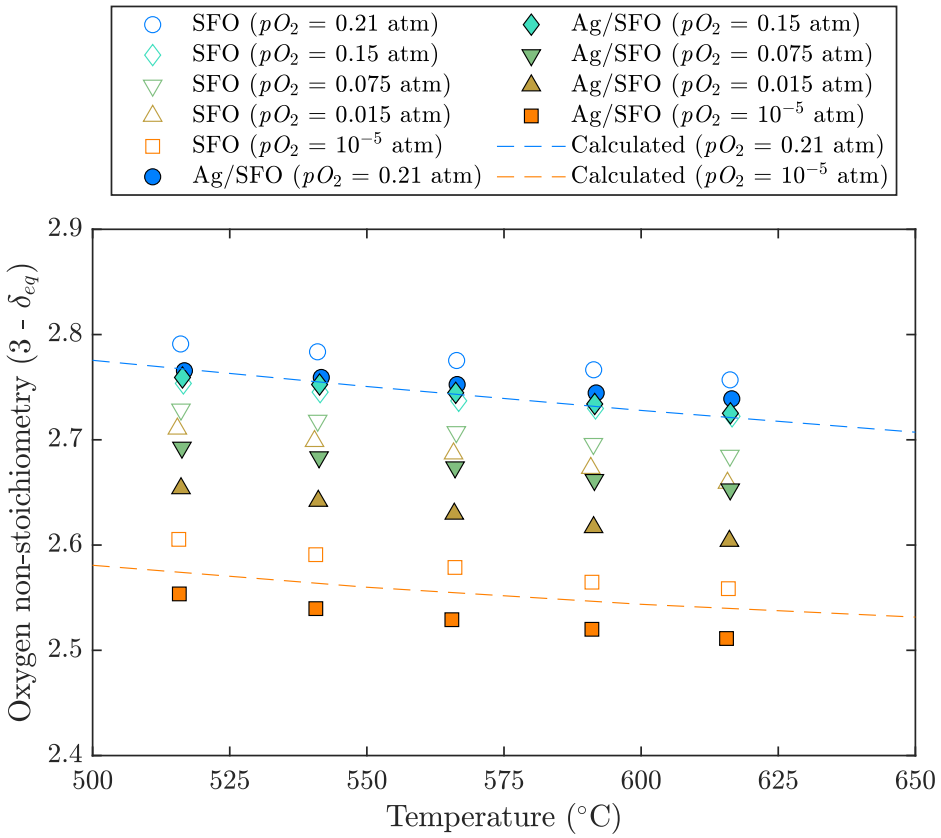


Fig. 3.11 Change in oxygen non-stoichiometry with temperature for SFO (hollow symbols) and Ag/SFO (filled symbols) in various $pO_2$ atmospheres. Dashed lines indicate calculated values of $(3 - \delta_{eq})$ for $SrFeO_{3-\delta}$ as a function of $T$ using reference thermodynamic parameters from Preis (2017).

of Ag on the surface of $SrFeO_{3-\delta}$ resulted in a structure with a higher concentration of oxygen vacancies under given $pO_2$–$T$ conditions.

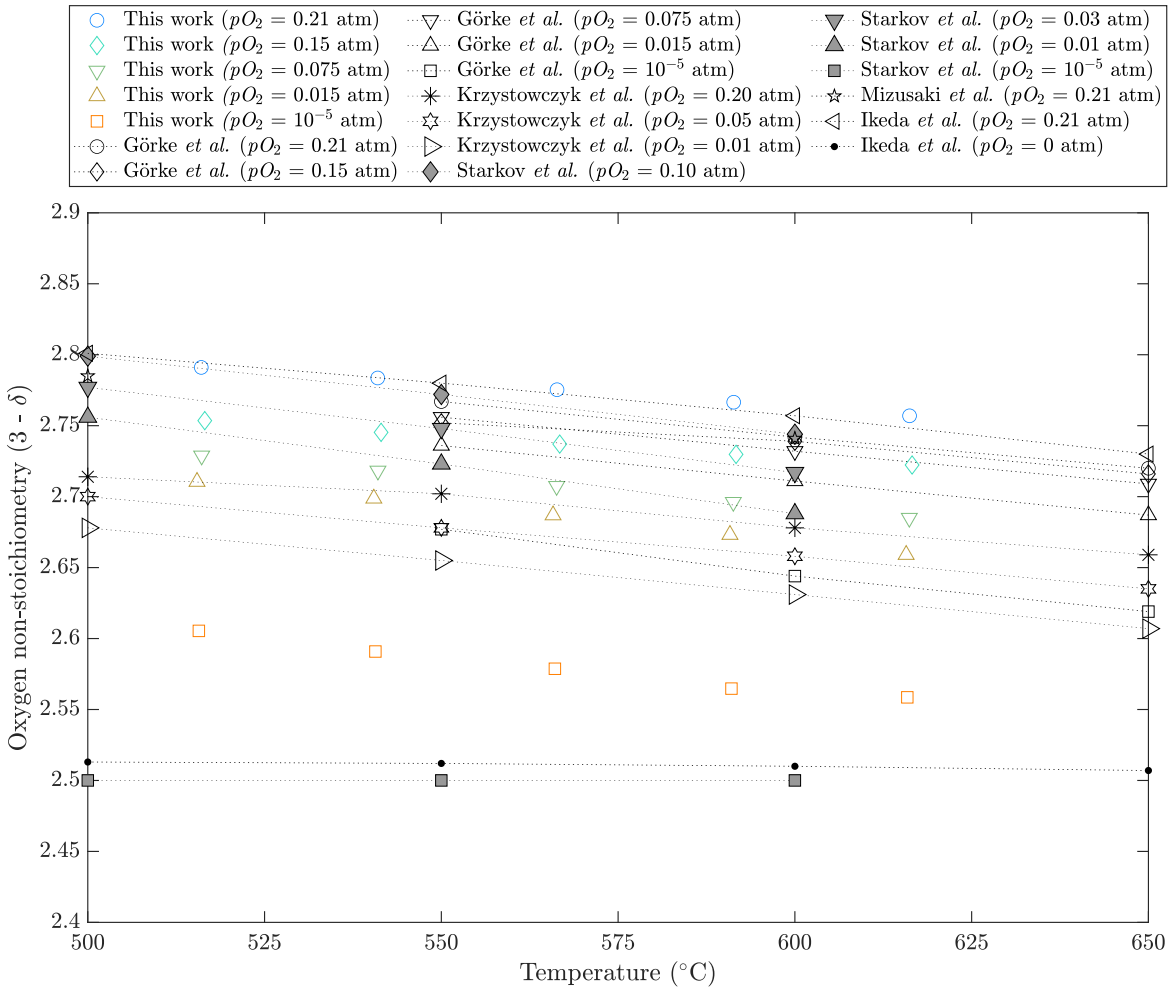


Fig. 3.12 Comparison between obtained equilibrium non-stoichiometry values for SFO with published values reported by Görke *et al.* (2020), Starkov *et al.* (2014), Krzystowczyk *et al.* (2020), Mizusaki *et al.* (1992), and Ikeda *et al.* (2016), with dotted lines included between points to aid interpretation.

### 3.4.3 Experiments in the packed bed reactor

The reduction and reoxidation profiles for the oxygen carrier materials undergoing redox cycling in air and $N_2$ are shown in Fig. 3.13. For all samples, a sharp, asymmetric peak in the concentration of oxygen measured at the outlet of the reactor was observed following gas switching from air to nitrogen, thus indicating rapid oxygen release, which then gradually decayed. When the feed gas was switched back to air, all samples reoxidised rapidly, with the observed oxygen uptake taking less than 5 s. For SFO, the measured rates of oxygen release and uptake were in good agreement with previously reported results (Görke *et al.*, 2020).

For all measurements, excluding SCeFO, the averaged oxygen balance over each cycle was >90%, assessed by comparing the amount of oxygen released to the amount of oxygen absorbed during reduction and reoxidation. The sample of $SrFeO_{3-\delta}$ structurally doped with Ce, SCeFO, showed an oxygen balance of only around 80%, with a greater extent of measured oxygen release than reuptake. The observed discrepancy for SCeFO might be caused by relatively slow reoxidation, resulting in deviations in $pO_2$ which were below the detection threshold of the oxygen sensor ($pO_{2,min} \approx 100$ Pa), and hence giving a systematic underestimate of oxygen uptake over a full oxidation cycle. The maximum instantaneous rates of oxygen release, calculated using Eq. 3.1, are shown in Fig. 3.14.

All samples showed stable total oxygen release and uptake over the course of 46–49 cycles, as presented in Fig. 3.15a. Hence, redox cycling was fully reversible with no changes in the oxygen storage capacity, and confirming that SFO was able to stably release and uptake oxygen over multiple redox cycles (Görke *et al.*, 2020), including when modified with $CeO_2$ or Ag.

Ratios of the amount of oxygen released from modified oxygen carriers, $n_{O_2}$, to the oxygen released from SFO, $n_{O_2,SFO}$, at each temperature are shown in Fig. 3.15b. At low temperatures (<550°C), $CeO_2$/SFO, $(CeO_2)_{ss}$SFO, SCeFO, and Ag/SFO all showed a marked increase in oxygen released *per* cycle. At all temperatures, Ag/SFO showed the greatest increase in total oxygen release, with Ag/SFO releasing approximately five times more oxygen *per* cycle at 475°C. Interestingly, despite showing an increase in $T_{onset}$ as compared to SFO, the sample of SCeFO released markedly more oxygen *per* cycle than the SFO and $CeO_2$/SFO, as can be observed for each temperature point in Fig. 3.15b. For all samples, the total oxygen released at 600°C was approximately the same, at around 95 $\mu$mol $g_{OC}^{-1}$ *per* cycle.

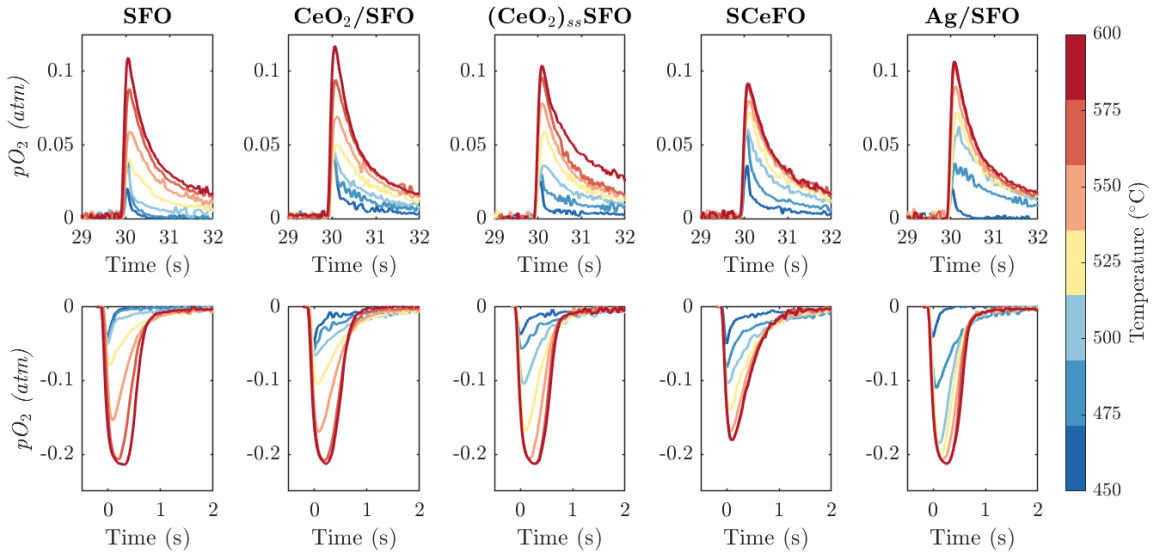


Fig. 3.13 Redox cycling of OC materials in a packed bed reactor in air and $N_2$, showing oxygen release during reduction (top row) and oxygen uptake during reoxidation (bottom row) of oxygen carrier materials. In all cases, the 25th of 46-49 performed cycles is shown.

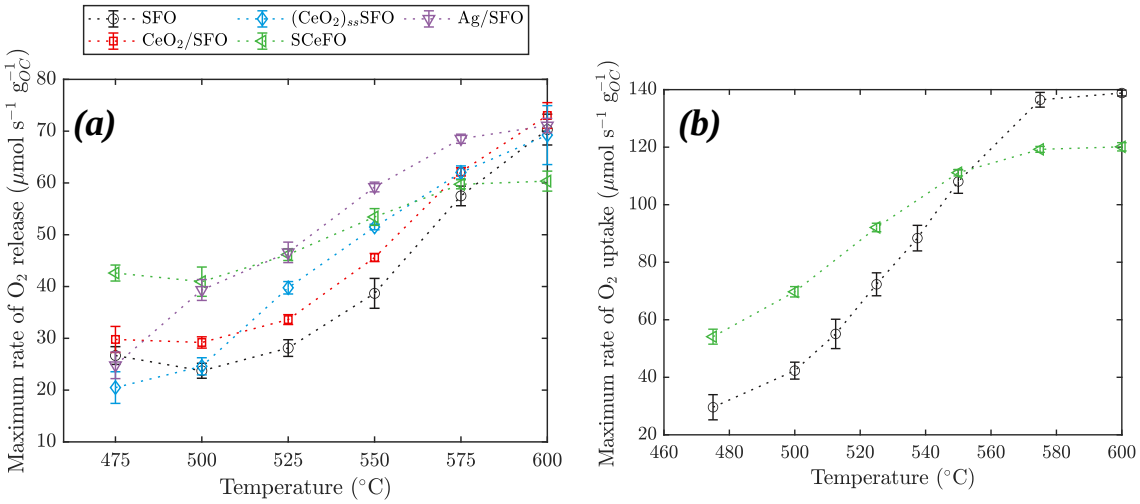


Fig. 3.14 Maximum observed rates of reaction for samples undergoing **(a)** reduction and **(b)** oxidation. Points indicate average over repeated redox cycles, error bars indicate standard deviation from 46-49 cycles

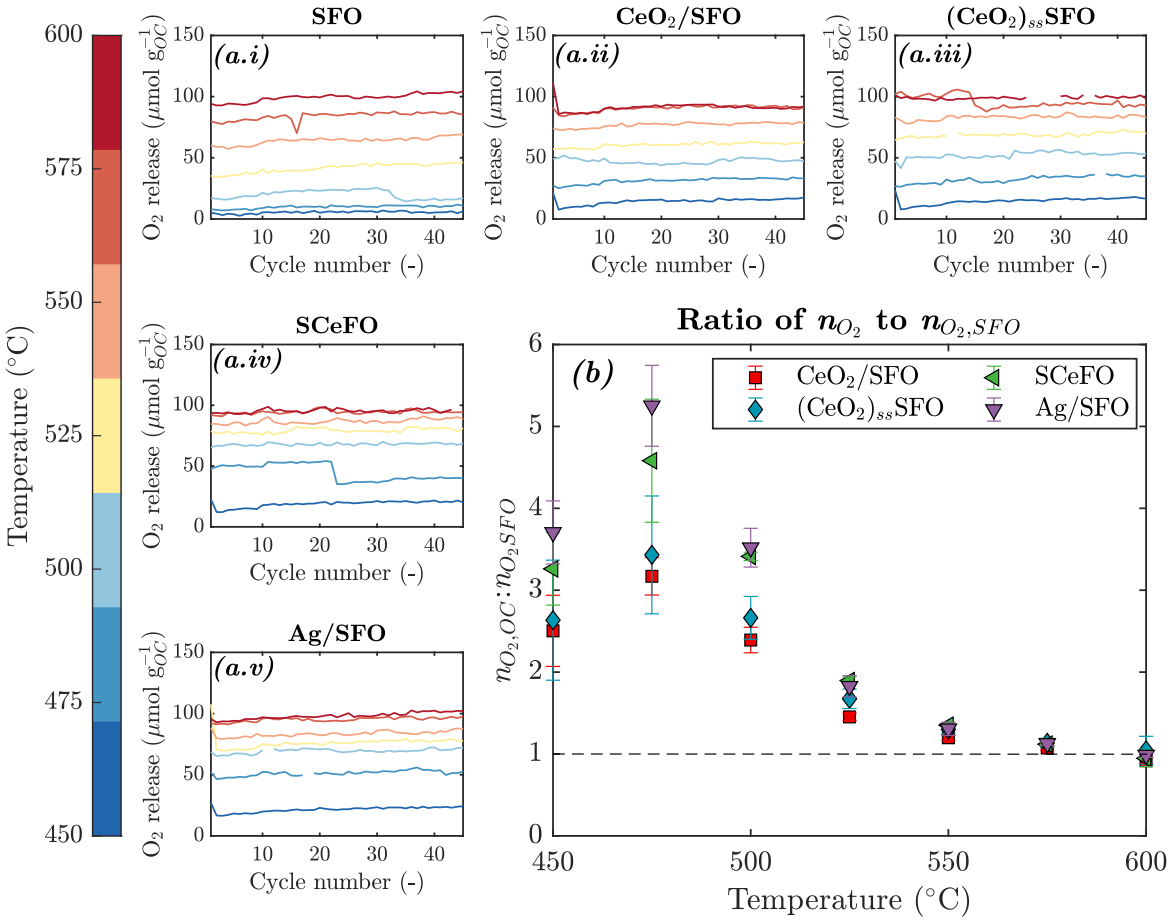


Fig. 3.15 **(a.i-v)** Oxygen release from SFO, $CeO_2$/SFO, $(CeO_2)_{ss}$SFO, and Ag/SFO oxygen carrier materials in packed bed and **(b)** ratio of moles of oxygen released *per* cycle from modified oxygen carriers ($n_{O_2}$) to moles of oxygen released from SFO ($n_{O_2,SFO}$). Markers indicate the average over 45-49 cycles, and error bars indicate the standard deviation over 45-49 cycles. Gaps indicate the removal of numerical artifacts, which resulted from imperfect alignment between blank and measured curves.

Reoxidation of OC samples occurred an order of magnitude more rapidly than reduction (shown in Fig. 3.13); hence, results collected using 0.40 g of OC material for all samples apart from SCeFO could not be used to extract the kinetic parameters of oxidation, because of a substantial increase in the reactor temperature above the controller set-point value and the depletion of oxygen in the flowing gas stream. To mitigate the problem of oxygen depletion, 100 mg of SFO material (*i.e.*, the sample with the slowest rate of oxidation) was used, using 5.05 vol% $O_2$ as the oxidising gas to decrease the rate of reaction, with the results shown in Fig. 3.16.

Nevertheless, measurements above 525°C could not be used for determination of kinetic parameters for SFO, as a substantial fraction of the oxygen provided in the feed was consumed. For Ag/SFO, reoxidation of the OC material in 5.05 vol% $O_2$ was attempted (shown in Fig. 3.17), but the reaction was sufficiently fast that there was no discernible difference between any measurements taken above 500°C, as oxygen in the gas phase became rapidly depleted.

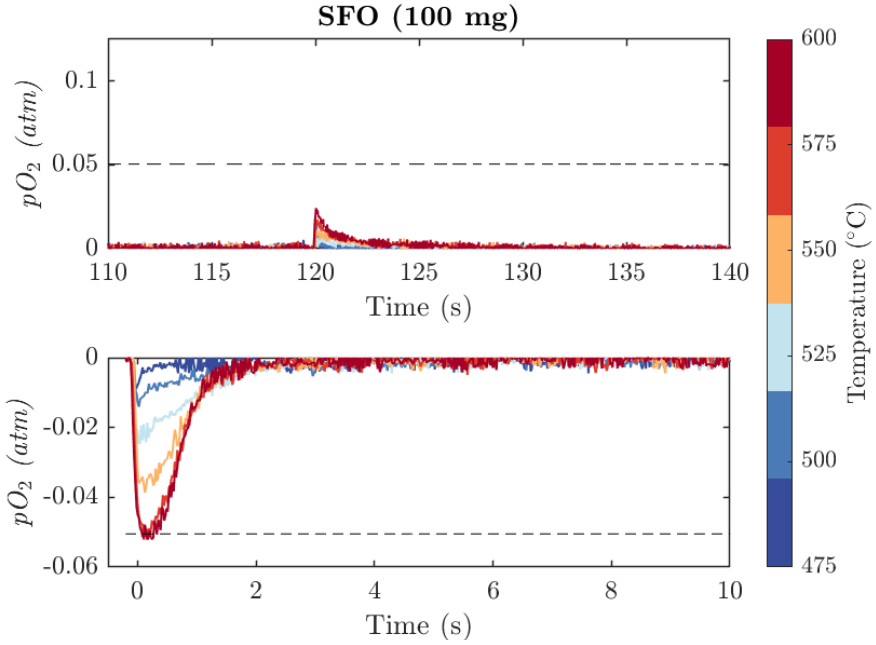


Fig. 3.16 Graphs showing oxygen release and reuptake for 0.10 g of SFO, reduced under $N_2$ for 120 s, and re-oxidised in 5.05vol% $O_2$ for 120 s. Dashed line corresponds to $pO_2 = 0.0505$ atm, indicating consumption of all available oxygen.

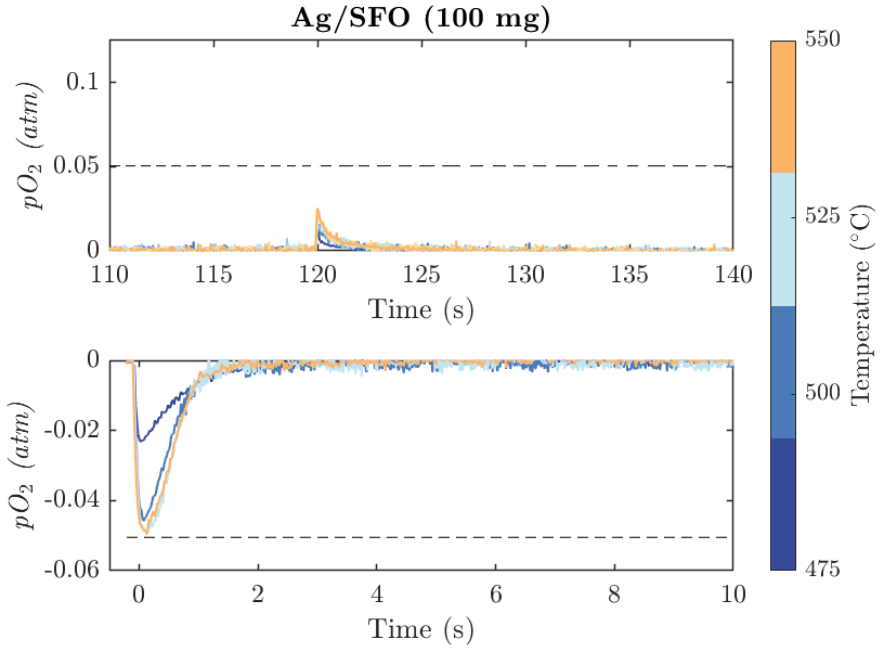


Fig. 3.17 Graphs showing oxygen release and reuptake for 0.10 g of Ag/SFO, reduced under $N_2$ for 120 s, and re-oxidised in 5.05vol% $O_2$ for 120 s. Dashed line corresponds to $pO_2 = 0.0505$ atm, indicating consumption of all available oxygen.

### Mass transfer and equilibrium limitations

Evaluating Eq. 3.10 between 500-600°C, the estimated limiting rate of external mass transfer of oxygen at the start of reduction was *c.* 50 mol $s^{-1}$ $g_{OC}^{-1}$, *i.e.* 6 orders of magnitude greater than the rates of reduction and 5 orders of magnitude greater than the maximum rate of oxidation measured from experiments. Hence, observed rates were not limited by external mass transfer.

However, at 600°C, the rate-limiting step for oxygen release might have changed from being limited by reaction kinetics to internal mass transfer as a result of diffusion within the pores of the particles of OC materials. For each measurement, the Thiele modulus, $\phi$, describing the relative influence of reaction kinetics and internal diffusion within pores, was estimated using Eq. 3.16. For reduction of SFO, $CeO_2$/SFO, $(CeO_2)_{ss}$SFO, and Ag/SFO, shown in Fig. 3.18a, measurements at ≤575°C were below the threshold for internal mass transfer limitation described in Section 3.3.2 ($\phi^2 < 0.603$, $\phi < 0.78$), with approximate values of $\phi = 0.44$-$0.77$ over the range 475-600°C. For SCeFO, the porosity from SEM images was markedly lower than the other samples (shown in Fig. 3.7), and so SCeFO was excluded from calculations of Thiele modulus.

For re-oxidation of SFO, shown in Fig. 3.18b, the estimated values of $\phi$ were substantially greater, with approximate values of $\phi$ = 2.5-8.2; hence, the observed rate of reaction was likely limited by internal mass transfer. Therefore, the estimated rate constants were recalculated to account for the effect of internal mass transport using Eq. 3.20, with the modified rate constants used for estimating kinetic parameters.

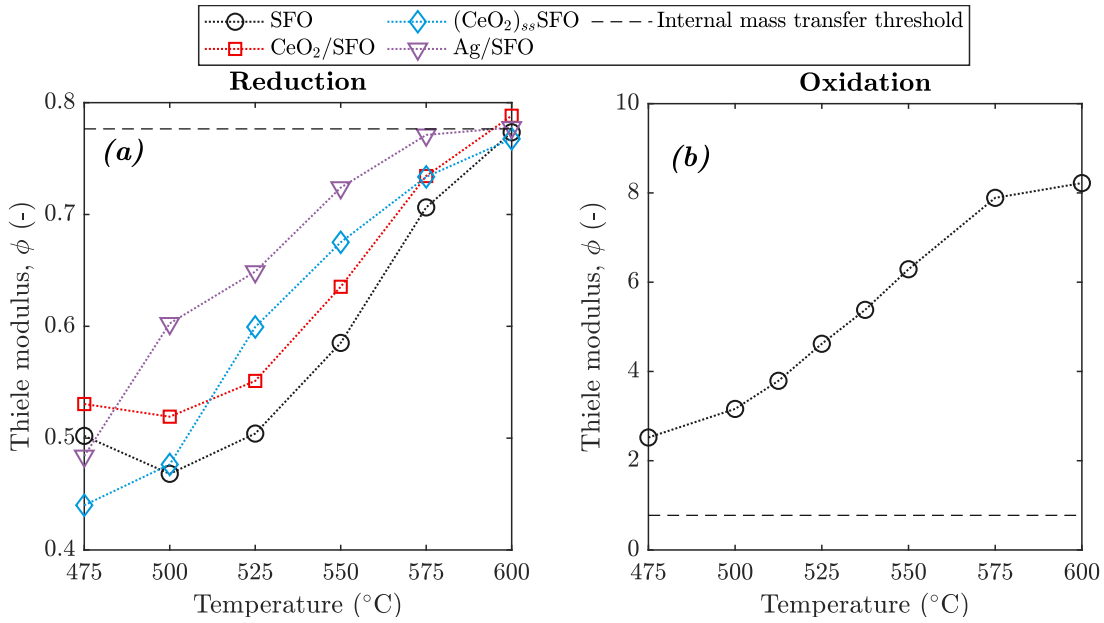


Fig. 3.18 Thiele modulus, $\phi$, estimated for **(a)** oxygen release, and **(b)** oxygen uptake with dashed lines indicating threshold below which internal mass transfer limitation was estimated to be negligible, $\phi^2 < 0.603$ (Vannice, 2005).

As described in Section 3.3.2, the rate of reaction can also be limited by the solid and gas phases approaching thermodynamic equilibrium along the length of the packed bed, *i.e.*, if the velocity of the reaction front is of the same order as the superficial velocity of gas traveling through the bed (Görke *et al.*, 2020). The extent of equilibrium limitation was described by the ratio $\frac{kRTL}{v}$, with estimated values for each measurement shown in Fig. 3.19.

For all measurements of reduction of the OC materials, shown in Fig. 3.19a, $\frac{kRTL}{v} < 1$, indicating little influence of equilibrium limitation on rate of oxygen release. However, for re-oxidation of SFO, and SCeFO, shown in Fig. 3.19b, $\frac{kRTL}{v} > 1$ for all temperatures investigated, indicating that the rate of oxygen uptake was affected by thermodynamic equilibrium. Hence, the values of $k$ estimated for oxidation of SFO and SCeFO are likely lower than would be observed in the case of kinetic limitation only.

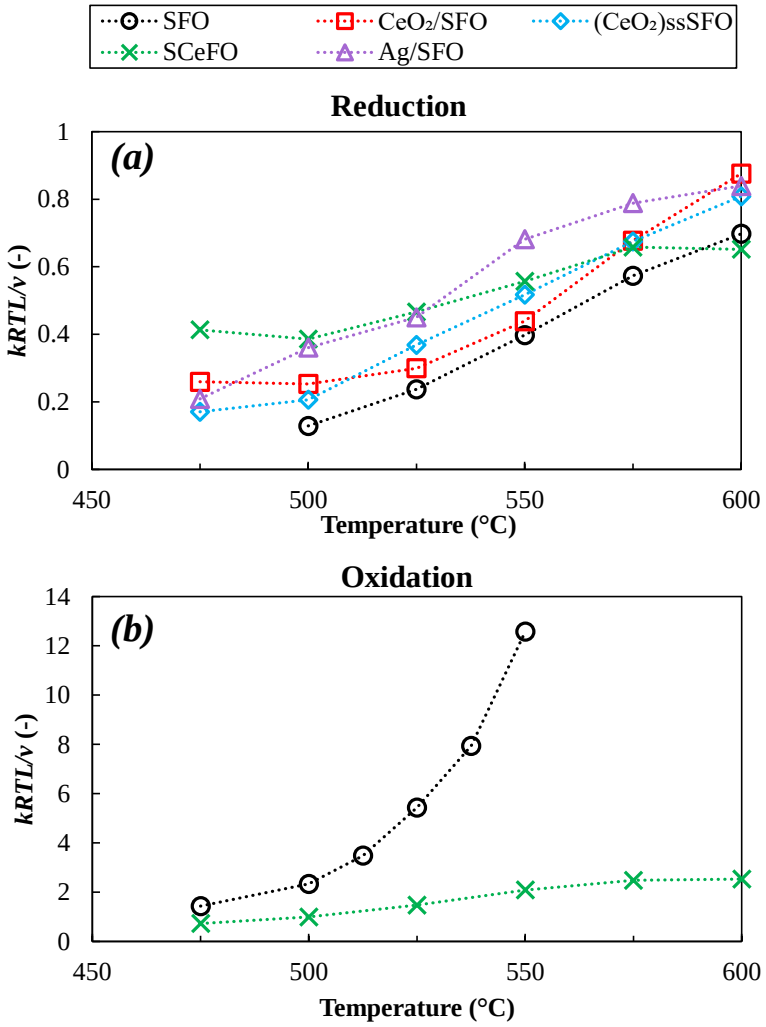


Fig. 3.19 Estimates of $\frac{kRTL}{v}$ for (a) reduction and (b) oxidation.

## 3.5 Discussion

### 3.5.1 Estimation of apparent kinetic parameters

#### Kinetics of oxygen uncoupling

The values of kinetic parameters reported in Table 3.4 were fitted using nonlinear regression to values of the rate constant $k$, estimated from maximum measured rates of reaction from experiments in the packed bed reactor (shown in Fig. 3.14) over the temperature range of 500-575°C for SFO and 475-575°C for modified samples (as shown in Fig. 3.20), with 95% confidence intervals for each parameter quoted.

Table 3.4 Extracted kinetic parameters from nonlinear regression of experimental measurements in the packed bed to Eq. 3.8. Values in parentheses indicate the estimated 95% confidence intervals for each fitted parameter.

| Sample | $E_a$ (kJ mol$^{-1}$) | $A$ (mol$_{O_2}$ s$^{-1}$ g$_{OC}^{-1}$) | $R^2$ (-) |
|---|---|---|---|
| SFO | 102.3 (97.9; 106.7) | 22,030 (8,103; 36,320) | 0.99 |
| $CeO_2$/SFO | 66.3 (63.1; 69.5) | 152 (81.0; 223) | 0.90 |
| $(CeO_2)_{ss}$SFO | 75.7 (73.9; 77.5) | 623 (459; 788) | 0.98 |
| SCeFO | 29.9 (26.7; 33.2) | 0.88 (0.46; 1.30) | 0.89 |
| Ag/SFO | 69.0 (66.0; 71.9) | 278 (158; 398) | 0.99 |

For SFO, SCeFO, and Ag/SFO, no significant difference at the 95% confidence level was found between the parameters estimated from nonlinear regression to Eq. 3.8, or linear regression to Eq. 3.9 (shown in Appendix B, Fig. B.4 and Table B.1). However, a difference between values of kinetic parameters estimated *via* linear and nonlinear regression, outside the 95% confidence intervals, was estimated for $CeO_2$/SFO, suggesting a significant contribution from the random error structure to the fitted parameters (Barrie, 2011a,b). Hence, the kinetic parameters for the sample of $CeO_2$/SFO should be treated with caution.

As shown in Fig. 3.20, the 95% prediction bands for SFO, $(CeO_2)_{ss}$SFO, and Ag/SFO did not overlap in the temperature range of 500-575°C. Hence, the values of $E_a$ and the values of $A$ for SFO, $(CeO_2)_{ss}$SFO, SCeFO, and Ag/SFO were significantly different at a 95% confidence level. Contrastingly, the differences in values of $E_a$ and $A$ between SFO and $CeO_2$/SFO, or between $CeO_2$/SFO and $(CeO_2)_{ss}$SFO, were found not to be statistically significant.

The sample structurally modified with Ce, SCeFO, showed markedly lower values of $E_a$ and $A$ than any other sample. However, since $E_a$ and $A$ are linked, the resulting

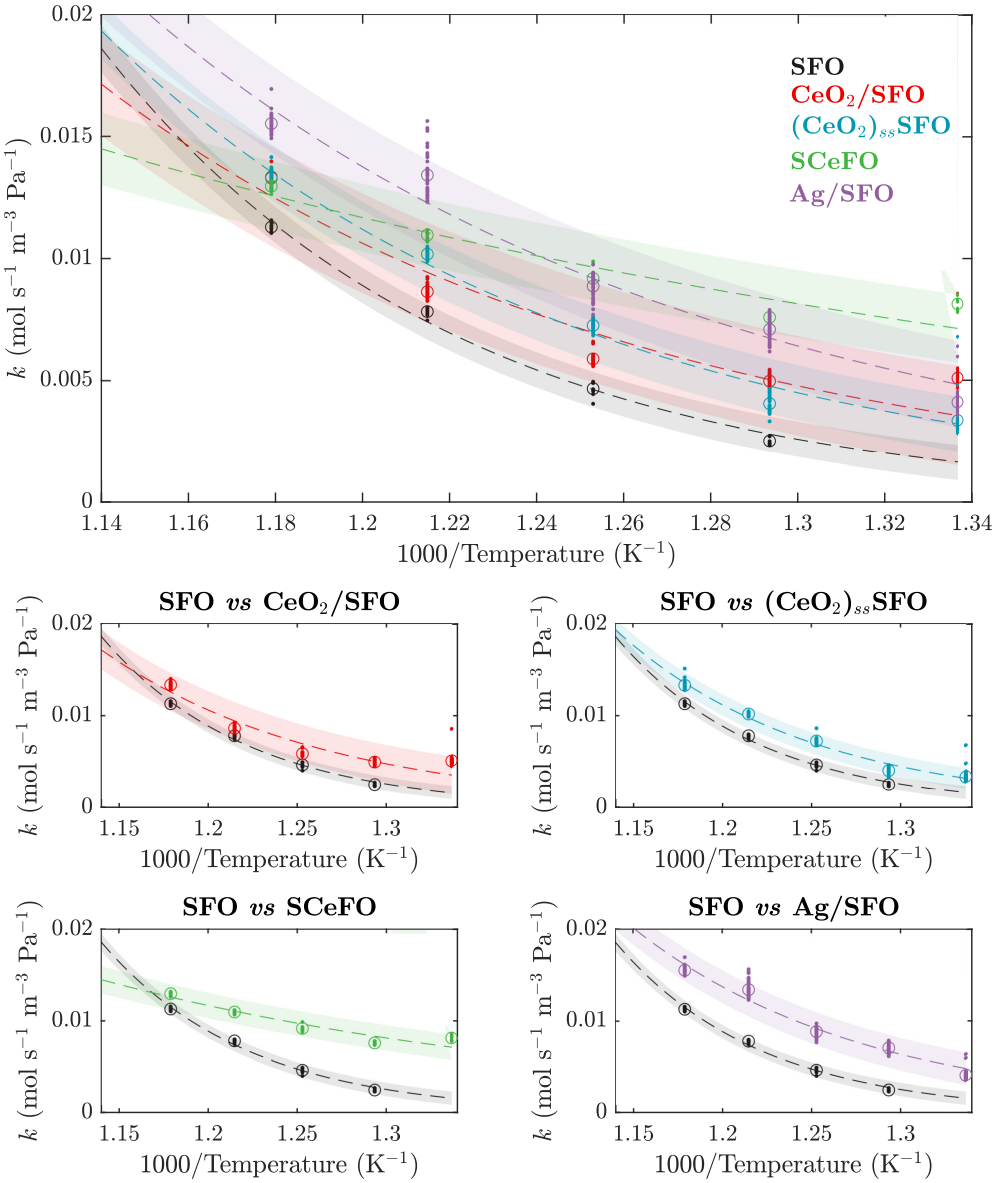


Fig. 3.20 Estimated rate constant, $k$, plotted against inverse temperature for SFO over the range of 500-575°C and for $CeO_2$/SFO, $(CeO_2)_{ss}$SFO, and Ag/SFO over the range of 475-575°C. Points indicate the experimental measurements from each cycle, circles indicate the average over cycles, dashed lines indicate the fitted exponential curves (Eq. 3.8), and shaded regions indicate the 95% prediction bands. Subplots show a pairwise comparison of each modified sample with SFO.

rates and rate constants are similar to those for other samples, demonstrating that here, in a model-free kinetic parametrisation, $E_a$ should not be interpreted without $A$ and, ideally, not without information regarding the full kinetic triplet of $E_a$, $A$, and $k$ (Vyazovkin, 2021). Hence, the assumption that all samples follow the same mechanism of oxygen release, allowing for comparable kinetic parameters, might not be valid for SCeFO. For example, given the low porosity of SCeFO observed from SEM images (shown in Fig. 3.7) as compared to that of SFO, oxygen uncoupling from SCeFO might become rate-limited by internal mass transfer rather than the reaction at the surface of the particles. However, the possible presence of micropores in the SCeFO material not visible under SEM, and, or, varying agglomerate size as a result of the milling and calcination procedure used in material preparation, might also contribute to the relatively low reactivity of the SCeFO sample.

The values estimated here for $E_a$ and $A$ for SFO are compared with other values reported in the literature for $SrFeO_{3-\delta}$ in Table 3.5, with literature values determined using different experimental methodologies (*e.g.*, electrical conductivity relaxation (Yoo *et al.*, 2005), TGA (Bulfin *et al.*, 2020) and packed bed experiments (Bychkov *et al.*, 2016)). In particular, the $E_a$ values reported here for SFO were somewhat lower than those reported previously in the literature (in the range of 128-144 kJ $mol^{-1}$).

Table 3.5 Comparison of estimated apparent kinetic parameters for reduction of SFO with literature values. Values in parentheses indicate estimated 95% confidence band for fitted parameters from this work; uncertainty in values from literature are reported where available.

| Experimental method | Temperature range (°C) | $E_a$ (kJ $mol^{-1}$) | $A$ ($mol_{O_2} s^{-1} m^{-3} Pa^{-1}$) | References |
|---|---|---|---|---|
| Packed bed reactor | 500-575 | 102.3 (97.9; 106.7) | 22030 (8103; 36320) | This work |
| Packed bed reactor | 500-600 | 128.9 ± 4.7 | 388000 | (Görke *et al.*, 2020) (Görke, 2018) |
| Thermogravimetric analysis | 177-477 | 144 ± 16 | 243000 | (Bulfin *et al.*, 2020) |
| Packed bed reactor | 500-900 | 135 | Not reported | (Bychkov *et al.*, 2016) |
| Electrical conductivity relaxation | 790-1000 | 128 ± 0.6 | Not reported | (Yoo *et al.*, 2005) |

All analyses of reaction rates in the packed bed reactor, including determination of kinetic parameters, assume that the reactor behaved isothermally; *i.e.*, at all times during reduction and oxidation, the entirety of the solid and gas in the packed bed was at the set-point of the temperature controller. However, during experiments with gas switching between air and $N_2$, some deviation was observed below the set-point

during reduction of the material (around 5°C) and above the set-point temperature during reoxidation (up to 15°C for oxidation in air) due to the slow response of the temperature controller as compared to the rapid rates of reactions of the solids. Hence, the decrease in temperature during the endothermic reduction step might result in somewhat underestimated rates of reactions at each temperature set-point, resulting in lower values of $E_a$ and $A$ than might be expected for an isothermal reactor (and *vice-versa* for reoxidation).

### Kinetics of oxygen uptake

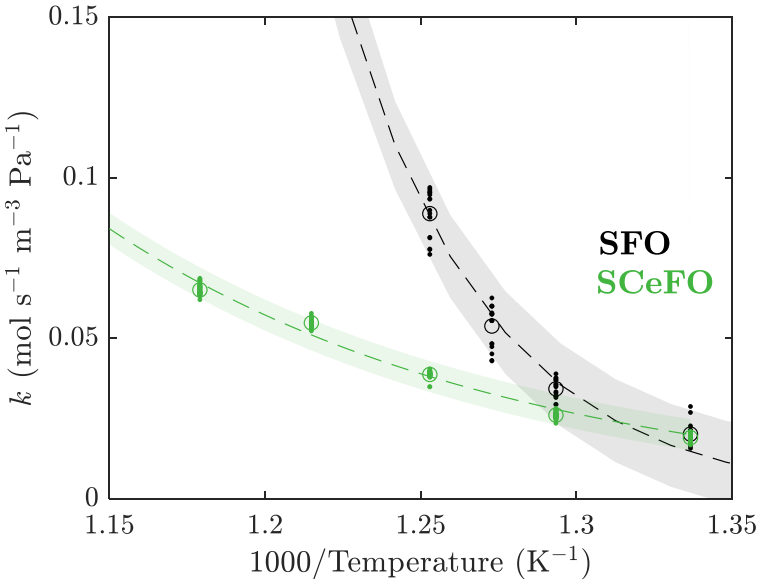


Fig. 3.21 Estimated rate constant, $k$, plotted against inverse temperature for oxidation of SFO in 5.05 vol% oxygen over the range of 475-525°C and SCeFO in air over the range of 475-575°C. Points indicate experimental measurements from each cycle, circles indicate average over cycles, dashed lines indicate fitted curves to Eq. 3.8 ($R^2 = 0.98$ for both SFO and SCeFO), and shaded regions indicate 95% confidence intervals.

Kinetic parameters for oxidation of SFO and SCeFO were extracted from measurements reported in Figs. 3.13 and 3.16, with fitted curves to Eq. 3.8 shown in Fig. 3.21. The extracted values of $E_a$ and $A$ for reoxidation of SFO were determined to be $E_a = 177.1$ kJ mol$^{-1}$ (with a 95% confidence interval of 163.3-191.0 kJ mol$^{-1}$) and $A = 3.40 \times 10^{10}$ mol$_{O_2}$ s$^{-1}$ g$_{OC}^{-1}$ (with a 95% confidence interval of -3.70 $\times$ $10^{10}$-10.5 $\times$ $10^{10}$ mol$_{O_2}$ s$^{-1}$ g$_{OC}^{-1}$). Interestingly, Yoo *et al.* (2005) reported little difference in activation energy between oxidation and reduction of $SrFeO_3$ from electrical conductivity relaxation measurements, at $E_a = 145 \pm 0.2$ kJ mol$^{-1}$, for small perturbations

about equilibrium at $pO_2 = 0.05$ atm. Additionally, the value of $E_a$ estimated here is substantially greater than the activation energy estimated for oxidation of SFO in pure $O_2$ by Bulfin *et al.* (2020), at $E_a = 92 \pm 16$ kJ mol$^{-1}$, determined from TGA measurements over the temperature range 177-477°C. Curiously, despite showing rapid kinetics of reduction, SCeFO showed a relatively slow observed rate of oxygen uptake in air (shown in Fig. 3.21) and hence a limited temperature increase during oxidation, allowing for extraction of kinetic parameters for reoxidation in air over the temperature range of 475–575°C, at $E_a = 64.0$ kJ mol$^{-1}$ (with a 95% confidence interval of 62.6-65.3 kJ mol$^{-1}$) and $A = 584$ mol$_{O_2}$ s$^{-1}$ g$_{OC}^{-1}$ (with a 95% confidence interval of 469-706 mol$_{O_2}$ s$^{-1}$ g$_{OC}^{-1}$).

### 3.5.2 Mechanistic considerations

Previous studies investigating modification of perovskite materials with Ag to enhance oxygen transport ascribed the enhanced rate of oxygen transport to a catalytic effect (Kovalev *et al.*, 2021; Leo *et al.*, 2009). Particles of silver deposited on the feed site of membranes used for air separation composed of perovskite materials have been found to catalyze the dissociation of molecular $O_2$ to lattice oxygen ions. The overall reaction is given in Eq. 3.23, with proposed reaction steps indicating the corresponding change in lattice Fe oxidation state as a result of oxygen incorporation given in Eqs. 3.24 and 3.25 (Merkle and Maier, 2006, 2008), where $V_O$ corresponds to an oxygen vacancy within the $SrFeO_{3-\delta}$ lattice.

$$\frac{1}{2}\,O_{2,(g)} + V_O \rightleftharpoons O_{lattice} \tag{3.23}$$

$$\frac{1}{2}\,O_{2,(g)} + Fe^{3+} \rightleftharpoons O^-_{ads} + Fe^{4+} \tag{3.24}$$

$$O^-_{ads} + Fe^{3+} + V_O \rightleftharpoons O_{lattice} + Fe^{4+} \tag{3.25}$$

The $O_{lattice}$ species formed are then able to diffuse through the perovskite material and recombine on the permeate side to form pure $O_2$. Hence, under conditions where the flow of oxygen from air through a membrane is limited by the rate of incorporation of oxygen into the material of the membrane (*i.e.* ionic membranes), the overall rate of oxygen transport is increased by the presence of silver. Furthermore, Wang *et al.* (2021) found that thin films of Ag deposited on the surface of $SrFeO_{3-\delta}$ altered the perovskite

crystal structure near the Ag-$SrFeO_3$ interface by forming a layer of weak Fe-O-Ag bonds, with net transfer of electrons from Ag to $SrFeO_3$. The modified structure of the Ag-$SrFeO_3$ interface decreased the energy barrier for $O^{2-}$ transport as compared to the unmodified $SrFeO_{3-\delta}$ perovskite, allowing for the phase transition from the perovskite to brownmillerite to occur at lower temperatures than would be expected thermodynamically for $SrFeO_3$. Furthermore, studies of Ag supported on $Ce_xZr_{1-x}O_{2-\delta}$ (Lee *et al.*, 2021; Wang *et al.*, 2023) found that strong interactions between the particles of Ag and the support aided the formation of oxygen vacancies in the $Ce_xZr_{1-x}O_{2-\delta}$ material.

Here, for partial reduction of $SrFeO_{3-\delta}$ (*i.e.* $\delta < 0.5$, with the material remaining in perovskite form throughout), the presence of Ag on the surface of $SrFeO_{3-\delta}$ affected both the rates of oxygen release and reuptake (as shown in Fig. 3.13) and the thermodynamic relationship between $pO_2$-$T$-$\delta$ at equilibrium (as shown in Fig. 3.11), with the presence of Ag increasing the concentration of oxygen vacancies at equilibrium under all investigated values of $pO_2$. Hence, under the experimental conditions investigated here, the role of silver is unlikely to be purely catalytic; rather, the influence of Ag translates to the observed enhancement in the rate of $SrFeO_{3-\delta}$ reduction employing both kinetic and thermodynamic effects. The interactions between Ag and $SrFeO_{3-\delta}$ during reduction and oxidation, including deep reduction to brownmillerite form, are discussed further in Chapter 4.

In a similar chemical looping system to the $SrFeO_{3-\delta}$ materials impregnated with Ag investigated here, Hwang *et al.* (2023) found that for reduction and oxidation of $Ce_{0.5}Zr_{0.5}O_{2-\delta}$ impregnated with Pt, the presence of Pt enhanced the rate of oxygen release but had no effect on the rate of oxygen uptake. Hence, the authors concluded that the rate of reduction of $Pt/Ce_{0.5}Zr_{0.5}O_{2-\delta}$ was limited by the surface reaction, (*i.e.* formation of $O_2$ molecules from $O^{2-}$ ions), whereas oxidation was limited by diffusion of $O^{2-}$ through the structure of $Ce_{0.5}Zr_{0.5}O_{2-\delta}$. Here, however, the presence of Ag on $SrFeO_{3-\delta}$ increased the rates of both oxygen release and uptake as compared to unmodified $SrFeO_{3-\delta}$ (shown in Fig. 3.20), indicating that, under the conditions investigated, both reduction and oxidation of Ag/SFO were affected by the surface reaction up to 575°C, with Ag possibly catalysing the removal of surface oxygen as $O_{2,gas}$, resulting in a faster rate of oxygen removal and reuptake, as discussed further in Chapter 4, Section 4.4.2.

At higher temperatures (600°C), the rate of reduction was limited by diffusion through the pores within the material (as discussed in Sections 3.3.2 and 3.4.3).

Additionally, as discussed in Section 4.4.2, during reduction of Ag/SFO some oxygen might be removed from the surface of silver by diffusion of atomic oxygen through the Ag nanoparticles (Chan *et al.*, 2018b). Therefore, under CLAS conditions, the diffusivity of oxygen in Ag relative to $SrFeO_{3-\delta}$ might also have partially limited observed rate of surface reaction.

A moderate increase in the rate of oxygen release from $SrFeO_{3-\delta}$ was observed for $CeO_2$/SFO and $(CeO_2)_{ss}$SFO. Materials modified with $CeO_2$ also showed decreased $T_{onset}$ values as compared to SFO. Machida *et al.* (2015, 2017) proposed that for composite oxygen carrier materials with $CeO_2$ on the surface, $CeO_2$ is able to act catalytically in a similar manner to Ag, that is, by facilitating formation of $O_2$ molecules from lattice oxygen atoms during reduction, and *vice versa* during oxidation. Moreover, Tian *et al.* (2022a) found from density functional theory calculations that $CeO_2$ deposited on $SrFeO_3$ decreased the energy barrier for formation of oxygen vacancies during reduction. Marek *et al.* (2020) also hypothesised that, for $(CeO_2)_{ss}$SFO, the presence of $CeO_2$ helps accelerate the ionic diffusivity of oxygen through the composite material by acting as a 'shortcut' through bulk $SrFeO_{3-\delta}$. However, from *in-situ* measurements reported in Chapter 4, Section 4.3.1, oxygen diffusion through $SrFeO_{3-\delta}$ under CLAS conditions was relatively rapid, limiting the influence of any possible shortcut available through $CeO_2$. Overall, given that here, only a small difference was observed between $T_{onset}$ values and kinetic parameters of reduction for $CeO_2$/SFO and $(CeO_2)_{ss}$SFO, it is not possible to determine conclusively which of the proposed mechanisms (surface catalysis, expected to be more significant for $CeO_2$/SFO, or aiding diffusion of oxygen, expected to be more significant for $(CeO_2)_{ss}$SFO) for enhancement of oxygen release had the greatest influence for materials containing $CeO_2$.

Contrastingly, for SCeFO, a substantial increase in $T_{onset}$ was observed as compared to SFO, but with a faster rate of oxygen release under redox conditions in packed bed experiments. Furthermore, the activation energies and pre-exponential factors estimated for reduction and oxidation of SCeFO were markedly lower than those of SFO. Hence, the rate-limiting step for reduction and oxidation of SCeFO might differ from that of SFO (*e.g.* as a result of the low porosity of SCeFO, leading to internal mass transfer effects dominating). Additionally, the 5 at% Ce doping level in the prepared SCeFO might be near the critical value, reported by Nikitin *et al.* (2021) to be in the range of around 5-15 at% Ce, above which the lattice distortion introduced by the large $Ce^{4+}$ ion to the perovskite crystal partially counterbalances the improvement

to oxygen transport induced by partial reduction of $Ce^{4+}$ to $Ce^{3+}$ (and *vice versa* for reoxidation), resulting in high $T_{onset}$ values.

The rates of oxygen release from OC materials modified with Ag and Ce at 500°C compare favorably with reported values for candidate materials for CLAS, with $CeO_2$/SFO, $(CeO_2)_{ss}$SFO, SCeFO, and Ag/SFO releasing 95.3, 106.1, 135.9, and 138.9 $\mu mol_{O_2}$ $g_{OC}^{-1}$ $min^{-1}$ respectively in packed bed experiments, as shown in Fig. 3.14. The rate of oxygen release surpasses $Sr_{0.8}Ca_{0.2}FeO_{3-\delta}$ (70.3 $\mu mol_{O_2}$ $g_{OC}^{-1}$ $min^{-1}$), as reported by Dou *et al.* (2020) and Krzystowczyk *et al.* (2021), however, none of the materials investigated here released oxygen as rapidly at 500°C as their co-doped $Sr_{0.8}Ca_{0.2}Fe_{0.4}Co_{0.6}O_{3-\delta}$ (173.1 $\mu mol_{O_2}$ $g_{OC}^{-1}$ $min^{-1}$).

## 3.6 Conclusions

The results presented in this Chapter demonstrated that materials composed of $SrFeO_{3-\delta}$ modified with Ag or $CeO_2$, as surface or bulk dopants, release oxygen faster than the unmodified perovskite. Impregnation of $SrFeO_{3-\delta}$ with 15 wt% Ag decreased the starting temperature of oxygen uncoupling from 370°C to 310°C, and considerably accelerated the rate of oxygen release. As well as inducing faster kinetics of oxygen uncoupling, the presence of Ag affected the thermodynamic equilibrium, leading to higher values of $\delta_{eq}$ in $SrFeO_{3-\delta}$ (*i.e.* a higher concentration of oxygen vacancies at equilibrium). Surface and bulk modification with $CeO_2$ also decreased $T_{onset}$, but only by around 10–20°C, slightly increasing the rate of oxygen release. Strontium ferrite which was structurally doped with Ce to form $Sr_{0.95}Ce_{0.05}FeO_{3-\delta}$, showed a higher $T_{onset}$, at around 411°C, and a slower rate of oxidation in air but a faster rate of reduction in $N_2$ than unmodified $SrFeO_{3-\delta}$.

Kinetic parameters were estimated for reduction of $SrFeO_3$-based OC materials modified with Ag, Ce, and $CeO_2$, and for oxidation of $SrFeO_{3-\delta}$ and $Sr_{0.95}Ce_{0.05}FeO_{3-\delta}$. The marked improvement in the release of oxygen at low temperatures from described modifications of $SrFeO_{3-\delta}$ considerably expands the design space of candidate materials to act as oxygen carriers at relatively mild temperatures ($\leq$500°C), facilitating development of novel chemical looping processes for selective oxidation, as discussed in Chapters 5 and 6.

# Chapter 4

# *In-situ* measurement of oxygen transport mechanisms in $Ag/SrFeO_{3-\delta}$

This Chapter investigates the bulk and surface behaviour of $Ag/SrFeO_{3-\delta}$ during chemical looping in $H_2$ and $O_2$ using *in-situ* characterisation.

## 4.1 Introduction

As demonstrated in Chapter 3, the addition of Ag nanoparticles to $SrFeO_{3-\delta}$ aided the removal of oxygen from the oxide lattice, and increased the rates of oxygen uncoupling and reuptake under relatively mild reducing conditions.

Silver-strontium ferrite composites have been investigated for catalytic selective oxidation processes (Gabra *et al.*, 2021; Gebers *et al.*, 2023), whereby oxygen is supplied from the lattice oxygen of the metal oxide support to the active site of Ag. However, the mechanism by which oxygen reaches the active site, and the oxygen species present under reducing and oxidising conditions, remain unknown. Furthermore, under strong reducing conditions, such as $H_2$ or CO at $\geq$500°C, $SrFeO_{3-\delta}$ undergoes a reversible phase change to brownmillerite $SrFeO_{2.5}$ (Marek *et al.*, 2018a). Phase transition from perovskite to brownmillerite, and further reduction to *e.g.* SrO and Fe allows for chemical looping processes at very low oxygen potentials, such as conversion of $CO_2$ to CO (Marek *et al.*, 2018a) or hydrogen production *via* thermo-chemical splitting of $H_2O$ (Chang *et al.*, 2023). From thin-film studies, Wang *et al.* (2021) found that the presence of Ag on $SrFeO_{3-\delta}$ aided phase transition to $SrFeO_{2.5}$ at *c.* 200°C lower temperature

than for $SrFeO_{3-\delta}$ alone, however, it is unknown whether the same behaviour applies for bulk samples.

Bulk and surface properties of candidate oxygen carriers for chemical looping processes have been studied using *in-situ* electron microscopy, X-ray diffraction, and spectroscopic techniques, recently reviewed by Song *et al.* (2023, 2024b). In this Chapter, the bulk and surface properties of $SrFeO_{3-\delta}$ impregnated with nanoparticles of Ag were investigated during reduction and oxidation, in order to elucidate the mechanisms of oxygen release and re-uptake at realistic reactor temperatures. The influence of Ag on the phase stability of $SrFeO_{3-\delta}$ was investigated using *in-situ* XRD under reducing and oxidising atmospheres, and the spatial variation in oxygen content under reduction assessed with TEM. Then, X-ray photoelectron spectroscopy (XPS), Raman spectroscopy, and temperature programmed reduction in $H_2$ were applied to probe the species present at the surface of $SrFeO_{3-\delta}$ and $Ag/SrFeO_{3-\delta}$ during reduction and oxidation in $H_2$ and air respectively. During reduction at a given temperature and gas environment, the distribution of oxygen species at the surface of the materials under investigation was expected to reach a pseudo-steady state, as surface oxygen species react with hydrogen, and are replenished by oxygen from the $SrFeO_{3-\delta}$ lattice (Merkle and Maier, 2008). Applying a temperature ramp under reducing conditions, the changes in relative abundance of different surface species detected by *in-situ* spectroscopy gave an indication of the mechanisms of oxygen transport between the $SrFeO_{3-\delta}$ support and the surface of Ag.

## 4.2 Experimental

For *in-situ* characterisation experiments, a batch of Ag/SFO was prepared by incipient wetness impregnation, as described in Section 2.1.2. A silver precursor solution was prepared, with volume equal to the approximate pore volume of the mass of $SrFeO_{3-\delta}$ used, and concentration of $AgNO_3$ set so as to achieve a nominal final loading of 10 wt% Ag. For *in-situ* electron microscopy experiments, the batch of Ag/SFO used for experiments described in Chapter 3 was used, with a higher nominal loading of 15 wt% Ag, to facilitate finding suitable particles of Ag on the sample.

### *In-situ* X-ray diffraction

For *in-situ* X-ray diffraction (XRD) experiments, a small sample (*c.* 10 mg) of SFO or Ag/SFO (180-355 $\mu$m) was loaded into an Anton Paar XRK-900 heated stage. To aid

dispersion of the powder sample, a drop of propan-2-ol was added to the sample, and allowed to evaporate before mounting the stage in the X-ray diffractometer. Further information describing the experimental arrangement is given in Section 2.2.1.

Experiments were performed by flowing 5 vol% $H_2$ in $N_2$ through the sample stage, while increasing the set-point temperature by 100°C over the range 200-800°C, then, switching the gas flow to compressed air, and decreasing the temperature from 800°C to 200°C in 100°C increments. Two scans over the angular range $2\theta$ = 20-70° were collected at each temperature step. An equivalent temperature program was also performed, but flowing compressed air through the sample stage for both the heating and cooling steps.

### *In-situ* transmission electron microscopy

*In-situ* transmission electron microscopy (TEM) experiments were performed on SFO and Ag/SFO, with sample preparation described in Section 2.2.5. Crushed samples of each material were mounted onto a heating chip, and inserted into the TEM instrument. For both samples, TEM images, SAED patterns, EELS and EDS scans were collected at room temperature, then, the sample was heated in a series of temperature steps (200, 400, and 600°C for SFO; 200, 300, 400, 500, 600 and 700°C for Ag/SFO). A further set of scans was collected for Ag/SFO after cooling to room temperature. For Ag/SFO, the TEM sample stage was tilted to align the electron beam with the [110] zone axis of a $SrFeO_{3-\delta}$ crystal, allowing the perovskite $SrFeO_3$ and brownmillerite $SrFeO_{2.5}$ phases to be readily distinguishable from their electron diffraction patterns (Batuk *et al.*, 2023). At each temperature, the sample was allowed to settle for 5-10 min, then, EELS and EDS scans were collected in parallel, with a total scan time of approximately 10 min, and subsequently bright-field, dark-field, and electron diffraction images were collected, with the sample held at each temperature for approximately 45 min. The time taken to heat or cool the sample was under 10 s for all temperature steps.

### Near-ambient pressure X-ray photoelectron spectroscopy

Samples of SFO and Ag/SFO were prepared for NAP-XPS measurements by compressing the powder samples into a pellet, then calcining at 650°C to remove surface impurities, as described in Section 2.2.7. The NAP-XPS experiments were conducted over multiple days, with the samples held in an inert (Ar) or vacuum environment at room temperature in between experiments. During NAP-XPS experiments, the

current through the sample stage was increased from 0 to 7.5 A, achieving sample temperatures of approximately 27, 58, 118, 180, 295, 357, and 439°C, then sequentially cooled, with scans collected at each temperature. During heating, the gas environment was set to 0.25 mbar $H_2$, and during cooling, to 1 mbar $O_2$, with total pressure kept constant at 5 mbar, to avoid shifts in binding energy induced by changing pressure (Jain *et al.*, 2019). For both samples, survey scans of the full instrument energy range, and high-resolution scans of the C1s, Sr3p, O1s, Fe3p, Sr3d, N1s, and Ag3d binding energy regions were collected, with a total scan time of approximately 45 min. For the sample of Ag/SFO, as sulphur impurities were detectable from the survey scan, scans of the S2p region were also collected. Furthermore, for Ag/SFO, immediately after the gas switch from $H_2$ to $O_2$, successive rapid scans of the O1s region (of duration 20 s) were collected for 20 min.

### *In-situ* Raman spectroscopy

For *in-situ* Raman spectroscopy, a pelletised sample of Ag/SFO, cleaned at 650°C in air to remove any surface impurities, was prepared and mounted into the heated sample stage, as described in Section 2.2.8. Reference spectra were collected at room temperature in air, then, the gas flowing through the sample stage was set to 5 vol% $H_2$ in $N_2$. The stage temperature was increased from 200-350°C in 50°C increments, with three scans collected at each temperature at a scan time of 2.5 min. Reference spectra at room temperature were also collected for a pellet of unmodified SFO, a sample of Ag supported on $Al_2O_3$ prepared by incipient wetness impregnation as for Ag/SFO, a sample of $Ag_2O$ supported on $Al_2O_3$ prepared by Mr Joseph Gebers (with details of synthesis given in Gebers *et al.* (2022)), and a sample of as-received $Ag_2CO_3$ (Sigma Aldrich, 99%).

### Temperature programmed reduction ($H_2$-TPR)

To confirm the observations from *in-situ* spectroscopy, temperature programmed reduction in hydrogen ($H_2$-TPR) was performed on SFO and Ag/SFO using the rig described in Section 2.2.3. Samples (*c.* 30-50 mg) of SFO and Ag/SFO were cleaned in air at 650°C for 2 h prior to measurements, then, the samples were ramped from 50-700°C under flow of 5 vol% $H_2$ (balance $N_2$) at a rate of 5°C $min^{-1}$. Hydrogen consumption was measured using an on-line thermal conductivity detector (TCD), calibrated towards $N_2$ and 5 vol% $H_2$.

# 4.3 Results

## 4.3.1 Bulk characterisation

### *In-situ* X-ray diffraction

X-ray diffraction patterns for SFO and Ag/SFO heated under 5 vol% $H_2$ in $N_2$ from 200-800°C, then cooled in air back to 200°C, are presented in Fig. 4.1. For SFO, upon heating in 5 vol% $H_2$, a phase change from perovskite $SrFeO_{3-\delta}$ to brownmillerite $SrFeO_{2.5}$ was observed at 500°C (Savinskaya *et al.*, 2008; Starkov *et al.*, 2014). No further phase changes, or decomposition of the $SrFeO_{2.5}$ phase, were observed upon heating to 800°C, in line with the findings of Marek *et al.* (2018a). Upon switching the gas atmosphere from 5% $H_2$ in $N_2$ to air, the SFO rapidly (<20 min) reoxidised to cubic perovskite structure.

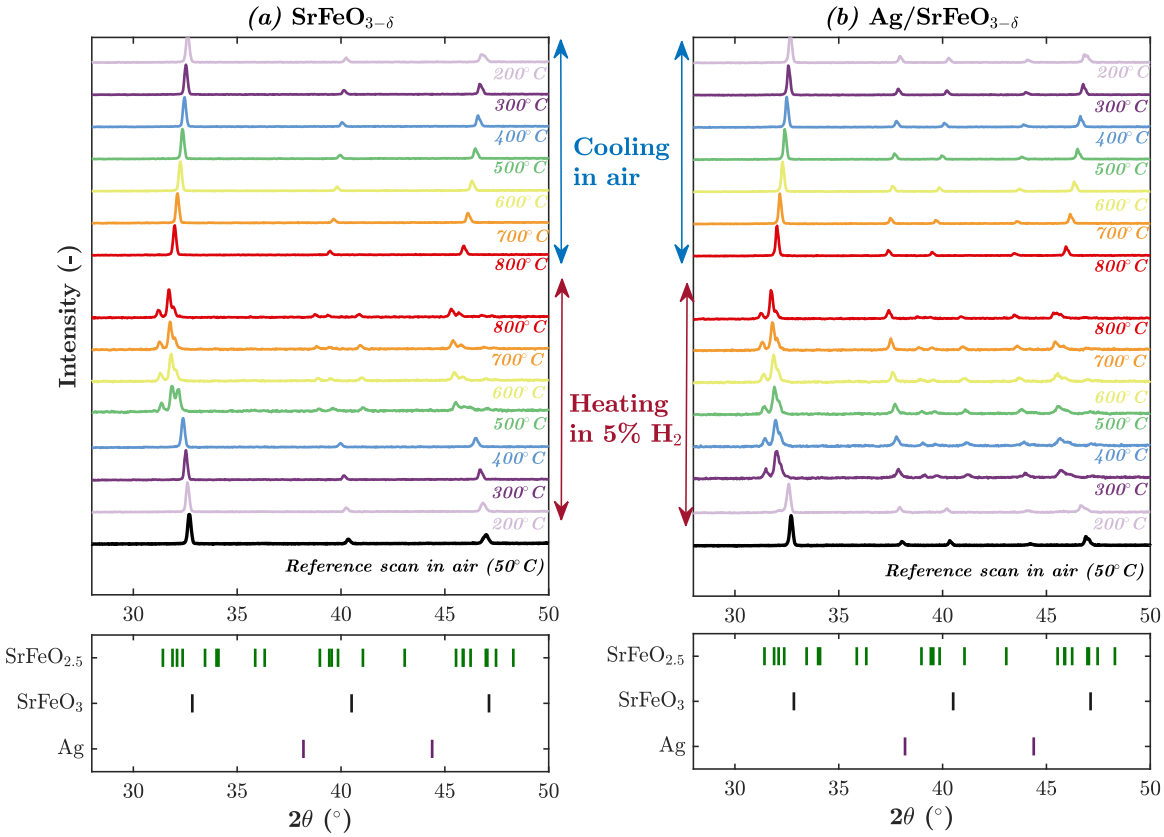


Fig. 4.1 *In-situ* XRD patterns showing reduction in 5 vol% $H_2$ and oxidation in air of $SrFeO_{3-\delta}$ and $Ag/SrFeO_{3-\delta}$. Tick marks indicate peak positions for identified phases.

For the sample of Ag/SFO, reduction of the perovskite $SrFeO_{3-\delta}$ phase to brownmillerite $SrFeO_{2.5}$ was also observed. However, the phase transition from $SrFeO_{3-\delta}$

to $SrFeO_{2.5}$ occurred at substantially lower temperature, with partial reduction at 200°C (indicated by formation of a peak shoulder at $2\theta = 32°$), and full reduction to $SrFeO_{2.5}$ at 300°C. The decrease in temperature required for phase transformation from perovskite to brownmillerite was in broad agreement with the findings from TGA measurements reported in Chapter 3, Fig. 3.8, where, under reduction with 5 vol% $H_2$ in $N_2$ as the reactive gas, $SrFeO_{2.5}$ formed at 585°C for SFO, and the sample of Ag/SFO formed $SrFeO_{2.52}$ at 354°C, before fully reducing to $SrFeO_{2.5}$ at 512°C. The lower temperatures of brownmillerite formation during XRD scans as compared to under TGA are explained by the sample being exposed to 5 vol% $H_2$ gas directly in the *in-situ* XRD stage, whereas, in the TGA, mixing between the reactive gas and inert purge and protective streams resulted in a lower hydrogen concentration in contact with the sample material (estimated at around 1.67-3.33 vol% $H_2$). Similarly to SFO, no further phase changes were observed during *in-situ* XRD measurements under $H_2$. The impregnated Ag remained as metallic silver throughout the experiment. When the gas was switched to air, as with SFO, the sample rapidly (<20 min) oxidised to re-form the perovskite phase, and after cooling to 200°C, the XRD measurements overlapped with the results collected for fresh samples, with peak positions within 0.1°.

*In-situ* XRD measurements of SFO and Ag/SFO heated in air from 200-800°C in 100°C increments, then, cooled in air back to 200°C are shown in Appendix C, Fig. C.1. For both samples, peaks corresponding to the perovskite $SrFeO_3$ phase shifted to lower $2\theta$ values, corresponding to expansion of the crystal lattice, in good agreement with previous reported measurements (Marek *et al.*, 2018a; Taylor *et al.*, 2016). In air, no phase changes occurred, and little difference in lattice parameter was observed between SFO and Ag/SFO with changing temperature, suggesting that differences in the concentration of oxygen vacancies between the samples were below the sensitivity of the XRD instrument used here.

### *In-situ* transmission electron microscopy

Samples of SFO and Ag/SFO were prepared and analysed by *in-situ* TEM as described in Sections 2.2.5 and 4.2. The thickness of each sample was estimated from EELS measurements, shown in Fig. 4.2. The region of SFO analysed comprised a thin section of material, with maximum thickness *c.* 200 nm at the centre and minimum thickness *c.* 30 nm at the edge, connected to a thicker section of bulk oxide. The particle of Ag/SFO had an approximately wedge-shaped profile perpendicular to the plane of the

incident electron beam, decreasing in thickness from *c.* 300 nm at the base to *c.* 30 nm at the tip.

For thick points on the sample, plural electronic scattering and signal attenuation resulted in diminished intensity of the Fe-$L_3$ and Fe-$L_2$ energy loss peaks; 250 nm thickness was selected as an arbitrary cutoff above which Fe-L peaks were not readily distinguishable from background noise, and hence points on the sample with thickness >250 nm were excluded from subsequent analysis. Thicker sections of the sample comprise a greater mass of material *per* point scanned, and hence might react more slowly when heated in the TEM. Therefore, the exclusion of thicker points might result in a slight overestimate of the changes in material properties with respect to the samples as a whole.

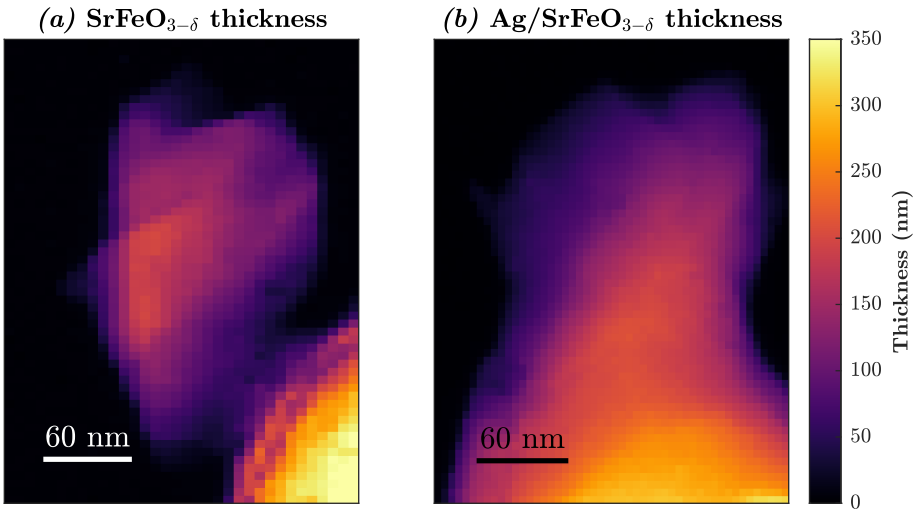


Fig. 4.2 Estimation of sample thickness from EELS measurements of particles of **(a)** $SrFeO_{3-\delta}$ and **(b)** $Ag/SrFeO_{3-\delta}$.

The average oxidation state of Fe at each point on the samples was estimated from EELS measurements of the Fe-$L_3$ and Fe-$L_2$ energy-loss peaks, corresponding to the local $Fe^{3+}/Fe^{4+}$ ratio, as described in Section 2.2.5. Hence, the local oxygen non-stoichiometry of $SrFeO_{3-\delta}$ was estimated, shown in Figs. 4.3. Given that EELS measurements correspond to the loss of energy of electrons passing through the sample into the plane of the image, the estimated stoichiometry at each point corresponds to the average oxygen content through the sample along the direction of the electron beam.

From EELS measurements of unmodified SFO at room temperature, the average stoichiometry over the sample shown in Fig. 4.4 was estimated to be approximately

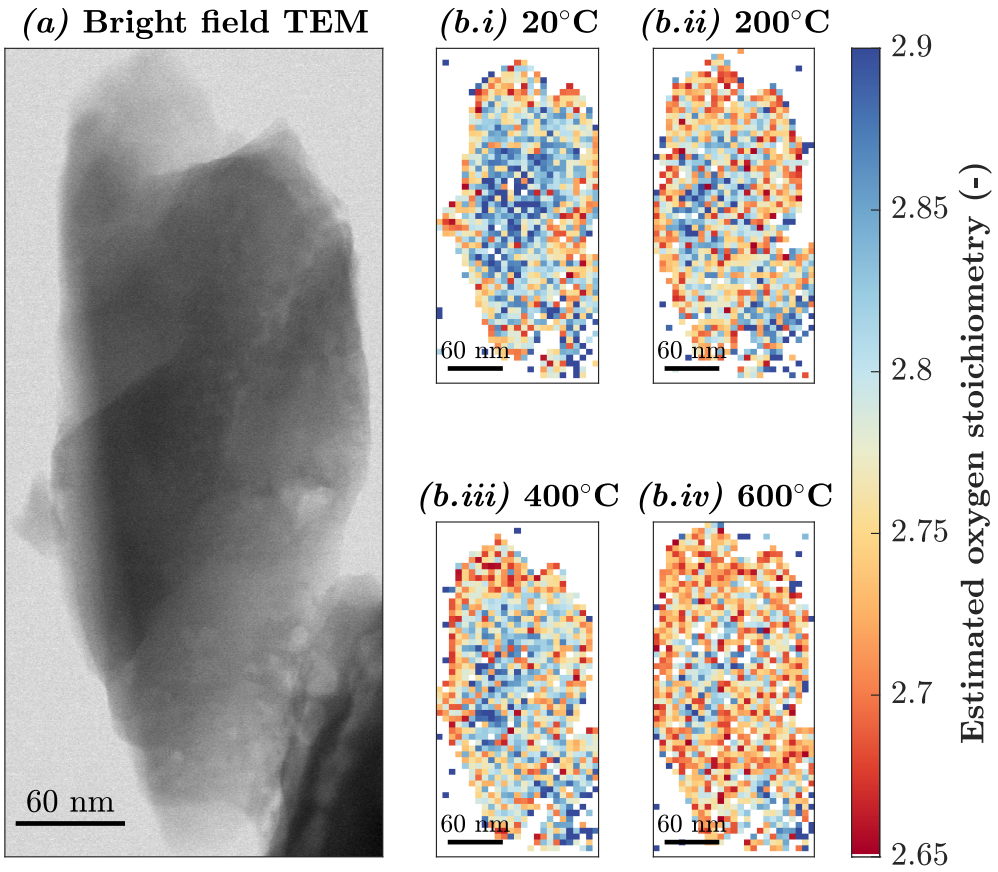


Fig. 4.3 *In-situ* TEM images with **(a)** bright-field image of $SrFeO_{3-\delta}$, **(b)** EELS maps showing changes in local oxidation state with increasing temperature, with regions of thickness >250 nm excluded.

$SrFeO_{2.83}$, in line with the initial stoichiometry of $SrFeO_{2.82}$ estimated from TGA measurements in Chapter 3, Figure 3.8. Given that each point in Fig. 4.3 corresponds to the average estimated stoichiometry through the thickness of the sample into the plane of the sample, the average of all points corresponds to the overall average for the whole three-dimensional sample.

Rate of oxygen release from SFO under vacuum at room temperature was assumed to be minimal, and hence the scans at room temperature were assumed to correspond to oxygen distribution in as-prepared SFO. The distribution of oxygen within the sample was found to show some spatial variation, with a lower oxygen stoichiometry around the edge of the sample, and higher oxygen stoichiometry in the centre. Upon heating under vacuum, the reduced region expanded inward uniformly through the sample, with a consequent decrease in average oxygen stoichiometry, with the reduced front nearing the centre of the particle at 600°C.

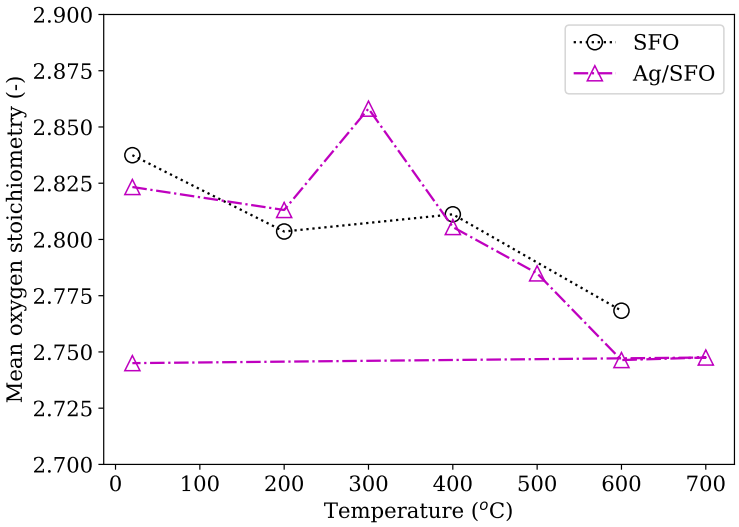


Fig. 4.4 Average oxygen stoichiometry of $SrFeO_{3-\delta}$ for samples of SFO and Ag/SFO, estimated from EELS measurements under vacuum ($pO_2$ = *c.* $10^{-7}$ $bar_{O_2}$).

The average oxygen non-stoichiometry at 600°C was estimated to be *c.* $SrFeO_{2.77}$. The estimated oxygen content was somewhat higher than in the isothermal TGA measurements reported in Chapter 3, Fig. 3.10, where SFO was reduced in an inert atmosphere ($N_2$, nominal $pO_2 = 10^{-5}$ $bar_{O_2}$, as compared to *c.* $10^{-7}$ $bar_{O_2}$ in the TEM chamber) at 600°C, giving a final composition of *c.* $SrFeO_{2.65}$.

For Ag/SFO, a similar spatial distribution of oxygen at room temperature was observed (shown in Fig. 4.5), with the material showing high oxygen content near

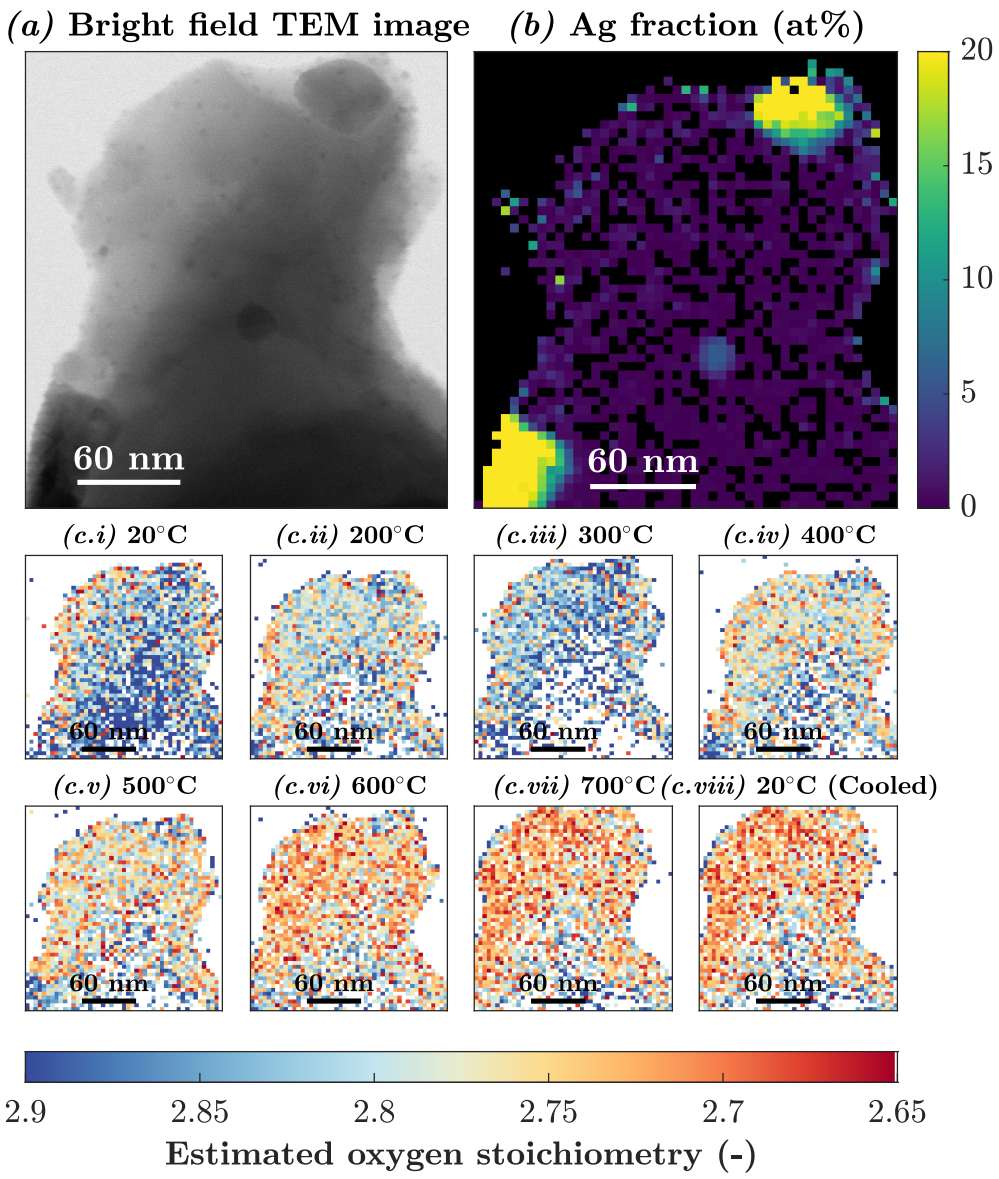


Fig. 4.5 *In-situ* TEM images with **(a)** bright-field image of $Ag/SrFeO_{3-\delta}$, **(b)** EDS map indicating particles of Ag, **(c)** EELS maps showing changes in local oxidation state with increasing temperature, with regions of thickness >250 nm excluded.

the centre of the particle, with partial reduction near the edges. The initial non-stoichiometry was estimated to be (3 - $\delta$) = 2.82, in close agreement with the TGA measurements reported in Chapter 3. From bright-field imaging and EDS measurements, two larger Ag particles (*c.* 40 nm diameter) were detected at the edge of the sample (shown in Fig. 4.5a and b), and a smaller Ag particle (*c.* 20 nm diameter) was found near the centre of the sample. Near the edge of the sample, a cluster of small (<10 nm, approximately equal to the spatial resolution of the EDS detector under the instrument settings used) nanoparticles were detected, visible in the top left-hand corner of Fig. 4.5a, possibly corresponding to smaller Ag nanoparticles, in line with the smallest particles detected from SEM images of the same sample, shown in Fig. 3.4. Alternatively, the small surface nanoparticles might correspond to exsolution of the B-site element from the perovskite lattice (here, Fe) to form metallic nanoparticles (Götsch *et al.*, 2017; Thalinger *et al.*, 2015), of sufficiently small size and low weight fraction to not be detected from XRD measurements. The presence of exsolved metallic iron would be in line with the observation from NAP-XPS measurements that a thin layer of SrO formed at the surface of SFO, hence maintaining a constant overall stoichiometric ratio between Sr and Fe. Furthermore, from Figs. 4.5a and 4.5b, the larger particles of Ag showed a large contact area with the SFO support, possibly suggesting partial embedding of the metallic particles within the SFO, hence straining the perovskite lattice. However, to confirm whether nanoparticles of Ag were partially embedded under the surface of SFO, repeated TEM measurements would be necessary, in order to view the sample from a wider range of angles and, or, by collecting images of cross-sectioned samples of Ag/SFO.

Upon heating Ag/SFO in the TEM, the reduced region expanded inwards from the edge of the particle, in a similar manner to SFO. Average oxygen stoichiometry declined with heating as expected, with Ag/SFO showing average oxygen content equal to or lower than SFO at temperatures ≥400°C. The reduced fronts expanded approximately uniformly through the sample, with only the thickest region at the centre of the particle remaining at higher oxygen content at 700°C. Reduced regions of Ag/SFO were not localised around particles of Ag, suggesting if oxygen was removed at Ag sites (as discussed further in Section 4.3.2), the transport of $O^{2-}$ ions within the $SrFeO_3$ lattice was relatively rapid (with respect to the *c.* 10 min timescale of measurements), as any local depletion of oxygen near particles of Ag was replenished from the bulk $SrFeO_{3-\delta}$.

The final average oxygen stoichiometry at 600°C (with little change observed upon further heating to 700°C) was estimated at (3 - $\delta$) = 2.75, somewhat less reduced than

expected from TGA measurements reported in Chapter 3, where Ag/SFO stabilised at *c.* (3 - $\delta$) = 2.6 after 45 min reduction in $N_2$ at 600°C. Hence, either reduction of the samples was inhibited by the experimental arrangement in the TEM relative to reduction in the TGA, or, the method of using EELS to estimate changes in oxygen non-stoichiometry tended to underestimate changes in local oxidation state during reduction. Upon cooling from 700°C back to room temperature, little change in oxygen distribution was observed and average non-stoichiometry remained constant, confirming that any residual oxygen gas present in the TEM sample chamber was not sufficient to re-oxidise the Ag/SFO.

Selected area electron diffraction (SAED) images of Ag/SFO collected at a point near the edge of the sample were compared with simulated patterns for perovskite $SrFeO_3$ ($Pm\bar{3}m$ symmetry, Hodges *et al.* (2000)) and brownmillerite $SrFeO_{2.5}$ (Ibm2 symmetry, Schmidt and Campbell (2001)), shown in Fig. 4.6. At room temperature, the sample holder was rotated to align the $SrFeO_{3-\delta}$ zone axis along the [110] direction, with the unit cell highlighted in the simulated and measured patterns.

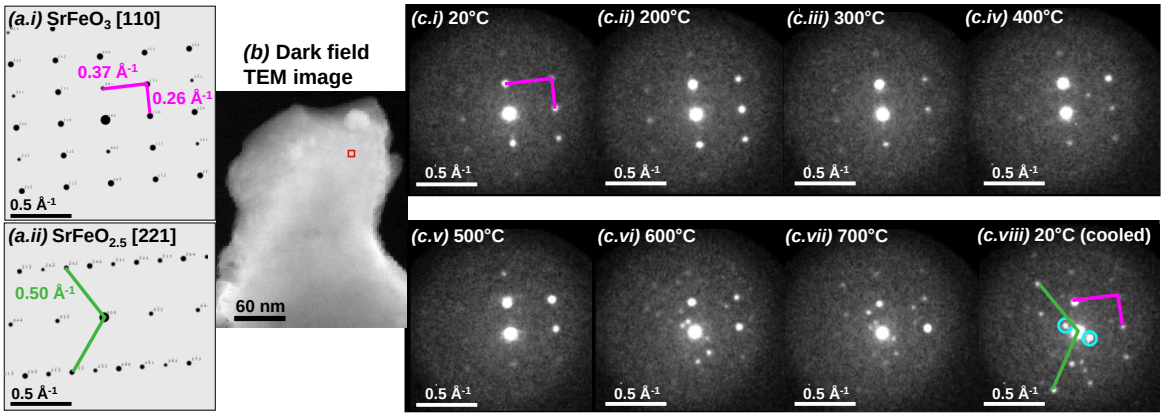


Fig. 4.6 **(a)** Simulated electron diffraction patterns along the [110] zone axis for perovskite $SrFeO_3$ with $Pm\bar{3}m$ symmetry, and along the [211] zone axis for brownmillerite $SrFeO_{2.5}$ with Ibm2 symmetry, **(b)** Dark field TEM image of Ag/SFO with red square corresponding to location of SAED images, **(c.i-viii)** SAED patterns of Ag/SFO collected at each temperature, with construction lines drawn to guide the eye (pink corresponding to the perovskite phase, green corresponding to the brownmillerite phase, and blue circles indicating reflections induced by $(FeO_4)_\infty$ chain ordering).

No major changes in the diffraction pattern were observed upon heating up to 500°C, indicating formation of oxygen vacancies in the perovskite structure without an overall phase change. However, at 600°C, additional reflections emerged, and became more intense with successive scans (shown in Figs. 4.6c.vi-viii), corresponding to formation of

a brownmillerite phase aligned along the [221] zone axis, as expected for topotactic phase transition of perovskite to brownmillerite structure (Batuk *et al.*, 2023). Additional reflections also emerged in the vicinity of the central spot (circled in Fig. 4.6c.viii), corresponding to interlayer ordering of $(FeO_4)_\infty$ chains in the brownmillerite structure (Batuk *et al.*, 2023; D'Hondt *et al.*, 2008). After cooling to room temperature under vacuum, reflections were visible corresponding to both brownmillerite and perovskite structures, suggesting incomplete conversion of $SrFeO_{3-\delta}$ to $SrFeO_{2.5+\delta}$, and substantial heterogeneity through the depth of the sample. Hence, the SAED patterns were in agreement with the EELS measurements reported in Fig 4.5, where the oxygen stoichiometry at each point on the sample exceeded (3 - $\delta$) = 2.5 even at 700°C, suggesting a mix of perovskite and brownmillerite phases and confirming partial reduction of the perovskite under vacuum at 700°C without complete conversion to $SrFeO_{2.5}$.

### 4.3.2 Surface characterisation

#### Near-ambient pressure X-ray photoelectron spectroscopy

To characterise the chemical environments at the surface of the samples, near-ambient pressure X-ray photoelectron spectroscopy (NAP-XPS) measurements were performed on pelletised samples of SFO and Ag/SFO. Alongside NAP-XPS measurements, photographs of the sample under investigation were taken periodically, shown in Fig. 4.7. During heating of the samples under 0.25 mbar $H_2$ in the NAP-XPS instrument, a change in colour was visible at the surface of the pellets, from black, corresponding to perovskite $SrFeO_{3-\delta}$, to orange, corresponding to brownmillerite $SrFeO_{2.5}$ (Gebers *et al.*, 2023). For SFO, upon heating to 357°C, an orange brownmillerite region began to form at the centre of the pellet, then spread outwards over the surface, covering the majority of the surface after 41 min. After storing the sample for 24 h, the entire surface of the pellet was covered by the orange outer layer of $SrFeO_{2.5}$. Upon switching the gas atmosphere to 1 mbar $O_2$, the pellet of SFO returned to a uniform black colour within 20 min. For the pellet of Ag/SFO, reduction of $SrFeO_{3-\delta}$ to $SrFeO_{2.5}$ was visible at lower temperatures, with initial formation of an orange surface layer at 177°C, approximately in line with the findings of Wang *et al.* (2021) for thin films of Ag/$SrFeO_{3-\delta}$, and nearly complete coverage after heating to 297°C. The formation of the orange layer of brownmillerite at a *c.* 180°C lower temperature for Ag/SFO than

SFO was in agreement with the findings from Section 4.3.1 that the presence of Ag on $SrFeO_{3-\delta}$ aided formation of $SrFeO_{2.5}$ during reduction in $H_2$.

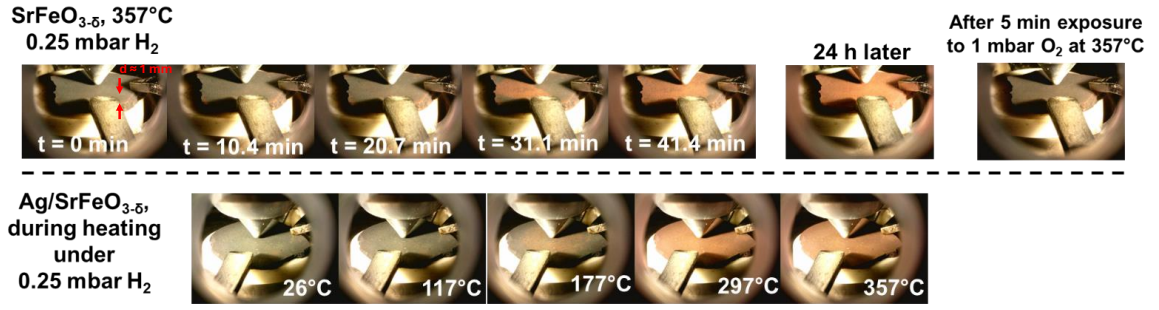


Fig. 4.7 Photographs of samples of $SrFeO_{3-\delta}$ and $Ag/SrFeO_{3-\delta}$ in the NAP-XPS instrument. Orange layer is $SrFeO_{2.5}$, black bulk is $SrFeO_3$.

From NAP-XPS scans of the O1s region for SFO at room temperature (shown in Fig. 4.8a), three distinct oxygen species were detected: $SrFeO_3$-lattice oxygen, SrO-lattice termination oxygen, chemisorbed oxygen species on the surface of the strontium ferrite (Crumlin *et al.*, 2012; Stoerzinger *et al.*, 2020; Zhou *et al.*, 2023), and residual carbonate impurities (Abd El-Naser *et al.*, 2021; Falcón *et al.*, 2002). The presence of residual carbonate on SFO and Ag/SFO up to 177°C was confirmed from the C1s spectra, shown in Appendix C, Fig. C.4. A full description of peak fitting parameters and assignments is given in Appendix C, Table C.1. For the sample of Ag/SFO at room temperature (Fig. 4.8d), an additional peak was detected at *c.* 532.5 eV, assigned to Ag-$O_x$ species (Pu *et al.*, 2022; Schön, 1973).

Upon heating SFO in 0.25 mbar $H_2$, the proportion of surface O species declined, with a rapid decrease above 357°C (shown in Figs. 4.8b and 4.9a, with further deconvoluted XPS peaks shown in Appendix C, Fig. C.2), and a corresponding increase in the relative fraction of bulk $SrFeO_3$ lattice oxygen was detected (Stoerzinger *et al.*, 2020). An overall shift in binding energy for $SrFeO_3$ lattice oxygen of *c.* +1.5 eV was observed relative to the measurements at room temperature, corresponding to a shift in the Fermi level for the reduced oxide (Nenning *et al.*, 2016). The differences in binding energy between peaks in the O1s spectrum remained approximately constant (±0.25 eV).

When the gas environment was switched to 1 mbar $O_2$ (while maintaining constant total pressure at 5 mbar), the proportion of surface oxygen species on SFO recovered rapidly, from 26.6 at% to 56.0 at% after 20 min exposure (shown in Fig. 4.8c). Upon cooling back down to room temperature under 1 mbar $O_2$, the proportion of surface

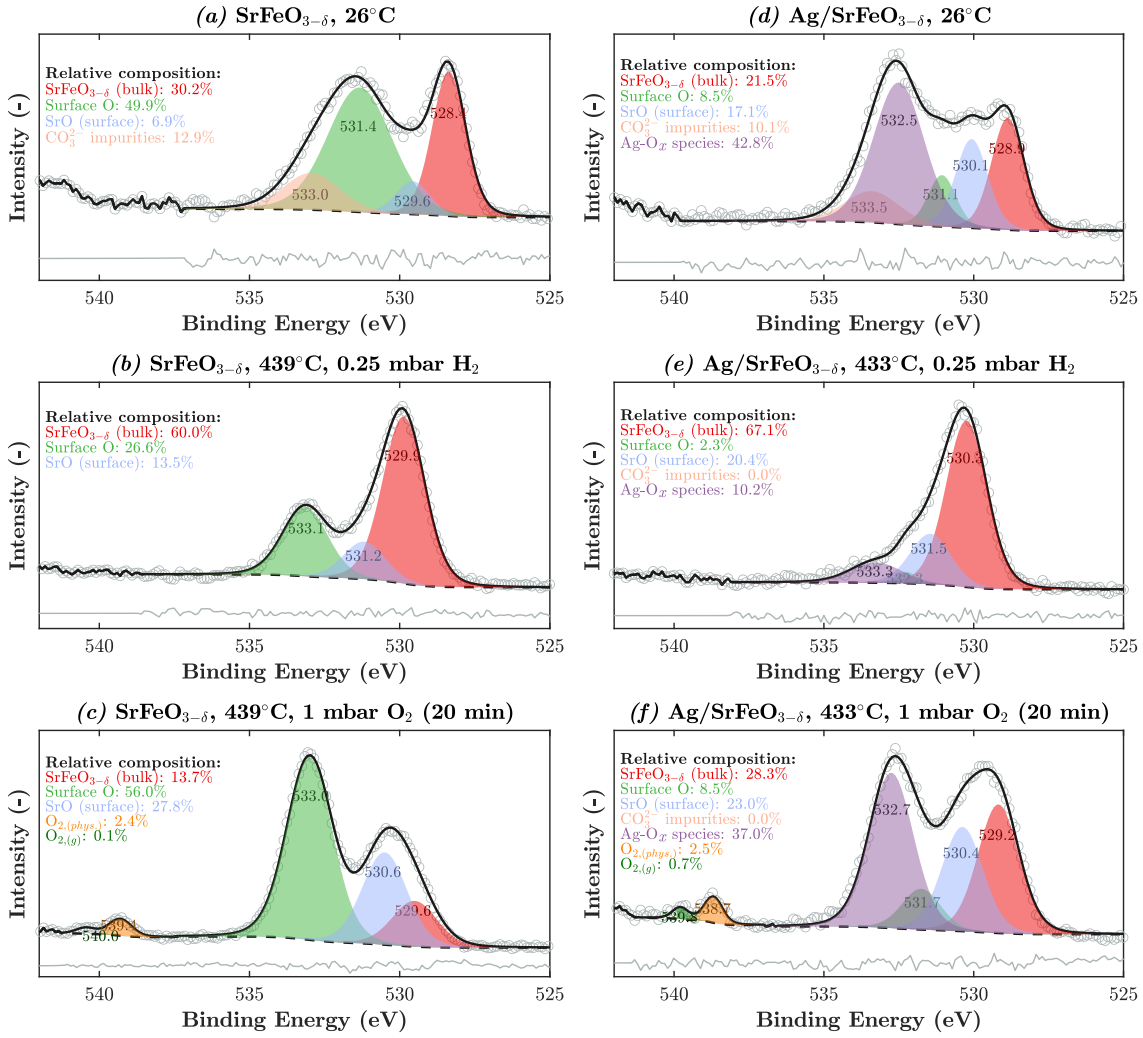


Fig. 4.8 NAP-XPS O1s spectra of $SrFeO_{3-\delta}$ **(a-c)** and $Ag/SrFeO_{3-\delta}$ **(d-f)** under 0.25 mbar $H_2$ and 1 mbar $O_2$. Circles indicate experimental measurements, solid black lines indicate overall fitted curve, shaded areas correspond to individual fitted peaks, dashed lines correspond to fitted baseline, and solid grey lines correspond to difference between fitted curve and measurements. Percentage areas estimated for each peak are given, corresponding to the approximate proportion (at%) of each species at the surface.

oxygen species continued to gradually increase, reaching *c.* 65 at% at 20°C (Fig. 4.9b). Additionally, two further peaks at *c.* 538-540 eV were observed, corresponding to physisorbed $O_2$ molecules at the surface of the sample (Puglia *et al.*, 1995), and molecules of oxygen gas in between the sample and the detector (Avval *et al.*, 2019).

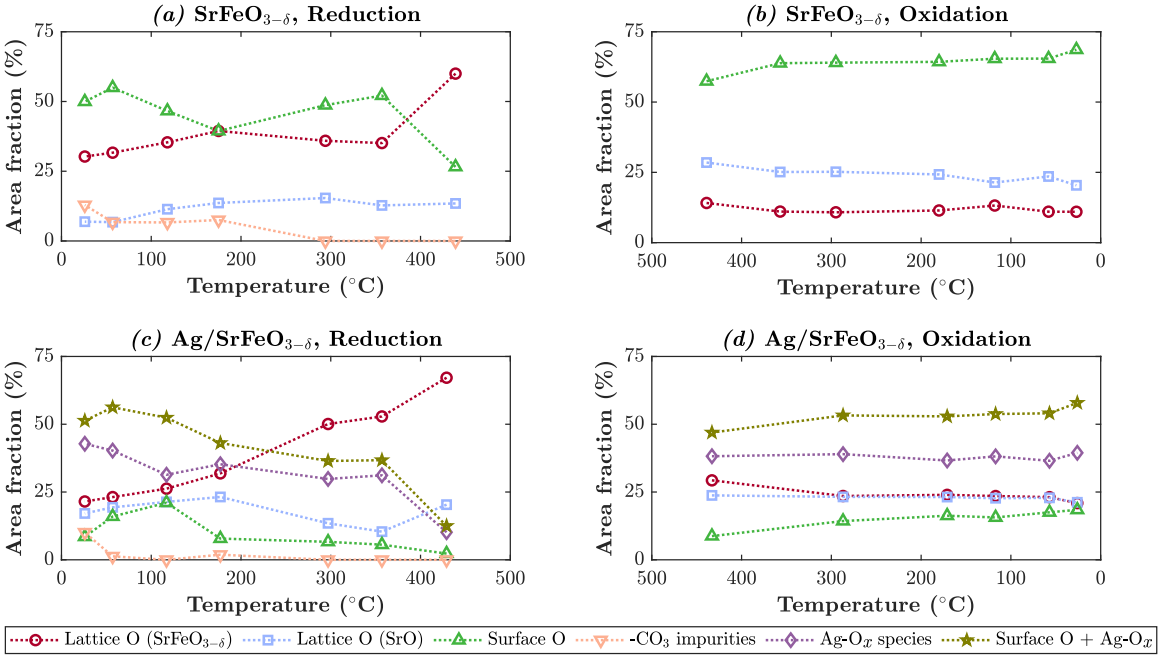


Fig. 4.9 Changes in surface composition with temperature for SrFeO$_{3-\delta}$ **(a-b)** and Ag/SrFeO$_{3-\delta}$ **(c-d)** under reducing (0.25 mbar $H_2$) and oxidising (1 mbar $O_2$) conditions, determined by NAP-XPS.

For Ag/SFO, upon heating under 0.25 mbar $H_2$, the proportion of surface O started to decrease at a lower temperature of 117°C, falling to around 6 at% by 357°C, whereupon the fraction of Ag-$O_x$ species also began to rapidly decline (shown in Figs. 4.8e and 4.9c, with further deconvoluted XPS peaks shown in Appendix C, Fig. C.3). The total fraction of non-lattice oxygen surface species (*i.e.* Ag-$O_x$ plus surface O) declined steadily throughout heating under $H_2$, reaching a final value of 12.5 at% at 433°C. The final fraction of total surface oxygen on Ag/SFO was substantially lower than the fraction of surface O detected on SFO at 439°C, showing that the presence of Ag aided the removal of surface oxygen.

When the gas environment over Ag/SFO was switched to 1 mbar $O_2$, the fraction of Ag-$O_x$ species rapidly increased, reaching a steady value of 37 at% within 20 min (Fig. 4.8f) and remaining approximately constant throughout reoxidation (Fig. 4.9d). By contrast, the fraction of surface oxygen increased gradually throughout cooling,

recovering to the initial value of 16 at% when the sample was cooled to room temperature. To better understand the behaviour of the surface oxygen species immediately after the gas switch from a reducing to oxidising atmosphere, rapid (20 s) scans of the O1s region for the sample of Ag/SFO were collected, shown in Fig. 4.10a. Given the relatively lower resolution of the rapid scans, surface O and Ag-$O_x$ could not be distinguished reliably, and so were fitted to a single peak.

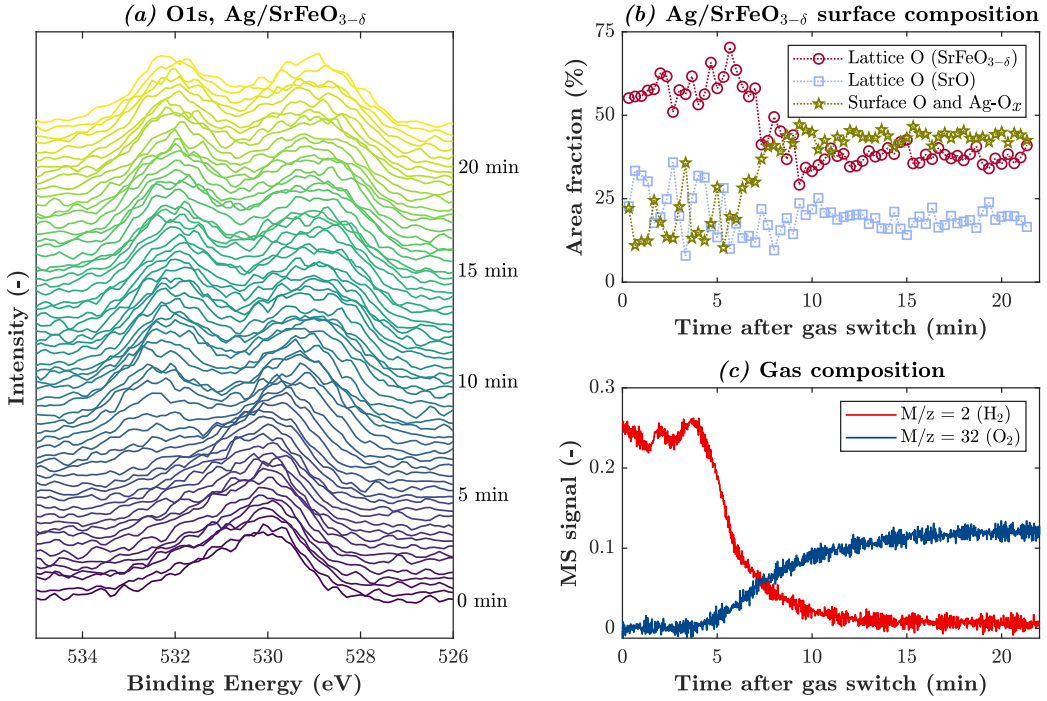


Fig. 4.10 **(a)** Rapid (20 s) scans of O1s region immediately after gas switch from 0.25 mbar $H_2$ to 1 mbar $O_2$, **(b)** estimated composition of surface species after gas switch, **(c)** composition of gas in sample chamber, measured by online mass spectrometry.

For the first 5 min after changing the set-points of the mass-flow controllers used to supply gas to the NAP-XPS sample chamber, no change was observed in the surface composition of Ag/SFO (shown in Fig. 4.10b), as a result of the delay between changing the gas supply, and the atmosphere around the sample changing. After approximately 5 min, the fraction of $H_2$ in the sample chamber began to decrease and the fraction of $O_2$ began to increase (monitored by online mass spectrometry, shown in Fig. 4.10c), and a peak at binding energy *c.* 532 eV, corresponding to the Ag-$O_x$ and surface O species, began to emerge almost immediately, with a corresponding increase in estimated

fraction of surface O and Ag-$O_x$ species, reaching a steady state approximately 10 min after the gas switch. The position of the lattice oxygen peak also shifted back from 530 eV to *c.* 529.5 eV when the $O_2$ entered the sample chamber, as the surface of the sample began to re-oxidise, resulting in a partial reverse of the shift in Fermi level observed previously.

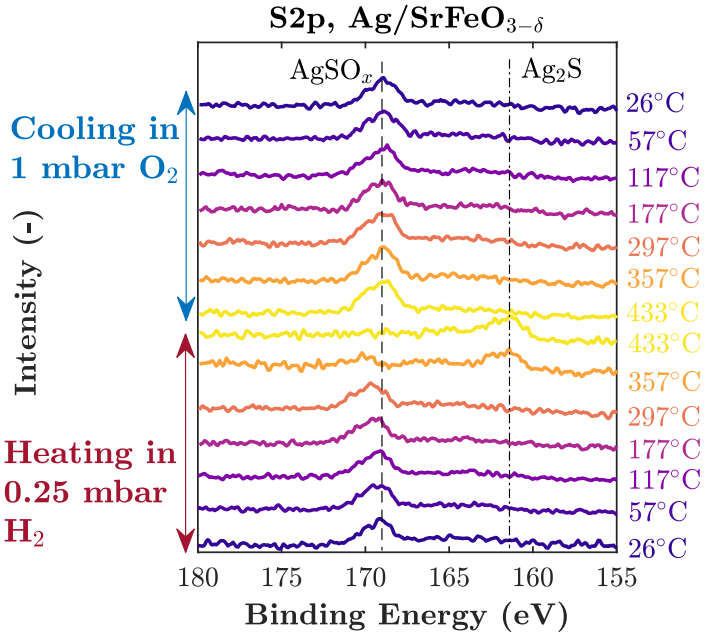


Fig. 4.11 NAP-XPS scans showing changes in S2p spectrum for $Ag/SrFeO_{3-\delta}$ during reduction and oxidation, with regions corresponding to sulphate and sulphide species indicated.

From XPS survey spectra of Ag/SFO, peaks in the S2p binding energy region were observed, and hence, scans of the S2p region were collected during *in-situ* experiments, shown in Fig. 4.11. At ambient conditions prior to heating, a single asymmetric peak was observed at binding energy *c.* 169.0 eV (the asymmetry in the overall peak was caused by overlapping $S2p_{3/2}$ and $S2p_{1/2}$ sub-peaks). The binding energy was consistent with the presence of silver sulphite or sulphate ($Ag_2SO_3$ and $Ag_2SO_4$) species from reaction of Ag with trace sulphur-containing compounds in laboratory air (*e.g.* $H_2S$, $SO_2$, carbonyl sulphide) (Mcmahon *et al.*, 2005; Sanders *et al.*, 2015).

Upon heating in 0.25 mbar $H_2$, at 357°C, the intensity of the peak at 169.0 eV started to decline, fully disappearing at 433°C, and, a new peak emerged at lower binding energy, *c.* 161.5 eV. The binding energy of the new peak was consistent with formation of silver sulphide, $Ag_2S$ (Kaushik, 1991; Sanders *et al.*, 2015). When the gas atmosphere was switched to 1 mbar $O_2$, the sulphide peak disappeared, and the

sulphate peak re-emerged, suggesting reaction of $Ag_2S$ with oxygen to form $Ag_2SO_x$. Hence, the S2p spectra reported here suggest that sulphur impurities at the surface of Ag on Ag/SFO underwent redox activity during chemical looping in $H_2$ and $O_2$, alongside $SrFeO_{3-\delta}$ and $AgO_x$ surface species. However, as the O1s binding energy of $Ag_2SO_x$ species at *c.* 531.5 eV overlapped with the peaks corresponding to Ag-$O_x$ and surface O, the reactions of $Ag_2SO_x$ were not verified by further deconvolution of the measured signals in the O1s region.

### Temperature programmed reduction ($H_2$-TPR)

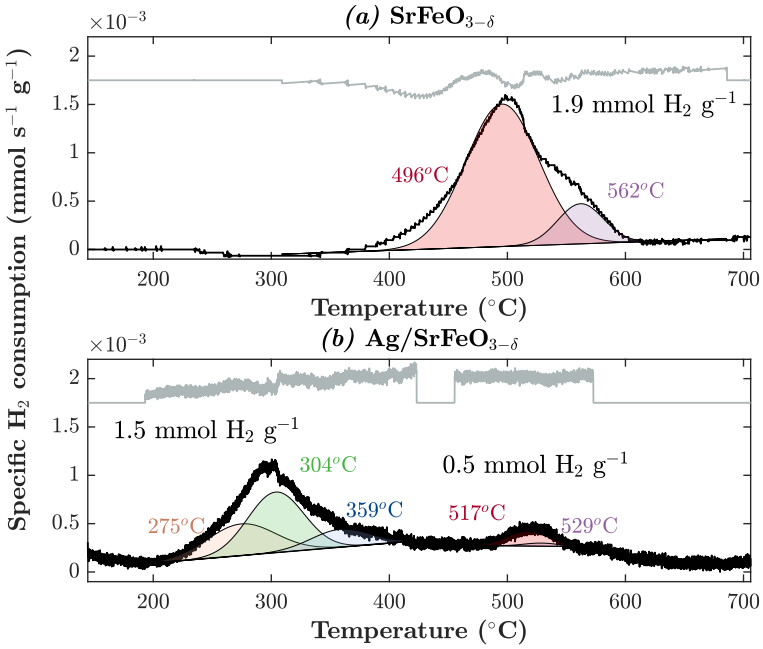


Fig. 4.12 Temperature-programmed reduction of SFO and Ag/SFO in 5 vol% $H_2$, with temperatures corresponding to centre of each fitted component, and total $H_2$ consumption for each feature. Samples were cleaned *in-situ* of carbonate and other impurities at 650°C in air for 3 h prior collecting the TPR measurements shown in the figure. Grey line above TCD signal indicates difference between measured values and fitted curves; flat regions in difference curve correspond to regions where peaks were not fitted.

To confirm the differences in surface behaviour during reduction, $H_2$-TPR measurements up to 700°C were performed for SFO and Ag/SFO, as shown in Fig. 4.12, with Gaussian curves fitted to deconvolute each observed peak in consumption of $H_2$.

The sample of SFO showed a single, broad peak in hydrogen consumption over the range 400-600°C, well-described by two components centred at 496°C and 562°C.

Contrastingly, the sample of Ag/SFO showed two distinct features: a large, broad peak between 200-400°C, fitted to three Gaussian components at 275°C, 304°C, and 359°C, and a shallow peak between 490-520°C, described by two peaks at 517°C and 529°C. The differences between the two samples under $H_2$-TPR suggest that the peak at 200-400°C for Ag/SFO corresponds to removal of adsorbed $AgO_x$ surface species, as detected by NAP-XPS, discussed in further detail in Section 4.4.2. Total hydrogen consumption for both samples was similar, at 1.9-2.0 mmol $g^{-1}$, corresponding to a final non-stoichiometry of approximately (3 - $\delta$) = 2.5 ± 0.05, as expected for reduction in $H_2$ up to 700°C from XRD measurements.

### *In-situ* Raman spectroscopy

Raman spectroscopy with simultaneous heating under 5 vol% $H_2$ was used to identify the Ag-$O_x$ species detected at the surface of Ag/SFO from NAP-XPS and $H_2$-TPR, with the measured spectra shown in Fig. 4.13a. All samples were calcined overnight in air prior to collecting Raman spectra, to remove surface impurities. The shaded bands span reported wavenumber ranges of peaks corresponding to different Ag-$O_x$ species: atomic Ag-O at 680-800 $cm^{-1}$, peroxide Ag-$O_2^{2-}$ at 880-1020 $cm^{-1}$, and superoxide Ag-$O_2^-$ at 1020-1080 $cm^{-1}$ (Alzahrani and Bravo-Suárez, 2023; Li *et al.*, 2023; Wang *et al.*, 1999; Zhao and Carpenter, 2013), with some overlap between Ag-O and silver oxide (bulk $Ag_2O$), and between Ag-$O_2^{2-}$ and $Ag_2CO_3$, shown in Fig. 4.13b.

For Ag/SFO at room temperature in air, clear peaks were observed in the wavenumber ranges corresponding to atomic Ag-O, peroxide Ag-$O_2^-$, and superoxide Ag-$O^{2-}$. No peaks in the regions of interest were observed on bare SFO without Ag, indicating minimal contribution from carbonate impurities or other species in the SFO support, as $SrCO_3$ has a characteristic Raman band at around 1070 $cm^{-1}$ (as shown in Chapter 5, Fig. 5.2). For metallic Ag supported on $Al_2O_3$, strong Raman bands were detected at 686 and 1052 $cm^{-1}$, assigned to atomic oxygen and superoxide respectively. A very weak band was detected at 990 $cm^{-1}$, suggesting that minimal peroxide Ag-$O_2^{2-}$ was present on the Ag/$Al_2O_3$, as reported by Li *et al.* (2023). The sample of $Ag_2O$/$Al_2O_3$ showed a Raman peak at around 668 $cm^{-1}$, at slightly lower wavenumber than the peak detected in the Ag-O region for Ag/$Al_2O_3$ and Ag/SFO. The sample of $Ag_2CO_3$ showed a peak at 1065 $cm^{-1}$, overlapping with the superoxide region, which halved in intensity upon collecting a second scan at the same point, as a result of beam damage (shown in Appendix A, Fig. A.1) to the photosensitive sample (Dai *et al.*, 2012).

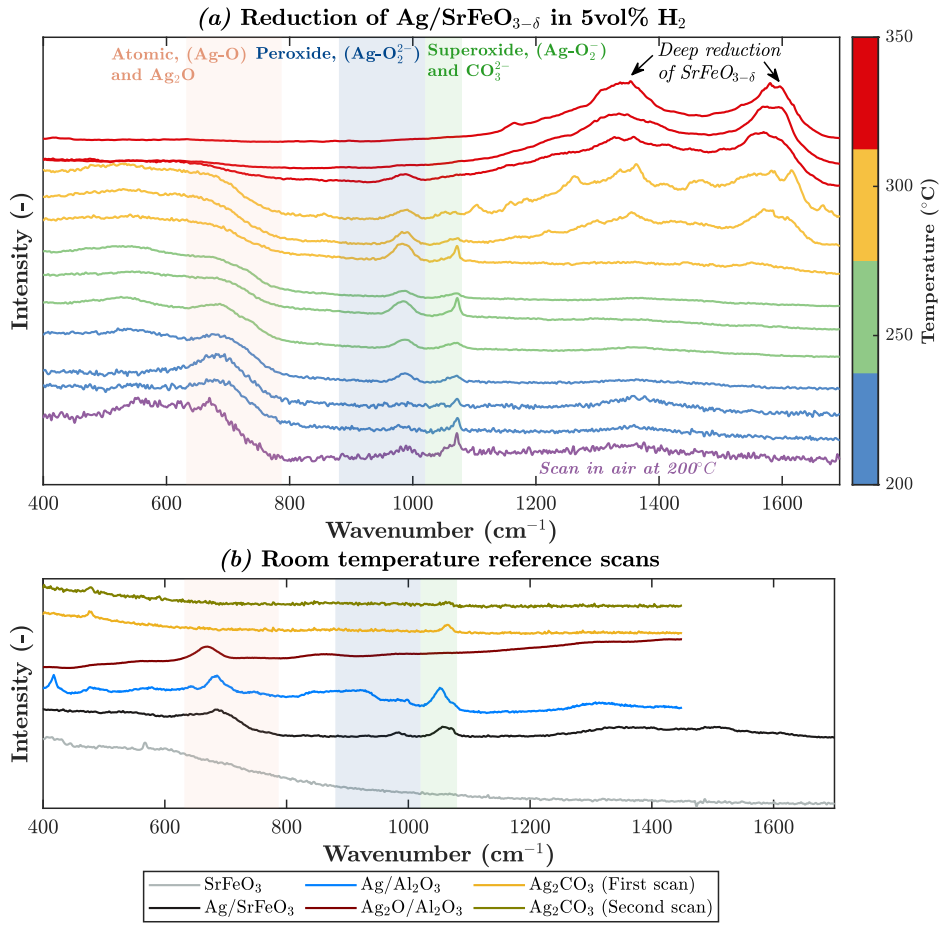


Fig. 4.13 **(a)** *In-situ* Raman spectroscopy of $Ag/SrFeO_{3-\delta}$ showing removal of $O_x$ surface species under 5 vol% $H_2$, with shaded wavenumber ranges from literature, **(b)** reference scans at room temperature. Reference scans are normalised with respect to maximum intensity detected in each scan.

Upon heating the sample of Ag/SFO to 200°C in air, all three main peaks remained, although the relative intensity of the atomic oxygen and superoxide peaks somewhat declined, possibly indicating removal of trace silver oxide and carbonate contaminants. With gas flow through the sample stage switched to 5 vol% $H_2$ in $N_2$, little change was observed at 200°C, then, upon heating to 250°C, the intensity of the peak corresponding to atomic oxygen declined, and almost entirely disappeared after three scans (*c.* 15 min dwell time at 250°C). With further heating to 300°C, the atomic oxygen feature fully disappeared, and over the course of three successive scans, the intensity of the superoxide peak began to decline. Then, at the highest temperature point investigated of 350°C, the superoxide peak disappeared entirely, and after two scans, the peroxide peak also disappeared. Hence, the temperatures of desorption of atomic oxygen, superoxide, and peroxide detected *via* Raman spectroscopy were in good alignment with the centres of the deconvoluted peaks fitted to $H_2$-TPR measurements for Ag/SFO. In addition, two prominent features at *c.* 1350 and 1580 cm$^{-1}$ emerged, corresponding to deep reduction of SrFeO$_{3-\delta}$ and possible formation of brownmillerite SrFeO$_{2.5}$ at the surface of the sample pellet (Barkalov *et al.*, 2022), in line with the observations shown in Fig. 4.7, where an orange brownmillerite surface layer formed at the surface of the SrFeO$_{3-\delta}$ pellet under reducing conditions at *c.* 350°C.

## 4.4 Discussion

### 4.4.1 Bulk reduction of $SrFeO_{3-\delta}$

The XRD results in Fig. 4.1 show that for reduction in 5 vol% $H_2$, the presence of Ag on $SrFeO_{3-\delta}$ aided phase transition from perovskite to brownmillerite, decreasing the temperature required by 200°C as compared to unmodified SFO.

Wang *et al.* (2021) also showed from high-temperature XRD measurements that noble metals deposited on strontium perovskites reduced the temperature required for transformation from perovskite to brownmillerite, albeit at lower overall temperatures. Samples composed of a thin film of $SrFeO_{3-\delta}$ grown on a $SrTiO_3$ substrate, with a further layer of 1.8 nm Ag deposited at the surface, showed topotactic phase transition to $SrFeO_{2.5}$ at 150°C, whereas for samples without the Ag film, heating to *c.* 300°C was required to induce a phase transition. From density functional theory calculations and TEM imaging of the Ag-$SrFeO_{3-\delta}$, the authors postulated that the presence of the noble metal film aided oxygen release by donating electrons to the perovskite support, weakening Fe-O bonds by forming an amorphous interfacial layer of Ag-O-Fe bonds. However, given the substantially higher temperatures and strong reducing agent ($H_2$) required to form a brownmillerite phase from the irregular, polycrystalline samples of SFO and Ag/SFO prepared in this study, the relative influence of such an interfacial interaction might be less significant than the contribution of surface reactions of Ag, discussed further in Section 4.4.2.

The TEM images, with parallel EDS and EELS mapping, shown in Figs. 4.3 and 4.5 demonstrate the changes in Fe oxidation state, and hence oxygen stoichiometry in $SrFeO_{3-\delta}$, during oxygen uncoupling induced by heating *in vacuo* for SFO and Ag/SFO. However, differences in reduction behavior between samples were much less pronounced than during *in-situ* XRD under $H_2$, or during TGA under an inert atmosphere as reported in Chapter 3.

Furthermore, Ag/SFO did not show significant localisation of reduced areas at or near particles of Ag - instead, both samples showed growth of reduced fronts moving inwards to the centre of the particle in an approximately uniform manner. The lack of spatial variation in Ag/SFO was in contrast with *in-situ* TEM studies of other noble metal-metal oxide systems under redox reactions, where for particles of Pd deposited on $CeO_{2-\delta}$ nanocubes, Mahadi *et al.* (2020) observed a reduced region of $Ce^{3+}$ at the Pd-$CeO_{2-\delta}$ interface, which then spread through the bulk $Ce^{4+}$ with successive STEM-EELS scans. However, *in-situ* EELS and NAP-XPS studies of $NiFe_2O_4$ under

strong reducing conditions ($H_2$ or CO at ≥850°C) showed little radial variation in Fe valance and oxygen content within nanoparticles of the metal oxide over 10 min reduction, with fast oxygen transport within the particles (Song *et al.*, 2024a), and concentration gradients in oxygen only developing within the particles over 120 min reduction (Song *et al.*, 2022) as the particles became deeply reduced.

Hence, for the experimental conditions applied here, with Ag/SFO uncoupling oxygen into an inert atmosphere, given the Ag/SFO system did not show localisation of reduced regions around Ag, relatively rapid transport of $O^{2-}$ ions within the $SrFeO_{3-\delta}$ lattice might have been sufficient to dissipate any spatial gradients in oxygen content near Ag resulting from oxygen removal at Ag-$SrFeO_{3-\delta}$ interfaces. Instead, the particle became reduced gradually, with transport of oxygen from the core to the surface, resulting in a front of lower-valence $Fe^{3+}$ moving inwards from the edge of the particle to the centre.

Additionally, electron diffraction images shown in Fig. 4.6 suggested partial formation of a brownmillerite phase in Ag/SFO at elevated temperature (≥600°C). However, the diffraction patterns also showed the clear presence of reflections corresponding to a cubic perovskite phase alongside the brownmillerite, indicating heterogeneity through the sample depth, possibly with thin layers of brownmillerite forming at external surfaces around a perovskite core. The relatively slow phase transition in TEM experiments is in contrast with the rapid phase transition observed in studies of $SrFeO_{3-\delta}$ thin films (Xing *et al.*, 2022), where brownmillerite regions expanded through the sample within 79 s at 300°C, surrounding 'islands' of unconverted perovskite.

At 700°C, the average oxygen stoichiometry at the point on the sample where a brownmillerite phase was visible (shown in Fig. 4.6b) was estimated to be *c.* $SrFeO_{2.67}$, exceeding (3 - $\delta$) = 2.5 as would be expected for pure brownmillerite, and hence further suggesting a mixture of perovskite and brownmillerite environments through the sample depth. Alternatively, the higher than expected stoichiometry might indicate formation of $SrFeO_{2.5+\delta}$, as the estimated stoichiometry was approximately in line with the oxygen content of (2 + $\delta$) = 2.625 measured by Xing *et al.* (2022) in regions of hyper-stoichiometric brownmillerite (corresponding to an average iron valence of *c.* $Fe^{3.25+}$).

For the Ag/SFO materials investigated here, local variation in temperature and material strain in the vicinity of nanoparticles of Ag might also have affected redox properties and distribution of oxygen during reduction. Given the differences in specific heat capacity and thermal conductivity between Ag and $SrFeO_3$, where

$C_{p,Ag}$ = 0.23 J $g^{-1}K^{-1}$, $C_{p,SrFeO_{3-\delta}}$ = 0.5 J $g^{-1}K^{-1}$ and $\kappa_{Ag}$ = 418 W $m^{-1}K^{-1}$, $\kappa_{SrFeO_{3-\delta}}$ = 3 W $m^{-1}K^{-1}$ (Bian *et al.*, 2023; Fulham *et al.*, 2024; Rakshit *et al.*, 2007; Renner *et al.*, 2001), local heating and cooling as a result of reaction might have resulted in the formation of hot or cold spots in the vicinity of particles of Ag (Enger *et al.*, 2008; Somani *et al.*, 1996), thereby altering the local (3 - $\delta_{eq}$) characteristics of the material at the nanoscale. Furthermore, local straining of the perovskite lattice as a result of interfacial contact or partial embedding of Ag nanoparticles might have aided local oxygen migration and vacancy formation (Mayeshiba and Morgan, 2015, 2017), facilitating reduction. Further TEM studies during reduction and oxidation would be necessary to assess the extent of nanoparticle embedding, and hence the influence of local strain effects.

Overall, the irregular, three-dimensional powder samples considered in this study showed some different behaviour from the well-defined thin film samples described in literature; however, the broad trend of Ag assisting oxygen release from $SrFeO_{3-\delta}$ was observed clearly.

### 4.4.2 Surface reactions and mechanisms of oxygen transport

#### Changes in surface species during NAP-XPS measurements

From NAP-XPS measurements, shown in Figs. 4.8 and 4.9, multiple different oxygen species were detected at the surface of SFO and Ag/SFO, with the relative fraction of each species varying substantially with temperature. For both SFO and Ag/SFO, upon heating from room temperature to ≥430°C in hydrogen, the proportion of oxygen surface species decreased with temperature, with a rapid decline in chemisorbed oxygen on SFO above 357°C.

The decrease in surface oxygen for SFO under heating is in good agreement with the findings of Crumlin *et al.* (2012), where thin film and pelletised samples of $La_{0.8}Sr_{0.2}CoO_{3-\delta}$ perovskite were heated under 1 mbar $O_2$ up to 520°C. At 220°C, peaks in the O1s spectrum were detected corresponding to chemisorbed surface oxygen species, lattice oxygen in the bulk perovskite, and oxygen in a surface termination layer of SrO (Rupp *et al.*, 2017; Zhu *et al.*, 2024), as in Fig. 4.8. For the pelletised sample, the proportion of surface oxygen decreased by around 11% upon heating to 520°C, whereas, for the thin film sample, surface oxygen decreased by around 7% upon heating to 370°C, and disappeared entirely at 520°C (with only lattice oxygen in the bulk $La_{0.8}Sr_{0.2}CoO_{3-\delta}$ and the surface termination layer of SrO remaining).

Here, using a stronger reducing agent (0.25 mbar $H_2$), surface oxygen content decreased by around 46% upon heating from room temperature to 439°C. However, the persistence of surface oxygen even at high temperatures under a relatively strong reducing gas indicated the difficulty of removing surface oxygen from SFO in the absence of Ag, especially for bulk samples rather than thin films.

The samples of Ag/SFO investigated here showed markedly different behaviour during reduction as compared to unmodified SFO, with the emergence of an additional peak at high binding energy corresponding to Ag-$O_x$ surface species. In studies of oxygen adsorbed on foil and powder samples of pure Ag, Rocha *et al.* (2012) assigned peaks in the O1s region to a series of surface and sub-surface Ag-O species - here, however, the overlap between Ag-$O_x$, $SrFeO_3$ and SrO spectra meant that Ag-$O_x$ were grouped into a single, relatively broad peak (with FWHM constrained to $\leq$ 2 eV). Additionally, under the conditions investigated here, the fraction of low binding energy ($\leq$528 eV) Ag-O species on Ag/SFO was negligible, as expected for measurements taken at or above room temperature (Carbonio *et al.*, 2018).

During reduction in $H_2$, the decrease in the relative area fraction of the Ag-$O_x$ peak with successive measurements suggested removal of oxygen by reaction with hydrogen at the surface of Ag. At each temperature investigated, the fraction of Ag-$O_x$ greatly exceeded the fraction of chemisorbed oxygen at the surface of $SrFeO_{3-\delta}$. The chemisorbed oxygen on $SrFeO_{3-\delta}$ was removed at lower temperatures for the sample of Ag/SFO than for bare SFO. During heating, the fraction of oxygen at the surface of $SrFeO_{3-\delta}$ declined at lower temperatures than Ag-$O_x$, reaching <10% at 177°C, whereas Ag-$O_x$ species gradually declined up to 357°C, then decreased sharply to *c.* 10% at 433°C.

Hence, the greater fraction of Ag-$O_x$ species might indicate that at elevated temperatures, lattice oxygen from the $SrFeO_{3-\delta}$ support was transported from the bulk to the surface, then rapidly migrated to Ag sites, with little chemisorbed oxygen remaining at the surface of the SFO. Moreover, given the final fraction of total surface oxygen was approximately 50% lower for Ag/SFO than SFO at >430°C, the mechanism of reduction likely proceeded *via* Ag facilitating removal of oxygen by forming reactive Ag-$O_x$ intermediate species, which were then able to react with hydrogen more easily than oxygen on bare SFO.

During reoxidation of both SFO and Ag/SFO, fractions of surface oxygen, and Ag-$O_x$ species, recovered rapidly after 20 min exposure to 1 mbar $O_2$, approximately equalling the initial fractions at room temperature, and therefore supporting the finding

from Chapter 3 that the reoxidation of $SrFeO_{3-\delta}$-based materials is substantially more rapid than reduction. Additionally, for SFO, the relative fraction of bulk $SrFeO_{3-\delta}$ lattice oxygen sharply decreased upon exposure to oxygen, and the fraction of SrO increased, with the relative fractions of all species remaining approximately constant through further cooling. The increase in SrO could indicate a consolidation of the SrO lattice termination layer during reoxidation after the sample had been deeply reduced. Furthermore, during reduction, the ratio between the total areas of peaks in the Sr3d and Fe2p regions (shown in Appendix C, Fig. C.5) remained approximately constant for both samples, whereas, during reoxidation, the area fraction of Sr increased as the sample was cooled. Consolidation of the SrO layer, and hence, A-site enrichment at the surface of the perovskite after reoxidation (Crumlin *et al.*, 2012), would be consistent with the observed removal of the orange brownmillerite layer at the surface of the pellet of SFO after switching to $O_2$, shown in Fig. 4.7, and with the increase in the ratio of areas between the Sr3d and Fe2p energy regions during reoxidation.

During rapid scans of the O1s region during reoxidation of Ag/SFO, shown in Fig. 4.10, the peak corresponding to surface oxygen species emerged almost instantaneously as concentration of $O_2$ in the sample chamber rose. The centre of the lattice oxygen peak began to shift to lower binding energy over 20 min by 0.5 eV, partially reversing the positive shift during heating associated with a change in Fermi level for reduced samples (Nenning *et al.*, 2016). Upon further cooling of Ag/SFO, the fraction of Ag-$O_x$ species remained approximately constant, and the fraction of surface O species increased; Ag-$O_x$ remained the dominant surface oxygen species at all temperatures during reoxidation. Hence, the NAP-XPS measurements during reoxidation suggest that the mechanism of oxidation for Ag/SFO proceeded by oxygen being absorbed from the gas phase to rapidly form surface Ag-$O_x$ species, which were then gradually incorporated into the $SrFeO_{3-\delta}$ lattice.

As well as the changes in oxygen species observed from measurement of the O1s binding energy region using NAP-XPS, the redox activity in the S2p region provided an insight into the catalytic activity of $Ag/SrFeO_{3-\delta}$ materials. When Ag is applied as a catalyst for epoxidation of olefins, recent literature (Carbonio *et al.*, 2018, 2023; Jones *et al.*, 2018) suggests that sulphur impurities participate in the selective oxidation pathway by forming reconstructed Ag-$SO_4$ surface structures, which then donate oxygen to the reaction (shown in Appendix C, Fig. C.7). Depletion of sulphate surface species over the course of the reaction results in a decrease in selectivity towards the epoxide product, and an increase in complete combustion, with periodic replenishment by

addition of $SO_2$ co-fed with the olefin substantially improving the overall selectivity (Carbonio *et al.*, 2023).

Therefore, the depletion of $AgSO_x$ species under reducing conditions to form sulphide species might help explain the decrease in selectivity over time observed by Gebers *et al.* (2022) during ethylene epoxidation over Ag/$SrFeO_{3-\delta}$ in a chemical looping mode. Despite oxidation of Ag/$SrFeO_{3-\delta}$ occurring substantially more rapidly than reduction (as demonstrated in Chapter 3), long ($\geq$10 min) reoxidation steps were required after 1.5 min reduction to achieve maximal selectivity towards the epoxide product, with shorter oxidation times resulting in a decrease in ethylene oxide produced. If anaerobic reduction of Ag/$SrFeO_{3-\delta}$ depletes Ag-$SO_4$ complexes more rapidly than they can be replenished by lattice oxygen from $SrFeO_{3-\delta}$, resulting in formation of $Ag_2S$, increased reduction time would result in a decrease in instantaneous selectivity over the course of each reduction step, as observed by Gebers *et al.* (2022), even if adequate oxygen were available from the $SrFeO_{3-\delta}$ support. Then, during exposure to air, reaction between $Ag_2S$ and gaseous $O_2$ would gradually replenish the sulphate species, restoring selectivity for the subsequent chemical looping cycle.

Future work considering the transport of oxygen during chemical looping epoxidation over Ag/$SrFeO_{3-\delta}$ should consider the dynamics of Ag-$SO_x$ species during reduction and oxidation, and, investigate whether co-feeding $SO_2$ helps maintain the population of selective Ag-$SO_4$ sites, as demonstrated for pseudo-steady state epoxidation (Carbonio *et al.*, 2023).

### Identification of oxygen species from $H_2$-TPR and Raman measurements

To distinguish the multiple different surface oxygen species identified in this study, $H_2$-TPR measurements were deconvoluted by fitting Gaussian curves to major features, shown in Fig. 4.12. For both samples of SFO and Ag/SFO, a prominent peak in hydrogen consumption was observed at around 500°C, which was well-described by two Gaussian peaks. However, for the sample of Ag/SFO, the area of the peak was 74% lower than for the equivalent peak for SFO without Ag. Furthermore, the sample of Ag/SFO showed a second, larger feature, composed of three deconvoluted peaks, over the temperature range 200-400°C. The three deconvoluted peaks, centred at 275, 304, and 359°C, were assigned to the reaction of Ag-O, Ag-$O_2^-$, and Ag-$O_2^{2-}$ species respectively, as detected by Raman spectroscopy (shown in Fig. 4.13), with good agreement between $H_2$-TPR and Raman in temperatures of desorption under 5 vol% $H_2$. The low temperature peak detected in $H_2$-TPR for Ag/SFO might also contain

some contribution from surface O species on $SrFeO_{3-\delta}$, and $AgSO_x$ species, both found to decline during reduction in the temperature range 200-400°C from NAP-XPS (Figs. 4.9 and 4.11). The higher temperature feature, present for both samples at around 500°C, was assigned to reaction of hydrogen directly with the lattice oxygen in $SrFeO_{3-\delta}$.

A similar process of peak-fitting was applied to deconvolute measurements for $H_2$-TPR of $SrFeO_{3-\delta}$, and $Ag/SrFeO_{3-\delta}$ (15 wt% Ag), reported by Gebers *et al.* (2023) (shown in Appendix C, Fig. C.6), with the temperature positions of the fitted peaks in good agreement with the measurements reported in Figs. 4.12 and 4.13 from $H_2$-TPR and Raman spectroscopy. Additionally, from $H_2$-TPR measurements of batches of $Ag/SrFeO_{3-\delta}$ synthesised under different calcination conditions, Marek and García-Calvo Conde (2021) observed a similar pattern of two distinct peaks in $H_2$ consumption, with the first in the region 200-400°C deconvoluted as four sub-peaks, centred at 244, 309, 399, and 439°C for a sample calcined in air at 650°C. The higher temperature peaks were detected in the region 650-800°C, somewhat higher than for the samples investigated here, possibly suggesting a less reactive $SrFeO_{3-\delta}$ support.

The findings from $H_2$-TPR of Ag/SFO also aligned with studies of Ag supported on $CeO_{2-\delta}$ (Wang *et al.*, 2023). The presence of Ag aided removal of oxygen from $CeO_2$, resulting in a shift in the peak corresponding to reduction of bulk $CeO_{2-\delta}$ from 529°C to 494°C, and introduced a new peak at 100-300°C corresponding to removal of surface oxygen from silver.

Assuming that the only consumption of hydrogen during $H_2$-TPR was reaction with oxygen to form water, the number of moles of $H_2$ consumed should equal the number of moles of O atoms removed from the samples. Hence, the total $H_2$ consumption in the lower temperature feature for Ag/SFO exceeded the theoretical amount of oxygen available from absorbed oxygen on Ag by three orders of magnitude, estimated at 6.4 $\mu mol_{O,ads}$ $g^{-1}$ for 10wt% Ag on $SrFeO_{3-\delta}$, and was three times larger than the maximum oxygen available if all Ag was present as $Ag_2O$, estimated at 0.46 mmol $g^{-1}$ (Gebers *et al.*, 2022). Therefore, for the sample of Ag/SFO, the additional oxygen removal at lower temperature came at the expense of oxygen removal in the peaks at *c.* 500°C. Moreover, the consumption of hydrogen at low temperatures ($\leq$300°C) over Ag/SFO was in agreement with previous studies of catalytic combustion of $H_2$ over Ag. Dokuchits *et al.* (2011, 2012, 2015) demonstrated that during combustion of $H_2$ in $O_2$ in the presence of particles of metallic Ag, $O_2$ molecules adsorbed on the surface of Ag and dissociated to form reactive surface Ag-O species, which then reacted

with $H_2$ to form $H_2O$ in the temperature range 150-200°C, with minimal adsorption of $H_2$ on Ag (Dokuchits *et al.*, 2015; Hillary and Stoukides, 1988). Hence, the $H_2$-TPR results support the hypothesis established in this Chapter that for Ag/SFO, oxygen is removed from the bulk of $SrFeO_{3-\delta}$ during reduction *via* the formation of Ag-$O_x$ intermediates, allowing reaction at lower temperatures than for bare $SrFeO_{3-\delta}$.

### Proposed mechanisms of oxygen transport

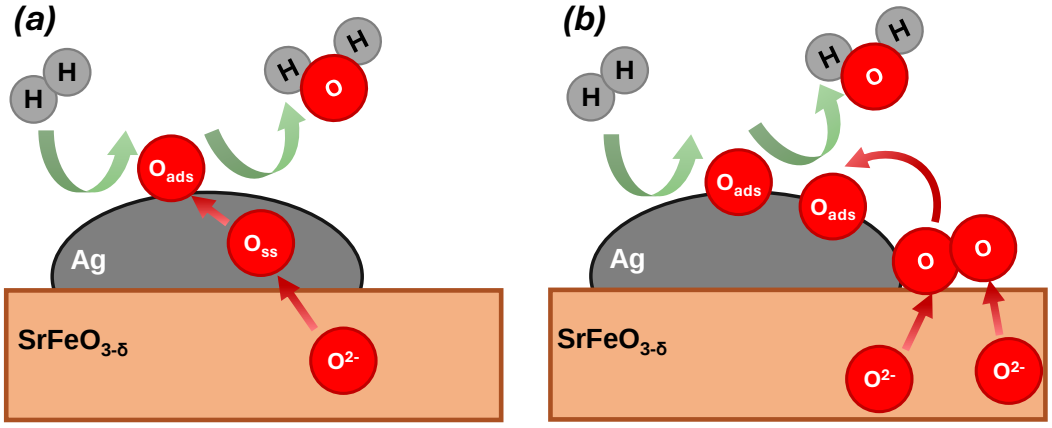


Fig. 4.14 Simplified mechanisms proposed for oxygen transport from bulk $SrFeO_{3-\delta}$ to the surface of Ag nanoparticles: **(a)** Diffusion through bulk Ag, proposed by Chan *et al.* (2018b), **(b)** Spillover of oxygen at the Ag-$SrFeO_{3-\delta}$-gas interface, analogous to the mechanism of oxygen removal from Ag/$CeO_{2-\delta}$ proposed by Lee *et al.* (2021).

From initial studies of the Ag/$SrFeO_{3-\delta}$ system, Chan *et al.* (2018b) hypothesised that oxygen migrated from the $SrFeO_{3-\delta}$ lattice to the surface of Ag by diffusion of atomic oxygen species through bulk Ag, to form atomic Ag-O surface species which were then removed during reaction with a reducing gas (shown in Fig 4.14a). However, other mechanisms of oxygen transport are possible for oxygen release in metal-metal oxide systems, including spillover of oxygen atoms from the surface of the oxide to the adsorb at the surface of the metal (Lee *et al.*, 2021; Ruiz Puigdollers *et al.*, 2017) (shown in Fig. 4.14b), and *vice-versa* during absorption of oxygen from the gas phase into the oxide support (Leo *et al.*, 2009).

Given when oxygen is removed from the lattice of $SrFeO_{3-\delta}$ during reduction, the initial state is as monoatomic $O^{2-}_{lattice}$ ions, the presence of diatomic peroxide and superoxide species at the surface of Ag/SFO detected by Raman spectroscopy was somewhat surprising. To explain the presence Ag-$O_2^-$ and Ag-$O_2^{2-}$ at the surface of Ag/SFO, the diatomic oxygen species might act as an intermediate during the

formation of atomic Ag-O species. Deng *et al.* (1995) found from that during methanol oxidation in air with *in-situ* Raman spectrocopy, Ag-$O_2^{2-}$ (peroxide) species, formed by absorption of $O_2$ from the gas phase, were a precursor to the formation of reactive Ag-O species.

Moreover, previous studies of chemical looping over iron-based oxygen carriers (Huang *et al.*, 2022; Song *et al.*, 2022; Wei *et al.*, 2010) suggested that oxygen species at the surface of the oxide reach a dynamic equilibrium of the form $2O^{2-}_{lattice} \rightleftharpoons 2O^{2-}_{ads} \rightleftharpoons 2O^{-}_{ads} \rightleftharpoons O^{2-}_{2,ads} \rightleftharpoons O^{-}_{2,ads} \rightleftharpoons O_{2,gas}$, with inter-conversion between lattice oxygen ions and diatomic species. Huang *et al.* (2022) proposed that during reduction of $NiFe_2O_4$ in $H_2$, the mechanism of reduction proceeded by $O^{2-}_{lattice}$ ions combining at the surface of the oxide to form peroxide $O_2^{2-}$, which then reacted with $H_2$ by forming hydroxyl $OH^-$ ions, and ultimately water. Gao *et al.* (2020) also determined that during chemical looping dehydrogenation of ethane over $Li_2CO_3/La_xSr_{1-x}FeO_{3-\delta}$ composites, peroxide species formed at the $Li_2CO_3$-$La_xSr_{1-x}FeO_{3-\delta}$ interface by reduction of $Fe^{4+}$ to $Fe^{3+}$, then acted as the active species in the oxidation reaction.

Hence, if similar reactions of $O^{2-}_{lattice}$ ions to form peroxide ions occurred in $SrFeO_{3-\delta}$, the mechanism of reduction could proceed by spillover of the peroxide ion at the Ag-$SrFeO_{3-\delta}$ interface to form Ag-$O_2^{2-}$ on the surface of Ag, followed by dissociation to form Ag-O species, which react with the reducing gas (as shown in Fig. 4.14b). Furthermore, from NAP-XPS of Ag/SFO (shown in Fig. 4.9c), the depletion of chemisorbed oxygen species (including peroxide) on the $SrFeO_{3-\delta}$ support at lower temperatures than Ag-$O_x$ species might indicate that the transfer of peroxide from the surface of SFO to Ag proceeded more rapidly than removal of Ag-$O_x$ by $H_2$, resulting a lower measured fraction at higher temperatures. However, the potential role of the superoxide Ag-$O_2^-$ species in such a mechanism remains unclear.

Alternatively, in the absence of spillover of diatomic species at the Ag-$SrFeO_{3-\delta}$ interface (*i.e.* if oxygen transport proceeded primarily *via* diffusion of atomic species through Ag, as shown in Fig 4.14a), a different explanation for the presence of diatomic oxygen species would be required. Given the material was exposed to air prior to reduction, diatomic species might have formed at the surface of Ag from adsorption of molecular oxygen from exposure to air (Zambelli *et al.*, 2002). Therefore, if atomic Ag-O species were preferentially removed by $H_2$ (as indicated by the rapid decline in atomic oxygen Raman peak intensity with heating), the residual diatomic species might act as relatively inert spectator molecules. Then, upon heating to higher temperature, the diatomic species could react with hydrogen and become removed, but otherwise

have little role in the transport of oxygen from SrFeO$_{3-\delta}$. However, from the H$_2$-TPR measurements of Ag/SFO reported here and by Gebers *et al.* (2023), the deconvoluted peaks assigned to diatomic species comprised 0.3-1.0 mmol g$^{-1}$ of oxygen removed, greatly exceeding the maximum estimated amount of adsorbed O$_2$ on Ag (6.4 $\mu$mol g$^{-1}$). Therefore, the diatomic oxygen species detected on Ag likely formed as an intermediate in the overall mechanism of reduction, rather than being merely residual chemisorbed oxygen from air, suggesting that diffusion of atomic oxygen through Ag was not the only step in removal of oxygen from Ag/SFO materials.

To further clarify the proposed mechanism of oxygen transport, and to confirm the manner in which diatomic oxygen species might participate as intermediates during reduction of Ag/SFO in H$_2$, future work could include isotopic exchange studies (Bouwmeester *et al.*, 2009), with a sample of Ag/SrFeO$_{3-\delta}$ exposed successively to $^{18}$O$_2$ and H$_2$. Then, using Raman spectroscopy and mass spectrometry to track the exchange of oxygen isotopes between the SrFeO$_{3-\delta}$ and the Ag surface (Mestl *et al.*, 1994; Stangl *et al.*, 2023), and between the Ag surface and the gas phase, the pathway of oxygen into and out of the SrFeO$_{3-\delta}$ lattice, and the intermediate species involved, could be further refined.

Additionally, the relative distribution of Ag-O$_x$ species on nanoparticles of Ag was found by Li *et al.* (2023) to be affected by interactions between the Ag and the support (in their study, $\alpha$-Al$_2$O$_3$ or SiO$_2$). When the materials were used as catalysts for the epoxidation of olefins (*e.g.* ethylene) by O$_2$, Ag-O$_2^-$ species favoured the epoxide product, and Ag-O and Ag-O$_2^{2-}$ species favoured the complete combustion pathway. Furthermore, Lee *et al.* (2019) found that when using Ag/CeO$_{2-\delta}$ as a catalyst for the oxidation of soot, the proportion of different oxygen species was influenced by the fraction of oxygen vacancies in the vicinity of the Ag, with higher concentrations of vacancies favouring Ag-O$^-$ and Ag-O$_2^-$ over Ag-O$_2^{2-}$. During chemical looping processes, the fraction of oxygen vacancies in the oxygen carrier support changes continuously during each reduction cycle as the material donates oxygen to the reaction, meaning the distribution of selective and non-selective surface species might vary over the course of each reduction step. Hence, to further understand the mechanisms of reactions of oxygen in Ag/SrFeO$_{3-\delta}$ materials during chemical looping, future work should consider whether the trends in desorption of surface species under H$_2$ apply for removal of oxygen by other gases (*e.g.* olefins), and, whether modification of the SrFeO$_{3-\delta}$ support influences the mechanism of reduction and distribution of oxygen surface species.

## 4.5 Conclusions

In this Chapter, the presence of Ag nanoparticles at the surface of particles of $SrFeO_{3-\delta}$ was found to strongly influence the reactive properties of the oxygen carrier during reduction in $H_2$. From *in-situ* XRD experiments, the sample of $Ag/SrFeO_{3-\delta}$ underwent phase transition to brownmillerite $SrFeO_{2.5}$ under 5 vol% $H_2$ at 300°C, as compared to unmodified $SrFeO_{3-\delta}$ which remained in the perovskite phase up to 500°C. Both materials rapidly returned to perovskite form after switching to air at 800°C. From TEM experiments, heating $SrFeO_{3-\delta}$ and $Ag/SrFeO_{3-\delta}$ from room temperature to 700°C, both samples showed a decrease in average oxygen stoichiometry, with reduced regions moving inwards from the edge of the particles. However, for $Ag/SrFeO_{3-\delta}$, localised reduction in the vicinity of nanoparticles of Ag was not observed, suggesting that transport of oxygen within the solid material was relatively rapid as compared to the rate of removal at the surface.

From NAP-XPS measurements during reduction and oxidation, chemisorbed oxygen on $SrFeO_{3-\delta}$ was observed to deplete during a temperature ramp in hydrogen, with the sample of $Ag/SrFeO_{3-\delta}$ showing a more rapid rate of depletion, and, the presence of Ag-$O_x$ surface species. At the highest temperatures investigated (433-439°C), the total content of adsorbed oxygen species on $Ag/SrFeO_{3-\delta}$ was around 47% lower than for $SrFeO_{3-\delta}$, suggesting that reactive Ag-$O_x$ species aided the removal of oxygen by the $H_2$ reducing agent. The Ag-$O_x$ surface species were assigned from Raman spectroscopy and $H_2$-TPR to atomic Ag-O, peroxide Ag-$O_2^{2-}$, and superoxide Ag-$O_2^-$. A mechanism for reduction was proposed by which lattice oxygen from $SrFeO_{3-\delta}$ was transported to the surface of Ag by spillover at the Ag-$SrFeO_{3-\delta}$ interface to form Ag-$O_2^{2-}$ species, which then dissociated to form Ag-O adatoms. However, the role of Ag-$O_2^-$ species during reduction remained unclear.

# Chapter 5

# Structured Ag-$Na_2CO_3$-$SrFeO_{3-\delta}$ materials for chemical looping

This Chapter concerns the synthesis, characterisation, and reactive behaviour of Ag-$Na_2CO_3$-$SrFeO_{3-\delta}$ materials, with chemical looping epoxidation applied as a model selective oxidation reaction.

## 5.1 Introduction

Structured oxygen carriers have been applied for dehydrogenation of alkanes, but have not been investigated extensively for other chemical looping oxidation processes. In this Chapter, chemical looping epoxidation is used as a model reaction to investigate the applicability of protective carbonate layers to prevent over-oxidation. In chemical looping epoxidation of ethylene to form ethylene oxide (EO) over Ag/SFO materials, the selectivity towards EO is limited by combustion of ethylene and EO over the $SrFeO_{3-\delta}$ support (Gabra, 2022; Marek and García-Calvo Conde, 2021). Hence, in this Chapter, structured Ag/$SrFeO_{3-\delta}$ materials were prepared incorporating a protective $Na_2CO_3$ layer using the synthesis method described by Luongo *et al.* (2022), to determine whether the carbonate would aid in preventing over-oxidation of ethylene and EO during chemical looping epoxidation.

Furthermore, in Chapter 4, NAP-XPS and Raman measurements during reduction and oxidation indicated that interactions between Ag and $SrFeO_{3-\delta}$ influenced the transport of lattice oxygen, and that the reduction of Ag/$SrFeO_{3-\delta}$ proceeded *via* formation of reactive $AgO_x$ intermediates. Therefore, this Chapter investigates how the presence of an internal carbonate layer in between the Ag and $SrFeO_{3-\delta}$, or, an

external layer covering the entire surface of the particle, would affect the availability of oxygen and reactive behaviour during chemical looping.

## 5.2 Experimental

A batch of $SrFeO_{3-\delta}$ (SFO) was prepared by ball-milling, drying, and calcination, as described in Section 2.1.1, and seived to 45-180 $\mu$m. Samples of SFO modified with Ag and $Na_2CO_3$ were prepared by incipient wetness impregnation with $AgNO_3$ and $NaNO_3$ as described in Section 2.1.2. Samples of $Ag/SrFeO_{3-\delta}$ and $Na_2CO_3/SrFeO_{3-\delta}$ were prepared (designated Ag/SFO and NCO/SFO respectively). Then, the samples were further impregnated with Na or Ag respectively, to form $Na_2CO_3(Ag/SrFeO_{3-\delta})$, with an external layer of $Na_2CO_3$ covering the nanoparticles of Ag, and $Ag(Na_2CO_3/SrFeO_{3-\delta})$, with Ag nanoparticles on the outside of the $Na_2CO_3$ layer (designated NCO(Ag/SFO) and Ag(NCO/SFO) respectively). The sequences of synthesis steps applied to prepare each sample are summarised in Fig. 5.1.

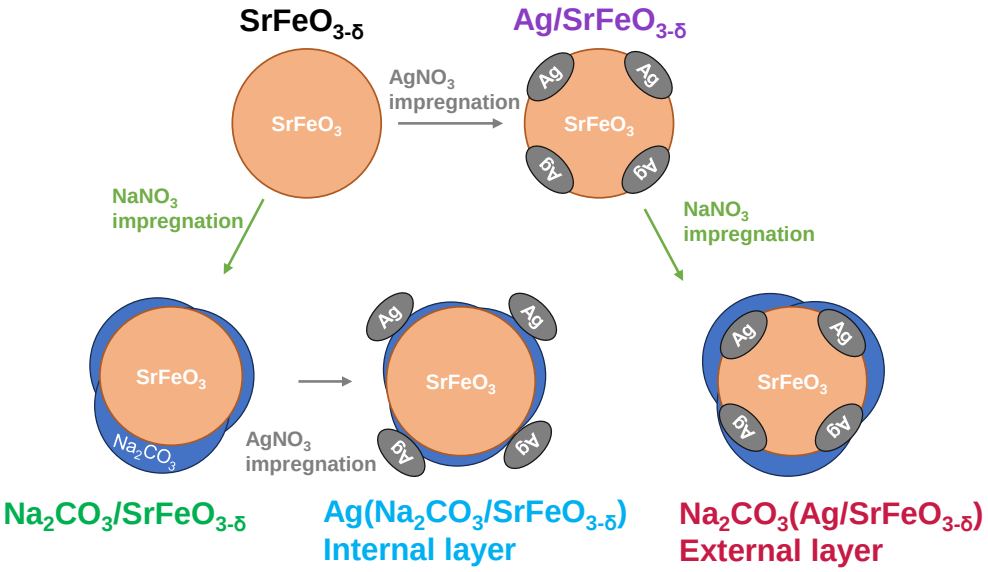


Fig. 5.1 Schematic showing summary of samples prepared by sequential impregnation of SFO with $AgNO_3$ and $NaNO_3$, to form Ag nanoparticles and layers of $Na_2CO_3$ in the final samples. 'Impregnation', refers to addition of a solution of $AgNO_3$ or $NaNO_3$, drying overnight, and calcination at 650-700°C, as described in Section 2.1.2.

A sample of $SrFeO_{3-\delta}$ with $NaNO_3$ impregnated, but not calcined, was also prepared for comparison with NCO/SFO, in order to verify that calcination in ambient air resulted in conversion of nitrate to carbonate. The loading of Ag and Na for each sample was estimated by ICP-AES analysis, as described in Section 2.2.4.

Raman spectra were collected at room temperature using a Horiba Jobin-Yvon LabRAM HR spectrometer, as described in Section 2.2.8. Reference spectra were collected for standards of $NaNO_3$ (Aldrich, 99%), $Na_2CO_3$ (Alfa Aesar, 98%), and $SrCO_3$ (Sigma Aldrich, >98%). Samples of SFO modified with Ag, and, or, $Na_2CO_3$ were compressed into a flat pellet prior to collecting Raman spectra, in order to improve signal quality. Spectra were collected at five points on each pellet and averaged.

X-ray photoelectron spectroscopy (XPS) measurements were collected under high-vacuum using a ThermoFisher Scientific Escalab 250Xi spectrometer, as described in Section 2.2.7, scanning the Na1s, O1s, Ag3d, and C1s binding energy regions. The energy scale was calibrated relative to the peak in the C1s spectrum corresponding to adventitious carbon, at 284.8 eV.

Scanning electron microscopy with energy dispersive X-ray spectroscopy (SEM-EDS) measurements were performed using a Tescan Mira3 FEG-SEM, as described in Section 2.2.6, to characterise the morphology and distribution of elements at the surface of each sample.

X-ray diffraction patterns were collected at ambient temperature using a Malvern Panalytical Empyrean diffractometer, as described in Section 2.2.1, with results shown in Appendix D.1.

Thermogravimetric analysis (TGA) experiments were performed using Mettler Toledo TGA/DSC 1 or TGA/DSC 3+ analysers as described in Section 2.2.2. Prior to all TGA measurements, the sample was heated in air from 50-800°C at 10°C $min^{-1}$, then cooled to 50°C, in order to remove adsorbed surface contaminants from exposure to laboratory air. Two different TGA programs were used. In temperature cycling experiments, the sample was heated from 50°C to 800°C at a heating rate of 10°C $min^{-1}$, with 5 vol% $H_2$ or $N_2$ fed through the reactive gas capillary. Then, the sample was cooled in air to 50°C at 10°C $min^{-1}$, with four cycles of heating and cooling performed for each sample. In isothermal TGA experiments, the sample was heated to a given temperature in the range 300-500°C in air, then, the reactive gas was switched to 5 vol% $H_2$ to reduce the sample for 45 min. The sample was then reoxidised in air for 15 min, with 5 cycles of reduction and oxidation performed at each temperature.

Chemical looping epoxidation experiments were performed in a packed bed reactor, with the experimental arrangement described in Section 2.3.2, and further detail given in Gebers and Marek (2024). A packed bed of 1.80 g of reactive material (45-180 $\mu$m) was assembled inside a stainless steel tube (15 mm I.D.), in between two layers of 4.0 g and 2.0 g SiC (241-559 $\mu$m, Alfa Aesar) above and below the bed respectively. The bed was secured in place in the tube using a plug of glass wool. All gas flows to the reactor were set to 180 mL $min^{-1}$ using calibrated rotameters, giving a space velocity of 9600 $h^{-1}$. The reactor was pre-heated under air flow at 270°C for 2 h prior to experiments, then, chemical looping cycles were performed by switching the feed between 5.4 vol% $C_2H_4$ (balance $N_2$, BOC) and air, with a purge step in nitrogen to prevent mixing between ethylene and air. Five cycles of 1.5 min reduction in $C_2H_4$, 2 min purge in $N_2$, and 15 min oxidation in air were performed for each sample, with additional cycles performed for some materials as described in Section 5.3.3.

Exhaust gas composition from the reactor was monitored using an on-line Fourier Transform Infra-Red gas analyser (FTIR), with concentrations quantified for $C_2H_4$, $CO_2$, ethylene oxide (EO), and water, as described in Section 2.3.2.

Average conversion of $C_2H_4$ over each cycle, $\bar{X}$, average selectivity towards EO, $\bar{S}$, and percentage yield of EO, $\bar{Y}$, were estimated by integrating measurements of outlet gas concentrations, as shown in Eqs. 5.1, 5.2, and 5.3 (Gebers *et al.*, 2022), assuming a constant molar flowrate of gas through the reactor. The term $y_i$ corresponds to the mole fraction of each species in the reactor outlet, $y_{C_2H_4,in}$ corresponds to the mole fraction of $C_2H_4$ in the reactor feed (5.4 vol% for all experiments) and $t_{red}$ corresponds to the duration of each reduction step (1.5 min for all experiments). The integration range, $t_{start} - t_{end}$ was taken between the time point in each cycle when $CO_2$ first exceeded 20 ppm, and when ethylene concentration reached a maximum value. The factor of 0.5 for $CO_2$ was included to account for the complete combustion of one mole of $C_2H_4$ forming two moles of $CO_2$. No other products, including CO, were detected above 20 ppm from FTIR measurements of gas concentrations, and so were omitted from subsequent analysis.

$$\bar{X} = \frac{\int_{t_{start}}^{t_{end}} (y_{EO} + 0.5 y_{CO_2})\, dt}{\int_{t_{start}}^{t_{end}} (y_{C_2H_4} + y_{EO} + 0.5 y_{CO_2})\, dt} \tag{5.1}$$

$$\bar{S} = \frac{\int_{t_{start}}^{t_{end}} (y_{EO})\, dt}{\int_{t_{start}}^{t_{end}} (y_{C_2H_4} + y_{EO} + 0.5 y_{CO_2})\, dt} \tag{5.2}$$

$$\bar{Y} = \bar{X} \times \bar{S} \tag{5.3}$$

The carbon balance for each experiment was determined from Eq. 5.4.

$$C_{bal} = \frac{\int_{t_{start}}^{t_{end}} (y_{C_2H_4} + y_{EO} + 0.5y_{CO_2})\, dt}{y_{C_2H_4} \times t_{red}} \tag{5.4}$$

## 5.3 Results

### 5.3.1 Characterisation of prepared materials

Assuming full conversion of $NaNO_3$ to $Na_2CO_3$, the weight fractions of Ag and $Na_2CO_3$ for each sample were estimated from ICP-AES measurements (shown in Table 5.1). Some deviation from target loadings was observed, with the sample of NCO(Ag/SFO) showing a somewhat higher than expected loading of $Na_2CO_3$. The sample of Ag(NCO/SFO) showed a lower than expected loading of $Na_2CO_3$, with high variance between measurements (in the range 0.43-7.71 wt% $Na_2CO_3$); hence, the value quoted in Table 5.1 represents the average over three repeat measurements, with high associated uncertainty. The variation in measured $Na_2CO_3$ loading from ICP-AES measurements might have been caused by partial dissolution of the internal carbonate layer during impregnation with aqueous $AgNO_3$ solution, as $Na_2CO_3$ is partially soluble in water (Eggeman, 2001). However, the liquid containing redissolved $Na_2CO_3$ during impregnation of NCO/SFO with $AgNO_3$ would be expected to remain within the pores of the solid sample, and therefore the origin of the discrepancy in loading of $Na_2CO_3$ between NCO/SFO and Ag(NCO/SFO) remains somewhat unclear. Hence, although comparisons between Ag/SFO and Ag(NCO/SFO), and Ag/SFO and NCO(Ag/SFO) can be made reliably, direct comparisons between Ag(NCO/SFO) and NCO(Ag/SFO) should be treated with caution, given the large difference in loading of $Na_2CO_3$.

From Raman spectroscopy measurements of $NaNO_3$, $SrCO_3$ and $Na_2CO_3$ standards, shown in Fig. 5.2, characteristic Raman peaks were detected at 1067, 1074, and 1080 $cm^{-1}$ respectively. A shift in peak centre from 1069 $cm^{-1}$ to 1079 $cm^{-1}$ was observed for the sample of SFO impregnated with $NaNO_3$ before and after calcination, in good agreement with the peak positions of the $NaNO_3$ and $Na_2CO_3$ standards. Hence, calcination in static air at 700°C was sufficient to induce decomposition of $NaNO_3$ and reaction with atmospheric $CO_2$ to form $Na_2CO_3$, with no residual $NaNO_3$ detected

Table 5.1 Loadings of $Na_2CO_3$ and Ag, determined from ICP-AES measurements of Na and Ag fraction, assuming all Na was present as $Na_2CO_3$. The values reported for $Na_2CO_3$ and Ag content in Ag(NCO/SFO) represent the average values over three measurements, with the range given in parentheses.

| Sample | Abbreviation | $Na_2CO_3$ (wt%) | Ag (wt%) |
|---|---|---|---|
| $Ag/SrFeO_{3-\delta}$ | Ag/SFO | 0.00 | 10.7 |
| $Na_2CO_3/SrFeO_{3-\delta}$ | NCO/SFO | 9.54 | 0.00 |
| $Ag(Na_2CO_3/SrFeO_{3-\delta})$ | Ag(NCO/SFO) | 2.93 *(0.43-7.71)* | 9.69 *(8.84-10.31)* |
| $Na_2CO_3(Ag/SrFeO_{3-\delta})$ | NCO(Ag/SFO) | 14.1 | 10.0 |

after calcination. For Ag(NCO/SFO) and NCO(Ag/SFO), clear peaks corresponding to $Na_2CO_3$ were detected, indicating that full conversion of $NaNO_3$ was achieved for both samples, despite the low total loading of $Na_2CO_3$ on Ag(NCO/SFO) detected from ICP-AES measurements. No Raman bands in the region 1060-1080 $cm^{-1}$ corresponding to nitrate or carbonate species were observed for the sample of Ag/SFO, as expected.

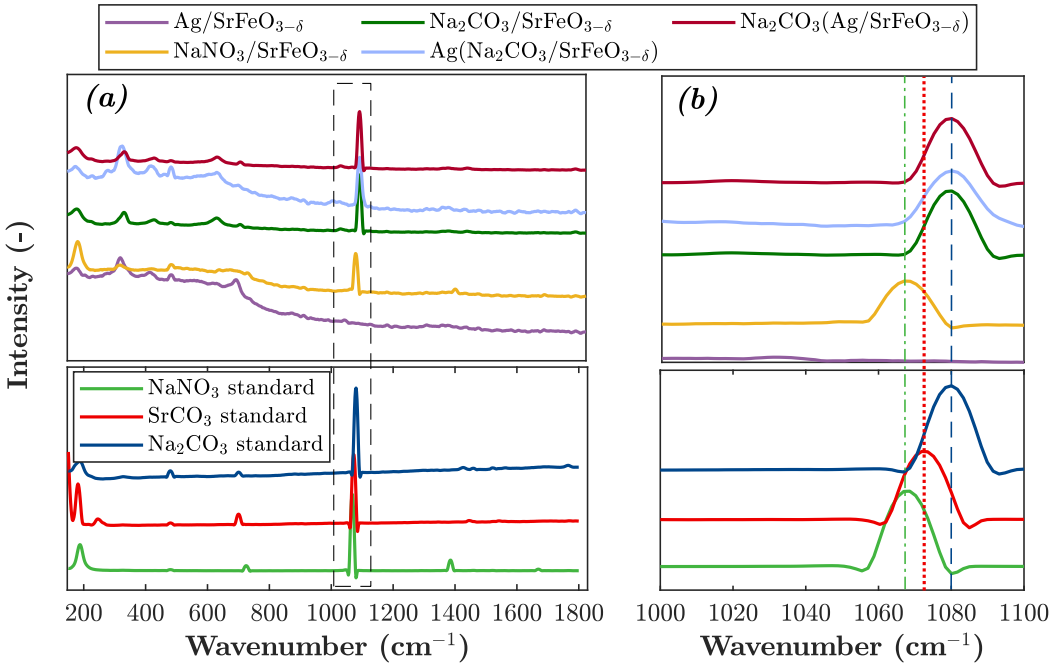


Fig. 5.2 Raman spectra **(a)** showing shift in peak following conversion of $NaNO_3$ to $Na_2CO_3$ after calcination in air, with zoomed-in section in dashed box shown in **(b)**. Vertical lines between peaks added to guide the eye.

X-ray diffraction measurements (reported in Appendix D, Fig. D.1) for the prepared materials showed the presence of the $SrFeO_{3-\delta}$ and Ag phases, with minimal $SrCO_3$ or other impurities. Hence, the addition of the $Na_2CO_3$ layer did not alter the phase

structure of the strontium ferrite support, as a change from, for example, perovskite to Ruddlesden-Popper, would alter the reactive properties of the material (Gabra *et al.*, 2021). Furthermore, carbonation of the $SrFeO_{3-\delta}$ did not occur during material preparation, as an increase in strontium carbonate content might have decreased the reactivity of the SFO-based material (Marek and García-Calvo Conde, 2021). However, diffraction peaks corresponding to crystalline $Na_2CO_3$ showed very low intensity, suggesting a largely amorphous carbonate phase.

From XPS measurements (with fitting constraints and peak assignments given in Appendix D,Table D.1), all samples impregnated with $NaNO_3$ (NCO/SFO, Ag(NCO/SFO) and NCO(Ag/SFO)) showed an appreciable signal in the Na1s region of binding energies, shown in Fig. 5.3a. The measured Na1s peak intensity was approximately 78% lower for Ag(NCO/SFO) than for NCO/SFO, as expected from the lower loading of $Na_2CO_3$ detected from ICP-AES analysis.

All three samples showed a major peak at 1071.6-1071.7 eV, corresponding to a majority of Na being present as $Na_2CO_3$ (Hammond *et al.*, 1981), and a shallow, broad peak centred at 1072.8-1073.0 eV, assigned to residual sodium oxide formed during synthesis (Barrie and Street, 1975; Savintsev *et al.*, 2016), and hydroxide surface impurities from exposure to moisture in laboratory air (Citrin, 1973). The XPS measurements of the Ag3d region for samples impregnated with Ag, shown in Appendix D, Fig. D.2a, confirmed the presence of metallic Ag for all samples, with the main $Ag3d_{5/2}$ peak at 368.3-368.7 eV (Seah *et al.*, 1998).

From measurements of the O1s binding energy region, shown in Fig. 5.3b, four peaks corresponding to oxygen species were detected at binding energy values of approximately 528.5, 529.7, 531.5, and 533.6 eV, assigned respectively to lattice oxygen in bulk $SrFeO_{3-\delta}$, lattice oxygen in the SrO surface termination layer, carbonates and surface O and Ag-$O_x$ species, and hydroxide impurities (Barrie and Street, 1975). Surface carbonate species were confirmed to be present on all samples from measurements of the C1s region, shown in Fig. D.2b.

The presence of carbonate species on Ag/SFO, detected from the O1s and C1s spectra, suggested contamination of the surface from contact with laboratory air during handling. Carbonation of the bulk solids in Ag/SFO to form strontium carbonate was ruled out from XRD and Raman measurements, where no $SrCO_3$ peaks were detected. Broad overlap between the binding energy regions expected for oxygen in carbonate species meant that sodium carbonate could not be distinguished reliably from surface oxygen on $SrFeO_{3-\delta}$ and Ag, as previously discussed in Sections 4.3.2 and

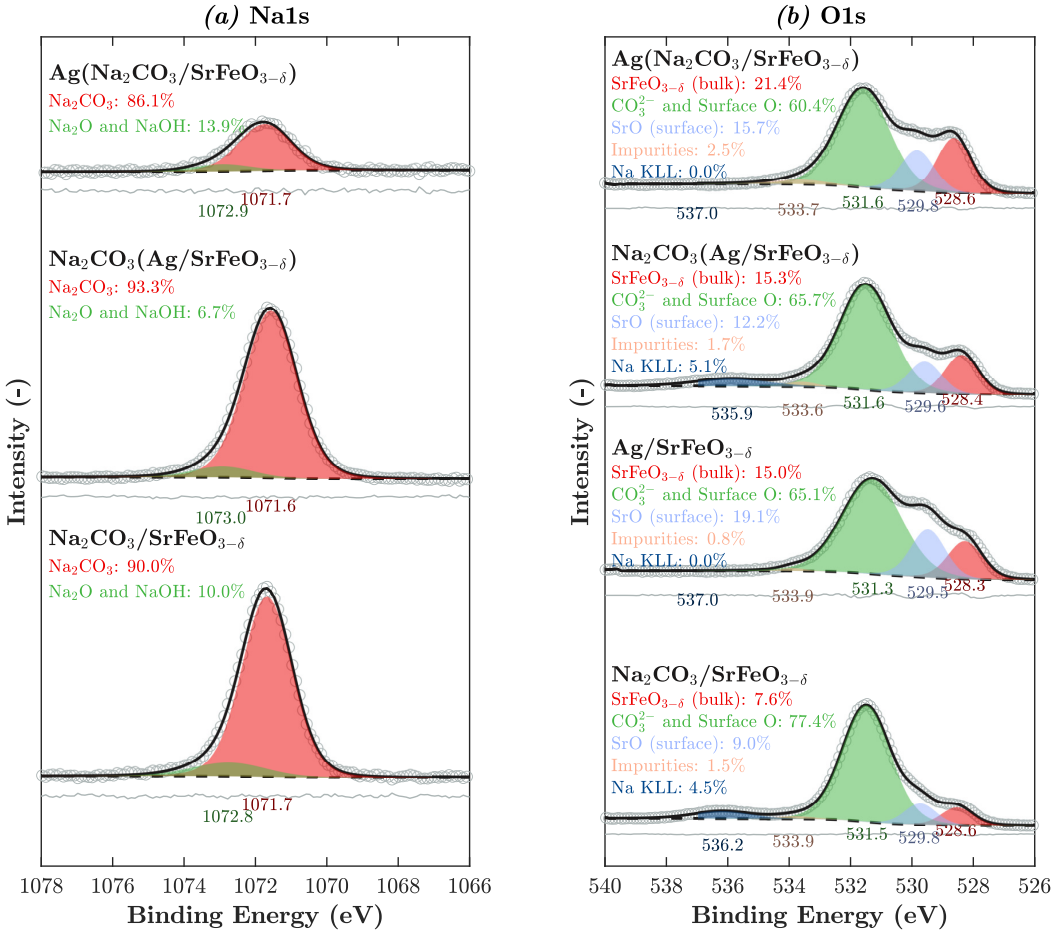


Fig. 5.3 XPS spectra corresponding the **(a)** Na1s and **(b)** O1s and Na KLL binding energy regions. Circles indicate normalised experimental measurements, solid black lines indicate overall fitted curve, shaded areas correspond to individual fitted peaks, dashed lines correspond to fitted baseline, and grey solid lines correspond to difference between fitted curve and measurements. Percentage areas estimated for each peak are given, corresponding to the approximate proportion (at%) of each species at the surface.

4.4.2. For the samples of NCO/SFO and NCO(Ag/SFO), a weak, broad peak centred at 535.9-536.2 eV was detected, corresponding to Na KLL Auger electrons (Shchukarev and Korolkov, 2004).

From SEM-EDS maps shown in Fig. 5.4, Na was found to be approximately uniformly distributed over the surface of NCO/SFO, NCO(Ag/SFO) and Ag(NCO/SFO), overlapping with the Ag signal for samples containing both Ag and $Na_2CO_3$. Given the lower loading of $Na_2CO_3$ achieved on the sample of Ag(NCO/SFO), the signal intensity for Na was substantially lower than for the other samples, and so a longer scan time (*c.* 5 min, as opposed to *c.* 1 min for the other samples) was applied to collect the EDS map. No Na was detected by SEM-EDS on the sample of Ag/SFO.

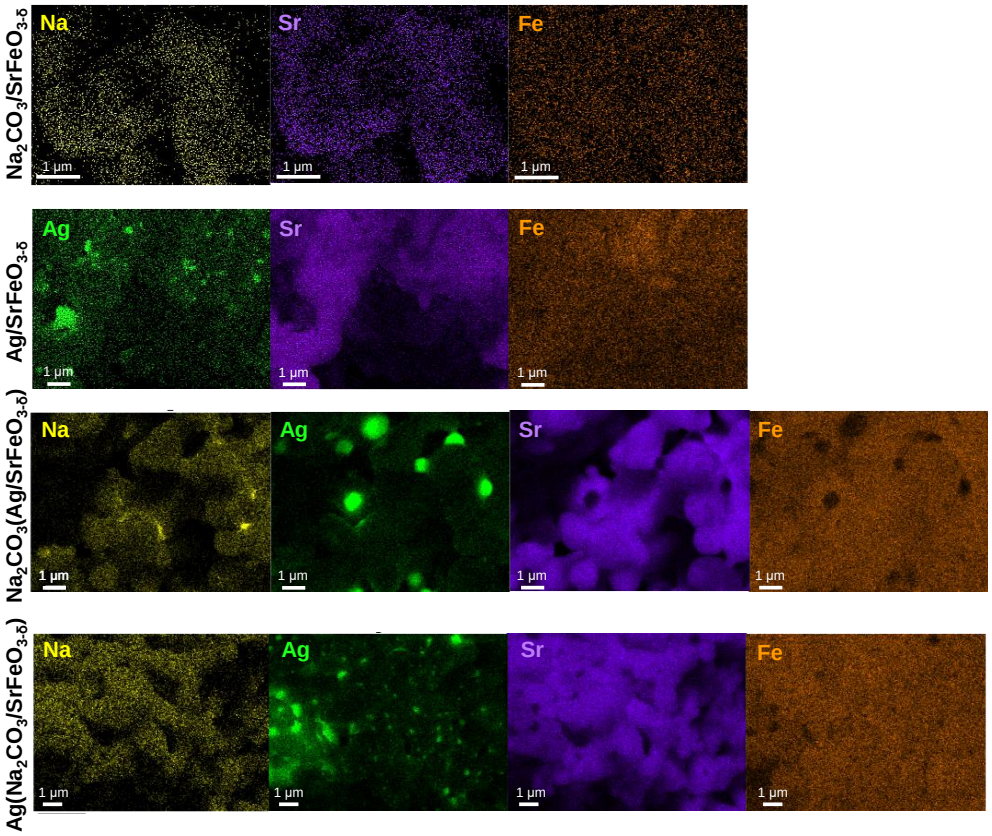


Fig. 5.4 EDS maps showing distribution of Na, Ag, Sr and Fe on NCO/SFO, Ag/SFO, NCO(Ag/SFO) and Ag(NCO/SFO).

From SEM images, shown in Fig. 5.5, nanoparticles of Ag were visible on the surface of Ag/SFO and Ag(NCO/SFO), but were not readily visible on NCO(Ag/SFO) despite being present in the EDS map, confirming that the Ag particles were covered by the layer of $Na_2CO_3$. For Ag(NCO/SFO), some regions of the sample showed elongated

particles of Ag (shown in Fig. 5.5c.i), and other regions showed approximately spherical particles (shown in Fig. 5.5c.ii). The overall size distributions of particles of Ag deposited on Ag/SFO and Ag(NCO/SFO) were approximately equal, with a Sauter mean diameter of 77.8-80.0 nm, within one standard deviation of the materials prepared and characterised in Chapters 3 and 6.

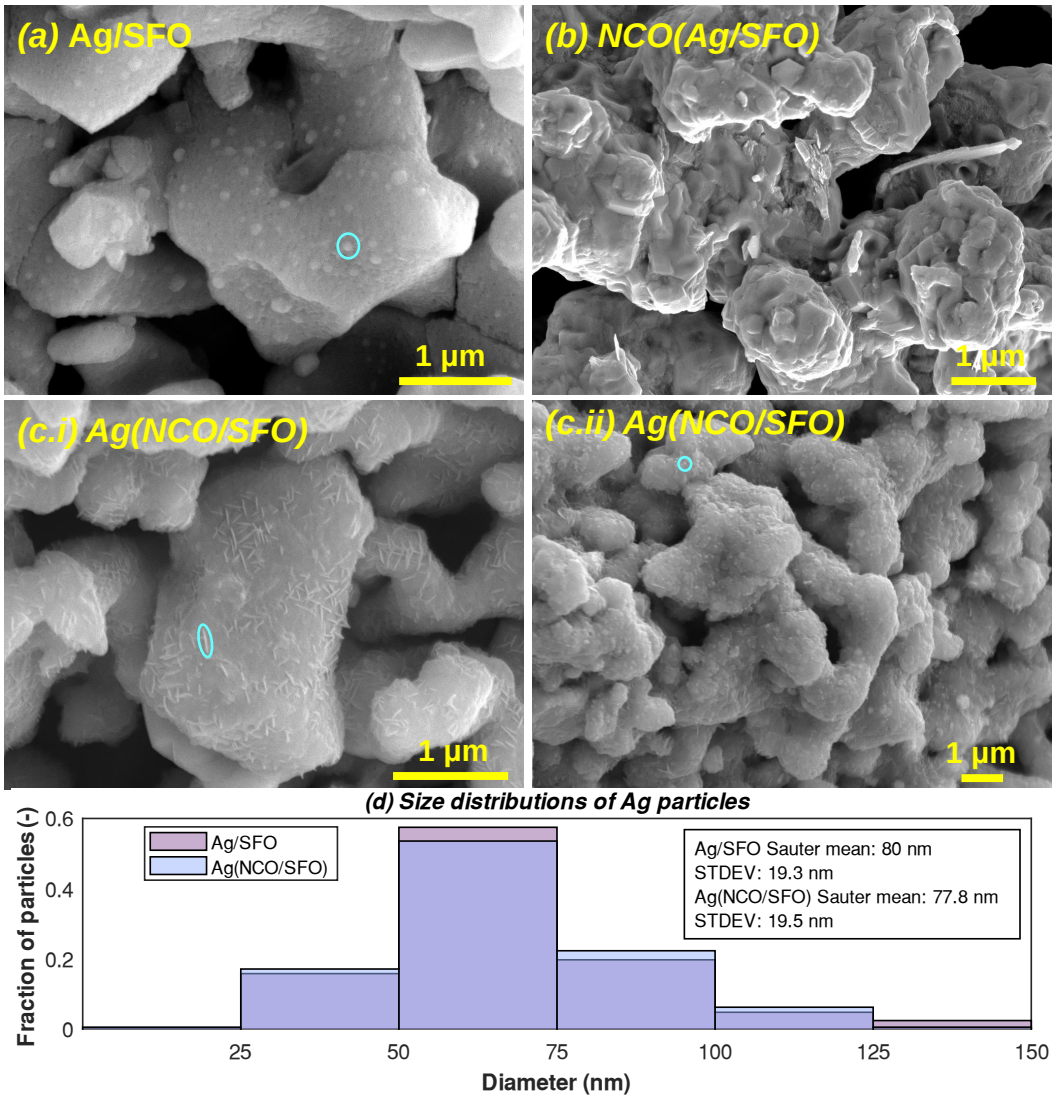


Fig. 5.5 SEM images of **(a)** Ag/SFO, **(b)** NCO(Ag/SFO), and **(c.i and ii)** Ag(NCO/SFO), with particles of Ag circled in blue, and **(d)** measured particle size distributions for Ag on Ag/SFO and Ag(NCO/SFO)

From the SEM-EDS images, the layer of $Na_2CO_3$ was assumed to cover the entire surface of the sample of Ag(NCO/SFO) and NCO(Ag/SFO), in line with previous studies (Luongo *et al.*, 2022). However, future work could estimate the true surface

coverage of $Na_2CO_3$, and hence, the fraction of exposed $SrFeO_{3-\delta}$, by exposing the samples to a probe molecule able to preferentially adsorb to $SrFeO_{3-\delta}$, but not $Na_2CO_3$ (or *vice-versa*), and measuring the difference in quantity adsorbed between Ag/SFO, Ag(NCO/SFO) and NCO(Ag/SFO).

### 5.3.2 Thermogravimetric analysis

From temperature ramping experiments in the TGA under reducing atmospheres between 50-800°C, shown in Fig. 5.6, differences in the minimum temperature required for reaction ($T_{onset}$) were observed between samples.

For both reducing gases (5 vol% $H_2$ in $N_2$, and pure $N_2$), samples showed $T_{onset}$ values in the order Ag/SFO < Ag(NCO/SFO) < NCO(Ag/SFO) < SFO ≈ NCO/SFO, with lower values of $T_{onset}$ indicating greater availability of oxygen. The differences between samples were markedly greater under stronger reducing conditions in 5 vol% $H_2$, with an overall range of 160°C between the $T_{onset}$ values of SFO and Ag/SFO, whereas, during reduction under $N_2$, the total range of $T_{onset}$ values was around 60°C. In particular, under reduction in $N_2$, all samples apart from Ag/SFO showed $T_{onset}$ values within 10°C of one another, whereas, under 5 vol% $H_2$, the trend in $T_{onset}$ values was more apparent, with differences of at least 20°C between all samples. The values of $T_{onset}$ in $N_2$ for SFO and Ag/SFO were in reasonable agreement with the equivalent measurements reported in Fig. 3.9, with differences ascribed to batch-to-batch variability between samples.

During reduction in 5 vol% $H_2$ up to 800°C, the samples containing $Na_2CO_3$ showed a permanent mass loss between cycles, with the samples losing approximately 2.5wt% of their initial mass after four redox cycles. A pure sample of $Na_2CO_3$ heated in the TGA under 5 vol% $H_2$, or $N_2$, up to 900°C at 10°C $min^{-1}$, started to lose mass at around 840°C, losing *c.* 8wt% mass over the course of one temperature ramp cycle (shown in Fig. 5.7), with little difference between decomposition in $H_2$ or $N_2$. However, samples of NCO/SFO showed a permanent mass loss during TGA cycling up to 800°C in 5 vol% $H_2$, but did not show a permanent loss during ramping experiments with $N_2$ as the reducing gas. Hence, contact between sodium carbonate and iron in $SrFeO_{3-\delta}$ might have increased the rate of decomposition of $Na_2CO_3$ at lower temperatures, by catalysing the reaction between $Na_2CO_3$ and $H_2$ to form $Na_2O$, $H_2O$, and CO or $CH_4$ (Lux *et al.*, 2018).

The trend in reactivity between samples with respect to $H_2$ was confirmed by isothermal TGA measurements, shown in Fig. 5.8, where each sample was held at a

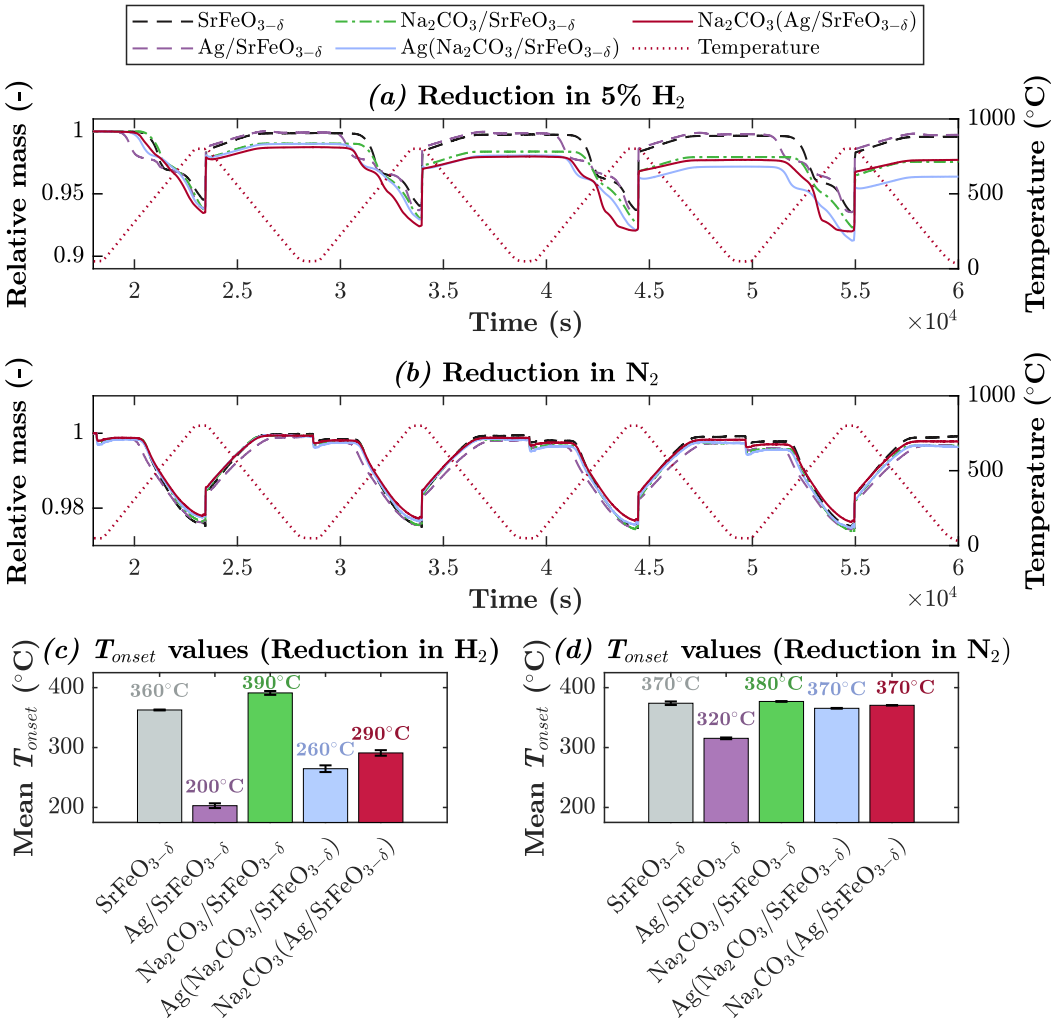


Fig. 5.6 Mass changes during temperature ramping from 50-800°C with reduction in **(a)** 5% $H_2$ in $N_2$ and **(b)** $N_2$, and oxidation in air, **(c)** $T_{onset}$ values during reduction in $H_2$ and **(d)** in $N_2$. Error bars in **(c)** and **(d)** correspond to standard deviation over 4 cycles. $T_{onset}$ was defined as the temperature at which the maximum change in rate of mass loss with respect to time occurred, identified as described in Section 2.2.2.

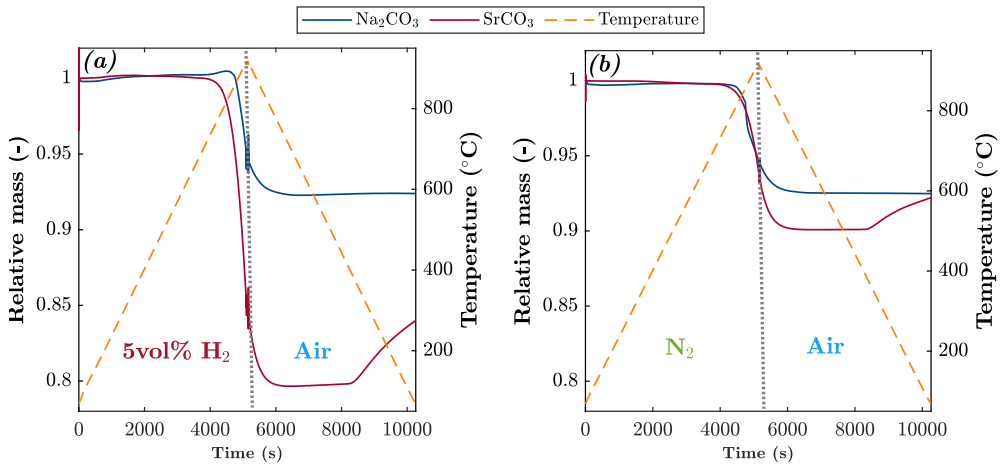


Fig. 5.7 Decomposition of pure $Na_2CO_3$ and $SrCO_3$ during temperature ramping in the TGA from 50-900°C at 10°C $min^{-1}$, with reactive gases **(a)** 5 vol% $H_2$ and **(b)** $N_2$ during heating, and air during cooling. The decomposition behaviour of $SrCO_3$, showing a greater mass loss under 5% $H_2$ than under pure $N_2$, was in good agreement with Reller *et al.* (1991).

temperature between 300-500°C, and subjected to three chemical looping cycles of 45 min reduction in 5 vol% $H_2$, followed by 15 min oxidation in air.

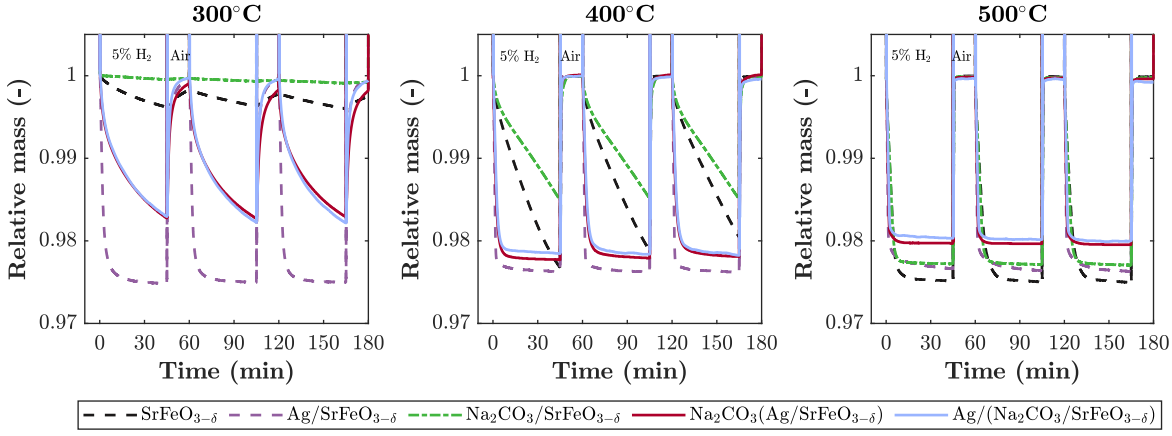


Fig. 5.8 Isothermal reduction and oxidation of Ag-$Na_2CO_3$-$SrFeO_{3-\delta}$ materials in $H_2$ at 300-500°C, showing changes in sample mass

At 300°C, Ag/SFO reduced rapidly, reaching a stable mass within *c.* 20 min, whereas SFO lost mass slowly, and NCO/SFO did not show any mass change. The mixed samples of Ag(NCO/SFO) and NCO(Ag/SFO) showed almost identical reduction patterns to one another, with intermediate rate of mass change between unmodified SFO, and Ag/SFO. Hence, the intermediate rate of reaction supports the finding from Fig. 5.6 that the presence of $Na_2CO_3$ in mixed Ag-$Na_2CO_3$ samples partially inhibited

the enhancement to oxygen availability from interactions between Ag and $SrFeO_{3-\delta}$, while allowing some improvement in reactivity as compared to bare SFO.

Reduction at 400°C showed a similar trend, as Ag/SFO, Ag(NCO/SFO) and NCO(Ag/SFO) all reduced rapidly, reaching a stable mass within *c.* 10 min, whereas SFO and NCO/SFO lost mass more slowly, indicating the enhancement to oxygen availability from the presence of Ag with or without $Na_2CO_3$. Over the course of 45 min of reduction, SFO reached approximately the same final mass as the samples containing Ag, whereas, the sample of NCO/SFO showed a total mass change that was approximately 35% lower, suggesting that the presence of $Na_2CO_3$ at the surface of SFO actively inhibited reaction.

At 500°C, all materials reduced rapidly and reached a stable mass within 10 min, with minimal difference observable between samples. No permanent mass loss was observed from isothermal cycling up to 500°, with all samples returning to their original mass after 15 min oxidation in air.

During isothermal reduction in 5 vol% $H_2$, little difference in reactive behaviour was observed between Ag(NCO/SFO) and NCO(Ag/SFO), despite the considerable difference in $Na_2CO_3$ loading detected from ICP-AES measurements. However, marked differences between the samples were observed during isothermal TGA experiments where the reducing gas was changed to 5.4 vol% ethylene, shown in Fig. 5.9.

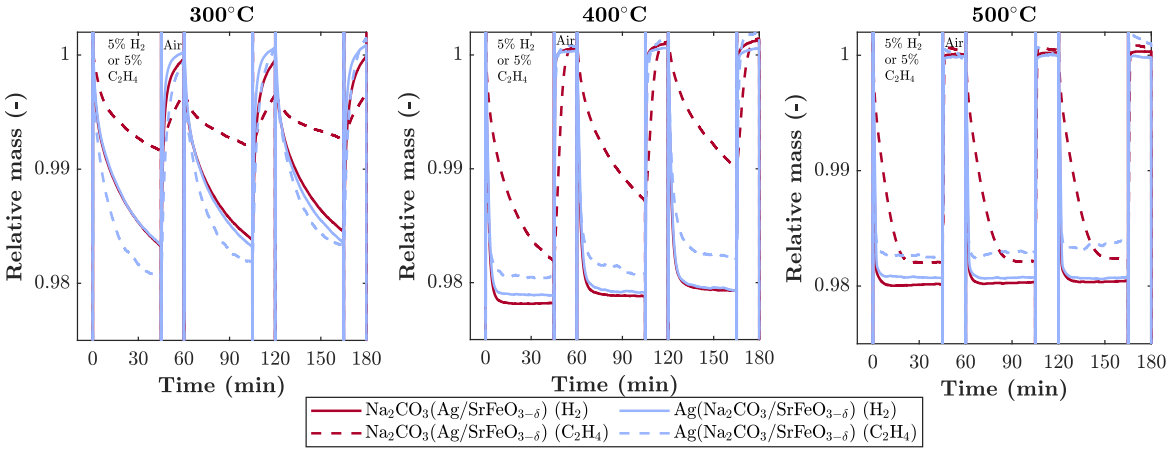


Fig. 5.9 Comparison between NCO(Ag/SFO) and Ag(NCO/SFO) during isothermal reduction in 5 vol% $H_2$ (solid lines) and 5 vol% $C_2H_4$ (dashed lines), both balance $N_2$, with re-oxidation in air.

At all temperatures during reduction in $C_2H_4$, Ag(NCO/SFO) lost mass more rapidly than NCO(Ag/SFO), reaching a greater extent of overall reduction at 300°C and 400°C, and reaching a steady state more rapidly at 500°C. For NCO(Ag/SFO),

reduction in $C_2H_4$ was substantially slower at all temperatures than reduction in $H_2$, whereas, for Ag(NCO/SFO), rate of reduction in ethylene was approximately equal to or slightly faster than reduction in hydrogen. Therefore, the differences in reactive behaviour with $H_2$ and $C_2H_4$ indicate that the location of the $Na_2CO_3$ layer within the sample altered the reaction mechanism between the reducing gas and the Ag-$Na_2CO_3$-$SrFeO_{3-\delta}$, with exposed Ag sites necessary for rapid reaction in $C_2H_4$, discussed in further detail in Section 5.4.

### 5.3.3 Performance in chemical looping epoxidation

The concentrations of EO, $CO_2$, and $H_2O$ in the exhaust stream from the packed bed reactor during chemical looping epoxidation experiments at 270°C are shown in Fig. 5.10, with peaks corresponding to production of products during the 1.5 min reduction steps in $C_2H_4$. All measurements showed an average carbon balance within 100 ± 10%.

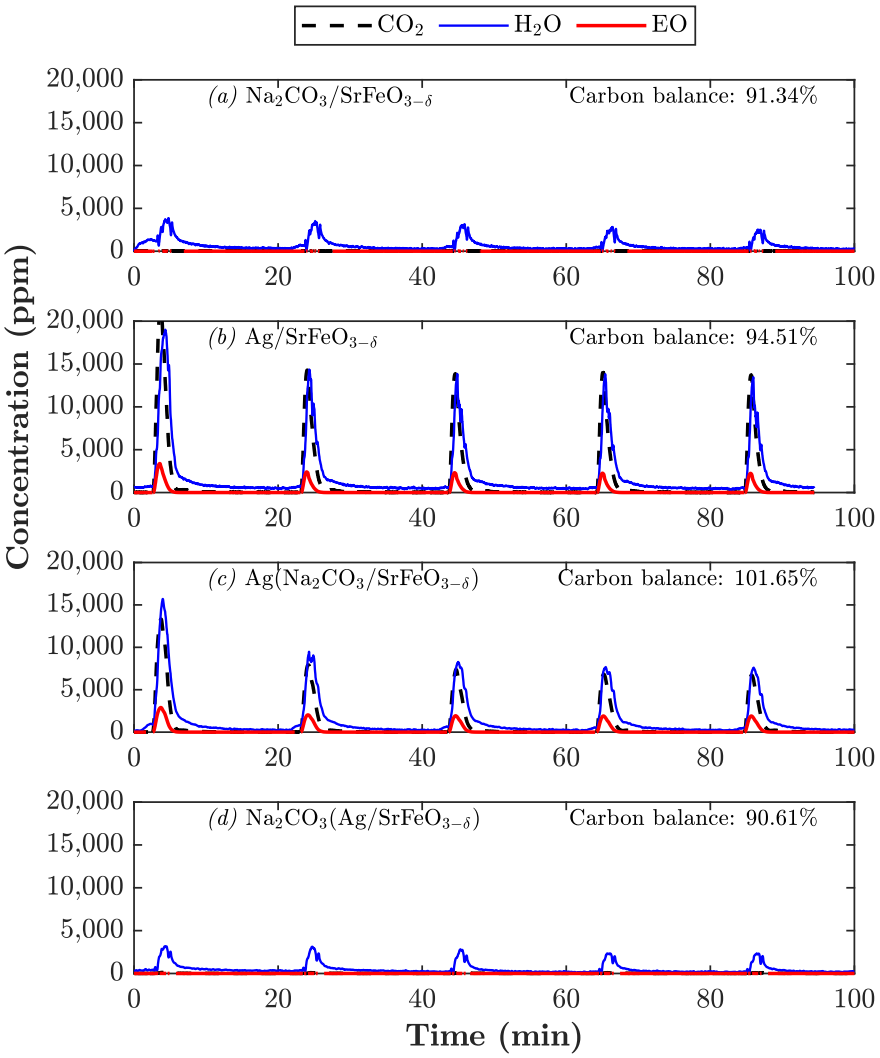


Fig. 5.10 Concentrations of reaction products measured by the FTIR during five cycles of chemical looping epoxidation at 270°C over 1.80 g of: **(a)** NCO/SFO, **(b)** Ag/SFO, **(c)** Ag(NCO/SFO), and **(d)** NCO(Ag/SFO). EO = ethylene oxide.

For NCO/SFO, shown in Fig. 5.10a, no appreciable concentration of EO or $CO_2$ was detected (the low peaks corresponding to $H_2O$ were attributed to residual cross-sensitivity of the FTIR instrument between water and unreacted ethylene). For Ag/SFO

and Ag(NCO/SFO), shown in Figs. 5.10b and 5.10c respectively, the $C_2H_4$ reacted to form EO and $CO_2$. The average peak concentration of EO over Ag/SFO was 2510 ppm over the 5 cycles, in good agreement with the concentration of *c.* 2500 ppm EO achieved by Marek and García-Calvo Conde (2021) for a sample prepared under equivalent conditions. The sample of Ag(NCO/SFO) showed slightly lower peak concentrations of 2130 ppm EO; however, approximately 53% less $CO_2$ was produced (6730 ppm vs 14300 ppm for Ag/SFO for the second and subsequent cycles), resulting in higher selectivity of 36% as compared to 23% for Ag/SFO.

For NCO(Ag/SFO), no carbon-containing reaction products were detected at 270°C, indicating minimal reaction of ethylene. To determine whether higher temperatures would be sufficient to allow for reaction of $C_2H_4$ over NCO(Ag/SFO), two further chemical looping cycles were performed at 300°C and 350°C, shown in Fig. D.3. No EO was detected at either temperature, however, at 300°C and 350°C, peak concentrations of 209 and 725 ppm $CO_2$ respectively were observed. Furthermore, the overall carbon balance was substantially lower than for all measurements at 270°C (78.6% *vs* 90.6-101.7%), suggesting deposition of carbon from $C_2H_4$ as a result of coking. Hence, the results agreed with the TGA measurements reported in Fig. 5.9, indicating that an exposed Ag surface (present in Ag/SFO and Ag(NCO/SFO) but absent in NCO/SFO and NCO(Ag/SFO)) was necessary for reaction with $C_2H_4$ at 270°C, and for formation of EO.

The selectivity towards EO, conversion of $C_2H_4$, and overall percentage yield of EO (calculated using Eqs. 5.1, 5.2, and 5.3) are shown in Fig. 5.11.

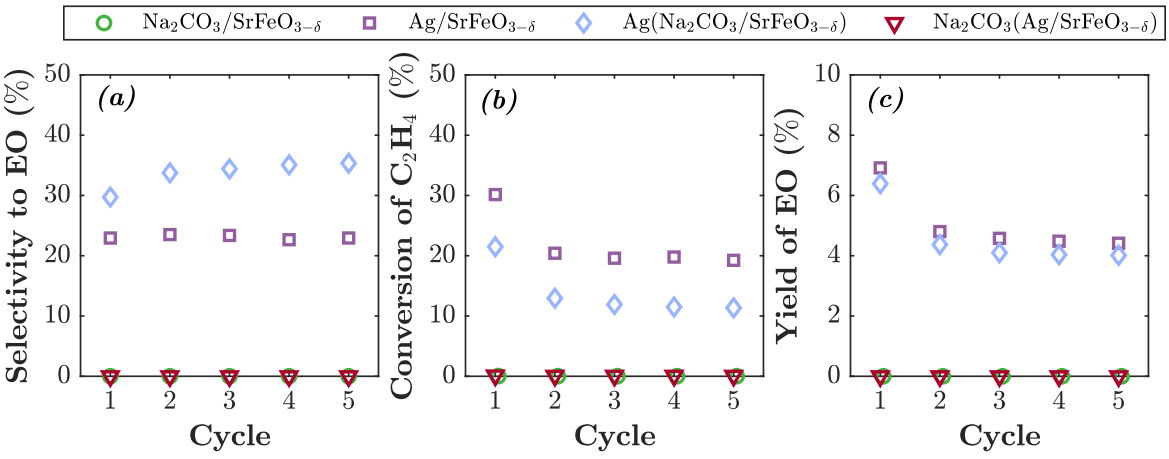


Fig. 5.11 Comparison of **(a)** selectivity towards EO, **(b)** conversion of $C_2H_4$, and **(c)** yield of ethylene oxide during chemical looping epoxidation over 5 redox cycles.

For NCO/SFO and NCO(Ag/SFO), no appreciable conversion of $C_2H_4$ was detected, and hence selectivity and yield were zero for all cycles. For Ag/SFO, the material showed stable selectivity towards EO of 23.1 ± 0.3%, whereas for Ag(NCO/SFO), selectivity gradually increased over successive cycles, stabilising at approximately 36.0% after the ninth cycle (shown in Fig. 5.12).

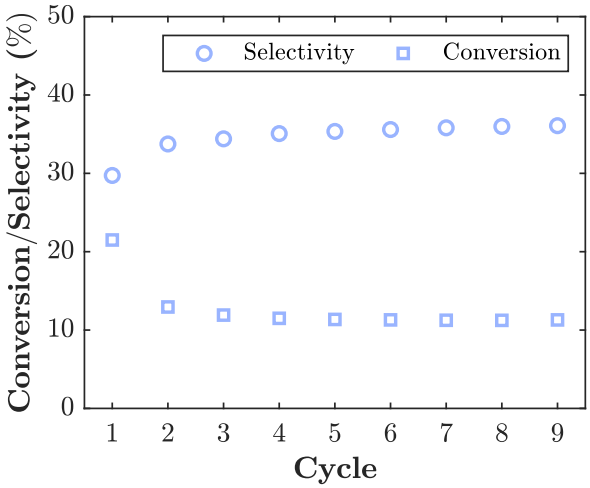


Fig. 5.12 Conversion of ethylene and selectivity towards EO over 9 cycles of chemical looping for Ag(NCO/SFO).

For both Ag/SFO and Ag(NCO/SFO), conversion dropped between the first and second cycle, then remained approximately stable for all successive cycles, in line with previous studies of chemical looping epoxidation over Ag/SFO (Damba *et al.*, 2024; Gebers *et al.*, 2022; Marek and García-Calvo Conde, 2021). For all cycles, the selectivity towards EO was higher for Ag(NCO/SFO) than Ag/SFO, whereas, the conversion of $C_2H_4$ was higher for Ag/SFO than Ag(NCO/SFO). Overall yield was similar for both samples, at approximately 4.3 ± 0.3% for the second and subsequent cycles, indicating that differences in conversion and selectivity approximately cancelled out. Assuming equal availability of oxygen from the strontium ferrite core (*i.e.* assuming equal initial oxygen stoichiometry of the $SrFeO_{3-\delta}$ for all samples, and neglecting the presence of any impurity phases, as discussed in Chapter 2, Section 2.1.1), a greater proportion of available oxygen from Ag(NCO/SFO) reacted with ethylene to form EO rather than $CO_2$, with less oxygen reacting overall as compared to Ag/SFO. Hence, the layer of $Na_2CO_3$ selectively inhibited complete combustion of ethylene, without substantially decreasing the amount of oxygen available for selective oxidation to form EO, with potential mechanisms discussed in Section 5.4.

## 5.4 Discussion

The TGA measurements reported in this Chapter (shown in Figs. 5.6 and 5.8) were in good agreement with the findings in Chapter 3, where the presence of Ag decreased the temperature required for reduction of $SrFeO_{3-\delta}$, and the improvement in oxygen availability was greater in the case of reaction between oxygen and an active reducing gas (5 vol% $H_2$), as opposed to oxygen uncoupling into an inert atmosphere ($N_2$). Furthermore, addition of $Na_2CO_3$ showed no enhancement in oxygen availability for SFO in the absence of Ag, and, partially inhibited the improvement from Ag in mixed samples. The external layer of $Na_2CO_3$ in the sample of NCO(Ag/SFO) showed a slightly greater degree of inhibition (*i.e.* a smaller decrease in $T_{onset}$ with respect to unmodified SFO) than the internal layer in Ag(NCO/SFO), however, the difference might be attributable to the large variation in estimated loading of $Na_2CO_3$ between the two samples.

Moreover, little difference in $T_{onset}$ between reduction in $H_2$ and $N_2$ was observed for SFO and NCO/SFO, suggesting that in the absence of an Ag catalyst to mediate reactions between $H_2$ and Ag-$O_x$ species, uncoupling of $O_2$ molecules was the primary mechanism of oxygen release.

Comparison between reduction of NCO(Ag/SFO) and Ag(NCO/SFO) in $H_2$ and $C_2H_4$, shown in Fig. 5.9, suggested two distinct mechanisms of reduction. At all temperatures investigated over the range 300-500°C, rate of reaction in $H_2$ was approximately equal for Ag(NCO/SFO) and NCO(Ag/SFO), whereas, during reduction in $C_2H_4$, rates of reaction were substantially slower for NCO(Ag/SFO) than for Ag(NCO/SFO). Luongo *et al.* (2022) established that for $Na_2CO_3/Sr_{0.8}Ca_{0.2}FeO_{3-\delta}$ materials prepared using a similar method to the NCO/SFO material used in this Chapter, the $Na_2CO_3$ layer was impermeable to $C_2H_6$ and $C_2H_4$ gases during oxidative dehydrogenation of ethane, while allowing transport of $O_2$ from the perovskite core to the surface of the carbonate layer. Furthermore, in Chapter 4, the reaction of reducing gases with Ag-$O_x$ intermediate species was determined to substantially enhance the rate of reduction of Ag/SFO.

Hence, the observed reactive behaviour in $H_2$ and $C_2H_4$ can be explained by the differing abilities of the reducing gases to penetrate the $Na_2CO_3$, with respect to the relative positions of the Ag particles. For reduction of Ag(NCO/SFO) in $H_2$, oxygen can diffuse through the carbonate layer to form Ag-$O_x$ species, which would then be able to react rapidly with $H_2$, in a similar matter to reduction of Ag/SFO (shown in

Fig. 5.13a). Similarly, during reaction of NCO(Ag/SFO) in hydrogen, $H_2$ molecules can diffuse into the $Na_2CO_3$ (Deng *et al.*, 2022; Reller *et al.*, 1991), allowing reaction at the particles of Ag underneath the carbonate layer (shown in Fig. 5.13b).

Contrastingly, during reduction in ethylene, $C_2H_4$ can readily react with oxygen at the surface of Ag on Ag(NCO/SFO) (Fig. 5.13c), but would not be able to diffuse into the $Na_2CO_3$ layer in NCO(Ag/SFO) to access the Ag sites, resulting in slow reaction (Fig. 5.13d).

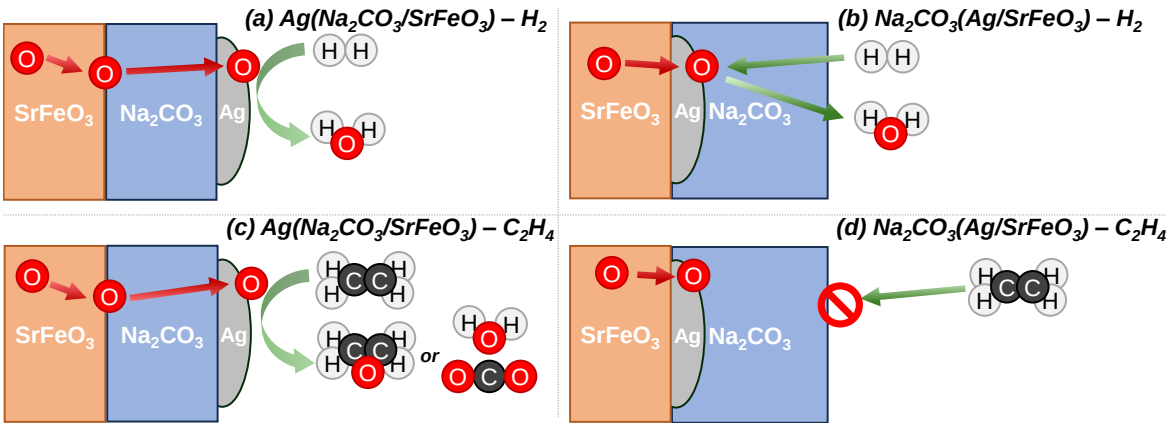


Fig. 5.13 Proposed reaction mechanisms of Ag(NCO/SFO) and NCO(Ag/SFO) with **(a,b)** $H_2$ and **(c,d)** $C_2H_4$ during isothermal gas cycling in the TGA, with diffusion of $H_2$ and O species, but not $C_2H_4$, through the carbonate layer.

The differences in reactivity with $C_2H_4$ between Ag(NCO/SFO) and NCO(Ag/SFO) were reinforced by observations from packed bed experiments, reported in Figs. 5.10 and 5.11. During chemical looping cycles, Ag(NCO/SFO) showed around 14% conversion of ethylene to EO and $CO_2$ at 270°C, whereas NCO(Ag/SFO) showed little to no formation of EO or $CO_2$ at 270°C. At higher temperatures, 300°C and 350°C, shown in Fig. D.3, some combustion of $C_2H_4$ was observed over NCO(Ag/SFO), but with no EO formation, confirming that access of ethylene to exposed Ag sites was necessary to form EO.

For the sample of Ag(NCO/SFO), improved selectivity towards EO was achieved as compared to Ag/SFO, indicating that the presence of the carbonate layer might have inhibited non-selective oxidation pathways. During oxidation of $C_2H_4$ over Ag/SFO, a small fraction of $C_2H_4$ reacts directly with the SFO support to form $CO_2$ and $H_2O$ (Marek and García-Calvo Conde, 2021), and, some of the EO formed by selective oxidation is over-oxidised to $CO_2$ and $H_2O$ (Gabra, 2022). For the Ag(NCO/SFO) material, access to the $SrFeO_{3-\delta}$ surface by $C_2H_4$ and EO might have been blocked

by the layer of $Na_2CO_3$, preventing direct reaction, thereby inhibiting the extent of non-selective oxidation (shown in Fig. 5.14). As the concentration of EO produced only slightly decreased between reaction over Ag/SFO and Ag(NCO/SFO), the carbonate layer might have primarily inhibited the non-selective reaction pathways, with limited decrease to the extent of selective oxidation to form EO. Therefore, future mechanistic studies could also measure the relative rates of diffusion of oxygen, hydrogen, ethylene, and EO through $Na_2CO_3$, in order to verify whether the mechanisms of $Na_2CO_3$ inhibiting complete combustion proposed in Figs. 5.13 and 5.14 are feasible.

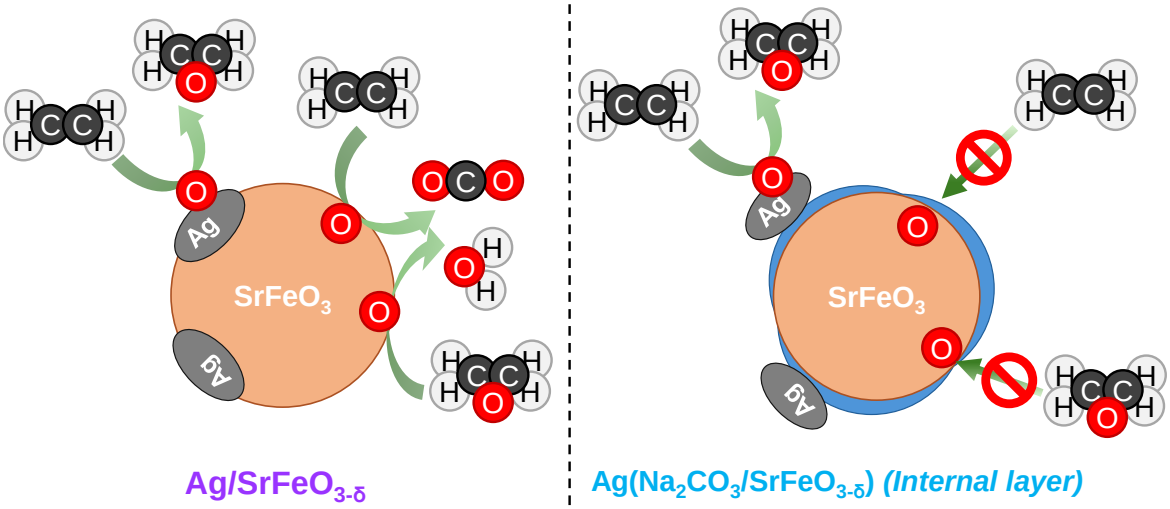


Fig. 5.14 Proposed reaction mechanisms of $C_2H_4$ oxidation over **(a)** Ag/SFO and **(b)** Ag(NCO/SFO), with the layer of $Na_2CO_3$ in **(b)** preventing direct reaction between the $SrFeO_{3-\delta}$ support, and $C_2H_4$ or EO.

Alternatively, Gao *et al.* (2020) found that for oxidative dehydrogenation of ethane *via* chemical looping over $La_{0.8}Sr_{0.2}FeO_{3-\delta}$, coated with a molten layer of $Li_2CO_3$, the presence of the carbonate layer influenced the distribution of oxygen species at the surface of the material. Peroxide $O_2^{2-}$ species, selective for ODH, were transported through the carbonate layer more easily than non-selective atomic oxygen $O^-$ species, and hence selectivity towards ethylene was improved. As discussed in Chapter 4, atomic, peroxide, and superoxide species were detected at the surface of Ag/SFO by Raman spectroscopy, with the relative proportion of each species changing during reduction. Hence, future studies could consider applying *in-situ* Raman spectroscopy to measure the Ag-$O_x$ species on Ag/SFO and Ag(NCO/SFO) during chemical looping, to determine whether the the distribution of oxygen species was influenced by the

internal layer of $Na_2CO_3$, and whether the carbonate layer influenced transport of oxygen from the SFO lattice to the surface of Ag.

Additionally, impregnation of Ag nanoparticles on top of the $Na_2CO_3$ resulted in a different particle morphology at a similar overall size distribution, with elongated particles of Ag (shown in Fig. 5.5), possibly affecting selectivity towards EO (Marek and García-Calvo Conde, 2021).

As observed from EDS maps in Fig. 5.4, Na was distributed over the surface of NCO(Ag/SFO), and, given that no appreciable reaction with ethylene was observed in the packed bed (as shown in Fig. 5.10d), the $Na_2CO_3$ layer was assumed to fully cover the Ag nanoparticles at the surface of the material. However, given the relatively large interaction volume of EDS measurements, the thickness and uniformity of the carbonate layer could not be readily quantified.

Furthermore, the target loading of 10 wt% $Na_2CO_3$ used here was chosen arbitrarily, and the true loading for the most selective sample, Ag(NCO/SFO) was likely somewhat lower, estimated at around 2 wt% from ICP-AES measurements. Hence, future work would need to confirm that the differences in conversion and selectivity between Ag/SFO and Ag(NCO/SFO) were indeed caused by the layer of $Na_2CO_3$ acting as a diffusion barrier, by investigating alternative synthesis and characterisation methods, allowing for a well-defined carbonate layer of known thickness covering the material. Understanding the source of the discrepancy between target and actual loading of $Na_2CO_3$ during the preparation of Ag(NCO/SFO) would also aid further research into the reactive properties of the material.

## 5.5 Conclusions

Composite oxygen carriers composed of $SrFeO_{3-\delta}$ impregnated with Ag nanoparticles and a layer of $Na_2CO_3$ were prepared by sequential impregnation with nitrate precursors and calcination in laboratory air, and characterised by Raman spectroscopy, SEM, and XPS. From TGA measurements, the presence of an internal or external layer of $Na_2CO_3$ was found to partially inhibit reduction under mild ($N_2$) or strong (5 vol% $H_2$) reducing atmospheres. During reduction in 5 vol% $H_2$, the minimum temperatures required for reduction of Ag($Na_2CO_3$/$SrFeO_{3-\delta}$) and $Na_2CO_3$(Ag/$SrFeO_{3-\delta}$) were 260°C and 290°C respectively, as compared to 200°C for Ag/$SrFeO_{3-\delta}$. The samples with internal and external layers of $Na_2CO_3$ reduced at an almost identical rate at 300°C under 5 vol% $H_2$, whereas, under 5 vol% $C_2H_4$, Ag($Na_2CO_3$/$SrFeO_{3-\delta}$) lost mass considerably

more rapidly than $Na_2CO_3$(Ag/$SrFeO_{3-\delta}$). Hence, the ability of the reducing molecule to access the surface of Ag, and hence the reactive Ag-$O_x$ surface species identified in Chapter 4, was determined likely to be necessary for rapid reduction.

During chemical looping epoxidation at 270°C, samples with an external layer of $Na_2CO_3$ (*i.e.* $Na_2CO_3$/$SrFeO_{3-\delta}$ and $Na_2CO_3$(Ag/$SrFeO_{3-\delta}$)) were inactive, whereas, Ag($Na_2CO_3$/$SrFeO_{3-\delta}$) showed higher selectivity towards EO than Ag/$SrFeO_{3-\delta}$ (36% *vs* 23% respectively), albeit with similar overall yield (around 4.3%). The carbonate layer was hypothesised to mitigate complete combustion of $C_2H_4$ and EO by preventing access to the surface of the $SrFeO_{3-\delta}$ oxygen carrier, while allowing reaction at selective sites on the exposed surface of Ag nanoparticles. The results demonstrate that incorporating an internal carbonate layer to prevent over-oxidation could be a useful strategy for improving selectivity in chemical looping oxidation processes.

# Chapter 6

# Selective formation of propan-1-ol from propylene using chemical looping

The Chapter discusses the preparation and characterisation of mixed Ag-AgCl-Au catalysts supported on $SrFeO_{3-\delta}$, for use in chemical looping oxidation of propylene, with propan-1-ol forming as the preferred product over AgCl-AgAu materials. Sections from this Chapter have been published in Harrison and Marek (2022), with all sections reproduced in this Dissertation comprising solely my own work.

## 6.1 Introduction

Selective oxidation of propylene to form value-added $C_3$ products, such as propylene oxide (PO), allyl alcohol (AA), and propan-1-ol, is a significant challenge in heterogeneous catalysis (Li *et al.*, 2007; McCoy, 2001; Trent, 2000). In particular, catalysts for producing propylene oxide from propylene using air as the oxidising agent have been studied extensively (Khatib and Oyama, 2015; Teržan *et al.*, 2020), but are not yet commercially competitive, despite the environmental and economic problems of the incumbent chlorohydrin and hydroperoxide processes (Trent, 2000). Production of propan-1-ol directly from propylene is also challenging as a result of the preferential formation of the secondary alcohol isomer, propan-2-ol, under most reaction conditions (Li *et al.*, 2007).

In this Chapter, Ag, AgCl, and Ag/Au catalysts, supported on $SrFeO_{3-\delta}$ perovskite, were investigated for chemical looping oxidation of propylene. Catalysts containing AgCl

and, or Au were found to give low levels of complete combustion, and high selectivity towards propan-1-ol. Interestingly, the AgCl and AgCl/Au catalysts produced a substantially different distribution of products as compared to typical distributions reported for direct epoxidation of propylene over Ag- and Au-based catalysts (Khatib and Oyama, 2015). The results provide an insight into potential future challenges in applying a chemical looping approach to propylene oxidation, and indicate that catalysts composed of AgCl and, or AgAu alloy supported on $SrFeO_{3-\delta}$ might be suitable for production of propan-1-ol from propylene *via* a chemical looping approach.

## 6.2 Experimental

Samples of $SrFeO_{3-\delta}$ (SFO) modified with Ag, AgCl, and Au were prepared by incipient wetness impregnation, as described in Section 2.1.2, with a summary of samples prepared given in Table 6.1. Samples of Ag/SFO were prepared by dropwise addition of $AgNO_3$ followed by drying at 120°C for 12 h, and calcination at 650°C for 5 h, whereas, AgCl/SFO was prepared by adding $AgNO_3$, then adding excess concentrated hydrochloric acid to convert the Ag to AgCl, followed by drying and calcination as previously.

For samples containing gold, two preparation methods were used to impregnate Au onto SFO. In the first method (termed 'direct impregnation', with Au-D designation in sample codes), $AuCl_3$ was dissolved in deionised water, then brought to pH 8 by addition of NaOH solution. The resulting alkaline solution was then added dropwise to SFO, followed by drying and calcination at 650°C.

A series of mixed AgCl/Au-D catalysts supported on SFO, with target metal loadings $x$ wt% Ag and (10-$x$) wt% Au ($x$ = 2.5, 5, 7.5), was prepared by varying the volume of $AgNO_3$ and $AuCl_3$ solutions added. The $AgNO_3$ reacted with $AuCl_3$ in solution to form AgCl and Au or AgAu. The solutions of Ag and Au precursor were prepared separately, then added sequentially to the support material in appropriate ratios to achieve the desired loading, followed by drying and calcination. Catalysts prepared by impregnation with $AgNO_3$ and $AuCl_3$ were designated $x$AgCl/(10-$x$)Au-D/SFO.

One batch of SFO modified with Ag and Au was also prepared by impregnating SFO with $AgNO_3$ and $AgCl_3$ solutions, followed by drying at 120°C and calcination at 700°C for 5 h. Calcination at 700°C as opposed to 650°C induced thermal decomposition of

some of the AgCl (Siddiqui *et al.*, 2013). The sample calcined at 700°C was designated Ag–AgCl/Au-H/SFO.

For chloride-free catalysts containing gold, a ligand complexation method from Murayama *et al.* (2017) was used, described in more detail in Section 2.1.2. Briefly, a solution of $HAuCl_4$, NaOH, and $\beta$-alanine was prepared in 70% ethanol, to form a Au-($\beta$-ala) complex (shown in Fig. 6.1). The Au-($\beta$-ala) precipitate was separated by centrifugation, dried in a dessicator, then dissolved in water and added dropwise to SFO, followed by drying at 120°C and calcination at 650°C. Materials containing Au prepared using Au–($\beta$-ala) were designated Au-L. The resulting Au loading was determined by inductively coupled plasma atomic emission spectroscopy (ICP-AES) to be 0.02 wt%, the lowest of all gold-containing materials that were prepared here.

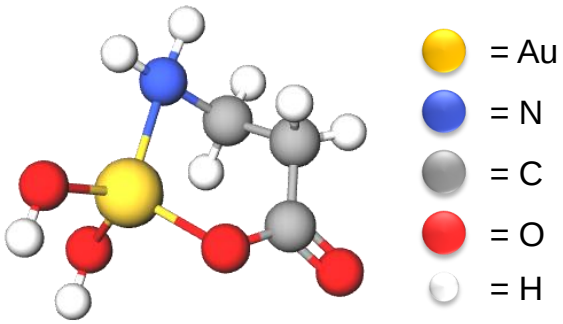


Fig. 6.1 Structure of the Au-($\beta$-ala) complex formed during peparation of Au-L samples, proposed by Murayama *et al.* (2017).

Table 6.1 Summary of catalyst samples used in chemical looping experiments, with a target total metal loading of 10 wt% for each sample. Catalyst loadings were estimated using X-ray diffraction (XRD) and ICP-AES measurements. Letter codes for samples containing gold refer to the method used to add Au to the surface of the material, as described in Section 2.1.2: D - impregnated with $AuCl_3$, H - impregnated with $AuCl_3$ followed by calcination at 700°C to partially decompose AgCl, L - impregnated with chloride-free Au-($\beta$-ala). Samples not containing gold were all prepared by incipient wetness impregnation, followed by drying, and calcination at 650°C.

| Sample | Catalyst | Estimated loading (wt%) |
|---|---|---|
| Ag/SFO | Ag | 11.8% Ag |
| Au-D/SFO | Au | 7.3% Au |
| AgCl/SFO | AgCl | 1.1% Ag, 8.8wt% AgCl |
| $x$AgCl/(10-x)Au-D/SFO ($x$ = 2.5, 5, 7.5) | AgCl/Au | $x$ = 2.5: 3.4% AgCl, 7.9% AgAu<br>$x$ = 5: 5.1% AgCl, 5.1% AgAu<br>$x$ = 7.5: 6.9% AgCl, 5.1% AgAu |
| Ag-AgCl/Au-H/SFO | Ag/AgCl/Au | 3.4% AgCl, 8.8% (Ag + AgAu) |
| Ag/Au-L/SFO | Ag/Au | 4.6% Ag, 0.02% Au |

| Sample | Catalyst precursors used | Heat treatment |
|---|---|---|
| Ag/SFO | $AgNO_{3,(aq)}$ | 120°C (12 h), 650°C (5 h) |
| Au-D/SFO | $AuCl_{3,(aq)}$ | 120°C (12 h), 650°C (5 h) |
| AgCl/SFO | $AgNO_{3,(aq)}$, conc. $HCl_{(aq)}$ | 120°C (12 h), 650°C (5 h) |
| $x$AgCl/(10-x)Au-D/SFO ($x$ = 2.5, 5, 7.5) | $AgNO_{3,(aq)}$, $AuCl_{3,(aq)}$ | 120°C (12 h), 650°C (5 h) |
| Ag-AgCl/Au-H/SFO | $AgNO_{3,(aq)}$, $AuCl_{3,(aq)}$ | 120°C (12 h), 700°C (5 h) |
| Ag/Au-L/SFO | $AgNO_{3,(aq)}$, Au-($\beta$-ala)$_{(aq)}$ | 120°C (12 h), 650°C (5 h) |

Powder X-ray diffraction (XRD) patterns were measured as described in Section 2.2.1, using a Bruker D8 Advance diffractometer. Phase compositions were estimated using Rietveld refinement.

Scanning electron microscopy (SEM) images were taken as described in Section 2.2.6 using a Tescan Mira3 FEG-SEM, with secondary electron (SE) and back-scattered electron (BSE) detectors in parallel. Scanning transmission electron microscopy (STEM) images and EDS maps were taken at room temperature as described in Section 2.2.5, using a Thermo Scientific (FEI) Talos F200X G2 TEM.

X-ray photoelectron spectroscopy (XPS) measurements were collected under high-vacuum using a ThermoFisher Scientific Escalab 250Xi spectrometer, as described in Section 2.2.7, scanning the Ag3d, Au4f, O1s, Cl2p, and C1s binding energy regions. The energy scale was calibrated relative the Au $4f_{7/2}$ peak on gold foil, at 84.00 eV.

The catalytic performance of the prepared materials was determined using a packed bed reactor, described in Section 2.3.2. A packed bed of 1.5 g active material, in between two layers of SiC (241-559 $\mu$m, Alfa Aesar, 2.00 g below the bed and 3.00 g above the bed), was assembled in a quartz reactor tube, with gases fed sequentially.

The gases used in experiments were 5 vol% propylene (balance Ar, BOC, 4.96 or 5.13 vol%) for reduction, $N_2$ (99.99+%, BOC) for purging, and compressed air (99.99+%, BOC) for re-oxidation. Gas flows to the reactor were set to 200 mL $min^{-1}$ (NTP). Reduction and oxidation cycles were performed by passing gases over the material in the sequence $N_2$-$C_3H_6$-$N_2$-air. Generally, in a single cycle, the active bed was reduced in $C_3H_6$ for 1.5 min, followed by a 2 min purge step in $N_2$, and then re-oxidised in air for 15 min. The effect of reduction time was also investigated, varying the reduction time from 1.5 min to 60 min, but keeping the 2 min purge in $N_2$ and 15 min reoxidation in air. The active bed was periodically regenerated by heating the packed reactor tube to 650°C for 5 h *ex-situ* in a muffle furnace under static air.

The exhaust gas from the packed-bed reactor was manually sampled from a port immediately downstream of the bed, using a gas syringe, then injected into an Agilent 7890A gas chromatograph as described in Section 2.3.3. Samples were collected 45 s after the start of each reduction step in $C_3H_6/N_2$. The response of the GC to propylene and propylene oxide (PO) was determined using a certified calibration mixture of 1000 ppm propylene/1000 ppm propylene oxide (balance $N_2$, BOC).

Further calibration gas mixtures of propan-1-ol, propan-2-ol, acetone, propanal, and allyl alcohol (AA) were generated using an Owlstone V-OVG vapour generator, as described in Section 2.3.3 and shown in Appendix A, Fig. 2.7.

The instantaneous conversion of propylene, $\bar{X}$, defined as the ratio of the total carbon in products to the total carbon detected, was estimated from the concentrations measured at the reactor outlet, using Eq. 6.1.

$$\bar{X} = \frac{y_{PO} + \frac{1}{3}y_{CO_2} + y_{Propan-1-ol} + y_{Acetone} + y_{Propanal} + y_{AA}}{y_{Propylene} + y_{PO} + \frac{1}{3}y_{CO_2} + y_{Propan-1-ol} + y_{Acetone} + y_{Propanal} + y_{AA}} \tag{6.1}$$

Given the relatively low (<10%) conversion of propylene, the total molar flowrate, $\dot{n}$, was taken to be approximately constant before and after the reactor. Selectivity towards a given product $i$, $\bar{S}_i$, (*i.e.* PO or propan-1-ol) was determined using Eq. 6.2.

$$\bar{S}_i = \frac{y_i}{y_{PO} + \frac{1}{3}y_{CO_2} + y_{Propan-1-ol} + y_{Acetone} + y_{Propanal} + y_{AA}} \tag{6.2}$$

Cumulative oxygen release during extended reduction in $C_3H_6$ was estimated using Eq. 6.3.

$$O_{released} = \dot{n} \int_0^{t_{reduction}} (y_{PO} + 3y_{CO_2} + y_{Propan-1-ol} + y_{Acetone} + y_{Propanal} + y_{AA})\, dt \tag{6.3}$$

where $t_{reduction}$ is the reduction time, and with integrals estimated using the trapezium rule. The factor of 3 is applied to the $CO_2$ concentration to account for oxygen participating in the formation of $CO_2$ and $H_2O$ during complete combustion, shown in Eq. 6.4, with the combustion products forming in a 1:1 molar ratio.

$$C_3H_6 + \frac{9}{2}O_2 \rightarrow 3CO_2 + 3H_2O \tag{6.4}$$

To confirm the validity of measurements, the carbon balance over each cycle was estimated using Eq. 6.5, where $y_{Propylene,Inlet}$ was taken to be equal to the concentration of propylene in the feed gas. For experiments using blended mixtures of gases, $y_{Propylene,Inlet}$ was determined using the GC. The overall carbon balance for all measurements was within ±10% of the expected value.

$$C_{bal} = \frac{y_{Propylene} + y_{PO} + \frac{1}{3}y_{CO_2} + y_{Propan-1-ol} + y_{Acetone} + y_{Propanal} + y_{AA}}{y_{Propylene,Inlet}} \tag{6.5}$$

To determine potential side-reactions of oxidation products, chemical looping oxidation experiments were also performed using a propylene feed stream with PO or propanal added. An electrical tube furnace was used to heat the reactor tube as opposed to heating tape, with the active bed placed in the isothermal region of the furnace, using a rig previously described by Gebers *et al.* (2022). An inlet gas mixture containing propylene and PO was produced by blending 5.13 vol% propylene (balance Ar) with 1000 ppm propylene/1000 ppm propylene oxide (balance $N_2$), using 100 mL $min^{-1}$ of each mixture for a nominal composition of 2.56 vol% propylene and 500 ppm propylene oxide.

In another set of experiments, inlet gas mixture containing propylene and propanal, or propylene and water, were produced by passing 5.13 vol% propylene through the vapour generator at 200 mL $min^{-1}$, loaded with propanal (Acros Organics, 99+%) or deionised water, thus, generating a stream containing 5 vol% propylene and *c.* 1200 ppm propanal, or 5 vol% propylene and 2700 ppm $H_2O$. The composition of gas mixtures blended in-house was confirmed using the GC. Similarly, the reaction of PO with hydrogen was investigated by blending 5 vol% $H_2$ (balance $N_2$; Air Liquide) with 1000 ppm propylene/1000 ppm propylene oxide (balance $N_2$), for a nominal composition of 500 ppm PO, 500 ppm propylene and 2.5 vol% $H_2$. The mixture of PO, propylene, and $H_2$ was then passed over the active bed, with the outlet stream composition measured using the GC.

## 6.3 Results

### 6.3.1 Material characterisation

The materials prepared were characterised using XRD, and the results are presented in Fig. 6.2, with further XRD patterns for the series of $x$Ag/(10-$x$)Au-D/SFO materials shown in Appendix E, Fig. E.1. From the XRD patterns for AgCl/SFO, AgCl/Au-D/SFO, Ag-AgCl/Au-H/SFO, peaks at $2\theta = 32.2°$ and 46.0° were detected, corresponding to the AgCl crystalline phase. The characteristic peaks for AgCl were absent in the patterns for Ag/SFO and Ag/Au-L/SFO. For the AgCl/Au-D/SFO samples, the peaks at $2\theta = 38.3°$ and 44.5° were fitted to the alloyed AgAu phase, as the XRD patterns for metallic Ag and Au were too similar to be readily distinguishable.

The estimated compositions calculated for each sample are presented in Table 6.2. The oxygen carrier was approximately pure $SrFeO_3$ (>95%). For the sample of

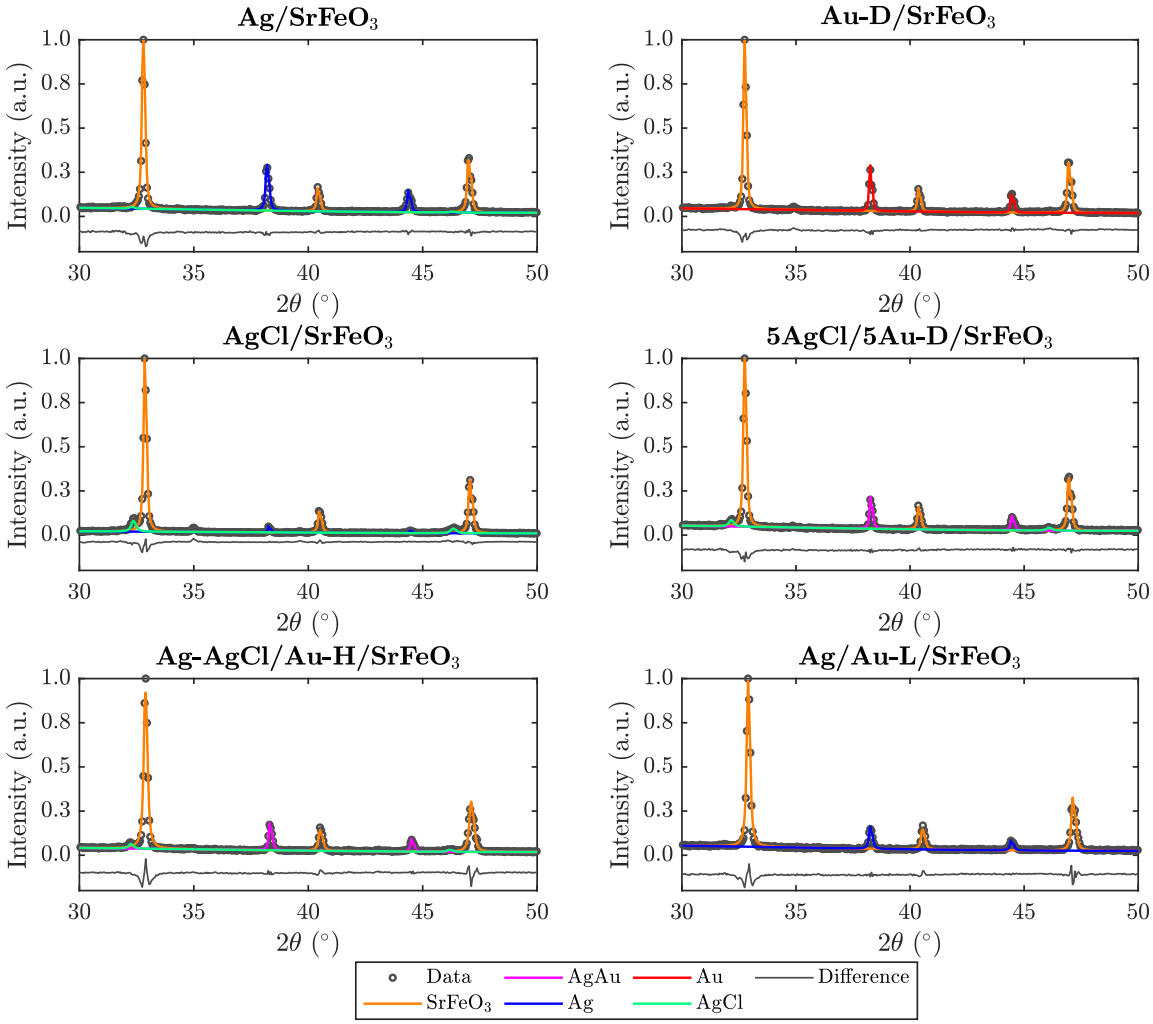


Fig. 6.2 Sections of collected XRD patterns for Ag/SFO, Au-D/SFO, AgCl/SFO, 5AgCl/5Au-D/SFO, Ag–AgCl/Au-H/SFO, and Ag/Au-L/SFO. Circles indicate experimental measurements; lines indicate fitted model using reference patterns.

Ag–AgCl/Au-H/SFO, calcined at 700°C, Fig. 6.2 shows a less prominent AgCl peak than in the Au-D samples calcined at 650°C, giving an AgCl loading of 3.4 wt%, as compared to 5.1 wt% for 5AgCl/5Au-D/SFO. The decreased relative intensity AgCl peak confirmed that calcination at 700°C induced thermal decomposition of AgCl, which starts around 650-700°C (Siddiqui *et al.*, 2013). No AgCl was detected in the sample prepared using the Au-($\beta$-ala) precursor (Ag/Au-L/SFO), where all Ag and Au were present as metallic nanoparticles, with an estimated Ag loading of 4.6 wt%. The mean crystallite sizes of Ag, AgCl, AgAu, and Au, estimated using Eq. 2.1, are reported in Appendix E, Table E.1.

Estimated phase compositions suggested that all samples contained approximately 1-4wt% of impurity phases containing strontium (*i.e.* $SrCO_3$ or $Sr_3Fe_2O_7$), as discussed in Section 2.1.3. Therefore, XRD refinement suggested that all samples were slightly strontium enriched, and iron deficient, suggesting either experimental error while preparing the initial batch of SFO used in experiments, or, the presence of iron-containing phases not readily detected by XRD, as discussed in Section 4.3.1.

In Fig. 6.3, XRD patterns are shown for AgCl/SFO as-prepared ('Fresh'), after 15 chemical looping cycles at 260-300°C ('Spent'), and after regeneration at 650°C ('Regenerated'); *i.e.* heated under the same calcination conditions as during synthesis, to remove surface impurities adsorbed from air (Marek and García-Calvo Conde, 2021). All samples showed a prominent peak corresponding to AgCl, indicating that reaction with propylene at 260-300°C or regeneration at 650°C in air did not strip the chloride from AgCl. Contrastingly, metallic Ag catalysts promoted with $Cl^-$ ions reported in literature (Charisteidis and Triantafyllidis, 2020; Seubsai and Senkan, 2011) were not stable under reaction conditions at 250-340°C, with the chloride being removed from the surface by reaction with propylene to form halogenated products including allyl chloride.

Table 6.2 Phase quantification from refinement of XRD patterns for SFO support and impregnated samples. Compositions in wt% . For phase quantification, metallic Ag, metallic Au, and AgAu alloy could not be distinguished unambiguously, as a result of the closeness of the peaks to one another.

| Fraction (wt%) | SFO | Ag/SFO | 7.5AgCl/2.5Au-D/SFO |
|---|---|---|---|
| Ag | - | 11.8 | - |
| AgCl | - | - | 6.9 |
| Au | - | - | - |
| AgAu | - | - | 5.1 |
| $SrFeO_3$ | 96.0 | 84.0 | 84.0 |
| $Sr_3Fe_2O_7$ | 2.0 | 2.0 | 0.7 |
| SrO | 0.1 | 0.0 | 0.3 |
| $SrCO_3$ | 1.5 | 3.0 | 3.0 |

| Fraction (wt%) | 5AgCl/5Au-D/SFO | 2.5AgCl/7.5Au-D/SFO | Au-D/SFO |
|---|---|---|---|
| Ag | - | - | - |
| AgCl | 5.1 | 3.4 | - |
| Au | - | - | 7.3 |
| AgAu | 6.0 | 7.9 | - |
| $SrFeO_3$ | 85.0 | 85.0 | 87.0 |
| $Sr_3Fe_2O_7$ | 2.0 | 1.0 | 3.0 |
| SrO | 0.1 | 0.1 | 0.6 |
| $SrCO_3$ | 2.0 | 3.0 | 2.1 |

| Fraction (wt%) | AgCl/SFO | Ag-AgCl/Au-H/SFO | Ag/Au-L/SFO |
|---|---|---|---|
| Ag | 1.1 | - | - |
| AgCl | 8.8 | 3.4 | - |
| Au | - | - | - |
| AgAu | - | 5.1 | 4.6 |
| $SrFeO_3$ | 85.0 | 90.0 | 92.0 |
| $Sr_3Fe_2O_7$ | 3.0 | 0.0 | 1.0 |
| SrO | 0.8 | 0.3 | 0.0 |
| $SrCO_3$ | 1.3 | 1.5 | 2.0 |

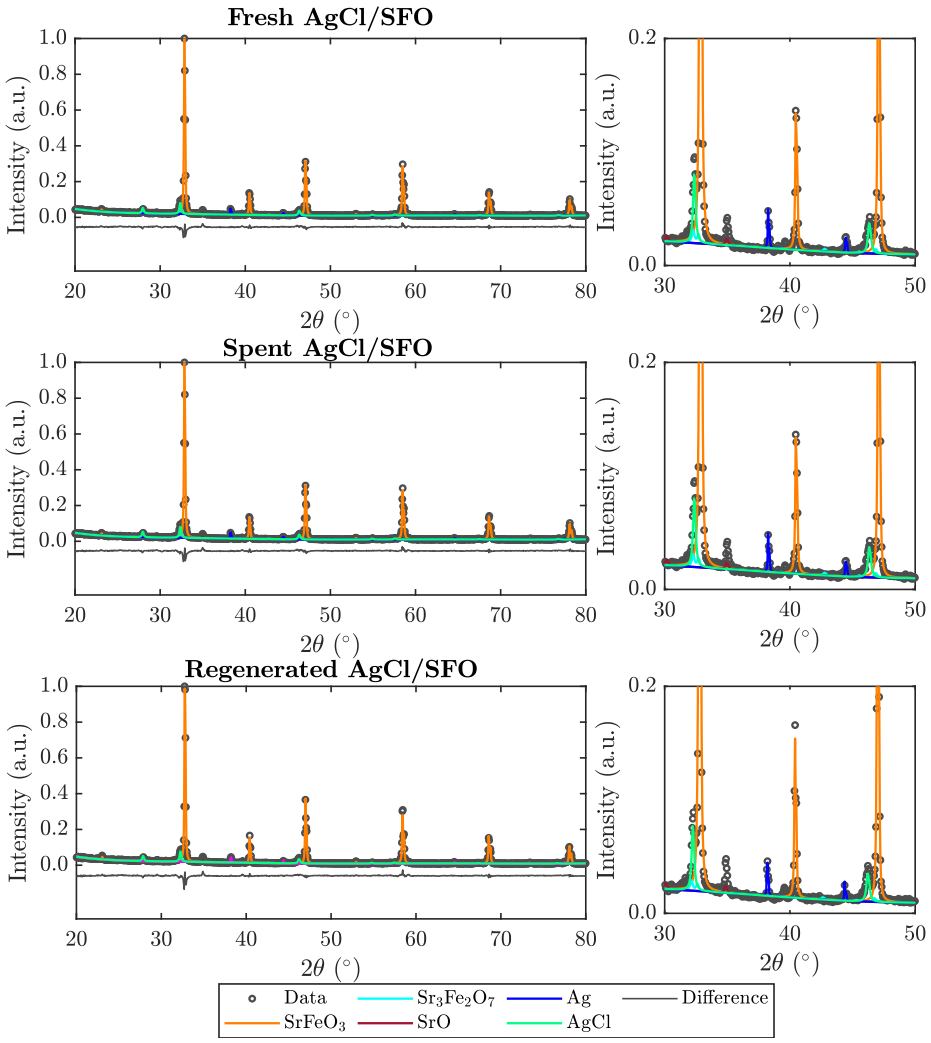


Fig. 6.3 XRD patterns for fresh, spent, and regenerated AgCl/SFO, with AgCl peaks indicated in green. Spent sample was withdrawn from reactor tube after 15 chemical looping cycles. The regenerated sample was produced by heating the spent sample to 650°C in air for 5 hours, followed by cooling in air to room temperature.

The presence of AgCl on the surface of the 5AgCl/5Au-D/SFO sample was confirmed *via* STEM-EDS mapping, shown in Fig. 6.4 (further STEM-EDS maps are shown in Appendix E, Fig. E.2). Particles composed of AgCl and AgAu were detected, with AgAu forming larger particles and AgCl smaller (Sauter mean diameter of 266 nm and 111 nm, respectively). Low atomic fractions of Cl were detected in particles of AgAu, and low atomic fractions of Au in particles of AgCl (<5.0 $at_{Cl}$% and <0.6 $at_{Au}$%, respectively for all analysed particles), demonstrating limited overlap between the AgAu and AgCl clusters. Analysis of the AgCl particles gave a molar ratio of Ag to Cl in the range 1–2, with an Ag:Cl ratio of 1 corresponding to pure AgCl, and an Ag:Cl ratio of 2 corresponding to 50 at% AgCl and 50 at% Ag. Thus, Ag was present either as particles of AgCl, clusters of metallic Ag with AgCl, or as AgAu alloy. For areas of bare SFO support, no Ag or Au was detected, and the Sr:Fe atomic ratio was close to 1 in all cases.

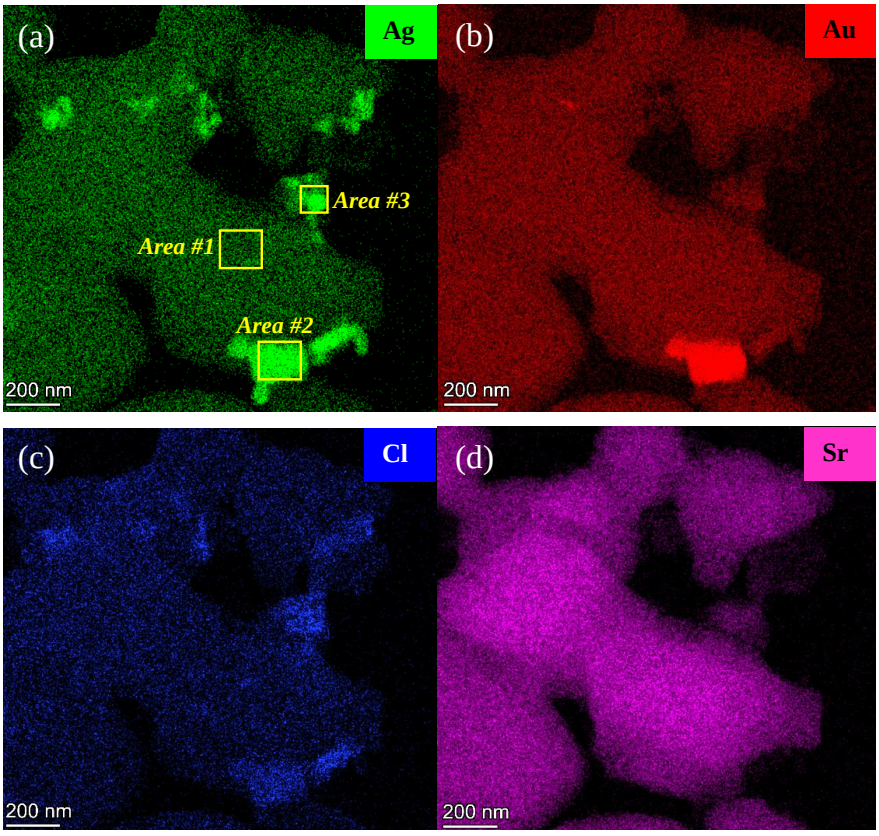


Fig. 6.4 STEM-EDS maps of crushed particles of 5Ag/5Au-D/SFO, showing distribution of **(a)** Ag, **(b)** Au, **(c)** Cl, **(d)** Sr. Area 1 corresponds to bare SFO support with no Ag or Au detected, Area 2 corresponds to a particle of AgAu, Area 3 corresponds to a particle of AgCl.

The surface of the samples was further characterised using SEM images (shown in Fig. 6.5). The sample of Ag/SFO, shown in Figs. 6.5a and 6.5b, with the Sauter mean diameter of Ag particles within one standard deviation of the values reported in Chapters 3 and 5, and showing similar surface morphology to the samples shown Fig. 5.5 and in Appendix B, Fig. 3.4. For 5Ag/5Au-D/SFO, two distinct surface particle morphologies were visible in Figs. 6.5d and 6.5e, with larger (*c.* 425 nm), approximately spherical particles, and smaller (*c.* 135 nm), elongated particles visible (particle size distributions are given in Figs. 6.5c and f). Additionally, the larger particles appeared brighter in the BSE image, corresponding to greater atomic number (Lloyd, 1987), indicating the mixture of AgAu, as compared to the smaller, darker particles, composed of AgCl.

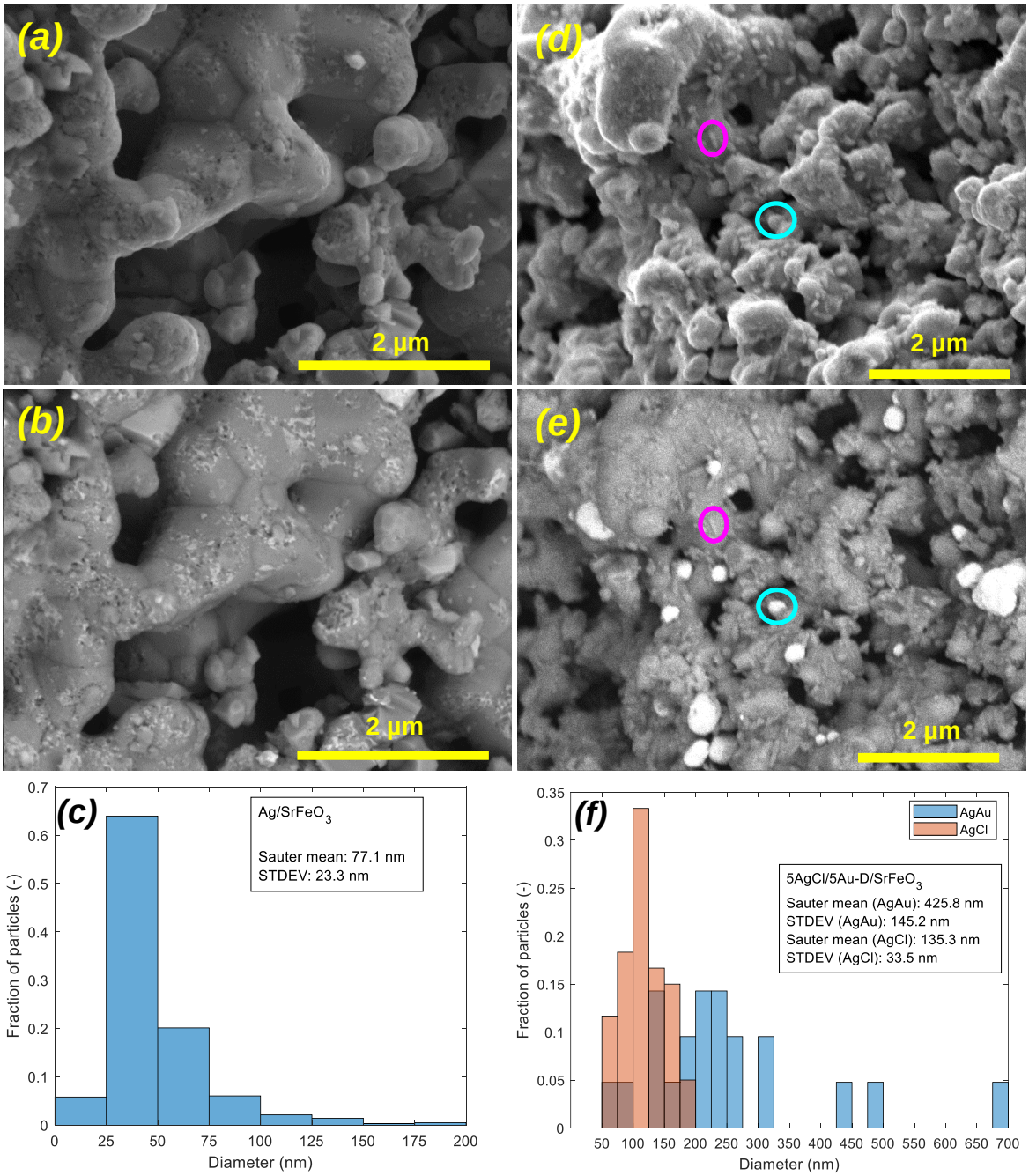


Fig. 6.5 SEM micrographs and particle size distributions for Ag/SFO ((**a**) SE, (**b**) BSE, (**c**) size distribution), and 5AgCl/5Au-D/SFO ((**d**) SE, (**e**) BSE, (**f**) size distributions). Circled areas correspond to the different particle morphologies observed, with pink = AgCl and blue = AgAu.

To further identify the surface species present, XPS measurements were collected for Ag/SFO, AgCl/SFO, and 5AgCl/5Au-D/SFO, and compared with Ag, Au, and AgCl standards. The experimental measurements, and fitted peaks, are shown in Fig. 6.6, with binding energy (BE) values for each peak given in Appendix E, Table E.2.

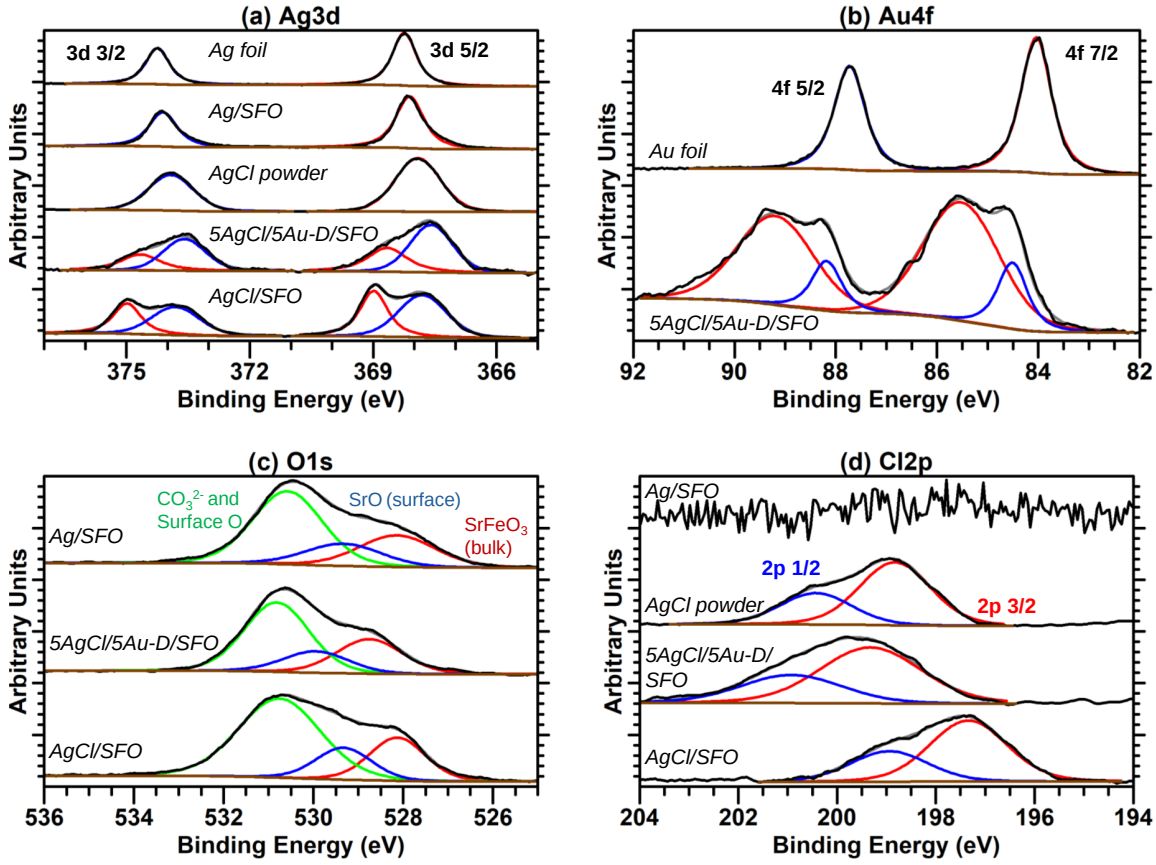


Fig. 6.6 XPS spectra for **(a)** Ag3d, **(b)** Au4f, (c) O1s, and (d) Cl2p scans, with deconvoluted peaks fitted to experimental measurements. Measurements calibrated with respect to $Au4f_{7/2}$ peak at BE = 84.0 eV.

The Ag foil standard (Fig. 6.6a) showed a single main peak for each of the $Ag3d_{5/2}$ and $Ag3d_{7/2}$ binding energy levels. The binding energy measured for $Ag3d_{5/2}$ was 368.2 eV, consistent with literature values for metallic $Ag^0$ (Seah *et al.*, 1998). The binding energy of $Ag3d_{5/2}$ measured for Ag/SFO showed a minimal shift with respect to the foil standard (<0.1 eV), indicating metallic particles of Ag. The AgCl standard showed a single peak at 367.9 eV, corresponding to a shift with respect to metallic $Ag^0$ of -0.35 eV, consistent with Gaarenstroom and Winograd (1977). The XPS spectra for AgCl/SFO and 5AgCl/5Au-D/SFO each showed two distinct $Ag3d_{5/2}$ features. The AgCl/SFO spectrum showed main peaks at 367.8 eV (assigned to AgCl), and

369.0 eV, assigned to strongly oxidised Ag species, as reported by Lu *et al.* (2002) for 10% NaCl-promoted Ag. The peak at 369.0 eV might therefore correspond to $Ag^+$ species in contact with $O_{lattice}$ in the SFO support, or in contact with strongly adsorbed $O_a$ adatoms.

For 5AgCl/5Au-D/SFO, two main $Ag3d_{5/2}$ peaks at 367.4 eV and 368.6 eV were detected. As AgCl and AgAu were known to be present at the surface as distinct phases from the STEM analyses in Fig. 6.4, the peak at 367.4 eV was assigned to Ag(I) in AgCl, and the peak at 368.6 eV was assigned to $Ag^0$ in particles of AgAu alloy. The peak shift of +0.4 eV with respect to the Ag standard for AgAu was within the range reported in previous literature studies of AgAu alloy nanoparticles (Chimentão *et al.*, 2006; Malathi *et al.*, 2014).

The fitted peaks for $Au4f_{7/2}$ for the Au foil standard, and for the sample of 5AgCl/5Au-D/SFO, are shown in Fig. 6.6b. The Au foil standard showed a single peak, set to 84.0 eV (Seah *et al.*, 1998). The 5AgCl/5Au-D/SFO sample showed two distinct peaks at 84.5 eV and 85.5 eV. Malathi *et al.* (2014) reported a shift of +1 eV (with respect to an $Au^0$ metallic standard, *i.e.* to 85 eV) for AgAu nanoparticles, approximately consistent with the spacing between the two major peaks for 5AgCl/5Au-D/SFO. Other studies (Kariuki *et al.*, 2004; Srnová-Šloufová *et al.*, 2004) also report a positive shift in binding energy for $Au4f_{7/2}$ in AgAu alloy nanoparticles, but with smaller magnitude (*c.* +0.2 eV). Therefore, the smaller peak at 84.5 eV (shown in blue) was assigned to $Au^0$ in a local environment of Au, and the larger peak at 85.5 eV (shown in red) was assigned to $Au^0$ in AgAu alloy (*i.e.* in contact with $Ag^0$). A small peak at around 86.5 eV was also detected, possibly corresponding to residual unreacted $AuCl_3$ from synthesis (Kim *et al.*, 2011).

The observed difference in Au electronic states might have been caused by heterogeneity within particles of AgAu (*c.* 200 nm in size), as no particles containing only Au were detected from STEM-EDS composition maps (shown in Figs. 6.4 and in Appendix E, Fig. E.2). The cause of the +0.5 eV overall shift of the $Au^0$ peak with respect to the metallic standard was unclear, but might have been caused by interaction between the particles of AgAu, and the SFO support resulting in the Au developing a partial positive charge (Casaletto *et al.*, 2006).

The O1s spectra for Ag/SFO, 5AgCl/5Au-D/SFO, and AgCl/SFO were in good agreement with the XPS spectra for Ag/SFO reported in Chapters 4 and 5, with the main peaks detected corresponding to lattice oxygen in bulk $SrFeO_3$ (shown in red), lattice oxygen in the surface termination layer of SrO (shown in blue) (Crumlin *et al.*,

2012; Stoerzinger *et al.*, 2020; Zhou *et al.*, 2023), and carbonate and surface $AgO_x$ species (shown in green) (Abd El-Naser *et al.*, 2021; Falcón *et al.*, 2002; Schön, 1973).

The Cl2p spectra for each sample are shown in Fig. 6.6d. For Ag/SFO, no chlorine peaks were detected, as expected. The lack of chlorine therefore confirms that the $SrCO_3$, $Fe_2O_3$ and $AgNO_3$ precursors used to produce the material were free from chloride impurities, and therefore any chloride species detected on the surface of other samples must be due to treatment with HCl (for AgCl/SFO) or $AuCl_3$ (for 5AgCl/5Au-D/SFO). The powder AgCl standard and AgCl/SFO sample showed a $Cl2p_{3/2}$ peak at 198.8 eV, and $2p_{3/2}$-$2p_{1/2}$ peak separation of *c.* 1.6 eV, in good agreement with literature (Kaushik, 1991). A peak shift of *c.*-1.5 eV was observed between the $2p_{3/2}$ AgCl standard and the AgCl/SFO sample, similar to the shift reported for thin layers (*c.* 5 nm) of AgCl in contact with Ag (Qin *et al.*, 2017). The 5AgCl/5Au-D/SFO sample showed a single $Cl2p_{3/2}$ peak at 199.1 eV, corresponding to a slight positive shift of *c.*+0.3 eV with respect to the AgCl standard.

### 6.3.2 Performance in chemical looping experiments

Results from experiments carried out in the packed bed for 5AgCl/5Au-D/SFO are presented in Fig. 6.7, showing considerable activity towards formation of propan-1-ol (concentrations of 100-500 ppm measured in outlet stream). Propan-1-ol was not a product detected in previous studies of propylene oxidation over AgCl or Au catalysts (Charisteidis and Triantafyllidis, 2020; Geenen *et al.*, 1982; Lu *et al.*, 2002; Rojluechai *et al.*, 2007; Seubsai and Senkan, 2011). Trace amounts of PO, acetone, propanal, and propan-2-ol (*c.* 5 ppm) were also detected.

Over five cycles of reduction and re-oxidation, the outlet concentrations of propan-1-ol and $CO_2$ remained approximately stable, indicating minimal sample deactivation with cycling. Increasing the reactor temperature from 260°C to 300°C resulted in greater overall conversion of propylene, from 0.5 to 1.5%, but with little effect on selectivity towards propan-1-ol, which remained at 60±4% over the temperature range. The approximately constant selectivity with temperature suggested the apparent rates of the formation of propan-1-ol, and of complete combustion, had similar dependence on temperature over the range 260-300°C, and hence, the ratio of propan-1-ol to $CO_2$ in the reaction products did not change substantially.

The effect of altering the molar flowrate of the propylene feed ($\dot{n}_{C_3H_6}$) to the bed of 5Ag/5Au-D/SFO was also investigated, shown in Fig. 6.8. Doubling the residence time in the packed bed ($0.5\dot{n}_{C_3H_6}$) increased conversion of $C_3H_6$ (from 0.6% to 0.8%),

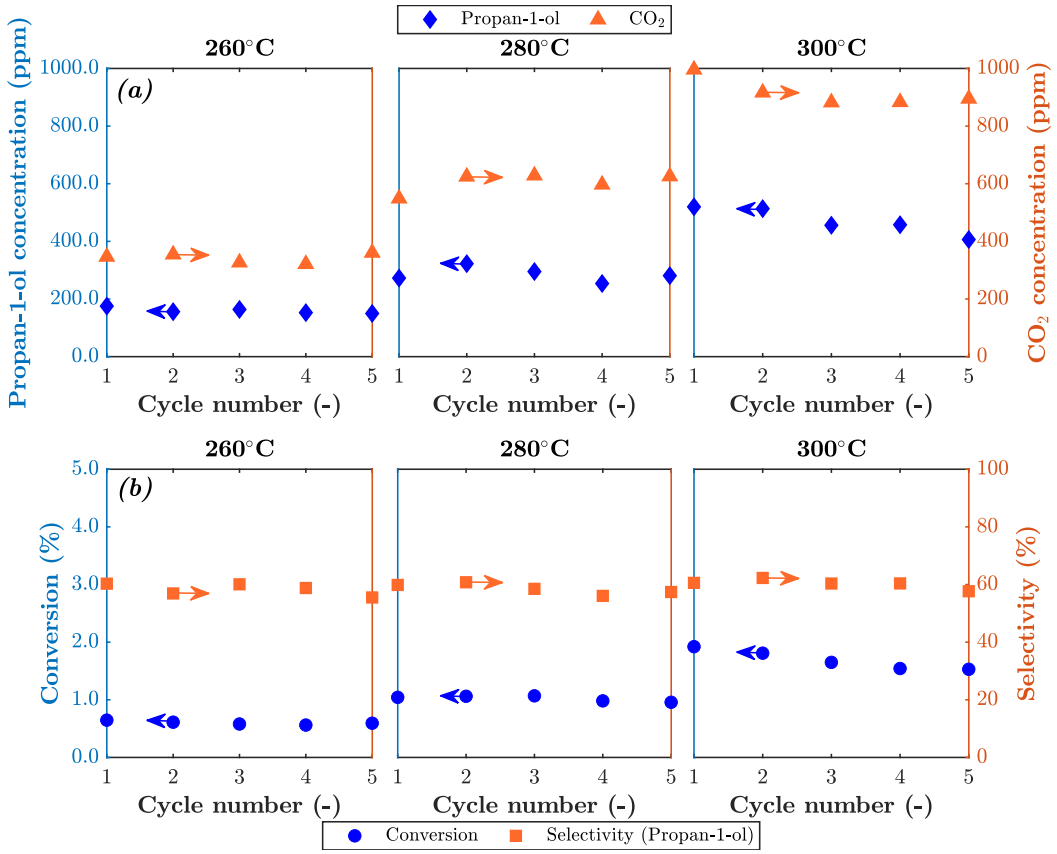


Fig. 6.7 **(a)** Concentrations of propan-1-ol and $CO_2$ and **(b)** calculated propylene conversion and selectivity towards propan-1-ol (shown on left and right axes, respectively) over the temperature range 260-300°C for 5AgCl/5Au-D/SFO.

and decreased selectivity towards propan-1-ol to 42%. When the residence time was halved ($2\dot{n}_{C_3H_6}$), the selectivity remained similar to at $\dot{n}_{C_3H_6}$ ($c.60\%$). The minimal change in selectivity with temperature, and residence time of propylene gave evidence of competing parallel and, or consecutive reactions. Possible reactions that lead to the formation of propan-1-ol are discussed in Section 6.4.2.

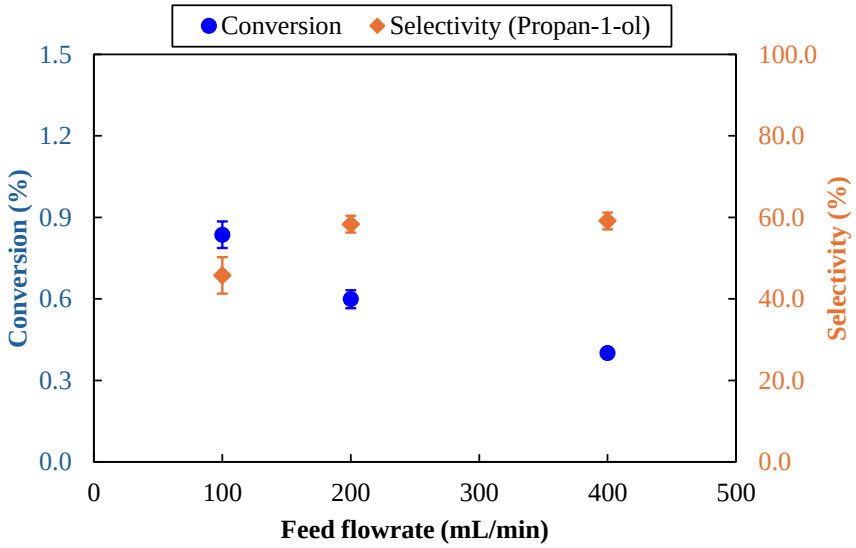


Fig. 6.8 Change in conversion of propylene, and selectivity towards propan-1-ol, over 5AgCl/5Au-D/SFO at 260°C, as a result of varying inlet flowrate. Error bars indicate standard deviation over three redox cycles.

Longer reduction steps (120 min) were performed over two AgCl/Au-D/SFO materials (shown in Appendix E.2, Fig. E.3), with total oxygen release greater than the oxygen available from $Ag_2O$ or from oxygen adsorbed at the catalyst surface (calculations of O availability are given in Appendix E.2). For the more active sample (7.5AgCl/2.5Au-D/SFO), the rate of oxygen release decreased with time, as expected for chemical looping operation (Bulfin *et al.*, 2020). Given that the overall propylene conversion in the cycling experiments reported in Fig. 6.7 was low, a reduction time of longer than 1.5 min was considered to be achievable without impacting the catalytic performance (Gebers *et al.*, 2022), as the amount of oxygen accumulated in the gaseous products after 1.5 min of reduction corresponded to a very small change in the stoichiometry of $SrFeO_{3-\delta}$ ($\Delta\delta \ll 0.01$).

To determine the feasibility of increasing the length of the reduction step in chemical looping, redox cycling was performed over 7.5AgCl/2.5Au-D/SFO, with the duration of the reduction step increased with each cycle, as presented in Fig. 6.9a. The conversion

of propylene rapidly decreased with reduction time up to 8–9 min reduction (shown in Fig. 6.9b), but declined slowly thereafter. Selectivity towards propan-1-ol remained approximately constant at around 40% for reduction steps shorter than 10 min, as shown in Fig. 6.9c.

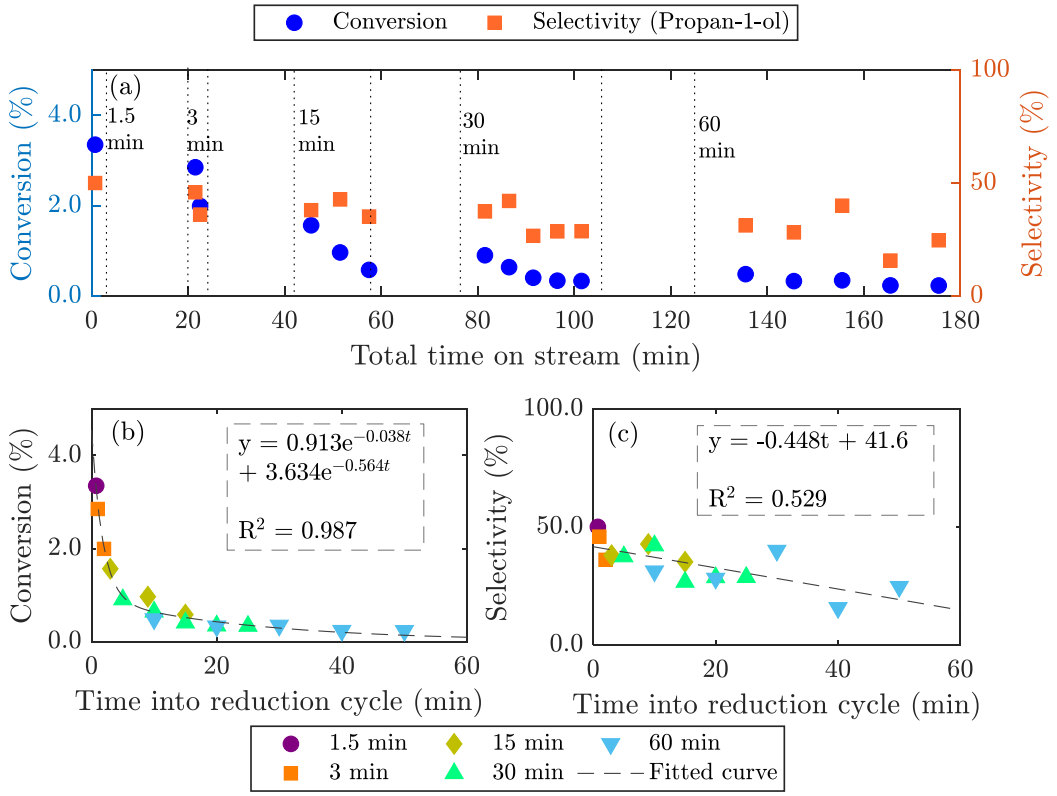


Fig. 6.9 Chemical looping over 7.5AgCl/2.5Au-D/SFO, with reduction time increased from 1.5 to 60 min. Vertical dotted lines in **(a)**indicate start and end of each reduction step. Change in conversion of propylene **(b)**, and in selectivity towards propan-1-ol **(c)**.

The effects of altering the Ag to Au ratio in $x$AgCl/(10-$x$)Au-D/SFO materials on conversion of propylene and selectivity towards propan-1-ol and PO are shown in Figs. 6.10a-c, with error bars indicating standard deviation over 5 chemical looping cycles. Increasing the Ag fraction increased the overall conversion of propylene, but the change was primarily driven by complete combustion rather than selective oxidation to desired products (with product concentrations in Figs. 6.10d-f). Therefore, combustion of propylene likely occurred on Ag sites, as previously reported in studies of propylene oxidation with gaseous oxygen (Khatib and Oyama, 2015).

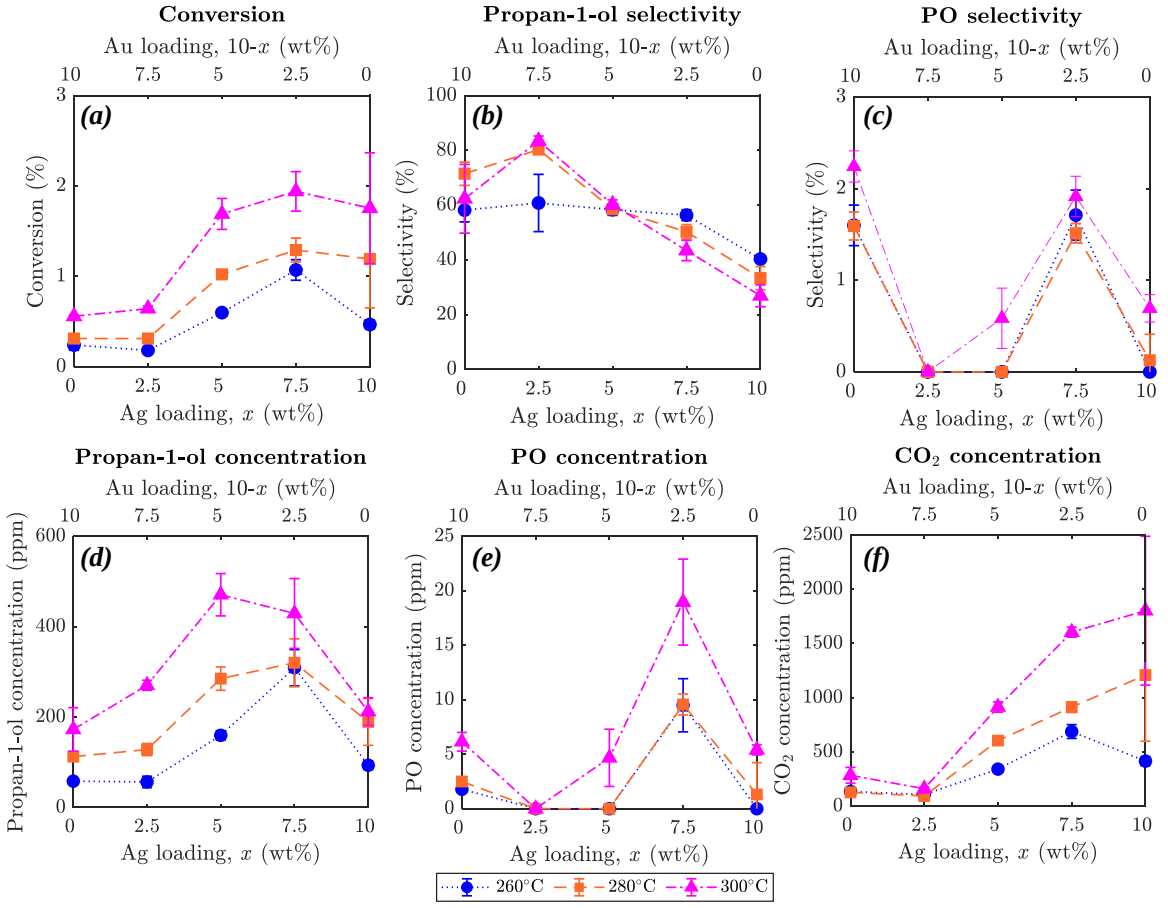


Fig. 6.10 Average values of **(a)** propylene conversion, **(b)** selectivity towards propan-1-ol, **(c)** selectivity towards PO, and concentrations **(d)** of propan-1-ol, **(e)** PO, and **(f)** $CO_2$, for chemical looping over $x$AgCl/10-*(x)*Au-D/SFO materials ($x$ = 0, 2.5, 5, 7.5, 10). Error bars show standard deviation over 5 cycles, with some error bars smaller than the datapoint markers. Sample at $x$ = 0 corresponds to Au-D/SFO; sample at $x$ = 10 corresponds to AgCl/SFO.

Selectivity towards propan-1-ol reached a maximum of around 80% for the sample with a loading of 2.5AgCl/7.5Au-D/SFO, with the selectivity decreasing with higher total Ag loading. The highest propan-1-ol concentration of 470 ppm in the outlet stream was observed in experiments with the 7.5AgCl/2.5Au-D/SFO sample (presented in Fig. 6.10d) at 300°C. However, the result was accompanied by a high concentration of $CO_2$, giving a lower overall selectivity for propan-1-ol than the sample of 2.5AgCl/7.5Au-D/SFO.

For PO, the oxygenate product detected with second-highest concentration (shown in Figs. 6.10c and f), altering the loading of Ag and Au in the AgCl/Au-D/SFO samples had only limited effect on selectivity. For samples where appreciable concentrations of PO (up to 20 ppm) were detected at the reactor outlet, namely Au-D/SFO and 7.5AgCl/2.5Au-D/SFO, selectivities towards PO remained low, regardless of the operating temperature.

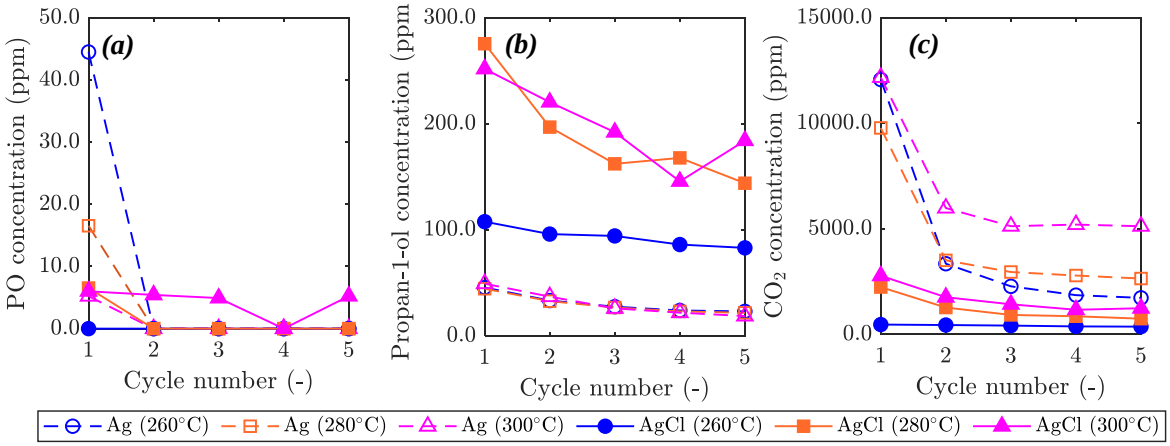


Fig. 6.11 Comparison of reaction products: **(a)** PO, **(b)** propan-1-ol, and **(c)** $CO_2$ in chemical looping over Ag/SFO and AgCl/SFO, in the temperature range 260-300°C. Lines between cycles included to help differentiate samples.

Results comparing the performance of Ag/SFO and AgCl/SFO are shown in Fig. 6.11. For the sample of Ag/SFO, a notable decrease in catalyst activity was observed after the first chemical looping cycle, with PO concentration decreasing to near-zero, and $CO_2$ concentration more than halving for all subsequent cycles. Contrastingly, the sample of AgCl/SFO sample showed comparatively stable performance over 5 cycles, with substantially greater propan-1-ol concentrations than observed with Ag/SFO, and lower concentrations of $CO_2$. All cycles over AgCl/SFO gave low concentrations of PO at the outlet, below 6.0 ppm. The rapid decrease in PO formation over Ag/SFO after the first cycle suggested that PO might have formed by reaction with trace species

which were not regenerated during oxidation, such as $Ag_2O$ or AgO, which are not thermodynamically stable at ≥260°C (Karakaya and Thompson, 1992). For both materials, raising the temperature from 260 to 300°C resulted in an increase in overall conversion, primarily driven by an increase in complete combustion to $CO_2$.

The effect of changing the preparation method for materials containing Au was also investigated, with the average product distributions over 5Ag/5Au-D/SFO (calcined at 650°C), Ag–AgCl/Au-H/SFO (calcined at 700°C to induce thermal decomposition of AgCl), and Ag/Au-L/SFO (prepared using Au–($\beta$-ala) precursor) shown in Fig. 6.12. The outlet gas compositions for each chemical looping cycle over Ag-AgCl/Au-H/SFO and Ag/Au-L/SFO are shown in Fig. 6.13.

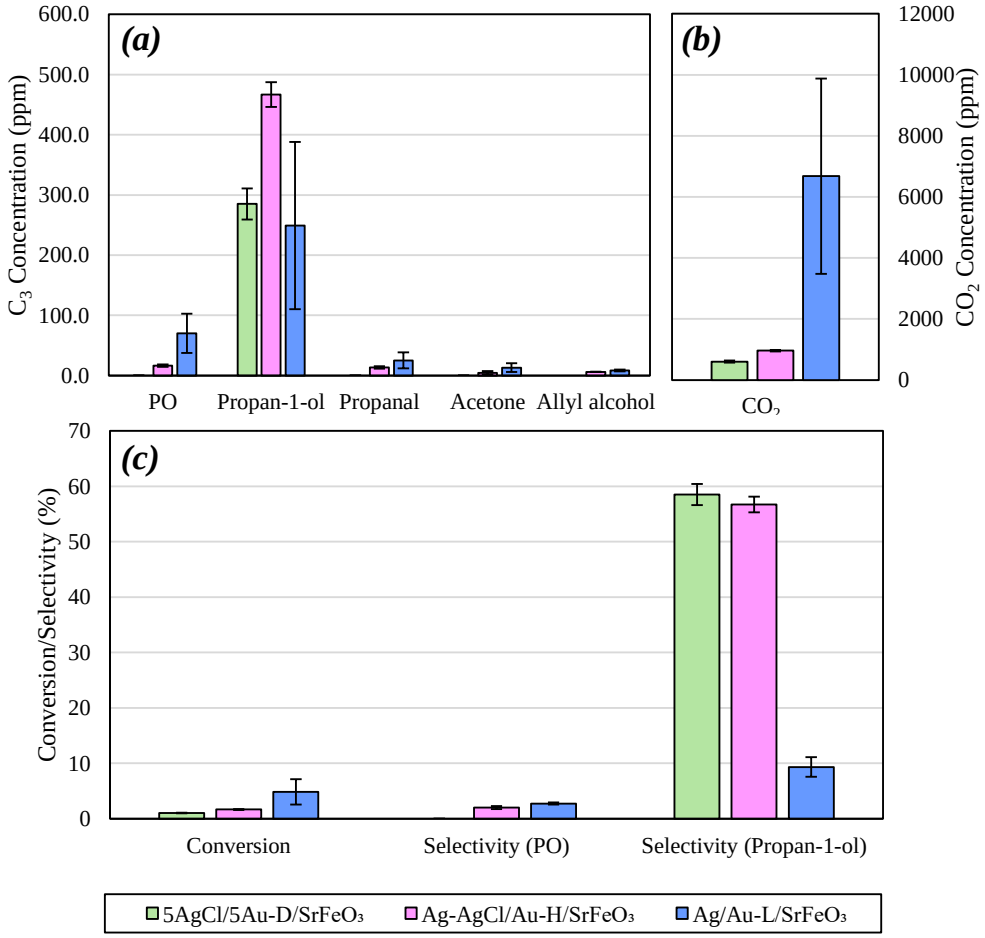


Fig. 6.12 Comparison of **(a)** concentrations of $C_3$ products, **(b)** concentrations of $CO_2$, and **(c)** overall conversion and selectivity, for 5AgCl/5Au-D/SFO, Ag-AgCl/Au-H/SFO, and Ag/Au-L/SFO at 280°C. Error bars correspond to standard deviation over 5 cycles.

Under chemical looping conditions at 280°C, the Ag-AgCl/Au-H/SFO produced a 65% greater concentration of propan-1-ol than the 5AgCl/5Au-D/SFO, with an average outlet concentration of 470 ppm propan-1-ol. However, the concentration of $CO_2$ was also around 60% greater. Propanal, allyl alcohol, and propylene oxide, were detected at low levels (10-20 ppm) for reaction over the sample of Ag-AgCl/Au-H/SFO, whereas none were detected for 5AgCl/5Au-D/SFO.

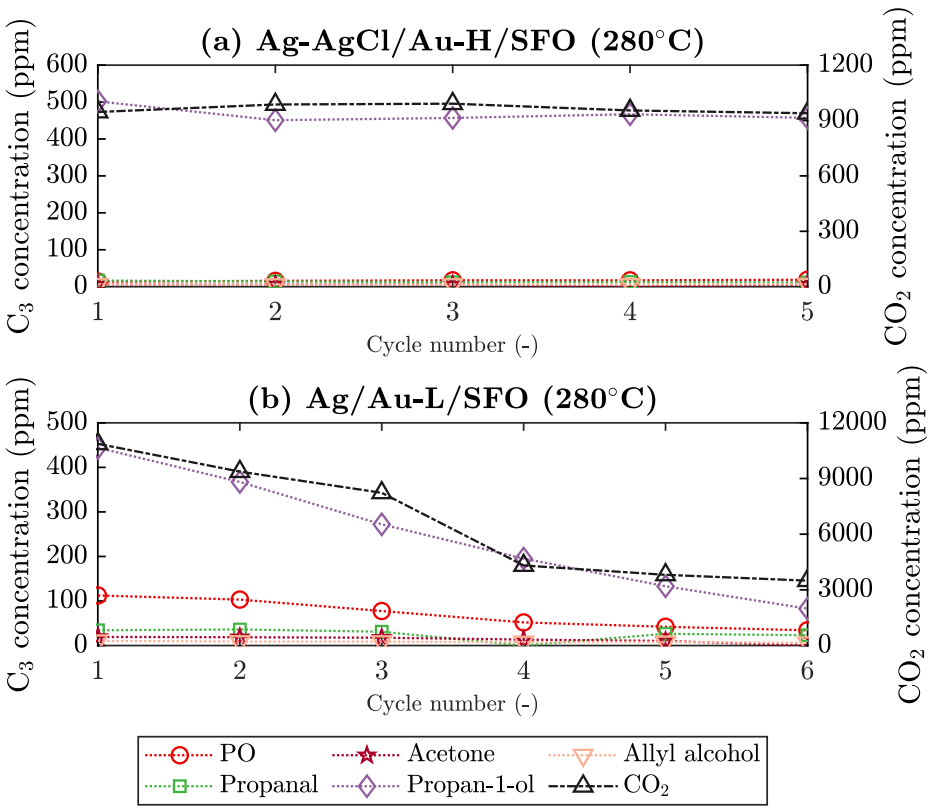


Fig. 6.13 Outlet composition for each chemical looping cycle over **(a)** Ag-AgCl/Au-H/SFO and **(b)** Ag/Au-L/SFO. Lines added to distinguish components.

For the chloride-free Ag/Au-L/SFO sample containing only small loading of Au (0.02 wt%), a substantially different product distribution was observed, as compared to the samples containing AgCl. The highest concentrations of PO for any sample, averaging *c.* 70 ppm over 5 cycles, were detected in the outlet stream for Ag/Au-L/SFO, alongside a slight decrease in propan-1-ol concentration as compared to 5AgCl/5Au-D/SFO or Ag-AgCl/Au-H/SFO. However, the total selectivity towards $C_3$ oxygenates was markedly lower, as a result of a substantial increase in complete combustion. Average concentrations of $CO_2$ detected were an order of magnitude greater than for other samples containing gold, and were comparable with Ag/SFO. Furthermore, for

reaction over Ag/Au-L/SFO, a substantial decrease in activity was measured over the course of 6 cycles (shown in Fig. 6.13, resulting in large error bars in the averaged values over the cycles), in a manner similar to the sample of Ag/SFO (shown in Fig. 6.11). Hence, the presence of gold, even in minimal quantities (here, 0.02 wt% Au) was essential for producing oxygenate products other than $CO_2$, but the overall behaviour of the Ag/Au-L/SFO material was dictated by the dominant metal, Ag.

In Appendix E.3, co-feeding experiments over bare SFO and Ag/SFO (shown in Fig. E.4a) showed that under conventional oxidation with gaseous oxygen, the materials were reactive towards complete combustion of propylene, but generated minimal concentrations of $C_3$ oxygenates. Chemical looping cycles over bare SFO showed some activity towards complete combustion, but no oxygenate products (shown in Fig. E.4b). Chemical looping cycles over Ag and AgCl/Au-D impregnated on an inert support, $Al_2O_3$, showed little activity, confirming that the oxygen was supplied to the reaction from the SFO support (shown in Fig. E.4c). Interestingly, the sample of bare SFO showed greater overall activity during chemical looping than Au-D/SFO, suggesting that unlike Ag, the presence of Au nanoparticles partially inhibited the availability of oxygen from Au/$SrFeO_{3-\delta}$.

## 6.4 Discussion

### 6.4.1 Effects of Cl and Au on product distribution

In this Chapter, AgCl catalysts were found to favour selective oxidation of propylene, whereas metallic Ag favoured complete combustion, both when comparing Ag/SFO and AgCl/SFO (Fig. 6.11), and when considering 5AgCl/5Au-D/SFO *vs* Ag–AgCl/Au-H/SFO and Ag/Au-L/SFO (Figs. 6.12 and 6.13). In previous studies with gaseous oxygen, unsupported bulk AgCl was found to be almost inert with respect to oxidation of propylene (Lu *et al.*, 2002; Luo *et al.*, 2003) although a three-phase mixture of Ag, AgCl and CuO was demonstrated to be somewhat selective towards formation of propylene oxide (Luo *et al.*, 2003). Furthermore, Ag promoted with 5 wt% NaCl to form mixed Ag–AgCl catalysts, both without supports (Lu and Zuo, 1999; Lu *et al.*, 2002) and with non-reactive metal oxide supports (Charisteidis and Triantafyllidis, 2020), have shown appreciable conversion and selectivity towards propylene oxide and acrolein. The lack of activity over AgCl alone is potentially caused by strong adsorption of molecular oxygen at the surface of AgCl with limited $O_{2,(g)}$ dissociation (Kim *et al.*,

2018), as compared to favourable dissociation of $O_2$ over Ag to form reactive Ag-$O_a$ sites, as discussed in Chapter 4.

The finding that the addition of Cl inhibited complete combustion, but enhanced selective oxidation, was in line with previous investigations into the effect of Cl on propylene oxidation (Charisteidis and Triantafyllidis, 2020; Lu and Zuo, 1999; Lu *et al.*, 2006, 2002; Seubsai and Senkan, 2011) However, previous studies focused on adding small quantities of Cl as a promoter for selective reactions. In studies on direct epoxidation of propylene with $O_{2(g)}$ (Lu *et al.*, 2002), promotion of Ag with NaCl to form a mixed Ag-AgCl catalyst substantially reduced the overall conversion of propylene, accompanied by an approximately proportional increase in selectivity towards propylene oxide. The presence of $Cl^-$ was found to suppress total oxidation of propylene by making adsorbed oxygen more electrophilic. Additionally, bulk AgCl has been demonstrated to be capable of accommodating and transporting oxygen, for example, Jayaraman and Yang (2005) used AgCl as a sorbent for pressure-swing adsorption of oxygen, demonstrating substantial capacity for adsorption of oxygen, and relatively rapid oxygen transport through the AgCl structure. Similarly, the results here demonstrated that AgCl on SFO can provide reactive atomic $O_a$ species to react with $C_3H_6$, forming oxygenated products.

For the sample of Ag/Au-L/SFO, the loading of Au was found to be low (0.02 wt%), and therefore the Au likely acted as a promoter for the Ag catalyst, rather than forming bulk AgAu alloy, although the exact mechanism remains unclear. The presence of Au strongly affected the selectivity of the reaction, with Ag/Au-L/SFO producing the highest concentration of PO, and limited propan-1-ol (as shown in Figs. 6.12 and 6.13). An order of magnitude more $CO_2$ was detected for reaction over the Ag/Au-L/SFO catalyst as compared to 5AgCl/5Au-D/SFO and Ag-AgCl/Au-H/SFO, with complete combustion expected to take place on the metallic Ag surface present in Ag/Au-L/SFO. The increase in $CO_2$ production for the chloride-free sample also supports the hypothesis that Cl species suppress complete combustion.

Given both AgCl/SFO and Au-D/SFO showed appreciable selectivity towards propan-1-ol, both AgCl and Au must be somewhat catalytically selective in the chemical looping arrangement towards propan-1-ol. From Fig. 6.10, maximum selectivity towards propan-1-ol was measured over the sample of 2.5AgCl/7.5Au/SFO, where both catalysts (AgCl and Au) were present. However, STEM-EDS images (Fig. 6.4) showed little overlap between particles of AgCl and AgAu, and therefore any possible synergy between the catalysts is unclear. Furthermore, from SEM and STEM-EDS (presented

in Figs. 6.4 and 6.5), AgCl was present as relatively small particles (*c.* 100 nm), which were likely to be catalytically active, whereas AgAu was present as larger chunks (*c.* 400 nm). For AgAu, the reaction might have occurred at atomic-scale Ag sites at the surface of the large AgAu particles, as demonstrated in previous studies (Geenen *et al.*, 1982; Rojluechai *et al.*, 2007).

The increase in propylene conversion with increasing ratio of Ag to Au on SFO (shown in Fig. 6.10a) suggests a faster rate of reaction at nanoparticles of AgCl catalyst than at the AgAu alloy. An extended reduction cycle (shown in Appendix E, Fig. E.3) showed a markedly faster rate of total release of oxygen in reactions over 7.5AgCl/2.5Au-D/SFO as compared to 2.5AgCl/7.5Au-D/SFO. For the latter material, the rate of oxygen release was approximately constant over 100 min, suggesting that the process was limited by surface reactions between propylene and $O_a$ species. In contrast, for the particles of 7.5AgCl/2.5Au-D/SFO, rate of oxygen release decreased over 100 min. Reduction times substantially longer than 1.5 min might be feasible over the catalysts investigated, however, chemical looping over 7.5AgCl/2.5Au-D/SFO showed that conversion rapidly decreased for reduction times up to 8-9 min before levelling off (shown in Fig. 6.9), and that selectivity gradually declined with longer reduction steps. Results presented in Fig. 6.7, however, confirmed that chemical looping with 1.5 min reduction (*i.e.* with more frquent regeneration of the oxygen carrier) lead to stable selectivity across at least 5 cycles.

### 6.4.2 Mechanisms of propan-1-ol formation

In this work, a different product distribution was detected as compared to other studies reported in literature (Khatib and Oyama, 2015; Teržan *et al.*, 2020) for propylene oxidation over Ag/Au catalysts, with propan-1-ol as a major reaction product.

While the main difference was the delivery of oxygen to reactions (here, from the SFO support in a chemical looping mode, whereas in other studies oxygen was supplied from the gas feed), the reason for the selective formation of propan-1-ol rather than any other possible oxygenates was unclear. Hence, several potential mechanisms for formation of the primary $C_3$ alcohol were considered, starting with direct hydration of propylene by $H_2O$ (Logsdon and Loke, 2000).

A hydration mechanism of propylene would predict formation of both primary and secondary alcohols. Propan-2-ol is generally the favoured product, as a result of the stabilisation of the secondary carbocation intermediate *via* electronic induction from the two methyl groups on either side of the localised positive charge (Li *et al.*,

2007; Logsdon and Loke, 2000). Given that <5 ppm of propan-2-ol was detected as compared to up to 500 ppm propan-1-ol under chemical looping conditions, the direct hydration mechanism appeared unlikely. Furthermore, addition of 2700 ppm $H_2O$ to propylene during reduction (delivered *via* the Owlstone vapour generator described in Section 2.3.3) did not result in a significant change in outlet concentration of propan-1-ol (shown in Fig. 6.14), suggesting that reaction between propylene and water was minimal. Interestingly, somewhat more PO and considerably more $CO_2$ was detected when $H_2O$ was added to the inlet stream, suggesting that water vapour promoted both epoxidation (Charisteidis and Triantafyllidis, 2020) and complete combustion.

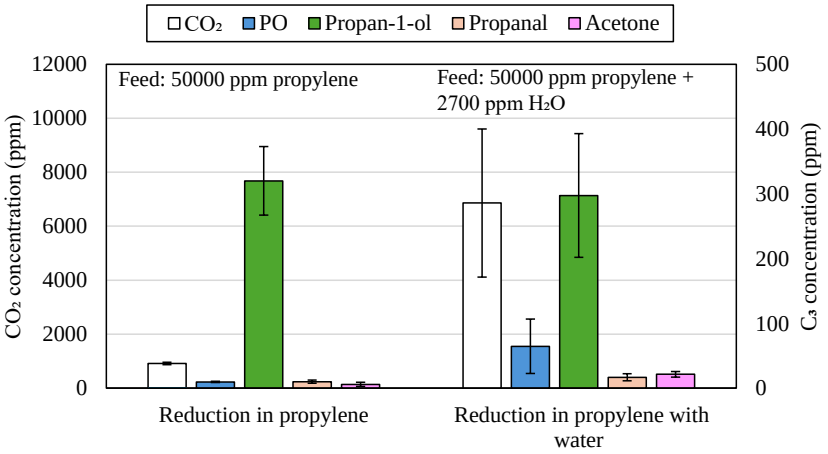


Fig. 6.14 Reaction products for reaction over 7.5AgCl/2.5Au-D/SFO, for 5vol% propylene with and without 2700 ppm $H_2O$ added. Error bars indicate standard deviation over three redox cycles.

Another possible mechanism considered involved an oxygenated intermediate, PO, which formed and reacted further *via* a two-step reaction, described in Eqs. 6.6 and 6.7. For the propan-1-ol formation step in Eq. 6.7, a list of possible reactions of PO with hydrogen to form other $C_3$ oxygenates were considered, summarised in Fig. 6.15, by formation of linear or branched oxametallacycle (OMC) surface species (shown in Fig. 6.16).

$$C_3H_6 + O \rightarrow C_3H_6O \tag{6.6}$$

$$C_3H_6O + 2H \rightarrow C_3H_7OH \tag{6.7}$$

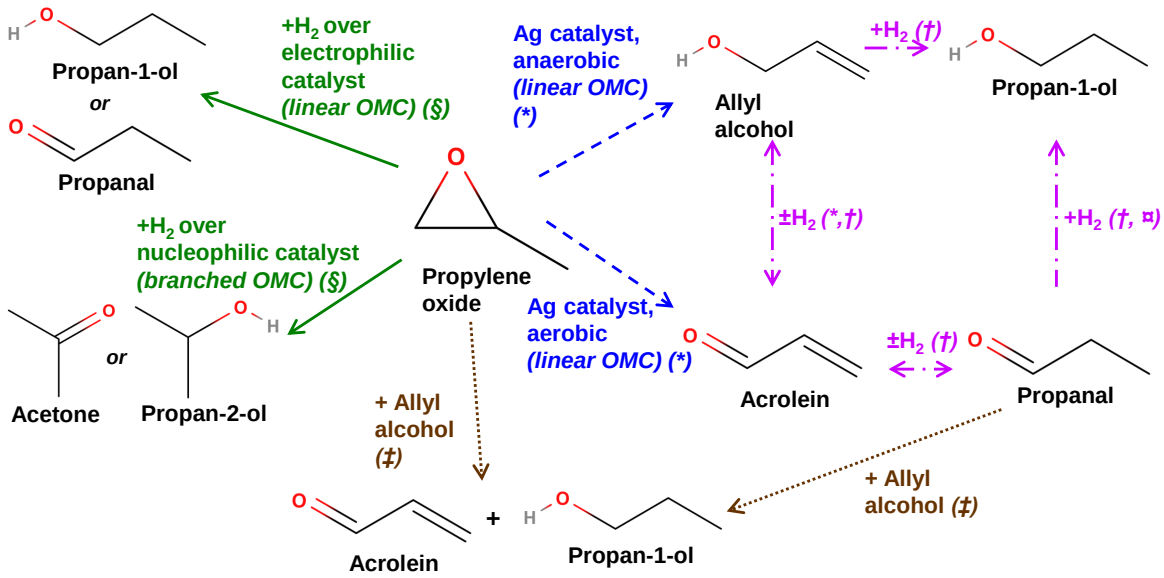


Fig. 6.15 Summary of main reactions of PO reported in literature. Symbols correspond to literature sources reporting each reaction (* = Kulkarni *et al.* (2012), †= Brandt *et al.* (2009) and Bron *et al.* (2005), §= Notheisz *et al.* (1986) and Bartók *et al.* (1980), ¤= Pan *et al.* (2012) and Pan *et al.* (2013), ‡= Imanaka *et al.* (1972) and Okamoto *et al.* (1973)).

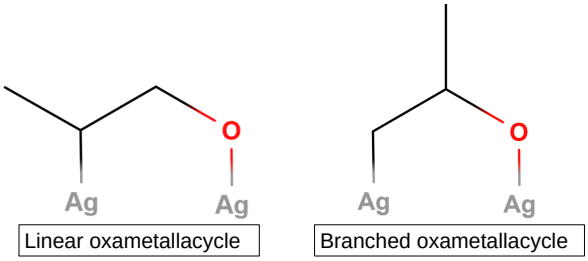


Fig. 6.16 Structures of linear and branched oxametallacycle (OMC) species formed by adsorption of $C_3H_6O$ on Ag, as described by Kulkarni *et al.* (2012) and Bartók *et al.* (1980).

The mechanisms shown in Fig. 6.15 involving a $C_3$ oxygenate intermediate reacting with hydrogen to form propan-1-ol require the presence of hydrogen in the reaction stream. A potential source of hydrogen in the chemical looping setup could be from propylene coking at the catalyst surface. With no oxygen present in the gas-phase during the step when the hydrocarbon is oxidised, any hydrogen formed might be able to go on to react with oxygenate intermediates to form propan-1-ol, or with lattice oxygen to form water. However, in the experiments presented, no residual hydrogen was detected in the outlet stream.

To identify the reaction of propylene in the presence of co-fed gaseous hydrogen, 2500 ppm $H_2$ was added to propylene for reduction over 7.5Ag/2.5Au-D/SFO, with comparison of outlet products shown in Fig. 6.17. Concentration of all $C_3$ oxygenates decreased as compared to the base-case without additional hydrogen, with a marked decrease in propan-1-ol, and a marked increase in the concentration of $CO_2$. However, conversion of hydrogen was high, at *c.* 85%, suggesting that the excess gaseous $H_2$ preferentially reacted with surface $O_a$ species on AgCl and AgAu, or with the SFO oxygen carrier, to form water. Therefore, the lattice oxygen available to react with propylene to form $C_3$ oxygenates might have been limited, with reduction of the support and the presence of water resulting in inferior selectivity towards propan-1-ol (as shown in Figs. 6.9 and 6.14).

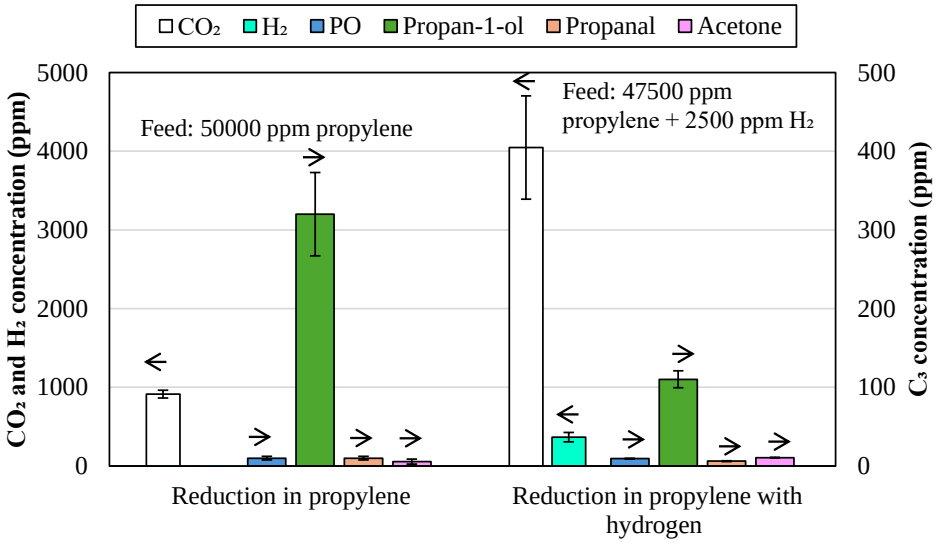


Fig. 6.17 Reaction products for reaction over 7.5Ag/2.5Au-D/SFO, for propylene with and without co-feeding of 2500 ppm $H_2$. Error bars indicate standard deviation over three redox cycles

Reactions between propylene oxide and $H_2$, as shown in Fig 6.15, have been investigated over various metal catalysts. Bartók *et al.* (1980) found that for propylene oxide, reaction over strongly electrophilic Ni or Cu catalysts resulted in the splitting of the more sterically hindered C–O bond in the PO molecule, forming a linear oxametallacycle species (shown in Fig. 6.16), which then reacted with $H_2$ and subsequently desorbed to form propan-1-ol or propanal (shown in Fig. 6.15, green solid lines). In contrast, when PO and $H_2$ were passed over less electrophilic catalysts, such as Pt or Pd, splitting of the less sterically hindered C–O bond was favoured, forming a branched oxametallacycle species. The branched surface species, could then react with $H_2$, desorbing to form propan-2-ol or acetone. As AgCl is highly electrophilic (Lu *et al.*, 2002), samples containing AgCl might behave similarly to the Ni or Cu surfaces when exposed to PO. Therefore, propan-1-ol may form over $x$AgCl/(10–$x$)Au-D/SFO catalysts by initial formation of PO, followed by the reaction of the PO with hydrogen at a strongly electrophilic AgCl surface. Gold and gold–silver surfaces might be expected to behave in a similar manner to Pt or Pd, *i.e.* by forming a non-electrophilic surface. The Au surface would then be expected to favour formation of branched oxametallacycle surface species and, consequently, secondary oxygenate products (acetone and propan-2-ol). However, Au-D/SFO was primarily active towards formation of propan-1-ol (shown in Fig. 6.10), with little to no selectivity towards acetone or propan-2-ol, suggesting electrophilic behaviour and reaction *via* the linear oxametallacycle route. The apparent electrophilic behaviour of Au agreed with the findings of Wang *et al.* (2021) that noble metals impregnated on perovskites transfer electrons to the perovskite oxide, resulting in an electrophilic metal surface. For reactions over Ag/SFO in the absence of chloride (shown in Fig. 6.11), the primary reaction product was $CO_2$, caused by catalytic combustion of propylene *via* allylic stripping of hydrogen (Khatib and Oyama, 2015), outweighing the contribution of any oxametallacycle species formed over the Ag surface (Kulkarni *et al.*, 2012).

To determine whether the mechanism of propan-1-ol formation *via* hydrogenation of PO was possible, chemical looping experiments were performed with PO added to the feed stream. Figure 6.18a compares the outlet compositions for reaction over 5AgCl/5Au/SFO, with and without 400 ppm PO added to the propylene feed stream. Adding PO resulted in 46% less propan-1-ol in the outlet, and 5 times more $CO_2$. When lower concentrations (500 ppm) of propylene and PO were fed over 5AgCl/5Au-D/SFO, as shown in Fig. 6.18b, propan-1-ol was not detected in the outlet, with acetone and propanal as the only $C_3$ oxygenate products with concentrations >5 ppm. Co-feeding

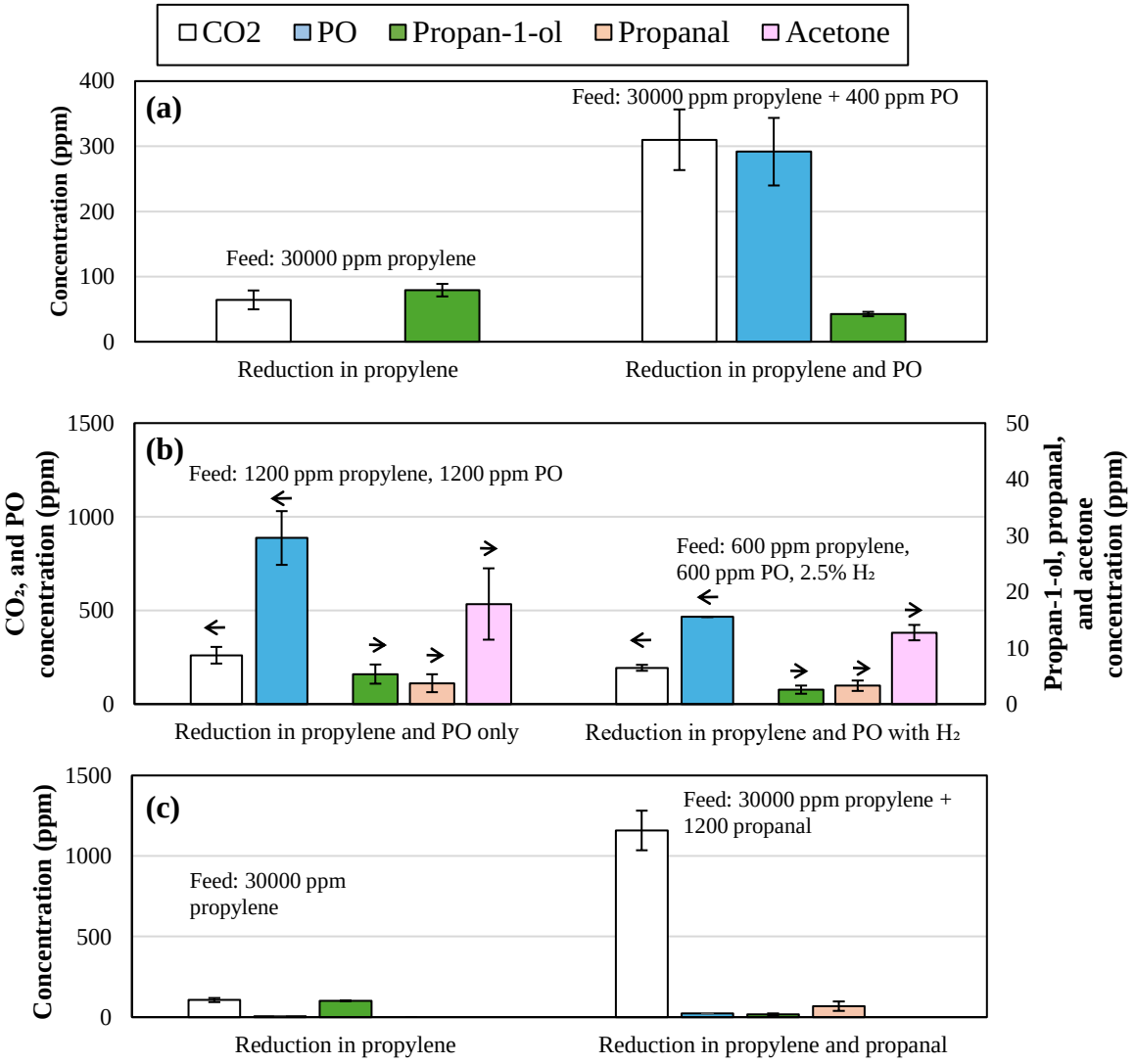


Fig. 6.18 Reaction products for reaction over 5AgCl/5Au-D/SFO, for **(a)** propylene with and without PO added **(b)** dilute PO/propylene, with and without co-feeding $H_2$ **(c)** for propylene with and without co-feeding propanal vapour. Error bars show standard deviation from 3 cycles, arrows indicate y-axis for each species. Feed composition given on each sub-figure, with balance gas $Ar/N_2$.

2.5 vol% $H_2$ (*i.e.* for a mixed feed of propylene, PO, and $H_2$) did not substantially alter the distribution of products. Hence, the consumption of the additional PO added to the feed stream to form $CO_2$ indicated that the PO competed with propylene for adsorption sites to react with $O_a$, with over-oxidation to form $CO_2$ after adsorbing, rather than hydrogenation to propan-1-ol. Therefore, hydrogenation of PO to form propan-1-ol appeared to be feasible only prior to the oxametallacycle desorbing.

Kulkarni *et al.* (2012) proposed that for PO adsorbed onto an Ag surface, the gaseous PO, and linear and branched oxametallacycle intermediates, are in dynamic equilibrium with one another. Therefore, any PO added to the inlet stream would increase the amount of all intermediates that can isomerise to propan-1-ol, but also to other $C_3$ oxygenates. The linear oxametallacycle is able to undergo a linear 1,2 hydrogen shift, and then desorb as allyl alcohol (shown in Fig. 6.15, blue dashed lines). Under aerobic conditions with $O_{2,(g)}$ in the feed stream, Kulkarni *et al.* (2012) found that any allyl alcohol formed was rapidly dehydrogenated to form acrolein, which then fully oxidised to $CO_2$, whereas under anaerobic conditions, the allyl alcohol was relatively stable.

Here, low levels (6–10 ppm) of allyl alcohol were detected in the outlet stream for reaction of propylene over Ag–AgCl/Au-H/SFO and Ag/Au-L/SFO samples (shown in Fig. 6.12a). Allyl alcohol adsorbed on Ag is also able to react with adsorbed hydrogen, $H_a$ (Brandt *et al.*, 2009; Bron *et al.*, 2005), to form propan-1-ol (shown in Fig. 6.15, pink dash-dotted lines). Therefore, allyl alcohol might form by reaction of propylene with $O_a$ without rapidly dehydrogenating to acrolein, and then undergo hydrogenation at the catalyst surface to form propan-1-ol.

Reactions between PO and allyl alcohol, and propanal and allyl alcohol, have been reported by Imanaka *et al.* (1972) and Okamoto *et al.* (1973). A hydrogen transfer reaction between one molecule of PO or propanal, and one molecule of allyl alcohol, can occur to form propan-1-ol and acrolein (shown in Fig. 6.15, brown dotted lines). Reaction between PO and allyl alcohol might occur over AgCl/Au/SFO catalysts; however, the hydrogen transfer reaction would predict acrolein forming in a 1:1 ratio with propan-1-ol. As no acrolein was detected in the chemical looping experiments, the reaction between PO and allyl alcohol was deemed unlikely to contribute significantly to overall propan-1-ol formation reported here. Furthermore, propanal was predicted to also undergo reaction with allyl alcohol to form propan-1-ol and acrolein (Okamoto *et al.*, 1973). Given that adding propanal to the feed stream during reduction (shown in Fig. 6.18c) resulted in a moderate decrease in formation of propan-1-ol, the reaction

between allyl alcohol and propanal was discounted as a major source of propan-1-ol in the outlet stream.

The reaction of aldehydes and ketones (*i.e.* propanal and acetone) with hydrogen over gold catalysts to form primary or secondary alcohols, respectively, has been investigated *via* temperature programmed desorption studies by Pan *et al.* (2013, 2012). The authors found that in the case of hydrogen atoms adsorbed on Au(111) surfaces, hydrogenation of propanal to propan-1-ol was favoured, and that minimal hydrogenation of acetone to propan-2-ol occurred, as the reaction pathway to form propan-2-ol was not thermodynamically favourable. To determine if propan-1-ol formation *via* propanal was feasible, *c.* 1200 ppm propanal was added to the 5 vol% propylene feed stream over 5AgCl/5Au-D/SFO. Figure 6.18c shows that the addition of propanal to the inlet feed did not increase the concentration of propan-1-ol measured in the outlet, and instead, showed an increase in complete combustion only. The lack of an increase in propan-1-ol concentration suggested that any propanal formed over AgCl/Au-D/SFO catalysts underwent further oxidation to $CO_2$, and so that the reaction mechanism for formation of propan-1-ol was unlikely to proceed *via* a propanal intermediate.

In summary, the most likely reaction mechanism for formation of propan-1-ol was concluded to proceed *via* initial reaction of propylene with adsorbed surface $O_a$ to form a linear oxametallacycle surface species. The linear oxametallacycle then either reacted directly with hydrogen to form propan-1-ol, or underwent a hydrogen shift to form allyl alcohol, which was then subsequently hydrogenated to propan-1-ol. The chloride in the AgCl/SFO and AgCl/Au-D/SFO materials was determined to likely affect the reaction mechanism by making the surface of Ag more electrophilic, promoting formation of the linear oxametallacycle species, hence favouring primary over secondary products, and suppressing complete combustion of propylene at the surface of metallic Ag (Lu *et al.*, 2002). However, the surface configurations of the linear oxametallacycle species, with respect to regions of chloride species at the surface of the catalyst, are not fully understood.

Further understanding of the surface mechanism might be achievable by performing density-functional theory calculations of the hypothesised transition states to determine the most thermodynamically feasible pathways, and through surface-sensitive experimental measurements (*e.g.* NAP-XPS and *in-situ* Raman measurements of Ag and Au surface states over chemical looping cycles, as performed in Chapter 4).

## 6.5 Conclusions

The selective oxidation of propylene using a chemical looping approach was demonstrated. Materials composed ofAgCl, AgAu, and mixed AgCl/Au catalysts supported on SFO showed considerable selectivity towards propan-1-ol, with limited formation of other oxygenates. Catalysts containing AgCl were more selective towards propan-1-ol than metallic Ag, which promoted complete combustion. Performance of the AgCl/Au catalysts was sensitive to the ratio of Ag and Au, with higher Ag content leading to complete combustion being favoured over formation of any oxygenated products. Selectivity towards propan-1-ol of 80% was achieved over 2.5AgCl/7.5Au-D/SFO, albeit at <1% propylene conversion. The results demonstrated that chemical looping operation can lead to new reaction pathways, strongly dependent on the oxygen carrier and the catalyst. The mechanism of the chemical looping formation of propan-1-ol was also discussed, suggesting that the most likely pathway proceeded by surface reactions of the linear oxametallacycle intermediate, rather than desorption and subsequent re-absorption of oxygenated species.

# Chapter 7

# Conclusions and future work

The work in this Dissertation investigated the reactive properties of materials for chemical looping composed of a non-stoichiometric oxygen carrier ($SrFeO_{3-\delta}$), modified with one or more elements as additives. The $Ag/SrFeO_{3-\delta}$ system, composed of particles of $SrFeO_{3-\delta}$ impregnated with nanoparticles of Ag, was of particular interest, as $Ag/SrFeO_{3-\delta}$ has been applied previously for catalytic oxidation processes operated in a chemical looping mode, including epoxidation of ethylene (Chan *et al.*, 2018b) and dehydrogenation of ethanol (Gebers *et al.*, 2023).

In previous studies, the interactions between the metal catalyst and the oxygen carrier had not been explained, and the mechanisms of oxygen transport within the material were unclear. Furthermore, although certain modifications to the oxygen carrier (*e.g.* surface or bulk impregnation of $Ag/SrFeO_{3-\delta}$ with $CeO_2$, or partial substitution of Sr with Ce) had been reported to improve performance for selective oxidation of ethylene *via* chemical looping, by improving oxygen availability from the material (Marek and García-Calvo Conde, 2021; Marek *et al.*, 2020), the effects of such modifications on the kinetics of oxygen release and reuptake had not been studied systematically.

Therefore, in this work, a series of $SrFeO_{3-\delta}$ materials with various surface, bulk, and structural modifications were prepared. The materials were investigated for chemical looping air separation, and for the selective catalytic oxidation of ethylene and propylene in a chemical looping mode. Modifications to the oxygen carrier, and to the Ag-based catalyst impregnated at the surface, were found to have a profound impact on the availability of oxygen from the material, and on the distribution of oxidation products.

In Chapter 3, the addition of $CeO_2$ to the bulk or surface of $SrFeO_{3-\delta}$ was shown to slightly increase the availability of oxygen, decreasing the minimum temperature required for oxygen release in $N_2$ by 10-20°C relative to unmodified $SrFeO_{3-\delta}$. The sample with $CeO_2$ mixed into the bulk of $SrFeO_{3-\delta}$ showed a small, but statistically significant, improvement in the kinetics of oxygen uncoupling.

Modification of $SrFeO_{3-\delta}$ with nanoparticles of Ag (15 wt%) had a larger impact on the availability of oxygen, decreasing the minimum temperature for oxygen uncoupling by 60°C, and substantially increasing the rates of oxygen release and re-uptake. The thermodynamic influence of Ag on $SrFeO_{3-\delta}$ was also investigated, with the presence of Ag increasing the proportion of oxygen vacancies (*i.e.* greater values of $\delta$) at equilibrium over the range of conditions investigated ($T$ = 500-600°C, $pO_2 = 10^{-5}$-0.21 atm), with experimental parameters relevant to chemical looping air separation selected. However, development of a full thermodynamic model for the $pO_2$-$T$-$\delta$ characteristics of $Ag/SrFeO_{3-\delta}$ was deemed beyond the scope of this Dissertation, given the large number of measurement points required.

Novel sampling methods (Wilson and Muhich, 2024) can the decrease the number of measurements required to form a complete thermodynamic model of $pO_2$-$T$-$\delta$ for a given material, by constructing a model based on a partial set of $pO_2$-$T$-$\delta$ data points, and identifying regions of $pO_2$-$T$ conditions with the greatest uncertainty in $\delta$ for further experimental measurements. Future work could apply such techniques to extend the range of $T$ and $pO_2$ conditions investigated, and hence able to model the behaviour of $Ag/SrFeO_{3-\delta}$ at conditions relevant for other applications (*e.g.* selective oxidation).

Furthermore, the loadings of Ag and $CeO_2$ used in experiments were selected arbitrarily in order to align with previous studies (Marek and García-Calvo Conde, 2021; Marek *et al.*, 2020). Gabra (2022) determined that higher loadings of Ag (up to 30 wt%) on $SrFeO_{3-\delta}$ altered the reduction characteristics of $Ag/SrFeO_{3-\delta}$, however, future work should investigate whether lower loadings of Ag can still achieve a meaningful improvement in availability of oxygen and rates of reaction. Additionally, given the relatively high cost of Ag, the behaviour of $SrFeO_{3-\delta}$ impregnated with nanoparticles of base metals, such as Ni (Orsini *et al.*, 2023; Zhong *et al.*, 2024; Zhu *et al.*, 2018), might be of interest for future studies.

Chapter 4 investigated the chemical changes of $Ag/SrFeO_{3-\delta}$ during reduction and oxidation. Bulk characterisation of $Ag/SrFeO_{3-\delta}$ using *in-situ* XRD during reduction in $H_2$ indicated that as well as improving oxygen availability at a relatively low extent

of reduction (*i.e.* $0 < \delta < 0.5$, as in Chapter 3), the presence of Ag also decreased the temperature required for phase transition to brownmillerite $SrFeO_{2.5}$, from around 500°C to 300°C. However, under further reduction in $H_2$ (*e.g.* 2 h at ≥850°C), the brownmillerite $SrFeO_{2.5}$ phase would be expected to segregate into strontium- and iron-rich phases (Savinskaya *et al.*, 2008), ultimately forming SrO and metallic Fe (Marek *et al.*, 2018a). The influence of Ag on the phase segregation behaviour of $SrFeO_{2.5}$ remains unknown, as the Ag/$SrFeO_{3-\delta}$ material was not reduced below (3-$\delta$) = 2.5. Furthermore, although metallic Fe and Ag are immiscible under most conditions (Boldman *et al.*, 2021; Sumiyama and Nakamura, 1984), the effect of substantial structural changes in the oxygen carrier on the stability of the Ag nanoparticles might merit further investigation.

Moreover, from *in-situ* TEM measurements, the reduction of particles of $SrFeO_{3-\delta}$ with and without Ag was observed to proceed approximately uniformly from the edge of the particle inwards, without localisation of reduced regions around nanoparticles of Ag. Hence, oxygen diffusion within Ag/$SrFeO_{3-\delta}$ was deemed to be relatively rapid. However, the scan time used for parallel TEM imaging, EDS scanning, EELS measurements, and SAED imaging was relatively slow (of the order 10 min *per* EELS scan, and 45 min *per* full set of measurements). Hence, information regarding any dissipation of spatial gradients in composition of the order of seconds or faster could not be captured. Future TEM studies could apply EELS scans of shorter duration at a constant temperature, in order to observe the faster-acting movement of oxygen in the immediate vicinity of Ag. Future experiments could also potentially investigate the use of samples with a well-defined Ag-$SrFeO_{3-\delta}$ interface where such phenomena could be readily visible, analogous to the Pd-$CeO_{2-\delta}$ nanocubes prepared by Mahadi *et al.* (2020).

The NAP-XPS experiments, with heating and cooling in $H_2$ and $O_2$ respectively, revealed the behaviour of the surface species on $SrFeO_{3-\delta}$ and Ag/$SrFeO_{3-\delta}$ during reduction and oxidation. Over the course of a reduction step, the fraction of chemisorbed oxygen present on $SrFeO_{3-\delta}$ declined relative to the lattice oxygen species in $SrFeO_{3-\delta}$ and the surface layer of SrO. Furthermore, when nanoparticles of Ag were added, Ag-$O_x$ species were detected, and the total fraction of adsorbed oxygen declined more rapidly, to a lower final value. Hence, the Ag-$O_x$ species were suggested to aid reduction of the Ag/$SrFeO_{3-\delta}$ material by reacting with incoming hydrogen, with the Ag nanoparticles acting as a 'gateway' for removal of oxygen from the material at lower temperatures. Raman spectroscopy and $H_2$-TPR identified the Ag-$O_x$ species as

atomic Ag-O, peroxide Ag-$O_2^{2-}$, and superoxide Ag-$O_2^-$. Mechanisms of oxygen transfer from the $SrFeO_{3-\delta}$ lattice to the surface of Ag were proposed, with peroxide Ag-$O_2^{2-}$ acting as a reaction intermediate. However, to confirm these proposed mechanisms, future work could incorporate *in-situ* Raman spectroscopy with isotope tagging, to identify whether the peroxide species do indeed act as intermediates, and, isothermal NAP-XPS experiments with gas switching between reducing and oxiding environments to track the removal and adsorption of surface species over time.

Furthermore, the NAP-XPS and Raman experiments reported in this Dissertation were performed using $H_2$ as a reducing agent. However, the experiments could be extended by using a hydrocarbon as the reducing agent, as a more realistic representation of chemical looping as applied for selective oxidation reactions, identifying the intermediate surface species formed during reaction. Additionally, scans of the S2p region suggested that as well the bulk $SrFeO_{3-\delta}$ oxygen carrier and Ag catalyst, sulphur impurities in the Ag/$SrFeO_{3-\delta}$ material also undergo redox activity during chemical looping. Given that $AgSO_x$ species are hypothesised to participate in the selective oxidation of alkenes over Ag (Carbonio *et al.*, 2023; Jones *et al.*, 2018), future work should confirm the redox behaviour of sulphur during chemical looping selective oxidation processes, and, identify whether deliberately adding additional sulphur affects the performance of the material.

Chapter 5 investigated the application of Ag-$Na_2CO_3$-$SrFeO_{3-\delta}$ materials incorporating a protective carbonate layer for selective oxidation, here, for the epoxidation of ethylene. Depending on the location of the carbonate layer, on top of the particles of Ag, or, in between Ag and $SrFeO_{3-\delta}$, the relative influence on oxygen availability of the interaction between Ag and $SrFeO_{3-\delta}$ (demonstrated in Chapter 3), and the formation of Ag-$O_x$ surface species (as identified in Chapter 4), could be determined.

The presence of the carbonate layer was found to slightly inhibit the release of oxygen during reduction in $H_2$ or $N_2$, increasing the minimum temperature required for reduction relative to Ag/$SrFeO_{3-\delta}$ by 50-90°C. The location of the carbonate layer was found to have little influence on the rate of reaction in hydrogen, whereas, during reduction in ethylene, the sample with an external layer of $Na_2CO_3$ covering the surface of the Ag nanoparticles reacted more slowly than the sample with Ag nanoparticles on the outside of the carbonate. The importance of the exposed Ag surface was in line with the conclusions of Chapter 4, where reactive Ag-$O_x$ surface species aided the removal of oxygen, and in Chapter 5 were shown to be necessary for rapid reaction with ethylene. Contrastingly, despite being shown to alter the $pO_2$-$T$-$\delta$ characteristics

of the material in Chapter 3, Ag-$SrFeO_{3-\delta}$ interactions played a less important role in determining effective oxygen availability during reduction in ethylene.

Chemical looping epoxidation experiments over Ag-$Na_2CO_3$-$SrFeO_{3-\delta}$ confirmed the importance of the exposed Ag surface. While samples without an exposed Ag surface were almost inactive for reaction in ethylene at 270°C, the sample with a $Na_2CO_3$ layer in between the Ag nanoparticles and the $SrFeO_{3-\delta}$ core was active, and showed slightly improved selectivity towards ethylene oxide as compared to Ag/$SrFeO_{3-\delta}$. However, the sequential impregnation method used to prepare samples of Ag-$Na_2CO_3$-$SrFeO_{3-\delta}$ resulted in considerable uncertainty as to the thickness and uniformity of the carbonate layer, especially in the sample with Ag deposited on top of the $Na_2CO_3$.

Future applications of Ag-$Na_2CO_3$-$SrFeO_{3-\delta}$ materials should attempt to refine the synthesis procedure, in order to achieve a uniform carbonate layer of accurately known thickness. Additionally, the 10 wt% target loading of $Na_2CO_3$ chosen for experiments was selected arbitrarily in order to aid characterisation (as samples with lower loadings showed very weak or no Raman signals). However, in terms of reactivity, lower loadings might be preferable, by preventing contact between the ethylene and $SrFeO_{3-\delta}$ while inhibiting the transport of oxygen as little as possible. Moreover, the selective oxidation reaction used as an example in Chapter 5, chemical looping epoxidation, might not be the best application for materials incorporating the protective layer. Reactions with high overall conversion, such as dehydrogenation of methanol over Ag, with typical conversion around 85-98% (Millar and Collins, 2017; Thrane *et al.*, 2021), might stand to gain a greater improvement in yield by preventing combustion of the reactants or products at the surface of the oxygen carrier.

In Chapter 6, chemical looping of propylene over Ag/$SrFeO_{3-\delta}$-based materials was investigated. Reaction over Ag/$SrFeO_{3-\delta}$ resulted in high conversion, but was not selective in either a chemical looping or co-feeding mode, producing $CO_2$ as the main product containing carbon. However, catalysts modified with Cl and, or Au showed promising selectivity for an unexpected oxidation product, propan-1-ol. The ratio of Ag to Au influenced the behaviour of the samples, with a higher ratio ratio of Au favouring higher selectivity at lower conversion, with a maximum selectivity towards propan-1-ol of 80% at around 0.75% conversion of propylene over the sample of 2.5AgCl/7.5Au/$SrFeO_{3-\delta}$. Interestingly, the results in Chapter 6 suggested that the enhancement in oxygen availability from the presence of a Ag reported in Chapters 3 and 4 applied even when Ag was partially present as AgCl, and, that nanoparticles of pure Au slightly inhibited oxygen availability relative to bare $SrFeO_{3-\delta}$.

A mechanism for propan-1-ol formation over AgCl was proposed by co-feeding possible intermediate products (propylene oxide and propanal) alongside propylene during reduction and monitoring the distribution of reaction products. However, to confirm the proposed mechanism, future studies should perform density functional theory calculations to determine whether the reactions of the linear oxametallacycle species in the proposed mechanism are feasible. Furthermore, the nature of the oxygen surface species present on AgCl, and, or, AgAu remain unclear; hence, an *in-situ* Raman spectroscopy and NAP-XPS study, similar to the experiments presented in Chapter 4, might help unravel the reactions at the catalyst surface.

Samples of chloride-free Ag/Au/$SrFeO_{3-\delta}$, prepared *via* a ligand complexation method, showed some promise towards propylene oxide formation. However, the loading of Au was much lower than expected from the synthesis, and hence the sample showed a considerable extent of complete combustion of propylene over metallic Ag. Hence, future work could consider alternative sythesis methods for preparing Cl-free AgAu nanoparticles supported on $SrFeO_{3-\delta}$, for example, by preparing alloy nanoparticles *ex-situ* (Csapó *et al.*, 2012), which could then be impregnated onto the $SrFeO_{3-\delta}$ support, or, using atomic layer deposition techniques to deposit Ag and Au metal directly onto the surface (Lu *et al.*, 2014; Wack *et al.*, 2019).

In summary, the research in this Dissertation describes the behaviour of the Ag/$SrFeO_{3-\delta}$ system under a variety of reactive conditions and applications, with an emphasis on the interactions between the Ag metal, the $SrFeO_{3-\delta}$ support, and any additional phases present (*e.g.* surface layers of $Na_2CO_3$, or $CeO_2$ mixed into the bulk). In particular, the findings in Chapters 3 and 4 demonstrate that the presence of Ag enhances the availability of lattice oxygen from $SrFeO_{3-\delta}$, and the rate of oxygen release and uptake. The mechanistic considerations proposed in this Dissertation would be well-complemented by computational density functional theory studies, to determine the most likely possible reaction pathways for oxygen uncoupling and selective oxidation over Ag/$SrFeO_{3-\delta}$, and applying the findings to develop new materials for chemical looping.

# References


Abd El-Naser, A., Abdel-Khalek, E. K., Nabhan, E., Rayan, D., Gaafar, M. S., & Abd El-Aal, N. S. (2021). Study the influence of oxygen-deficient ($\delta = 0.135$) in SrFeO 3-$\delta$ nanoparticles perovskite on structural, electrical and magnetic properties. *Philosophical Magazine*, *101*(6), 710–728, https://doi.org/10.1080/14786435.2020.1862427.

Adar, F., Lee, E., Mamedov, S., & Whitley, A. (2010). Experimental Evaluation of the Depth Resolution of a Raman Microscope. *Microscopy and Microanalysis*, *16*(S2), 360–361, https://doi.org/10.1017/S1431927610055352.

Alzahrani, H. A. & Bravo-Suárez, J. J. (2023). In situ Raman spectroscopy study of silver particle size effects on unpromoted Ag/$\alpha$-Al2O3 during ethylene epoxidation with molecular oxygen. *Journal of Catalysis*, *418*, 225–236, https://doi.org/10.1016/J.JCAT.2023.01.016.

Avval, T. G., *et al.* (2019). Oxygen gas, O2(g), by near-ambient pressure XPS. *Surface Science Spectra*, *26*(1), 014021, https://doi.org/10.1116/1.5100962.

Bale, C., *et al.* (2016). FactSage thermochemical software and databases, 2010–2016. *Calphad*, *54*, 35–53, https://doi.org/10.1016/j.calphad.2016.05.002.

Banaszkiewicz, T., Chorowski, M., & Gizicki, W. (2015). Comparative analysis of cryogenic and PTSA technologies for systems of oxygen production. *AIP Conference Proceedings*, *1573*(1), 1373, https://doi.org/10.1063/1.4860866.

Barkalov, O. I., Zaitsev, S. V., & Sedykh, V. D. (2022). Strontium ferrite SrFeO3-$\delta$ (2.50 3-$\delta$ 2.87) studied by Raman and Mössbauer spectroscopy. *Solid State Communications*, *354*(April), 114912, https://doi.org/10.1016/j.ssc.2022.114912.

Barrie, A. & Street, F. J. (1975). An Auger and X-ray photoelectron spectroscopic study of sodium metal and sodium oxide. *Journal of Electron Spectroscopy and Related Phenomena*, *7*(1), 1–31, https://doi.org/10.1016/0368-2048(75)80052-1.

Barrie, P. J. (2011a). The mathematical origins of the kinetic compensation effect: 1. the effect of random experimental errors. *Physical Chemistry Chemical Physics*, *14*(1), 318–326, https://doi.org/10.1039/C1CP22666E.

Barrie, P. J. (2011b). The mathematical origins of the kinetic compensation effect: 2. the effect of systematic errors. *Physical Chemistry Chemical Physics*, *14*(1), 327–336, https://doi.org/10.1039/C1CP22667C.

## References


Bartók, M., Notheisz, F., & Zsigmond, (1980). Stereochemistry of heterogeneous catalytic hydrogenolysis and isomerization of oxiranes. *Journal of Catalysis*, *63*(2), 364–371, https://doi.org/10.1016/0021-9517(80)90089-5.

Batuk, M., Vandemeulebroucke, D., Ceretti, M., Paulus, W., & Hadermann, J. (2023). Topotactic redox cycling in SrFeO2.5+$\delta$ explored by 3D electron diffraction in different gas atmospheres. *Journal of Materials Chemistry A*, *11*(1), 213–220, https://doi.org/10.1039/D2TA03247C.

Belsky, A., Hellenbrandt, M., Karen, V. L., & Luksch, P. (2002). New developments in the Inorganic Crystal Structure Database (ICSD): accessibility in support of materials research and design. *Acta Crystallographica Section B Structural Science*, *58*(3), 364–369, https://doi.org/10.1107/s0108768102006948.

Beppu, K., Hosokawa, S., Asakura, H., Teramura, K., & Tanaka, T. (2018). Role of lattice oxygen and oxygen vacancy sites in platinum group metal catalysts supported on Sr 3 Fe 2 O 7$\delta$ for NO-selective reduction. *Catalysis Science & Technology*, *8*(1), 147–153, https://doi.org/10.1039/C7CY01861D.

Beppu, K., *et al.* (2017). Enhanced oxygen-release/storage properties of Pd-loaded Sr 3 Fe 2 O 7$\delta$. *Physical Chemistry Chemical Physics*, *19*(21), 14107–14113, https://doi.org/10.1039/C7CP01614J.

Bian, Z., *et al.* (2023). Solid-State Electrochemical Thermal Transistors with Strontium Cobaltite-Strontium Ferrite Solid Solutions as the Active Layers. *ACS Applied Materials and Interfaces*, *15*(19), 23512–23517, https://doi.org/10.1021/acsami.3c03660.

Biesinger, M. C. (2022). Accessing the robustness of adventitious carbon for charge referencing (correction) purposes in XPS analysis: Insights from a multi-user facility data review. *Applied Surface Science*, *597*, 153681, https://doi.org/10.1016/J.APSUSC.2022.153681.

Bischoff, K. (1967). An extension of the general criterion for importance of pore diffusion with chemical reactions. *Chemical Engineering Science*, *22*(4), 525–530, https://doi.org/10.1016/0009-2509(67)80035-6.

Bohn, C. D. (2010). *The Production of Pure Hydrogen with Simultaneous Capture of Carbon Dioxide*. PhD thesis, University of Cambridge https://www.repository.cam.ac.uk/handle/1810/226854.

Boldman, W. L., Garfinkel, D. A., Collette, R., Jorgenson, C. S., Pradhan, D. K., Gilbert, D. A., & Rack, P. D. (2021). Exploring the composition, phase separation and structure of AgFe alloys for magneto-optical applications. *Materials Science and Engineering: B*, *266*, 115044, https://doi.org/10.1016/j.mseb.2021.115044.

Bond, B. & Jacobs, P. (1966). The thermal decomposition of sodium nitrate. *Journal of the Chemical Society A: Inorganic, Physical, Theoretical*, *60*(0), 1265–1268, https://doi.org/10.1039/J19660001265.

Bouwmeester, H. J., Song, C., Zhu, J., Yi, J., Van Sint Annaland, M., & Boukamp, B. A. (2009). A novel pulse isotopic exchange technique for rapid determination of the oxygen surface exchange rate of oxide ion conductors. *Physical Chemistry Chemical Physics*, *11*(42), 9640–9643, https://doi.org/10.1039/B912712G.

Brandt, K., Chiu, M. E., Watson, D. J., Tikhov, M. S., & Lambert, R. M. (2009). Chemoselective Catalytic Hydrogenation of Acrolein on Ag(111): Effect of Molecular Orientation on Reaction Selectivity. *Journal of the American Chemical Society*, *131*(47), 17286–17290, https://doi.org/10.1021/ja9063469.

Bron, M., *et al.* (2005). Bridging the pressure and materials gap: in-depth characterisation and reaction studies of silver-catalysed acrolein hydrogenation. *Journal of Catalysis*, *234*(1), 37–47, https://doi.org/10.1016/j.jcat.2005.05.018.

Bulfin, B., *et al.* (2019). Air separation and selective oxygen pumping via temperature and pressure swing oxygen adsorption using a redox cycle of SrFeO3 perovskite. *Chemical Engineering Science*, *203*, 68–75, https://doi.org/10.1016/j.ces.2019.03.057.

Bulfin, B., *et al.* (2020). Isothermal relaxation kinetics for the reduction and oxidation of SrFeO3 based perovskites. *Physical Chemistry Chemical Physics*, *22*(4), 2466–2474, https://doi.org/10.1039/c9cp05771d.

Bush, H. E., Nguyen, N. P., Farr, T., Loutzenhiser, P. G., & Ambrosini, A. (2021). Air separation via a two-step solar thermochemical cycle based on (Ba,La)xSr1-xFeO3-$\delta$: Thermodynamic analysis. *Solid State Ionics*, *368*, 115692, https://doi.org/10.1016/J.SSI.2021.115692.

Bychkov, S. F., Popov, M. P., & Nemudry, A. P. (2016). Study of the oxygen exchange kinetics in the nonstoichiometric oxide SrFeO3–$\delta$ under isostoichiometric conditions using the oxygen partial pressure relaxation technique. *Kinetics and Catalysis*, *57*(5), 697–703, https://doi.org/10.1134/S0023158416050050.

Cai, R., Dou, J., Krzystowczyk, E., Richard, A., & Li, F. (2022). Chemical looping air separation with Sr0.8Ca0.2Fe0.9Co0.1O3-$\delta$ perovskite sorbent: Packed bed modeling, verification, and optimization. *Chemical Engineering Journal*, *429*, 132370, https://doi.org/10.1016/J.CEJ.2021.132370.

Cai, R., Krzystowczyk, E., Braunberger, B., Li, F., & Neal, L. (2024). Techno-economic analysis of chemical looping air separation using a perovskite oxide sorbent. *International Journal of Greenhouse Gas Control*, *132*(January), 104070, https://doi.org/10.1016/j.ijggc.2024.104070.

Carbonio, E. A., *et al.* (2018). Are multiple oxygen species selective in ethylene epoxidation on silver? *Chemical Science*, *9*(4), 990–998, https://doi.org/10.1039/C7SC04728B.

Carbonio, E. A., *et al.* (2023). Adjusting the Chemical Reactivity of Oxygen for Propylene Epoxidation on Silver by Rational Design: The Use of an Oxyanion and Cl. *ACS Catalysis*, *13*(9), 5906–5913, https://doi.org/10.1021/acscatal.3c00297.

Casaletto, M. P., Longo, A., Martorana, A., Prestianni, A., & Venezia, A. M. (2006). XPS study of supported gold catalysts: the role of Au0 and Au+$\delta$ species as active sites. *Surface and Interface Analysis*, *38*(4), 215–218, https://doi.org/10.1002/SIA.2180.

Chan, M. S., Baldovi, H. G., & Dennis, J. S. (2018a). Enhancing the capacity of oxygen carriers for selective oxidations through phase cooperation: bismuth oxide and ceria–zirconia. *Catalysis Science & Technology*, *8*(3), 887–897, https://doi.org/10.1039/C7CY01992K.

Chan, M. S., Marek, E., Scott, S. A., & Dennis, J. (2018b). Chemical looping epoxidation. *Journal of Catalysis*, *359*, 1–7, https://doi.org/10.1016/j.jcat.2017.12.030.

Chang, W., *et al.* (2023). Recent Advances of Oxygen Carriers for Hydrogen Production via Chemical Looping Water-Splitting. *Catalysts*, *13*(2), 279, https://doi.org/10.3390/CATAL13020279.

Charisteidis, I. D. & Triantafyllidis, K. S. (2020). Propylene epoxidation by molecular oxygen using supported silver catalysts: Effect of support type, preparation method and promotion with alkali chloride and/or steam. *Catalysis Today*, *355*, 654–664, https://doi.org/10.1016/j.cattod.2019.06.057.

Chen, Y. ., Yan, B. ., Cheng, Y., Hossain, M. M., Chen, Y., Yan, B., & Cheng, Y. (2023). State-of-the-Art Review of Oxidative Dehydrogenation of Ethane to Ethylene over MoVNbTeOx Catalysts. *Catalysts*, *13*(1), 204, https://doi.org/10.3390/CATAL13010204.

Cheng, Z., Wang, Y., Li, K., Wang, H., Jiang, L., & Zheng, Y. (2024). Encapsulated Pd clusters in S-1 promote the reactivity of chemical looping via synergistic effect of catalysis and oxygen storage. *Applied Surface Science*, *672*, 160800, https://doi.org/10.1016/J.APSUSC.2024.160800.

Chimentão, R. J., *et al.* (2006). Synthesis of silver-gold alloy nanoparticles by a phase-transfer system. *Journal of Materials Research*, *21*(1), 105–111, https://doi.org/10.1557/jmr.2006.0014.

Chizhik, S. A. & Nemudry, A. P. (2018). Nonstoichiometric oxides as a continuous homologous series: linear free-energy relationship in oxygen exchange. *Physical Chemistry Chemical Physics*, *20*(27), 18447–18454, https://doi.org/10.1039/C8CP02924E.

Chizhik, S. A., Popov, M. P., Kovalev, I. V., Bychkov, S. F., & Nemudry, A. P. (2022). Comparison of stationary and transient kinetic methods in determining the rate of surface exchange reaction between molecular oxygen and MIEC perovskite. *Chemical Engineering Journal*, *450*, 137970, https://doi.org/10.1016/J.CEJ.2022.137970.

Chuang, S. Y., Dennis, J. S., Hayhurst, A. N., & Scott, S. A. (2009). Kinetics of the chemical looping oxidation of CO by a co-precipitated mixture of CuO and Al2O3. *Proceedings of the Combustion Institute*, *32 II*(2), 2633–2640, https://doi.org/10.1016/j.proci.2008.06.112.

Citrin, P. H. (1973). High-Resolution X-Ray Photoemission from Sodium Metal and Its Hydroxide. *Physical Review B*, *8*(12), 5545, https://doi.org/10.1103/PhysRevB.8.5545.

Cliff, G. & Lorimer, G. W. (1975). The quantitative analysis of thin specimens. *Journal of Microscopy*, *103*(2), 203–207, https://doi.org/10.1111/J.1365-2818.1975.TB03895.X.

Coelho, A. A. (2018). TOPAS and TOPAS-Academic: an optimization program integrating computer algebra and crystallographic objects written in C++. *Journal of Applied Crystallography*, *51*(1), 210–218, https://doi.org/10.1107/S1600576718000183.

Contractor, R. M. (1999). Dupont's CFB technology for maleic anhydride. *Chemical Engineering Science*, *54*(22), 5627–5632, https://doi.org/10.1016/S0009-2509(99)00295-X.

Cooper, T., Scheffe, J. R., Galvez, M. E., Jacot, R., Patzke, G., & Steinfeld, A. (2015). Lanthanum Manganite Perovskites with Ca/Sr A-site and Al B-site Doping as Effective Oxygen Exchange Materials for Solar Thermochemical Fuel Production. *Energy Technology*, *3*(11), 1130–1142, https://doi.org/10.1002/ENTE.201500226.

Criado, J. M. & Ortega, A. (1986). Non-isothermal transformation kinetics: Remarks on the Kissinger method. *Journal of Non-Crystalline Solids*, *87*(3), 302–311, https://doi.org/10.1016/S0022-3093(86)80004-7.

Crumlin, E. J., *et al.* (2012). Surface strontium enrichment on highly active perovskites for oxygen electrocatalysis in solid oxide fuel cells. *Energy & Environmental Science*, *5*(3), 6081–6088, https://doi.org/10.1039/C2EE03397F.

Csapó, E., *et al.* (2012). Synthesis and characterization of Ag/Au alloy and core(Ag)–shell(Au) nanoparticles. *Colloids and Surfaces A: Physicochemical and Engineering Aspects*, *415*, 281–287, https://doi.org/10.1016/J.COLSURFA.2012.09.005.

Cushman, C., *et al.* (2017). Trends in Advanced XPS Instrumentation. 5. Near-Ambient Pressure XPS. *Vacuum Technology and Coating*, *18*(August), 23–31.

Dai, G., Yu, J., & Liu, G. (2012). A New Approach for Photocorrosion Inhibition of Ag 2 CO 3 Photocatalyst with Highly Visible-Light-Responsive Reactivity. *The Journal of Physical Chemistry C*, *116*(29), 15519–15524, https://doi.org/10.1021/jp305669f.

Damasceno, S., Trindade, F. J., Fonseca, F. C., Florio, D. Z., & Ferlauto, A. S. (2022). Oxidative coupling of methane in chemical looping design. *Fuel Processing Technology*, *231*, 107255, https://doi.org/10.1016/J.FUPROC.2022.107255.

Damba, C., Beas, I. N., Mapolelo, M. M., Darkwa, J., & Marek, E. J. (2024). Mechanosynthesis of a AgSrFeO 3 catalyst for epoxidation of ethylene in a chemical looping set-up. *Materials Advances*, https://doi.org/10.1039/D4MA00485J.

de Vos, Y., Jacobs, M., van der Voort, P., van Driessche, I., Snijkers, F., & Verberckmoes, A. (2020). Development of stable oxygen carrier materials for chemical looping processes—A review. *Catalysts*, *10*(8), https://doi.org/10.3390/catal10080926.

Deganello, F., Liotta, L., Longo, A., Casaletto, M., & Scopelliti, M. (2006). Cerium effect on the phase structure, phase stability and redox properties of Ce-doped strontium ferrates. *Journal of Solid State Chemistry*, *179*(11), 3406–3419, https://doi.org/10.1016/j.jssc.2006.06.027.

Deng, J., Xu, X., Wang, J., Liao, Y., & Hong, B. (1995). In situ surface Raman spectroscopy studies of oxygen adsorbed on electrolytic silver. *Catalysis Letters*, *32*(1-2), 159–170, https://doi.org/10.1007/BF00806111.

Deng, X., Zhang, Q., Zhang, Z., Li, Q., & Liu, X. (2022). Adsorption and diffusion behavior of CO2/H2 mixture in calcite slit pores: A molecular simulation study. *Journal of Molecular Liquids*, *346*, https://doi.org/10.1016/j.molliq.2021.118306.

Dibenedetto, A., *et al.* (2008). High throughput experiment approach to the oxidation of propene-to-propene oxide with transition-metal oxides as O-donors. *Catalysis Today*, *137*(1), 44–51, https://doi.org/10.1016/j.cattod.2008.03.010.

Dietrich, P. M., Bahr, S., Yamamoto, T., Meyer, M., & Thissen, A. (2019). Chemical surface analysis on materials and devices under functional conditions – Environmental photoelectron spectroscopy as non-destructive tool for routine characterization. *Journal of Electron Spectroscopy and Related Phenomena*, *231*, 118–126, https://doi.org/10.1016/J.ELSPEC.2017.12.007.

Doebelin, N. & Kleeberg, R. (2015). Profex: a graphical user interface for the Rietveld refinement program BGMN. *Journal of Applied Crystallography*, *48*(5), 1573–1580, https://doi.org/10.1107/S1600576715014685.

Dokuchits, E. V., Khasin, A. V., & Khassin, A. A. (2011). Interaction of hydrogen and water with oxygen adsorbed on silver. *Reaction Kinetics, Mechanisms and Catalysis*, *103*(2), 261–266, https://doi.org/10.1007/S11144-011-0319-Y.

Dokuchits, E. V., Khasin, A. V., & Khassin, A. A. (2012). Mechanism and kinetics of hydrogen oxidation on silver. *Russian Chemical Bulletin*, *61*(12), 2225–2229, https://doi.org/10.1007/S11172-012-0316-Y.

Dokuchits, E. V., Khasin, A. V., & Khassin, A. A. (2015). Mechanism of the catalytic synthesis of water on silver. *Mendeleev Communications*, *25*(2), 155–156, https://doi.org/10.1016/j.mencom.2015.03.028.

Doornkamp, C. & Ponec, V. (2000). The universal character of the Mars and Van Krevelen mechanism. *Journal of Molecular Catalysis A: Chemical*, *162*(1-2), 19–32, https://doi.org/10.1016/S1381-1169(00)00319-8.

Dou, J., Krzystowczyk, E., Wang, X., Robbins, T., Ma, L., Liu, X., & Li, F. (2020). A- and B-site Codoped SrFeO <sub>3</sub> Oxygen Sorbents for Enhanced Chemical Looping Air Separation. *ChemSusChem*, *13*(2), 385–393, https://doi.org/10.1002/cssc.201902698.

Dueso, C., Thompson, C., & Metcalfe, I. (2015). High-stability, high-capacity oxygen carriers: Iron oxide-perovskite composite materials for hydrogen production by chemical looping. *Applied Energy*, *157*, 382–390, https://doi.org/10.1016/J.APENERGY.2015.05.062.

D'Hondt, H., Abakumov, A. M., Hadermann, J., Kalyuzhnaya, A. S., Rozova, M. G., Antipov, E. V., & Van Tendeloo, G. (2008). Tetrahedral Chain Order in the Sr 2 Fe 2 O 5 Brownmillerite. *Chemistry of Materials*, *20*(22), 7188–7194, https://doi.org/10.1021/cm801723b.

Eggeman, T. (2001). Sodium Carbonate. *Kirk-Othmer Encyclopedia of Chemical Technology*, https://doi.org/10.1002/0471238961.1915040918012108.A01.PUB2.

Enger, B. C., Lødeng, R., & Holmen, A. (2008). A review of catalytic partial oxidation of methane to synthesis gas with emphasis on reaction mechanisms over transition metal catalysts. *Applied Catalysis A: General*, *346*(1-2), 1–27, https://doi.org/10.1016/j.apcata.2008.05.018.

Evans, B. (2022). *X-ray Studies of Molecular Structure during the Crystallisation of Organic Salts*. PhD thesis, University of Leeds https://etheses.whiterose.ac.uk/31144/1/Evans_B_SCAPE_PhD_2022.pdf.

Fairley, N., *et al.* (2021). Systematic and collaborative approach to problem solving using X-ray photoelectron spectroscopy. *Applied Surface Science Advances*, *5*, 100112, https://doi.org/10.1016/j.apsadv.2021.100112.

Falcón, H., Barbero, J. A., Alonso, J. A., Martínez-Lope, M. J., & Fierro, J. L. G. (2002). SrFeO 3 - $\delta$ Perovskite Oxides: Chemical Features and Performance for Methane Combustion. *Chemistry of Materials*, *14*(5), 2325–2333, https://doi.org/10.1021/cm011292l.

Fattore, V. (1975a). Oxidation of propene in the absence of gaseous oxygen I. Single metal oxides. *Journal of Catalysis*, *37*(2), 215–222, https://doi.org/10.1016/0021-9517(75)90155-4.

Fattore, V. (1975b). Oxidation of propene in the absence of gaseous oxygen II. Bismuth molybdates and iron antimonates. *Journal of Catalysis*, *37*(2), 223–231, https://doi.org/10.1016/0021-9517(75)90156-6.

Fossdal, A., Einarsrud, M. A., & Grande, T. (2004). Phase equilibria in the pseudo-binary system SrO–Fe2O3. *Journal of Solid State Chemistry*, *177*(8), 2933–2942, https://doi.org/10.1016/J.JSSC.2004.05.007.

Fulham, G. J., Gebers, J. C., & Marek, E. J. (2024). Application of Copper-Based Catalysts and Strontium Ferrite as Bed Materials for Plasma-Driven CO2 Splitting. *Energy and Fuels*, https://doi.org/10.1021/acs.energyfuels.4c03665.

Gaarenstroom, S. W. & Winograd, N. (1977). Initial and final state effects in the ESCA spectra of cadmium and silver oxides. *The Journal of Chemical Physics*, *67*(8), 3500–3506, https://doi.org/10.1063/1.435347.

Gabra, S. (2022). *Selective Oxidation Reactions: A Chemical Looping Approach*. PhD thesis, University of Cambridge https://www.repository.cam.ac.uk/handle/1810/339267.

Gabra, S., Marek, E., Poulston, S., Williams, G., & Dennis, J. (2021). The use of strontium ferrite perovskite as an oxygen carrier in the chemical looping epoxidation of ethylene. *Applied Catalysis B: Environmental*, *286*, 119821, https://doi.org/10.1016/j.apcatb.2020.119821.

Gan, Z., Brazdil, J. F., Grabow, L. C., & Epling, W. S. (2024). Propene ammoxidation over an industrial bismuth molybdate-based catalyst using forced dynamic operation. *Applied Catalysis A: General*, *672*, 119585, https://doi.org/10.1016/j.apcata.2024.119585.

Gao, W., *et al.* (2018). Production of ammonia via a chemical looping process based on metal imides as nitrogen carriers. *Nature Energy*, *3*(12), 1067–1075, https://doi.org/10.1038/s41560-018-0268-z.

Gao, Y., Neal, L. M., & Li, F. (2016). Li-Promoted LaxSr2-xFeO4-$\delta$ Core-Shell Redox Catalysts for Oxidative Dehydrogenation of Ethane under a Cyclic Redox Scheme. *ACS Catalysis*, *6*(11), 7293–7302, https://doi.org/10.1021/acscatal.6b01399.

Gao, Y., Wang, X., Corolla, N., Eldred, T., Bose, A., Gao, W., & Li, F. (2022). Alkali metal halide–coated perovskite redox catalysts for anaerobic oxidative dehydrogenation of n -butane. *Science Advances*, *8*(30), 7343, https://doi.org/10.1126/sciadv.abo7343.

Gao, Y., *et al.* (2020). A molten carbonate shell modified perovskite redox catalyst for anaerobic oxidative dehydrogenation of ethane. *Science Advances*, *6*(17), https://doi.org/10.1126/sciadv.aaz9339.

Garvie, L. A., Craven, A. J., & Brydson, R. (1994). Use of electron-energy loss near-edge fine structure in the study of minerals. *American Mineralogist*, *79*(5-6), 411–425.

Gebers, J. C., Abu Kasim, A. F. B., Fulham, G. J., Kwong, K. Y., & Marek, E. J. (2023). Production of Acetaldehyde via Oxidative Dehydrogenation of Ethanol in a Chemical Looping Setup. *ACS Engineering Au*, *3*(3), 184–194, https://doi.org/10.1021/acsengineeringau.2c00052.

Gebers, J. C., Harrison, A. R. P., & Marek, E. J. (2022). How does the oxidation and reduction time affect the chemical looping epoxidation of ethylene? *Discover Chemical Engineering*, *2*(1), 4, https://doi.org/10.1007/s43938-022-00011-4.

Gebers, J. C. & Marek, E. J. (2024). Demonstrating on-demand production of bio-ethylene oxide in a two-step dehydration-epoxidation process with chemical looping operations. *Chemical Engineering Journal*, *481*, 148804, https://doi.org/10.1016/J.CEJ.2024.148804.

Geenen, P., Boss, H., & Pott, G. (1982). A study of the vapor-phase epoxidation of propylene and ethylene on silver and silver-gold alloy catalysts. *Journal of Catalysis*, *77*(2), 499–510, https://doi.org/10.1016/0021-9517(82)90190-7.

Godefroy, A., Patience, G. S., Cenni, R., & Dubois, J.-L. (2010). Regeneration studies of redox catalysts. *Chemical Engineering Science*, *65*(1), 261–266, https://doi.org/10.1016/j.ces.2009.05.037.

Görke, R., Marek, E., Donat, F., & Scott, S. (2020). Reduction and oxidation behavior of strontium perovskites for chemical looping air separation. *International Journal of Greenhouse Gas Control*, *94*, 102891, https://doi.org/10.1016/j.ijggc.2019.102891.

Görke, R. H. (2018). *Evaluating New Oxygen Transfer Materials for Air Separation, Oxy-Fuel Combustion and Other Processes*. PhD thesis, University of Cambridge https://www.repository.cam.ac.uk/handle/1810/300813.

Götsch, T., *et al.* (2017). Iron Exsolution Phenomena in Lanthanum Strontium Ferrite SOFC Anodes. *ECS Meeting Abstracts*, *MA2017-03*(1), 283–283, https://doi.org/10.1149/ma2017-03/1/283.

Grabchenko, M., Mamontov, G., Zaikovskii, V., La Parola, V., Liotta, L., & Vodyankina, O. (2019). Design of Ag-CeO2/SiO2 catalyst for oxidative dehydrogenation of ethanol: Control of Ag–CeO2 interfacial interaction. *Catalysis Today*, *333*, 2–9, https://doi.org/10.1016/j.cattod.2018.05.014.

Greczynski, G. & Hultman, L. (2020). X-ray photoelectron spectroscopy: Towards reliable binding energy referencing. *Progress in Materials Science*, *107*, 100591, https://doi.org/10.1016/J.PMATSCI.2019.100591.

Hacker, V., Fankhauser, R., Faleschini, G., Fuchs, H., Friedrich, K., Muhr, M., & Kordesch, K. (2000). Hydrogen production by steam–iron process. *Journal of Power Sources*, *86*(1-2), 531–535, https://doi.org/10.1016/S0378-7753(99)00458-9.

Hammond, J. S., Holubka, J. W., deVries, J. E., & Dickie, R. A. (1981). The application of x-ray photo-electron spectroscopy to a study of interfacial composition in corrosion-induced paint de-adhesion. *Corrosion Science*, *21*(3), 239–253, https://doi.org/10.1016/0010-938X(81)90033-0.

Harrison, A. R. P., Kwong, K. Y., Zheng, Y., Balkrishna, A., Dyson, A., & Marek, E. J. (2023). Kinetic and Thermodynamic Enhancement of Low-Temperature Oxygen Release from Strontium Ferrite Perovskites Modified with Ag and CeO 2. *Energy & Fuels*, *37*(13), 9487–9499, https://doi.org/10.1021/acs.energyfuels.3c01263.

Harrison, A. R. P. & Marek, E. J. (2022). Selective formation of propan-1-ol from propylene via a chemical looping approach. *Reaction Chemistry & Engineering*, *7*, 2534–2549, https://doi.org/10.1039/D2RE00222A.

He, Y., Zhu, X., Li, Q., & Yang, W. (2009). Perovskite oxide absorbents for oxygen separation. *AIChE Journal*, *55*(12), 3125–3133, https://doi.org/10.1002/AIC.11931.

Hillary, A. & Stoukides, M. (1988). Solid electrolyte aided study of hydrogen oxidation on polycrystalline silver. *Journal of Catalysis*, *113*(2), 295–306, https://doi.org/10.1016/0021-9517(88)90258-8.

Hodges, J. P., Short, S., Jorgensen, J. D., Xiong, X., Dabrowski, B., Mini, S. M., & Kimball, C. W. (2000). Evolution of Oxygen-Vacancy Ordered Crystal Structures in the Perovskite Series SrnFenO3n1 (n=2, 4, 8, and ), and the Relationship to Electronic and Magnetic Properties. *Journal of Solid State Chemistry*, *151*(2), 190–209, https://doi.org/10.1006/JSSC.1999.8640.

Hodoroaba, V. D. (2020). Energy-dispersive X-ray spectroscopy (EDS). *Characterization of Nanoparticles: Measurement Processes for Nanoparticles*, (pp. 397–417)., https://doi.org/10.1016/B978-0-12-814182-3.00021-3.

Hofer, F., Schmidt, F. P., Grogger, W., & Kothleitner, G. (2016). Fundamentals of electron energy-loss spectroscopy. *IOP Conference Series: Materials Science and Engineering*, *109*(1), 012007, https://doi.org/10.1088/1757-899X/109/1/012007.

Hu, W., Donat, F., Scott, S. A., & Dennis, J. S. (2016). Kinetics of oxygen uncoupling of a copper based oxygen carrier. *Applied Energy*, *161*, 92–100, https://doi.org/10.1016/J.APENERGY.2015.10.006.

Huang, Z., *et al.* (2022). Exploring the migration and transformation of lattice oxygen during chemical looping with NiFe2O4 oxygen carrier. *Chemical Engineering Journal*, *429*, 132064, https://doi.org/10.1016/J.CEJ.2021.132064.

Hubble, R. (2018). *Studies of Carbon Dioxide Methanation and Related Phenomena in Porous Catalysts*. PhD thesis, University of Cambridge https://www.repository.cam.ac.uk/handle/1810/286588.

Hwang, A., Wu, J., Getsoian, A. B., & Iglesia, E. (2023). Kinetic Relevance of Surface Reactions and Lattice Diffusion in the Dynamics of Ce–Zr Oxides Reduction–Oxidation Cycles. *The Journal of Physical Chemistry C*, *127*(6), 2936–2952, https://doi.org/10.1021/ACS.JPCC.2C08117.

Iakoubovskii, K., Mitsuishi, K., Nakayama, Y., & Furuya, K. (2008). Thickness measurements with electron energy loss spectroscopy. *Microscopy Research and Technique*, *71*(8), 626–631, https://doi.org/10.1002/JEMT.20597.

Ikeda, H., Nikata, S., Hirakawa, E., Tsuchida, A., & Miura, N. (2016). Oxygen sorption/desorption behavior and crystal structural change for SrFeO3$\delta$. *Chemical Engineering Science*, *147*, 166–172, https://doi.org/10.1016/J.CES.2016.03.034.

Imanaka, T., Okamoto, Y., & Teranishi, S. (1972). The Isomerization of Propylene Oxide on Metal Phosphate Catalysts. *Bulletin of the Chemical Society of Japan*, *45*(5), 1353–1357, https://doi.org/10.1246/bcsj.45.1353.

Imtiaz, Q., Hosseini, D., & Müller, C. R. (2013). Review of Oxygen Carriers for Chemical Looping with Oxygen Uncoupling (CLOU): Thermodynamics, Material Development, and Synthesis. *Energy Technology*, *1*(11), 633–647, https://doi.org/10.1002/ente.201300099.

Jain, V., Bahr, S., Dietrich, P., Meyer, M., Thißen, A., & Linford, M. R. (2019). Polytetrafluoroethylene, by near-ambient pressure XPS. *Surface Science Spectra*, *26*(1), https://doi.org/10.1116/1.5063808.

Jayaraman, A. & Yang, R. T. (2005). Stable oxygen-selective sorbents for air separation. *Chemical Engineering Science*, *60*(3), 625–634, https://doi.org/10.1016/j.ces.2004.08.032.

Jensen, W. B. (2009). The origin of the brin process for the manufacture of oxygen. *Journal of Chemical Education*, *86*(11), 1266–1267, https://doi.org/10.1021/ed086p1266.

Jones, T. E., *et al.* (2018). The Selective Species in Ethylene Epoxidation on Silver. *ACS Catalysis*, *8*(5), 3844–3852, https://doi.org/10.1021/acscatal.8b00660.

Joshi, A., *et al.* (2024). Chemical looping methanol oxidation using supported vanadium phosphorous oxide carriers for formaldehyde production. *Journal of Materials Chemistry A*, https://doi.org/10.1039/D3TA07468D.

Joshi, A., *et al.* (2021). Chemical looping-A perspective on the next-gen technology for efficient fossil fuel utilization. *Advances in Applied Energy*, *3*, 100044, https://doi.org/10.1016/J.ADAPEN.2021.100044.

Karakaya, I. & Thompson, W. T. (1992). The Ag-O (silver-oxygen) system. *Journal of Phase Equilibria*, *13*(2), 137–142, https://doi.org/10.1007/bf02667476.

Kariuki, N. N., *et al.* (2004). Composition-Controlled Synthesis of Bimetallic GoldSilver Nanoparticles. *Langmuir*, *20*(25), 11240–11246, https://doi.org/10.1021/la048438q.

Kaushik, V. K. (1991). XPS core level spectra and Auger parameters for some silver compounds. *Journal of Electron Spectroscopy and Related Phenomena*, *56*(3), 273–277, https://doi.org/10.1016/0368-2048(91)85008-H.

Khatib, S. J. & Oyama, S. T. (2015). Direct Oxidation of Propylene to Propylene Oxide with Molecular Oxygen: A Review. *Catalysis Reviews*, *57*(3), 306–344, https://doi.org/10.1080/01614940.2015.1041849.

Kim, S.-j., Lee, S.-C., Lee, C., Kim, M. H., & Lee, Y. (2018). Evolution of silver to a better electrocatalyst: Water-assisted oxygen reduction reaction at silver chloride nanowires in alkaline solution. *Nano Energy*, *48*, 134–143, https://doi.org/10.1016/j.nanoen.2018.03.041.

Kim, S. M., *et al.* (2011). Role of anions in the AuCl3-doping of carbon nanotubes. *ACS Nano*, *5*(2), 1236–1242, https://doi.org/10.1021/NN1028532.

Kleveland, K., Einarsrud, M. A., & Grande, T. (2000). Sintering Behavior, Microstructure, and Phase Composition of Sr(Fe,Co)O3$\delta$ Ceramics. *Journal of the American Ceramic Society*, *83*(12), 3158–3164, https://doi.org/10.1111/J.1151-2916.2000.TB01698.X.

Kovalev, I. V., *et al.* (2021). Microtube Membranes for the Selective Synthesis of Oxygen and Hydrogen. *Russian Journal of Electrochemistry*, *57*(10), 1019–1027, https://doi.org/10.1134/S1023193521100074.

Kraut, J. C. & Stern, W. B. (2000). The density of gold-silver-copper alloys and its calculation from the chemical composition. *Gold Bulletin*, *33*(2), 52–55, https://doi.org/10.1007/BF03216580.

Krishnamurthy, K., Acharya, D., & Fitch, F. (2008). Pilot-Scale Demonstration of a Novel, Low-Cost Oxygen Supply Process and its Integration with Oxy-Fuel Coal-Fired Boilers. *U.S. Department of Energy Office of Scientific and Technical Information*, https://doi.org/10.2172/966357.

## References


Krzystowczyk, E., Haribal, V., Dou, J., & Li, F. (2021). Chemical Looping Air Separation Using a Perovskite-Based Oxygen Sorbent: System Design and Process Analysis. *ACS Sustainable Chemistry & Engineering*, *9*(36), 12185–12195, https://doi.org/10.1021/acssuschemeng.1c03612.

Krzystowczyk, E., Wang, X., Dou, J., Haribal, V., & Li, F. (2020). Substituted SrFeO3 as robust oxygen sorbents for thermochemical air separation: correlating redox performance with compositional and structural properties. *Physical Chemistry Chemical Physics*, *22*(16), 8924–8932, https://doi.org/10.1039/D0CP00275E.

Kulkarni, A., Bedolla-Pantoja, M., Singh, S., Lobo, R. F., Mavrikakis, M., & Barteau, M. A. (2012). Reactions of Propylene Oxide on Supported Silver Catalysts: Insights into Pathways Limiting Epoxidation Selectivity. *Topics in Catalysis*, *55*(1-2), 3–12, https://doi.org/10.1007/s11244-012-9773-7.

Kwong, K. Y., Harrison, A. R. P., Gebers, J. C., Dennis, J. S., & Marek, E. J. (2022). Chemical Looping Combustion of a Biomass Char in Fe 2 O 3 -, CuO-, and SrFeO 3$\delta$ -Based Oxygen Carriers. *Energy & Fuels*, *36*(17), 9437–9449, https://doi.org/10.1021/acs.energyfuels.2c01269.

Lau, C. Y., Dunstan, M. T., Hu, W., Grey, C. P., & Scott, S. A. (2017). Large scale in silico screening of materials for carbon capture through chemical looping. *Energy and Environmental Science*, *10*(3), 818–831, https://doi.org/10.1039/c6ee02763f.

Lee, J. H., Jo, D. Y., Choung, J. W., Kim, C. H., Ham, H. C., & Lee, K.-Y. (2021). Roles of noble metals (M = Ag, Au, Pd, Pt and Rh) on CeO2 in enhancing activity toward soot oxidation: Active oxygen species and DFT calculations. *Journal of Hazardous Materials*, *403*, 124085, https://doi.org/10.1016/j.jhazmat.2020.124085.

Lee, J. H., Lee, S. H., Choung, J. W., Kim, C. H., & Lee, K.-Y. (2019). Ag-incorporated macroporous CeO2 catalysts for soot oxidation: Effects of Ag amount on the generation of active oxygen species. *Applied Catalysis B: Environmental*, *246*, 356–366, https://doi.org/10.1016/j.apcatb.2019.01.064.

Leo, A., Liu, S., & Diniz da Costa, J. C. (2009). The enhancement of oxygen flux on Ba0.5Sr0.5Co0.8Fe0.2O3$\delta$ (BSCF) hollow fibers using silver surface modification. *Journal of Membrane Science*, *340*(1-2), 148–153, https://doi.org/10.1016/j.memsci.2009.05.022.

Li, J., Qin, Z., Xu, H., Dong, M., Dong, J., & Wang, J. (2007). Enhancement of 1-Propanol Selectivity in Propene Hydration over Zeolites HNU-3 and HZSM-5. *Industrial & Engineering Chemistry Research*, *46*(26), 9000–9005, https://doi.org/10.1021/ie070171d.

Li, R., Liu, C., Fan, Y., Fu, Q., & Bao, X. (2023). Metal-oxide interaction modulating activity of active oxygen species on atomically dispersed silver catalyst. *Chemical Communications*, *59*, 3854–3857, https://doi.org/10.1039/D3CC00617D.

Liu, H., Li, L., Liu, C., Sun, Z., Lu, D., & Duan, L. (2024). Quantitative Analysis of Catalytic Oxidation Reactions in Oxygen Carrier Aided Fluidized Bed Combustion. *Energy and Fuels*, https://doi.org/10.1021/acs.energyfuels.4c03659.

Liu, J. & Li, F. (2023). Mixed oxides as multi-functional reaction media for chemical looping catalysis. *Chemical Communications*, https://doi.org/10.1039/D2CC05502C.

Liu, J., *et al.* (2022a). Redox oxide@molten salt as a generalized catalyst design strategy for oxidative dehydrogenation of ethane via selective hydrogen combustion. *Applied Catalysis A: General*, *646*, 118869, https://doi.org/10.1016/J.APCATA.2022.118869.

Liu, L., Li, Z., Wang, Y., Li, Z., Larring, Y., & Cai, N. (2022b). Industry-scale production of a perovskite oxide as oxygen carrier material in chemical looping. *Chemical Engineering Journal*, *431*, 134006, https://doi.org/10.1016/J.CEJ.2021.134006.

Liu, W. (2021). Controlling lattice oxygen activity of oxygen carrier materials by design: a review and perspective. *Reaction Chemistry & Engineering*, *6*(9), 1527–1537, https://doi.org/10.1039/D1RE00209K.

Lloyd, G. E. (1987). Atomic number and crystallographic contrast images with the SEM: a review of backscattered electron techniques. *Mineralogical Magazine*, *51*(359), 3–19, https://doi.org/10.1180/minmag.1987.051.359.02.

Logsdon, J. E. & Loke, R. A. (2000). Isopropyl Alcohol. *Kirk-Othmer Encyclopedia of Chemical Technology*, https://doi.org/10.1002/0471238961.0919151612150719.a01.

Lopez-Adams, R., *et al.* (2022). Elucidating heterogeneous iron biomineralization patterns in a denitrifying As( iii )-oxidizing bacterium: implications for arsenic immobilization. *Environmental Science: Nano*, *9*(3), 1076–1090, https://doi.org/10.1039/D1EN00905B.

Lu, G. & Zuo, X. (1999). Epoxidation of propylene by air over modified silver catalyst. *Catalysis Letters*, *58*(1), 67–70, https://doi.org/10.1023/a:1019001211379.

Lu, J., Bravo-Suárez, J. J., Haruta, M., & Oyama, S. T. (2006). Direct propylene epoxidation over modified Ag/CaCO3 catalysts. *Applied Catalysis A: General*, *302*(2), 283–295, https://doi.org/10.1016/j.apcata.2006.01.023.

Lu, J., Bravo-Suárez, J. J., Takahashi, A., Haruta, M., & Oyama, S. T. (2005). In situ UV-vis studies of the effect of particle size on the epoxidation of ethylene and propylene on supported silver catalysts with molecular oxygen. *Journal of Catalysis*, *232*(1), 85–95, https://doi.org/10.1016/j.jcat.2005.02.013.

Lu, J., Low, K. B., Lei, Y., Libera, J. A., Nicholls, A., Stair, P. C., & Elam, J. W. (2014). Toward atomically-precise synthesis of supported bimetallic nanoparticles using atomic layer deposition. *Nature Communications*, *5*(1), 1–9, https://doi.org/10.1038/ncomms4264.

Lu, J., Luo, M., Lei, H., & Li, C. (2002). Epoxidation of propylene on NaCl-modified silver catalysts with air as the oxidant. *Applied Catalysis A: General*, *237*(1-2), 11–19, https://doi.org/10.1016/s0926-860x(02)00062-5.

Luo, M., Lu, J., & Li, C. (2003). Epoxidation of propylene over Ag-CuCl catalysts using air as the oxidant. *Catalysis Letters*, *86*(1-3), 43–49, https://doi.org/10.1023/A:1022650723251.

Luo, M., Yi, Y., Wang, S., Wang, Z., Du, M., Pan, J., & Wang, Q. (2018). Review of hydrogen production using chemical-looping technology. *Renewable and Sustainable Energy Reviews*, *81*, 3186–3214, https://doi.org/10.1016/j.rser.2017.07.007.

Luongo, G., Donat, F., Bork, A. H., Willinger, E., Landuyt, A., & Müller, C. R. (2022). Highly Selective Oxidative Dehydrogenation of Ethane to Ethylene via Chemical Looping with Oxygen Uncoupling through Structural Engineering of the Oxygen Carrier. *Advanced Energy Materials*, *12*(23), 2200405, https://doi.org/10.1002/AENM.202200405.

Lux, S., Baldauf-Sommerbauer, G., & Siebenhofer, M. (2018). Hydrogenation of Inorganic Metal Carbonates: A Review on Its Potential for Carbon Dioxide Utilization and Emission Reduction. *ChemSusChem*, *11*(19), 3357–3375, https://doi.org/10.1002/CSSC.201801356.

Machida, M., Kawada, T., Fujii, H., & Hinokuma, S. (2015). The Role of CeO2 as a Gateway for Oxygen Storage over CeO2-Grafted Fe2O3 Composite Materials. *Journal of Physical Chemistry C*, *119*(44), 24932–24941, https://doi.org/10.1021/ACS.JPCC.5B09876.

Machida, M., *et al.* (2017). CeO2-Grafted Mn-Fe Oxide Composites as Alternative Oxygen-Storage Materials for Three-Way Catalysts: Laboratory and Chassis Dynamometer Tests. *Industrial and Engineering Chemistry Research*, *56*(12), 3184–3193, https://doi.org/10.1021/ACS.IECR.6B04468.

Mahadi, A. H., *et al.* (2020). Beyond surface redox and oxygen mobility at pd-polar ceria (100) interface: Underlying principle for strong metal-support interactions in green catalysis. *Applied Catalysis B: Environmental*, *270*, 118843, https://doi.org/10.1016/j.apcatb.2020.118843.

Majewski, A. J. & Dhir, A. (2018). Application of silver in microtubular solid oxide fuel cells. *Materials for Renewable and Sustainable Energy*, *7*(3), 1–13, https://doi.org/10.1007/S40243-018-0123-Y.

Malathi, S., Ezhilarasu, T., Abiraman, T., & Balasubramanian, S. (2014). One pot green synthesis of Ag, Au and Au–Ag alloy nanoparticles using isonicotinic acid hydrazide and starch. *Carbohydrate Polymers*, *111*, 734–743, https://doi.org/10.1016/j.carbpol.2014.04.105.

Malis, T., Cheng, S. C., & Egerton, R. F. (1988). EELS log-ratio technique for specimen-thickness measurement in the TEM. *Journal of Electron Microscopy Technique*, *8*(2), 193–200, https://doi.org/10.1002/JEMT.1060080206.

Marek, E. & García-Calvo Conde, E. (2021). Effect of catalyst preparation and storage on chemical looping epoxidation of ethylene. *Chemical Engineering Journal*, *417*, 127981, https://doi.org/10.1016/j.cej.2020.127981.

Marek, E., Hu, W., Gaultois, M., Grey, C. P., & Scott, S. A. (2018a). The use of strontium ferrite in chemical looping systems. *Applied Energy*, (223), 369–382, https://doi.org/10.1016/j.apenergy.2018.04.090.

Marek, E. J., Gabra, S., Dennis, J. S., & Scott, S. A. (2020). High selectivity epoxidation of ethylene in chemical looping setup. *Applied Catalysis B: Environmental*, *262*, 118216, https://doi.org/10.1016/j.apcatb.2019.118216.

Marek, E. J., Zheng, Y., & Scott, S. A. (2018b). Enhancement of char gasification in CO2 during chemical looping combustion. *Chemical Engineering Journal*, *354*, 137–148, https://doi.org/10.1016/J.CEJ.2018.07.215.

Markov, A. A., Nikitin, S. S., Leonidov, I. A., & Patrakeev, M. V. (2020). Oxygen and electron transport in Ce0.1Sr0.9FeO3$\delta$. *Solid State Ionics*, *344*, 115131, https://doi.org/10.1016/j.ssi.2019.115131.

Mars, P. & van Krevelen, D. W. (1954). Oxidations carried out by means of vanadium oxide catalysts. *Chemical Engineering Science*, *3*, 41–59, https://doi.org/10.1016/S0009-2509(54)80005-4.

Mattisson, T. (2013). Materials for Chemical-Looping with Oxygen Uncoupling. *ISRN Chemical Engineering*, *2013*, 1–19, https://doi.org/10.1155/2013/526375.

Mattisson, T., Lyngfelt, A., & Leion, H. (2009). Chemical-looping with oxygen uncoupling for combustion of solid fuels. *International Journal of Greenhouse Gas Control*, *3*(1), 11–19, https://doi.org/10.1016/j.ijggc.2008.06.002.

Mayeshiba, T. & Morgan, D. (2015). Strain effects on oxygen migration in perovskites. *Physical Chemistry Chemical Physics*, *17*(4), 2715–2721, https://doi.org/10.1039/c4cp05554c.

Mayeshiba, T. & Morgan, D. (2017). Strain effects on oxygen vacancy formation energy in perovskites. *Solid State Ionics*, *311*(September), 105–117, https://doi.org/10.1016/j.ssi.2017.09.021.

McCoy, M. (2001). New routes to propylene oxide. *Chemical & Engineering News Archive*, *79*(43), 19–20, https://doi.org/10.1021/cen-v079n043.p019.

Mcmahon, M. D., Lopez, R., Meyer, H. M., Feldman, L. C., & Haglund, R. F. (2005). Rapid tarnishing of silver nanoparticles in ambient laboratory air. *Applied Physics B: Lasers and Optics*, *80*(7), 915–921, https://doi.org/10.1007/s00340-005-1793-6.

Merkle, R. & Maier, J. (2006). The significance of defect chemistry for the rate of gas-solid reactions: Three examples. *Topics in Catalysis*, *38*(1-3), 141–145, https://doi.org/10.1007/S11244-006-0079-5.

Merkle, R. & Maier, J. (2008). How Is Oxygen Incorporated into Oxides? A Comprehensive Kinetic Study of a Simple Solid-State Reaction with SrTiO3 as a Model Material. *Angewandte Chemie International Edition*, *47*(21), 3874–3894, https://doi.org/10.1002/ANIE.200700987.

Messerschmitt, A. (1908). Process of producing hydrogen (US Patent US971206A) https://patents.google.com/patent/US971206A/en.

Mestl, G., Ruiz, P., Delmon, B., & Kntizinger, H. (1994). In Situ Raman Spectroscopy Characterization of 180 Exchange in Physical Mixtures of Antimony Oxides and Molybdenum Oxide The interaction of 1803 with physical mixtures of M0O3 and Sb204 and of M0O3 and. *J. Phys. Chem*, *98*, 11283–11292, https://doi.org/10.1021/j100095a009.

Metcalfe, I. S., *et al.* (2019). Overcoming chemical equilibrium limitations using a thermodynamically reversible chemical reactor. *Nature Chemistry*, *11*(7), 638–643, https://doi.org/10.1038/s41557-019-0273-2.

Millar, G. J. & Collins, M. (2017). Industrial Production of Formaldehyde Using Polycrystalline Silver Catalyst. *Industrial and Engineering Chemistry Research*, *56*(33), 9247–9265, https://doi.org/10.1021/ACS.IECR.7B02388.

Miller, D. J., Biesinger, M. C., & McIntyre, N. S. (2002). Interactions of CO2 and CO at fractional atmosphere pressures with iron and iron oxide surfaces: one possible mechanism for surface contamination? *Surface and Interface Analysis*, *33*(4), 299–305, https://doi.org/10.1002/SIA.1188.

Mishanin, I. I., Kalenchuk, A. N., Maslakov, K. I., Lunin, V. V., Koklin, A. E., Finashina, E. D., & Bogdan, V. I. (2017). Oxidative dehydrogenation of ethane over a Mo–V–Nb–Te–O mixed-oxide catalyst in a cyclic mode. *Kinetics and Catalysis*, *58*(2), 156–160, https://doi.org/10.1134/S0023158417020094.

Mizusaki, J., Okayasu, M., Yamauchi, S., & Fueki, K. (1992). Nonstoichiometry and phase relationship of the SrFeO2.5SrFeO3 system at high temperature. *Journal of Solid State Chemistry*, *99*(1), 166–172, https://doi.org/10.1016/0022-4596(92)90301-B.

Moghtaderi, B. (2010). Application of chemical looping concept for air separation at high temperatures. *Energy and Fuels*, *24*(1), 190–198, https://doi.org/10.1021/ef900553j.

Murayama, H., *et al.* (2017). Chloride-free and water-soluble Au complex for preparation of supported small nanoparticles by impregnation method. *Journal of Catalysis*, *353*, 74–80, https://doi.org/10.1016/j.jcat.2017.07.002.

Neagu, D., *et al.* (2020). Tracking the evolution of a single composite particle during redox cycling for application in H2 production. *Scientific Reports*, *10*, 5266, https://doi.org/10.1038/s41598-020-62237-y.

Neal, L. M., Yusuf, S., Sofranko, J. A., & Li, F. (2016). Oxidative Dehydrogenation of Ethane: A Chemical Looping Approach. *Energy Technology*, *4*(10), 1200–1208, https://doi.org/10.1002/ente.201600074.

Nenning, A., *et al.* (2016). Ambient pressure XPS study of mixed conducting perovskite-type SOFC cathode and anode materials under well-defined electrochemical polarization. *Journal of Physical Chemistry C*, *120*(3), 1461–1471, https://doi.org/10.1021/ACS.JPCC.5B08596/.

Nikitin, S. S., Markov, A. A., Leonidov, I. A., & Patrakeev, M. V. (2021). Impact of Cerium Content on Ion and Electron Transport in Sr1- xCe xFeO3-$\delta$. *Journal of Physical Chemistry C*, *125*(31), 17546–17555, https://doi.org/10.1021/acs.jpcc.1c05144.

Notheisz, F., Molnár, , Zsigmond, , & Bartók, M. (1986). The mechanism of hydrogenolysis and isomerization of oxacycloalkanes on metals *1IV. Mechanism of transformation of oxiranes on Cu catalyst. *Journal of Catalysis*, *98*(1), 131–137, https://doi.org/10.1016/0021-9517(86)90303-9.

Okamoto, Y., Imanaka, T., & Teranishi, S. (1973). The Isomerization of Propylene Oxide on Metal Oxides and Silica-Magnesia Catalysts. *Bulletin of the Chemical Society of Japan*, *46*(1), 4–8, https://doi.org/10.1246/bcsj.46.4.

Orlando, A., Franceschini, F., Muscas, C., Pidkova, S., Bartoli, M., Rovere, M., & Tagliaferro, A. (2021). A Comprehensive Review on Raman Spectroscopy Applications. *Chemosensors*, *9*(9), 262, https://doi.org/10.3390/CHEMOSENSORS9090262.

Orsini, F., *et al.* (2023). Exsolution-enhanced reverse water-gas shift chemical looping activity of Sr2FeMo0.6Ni0.4O6-$\delta$ double perovskite. *Chemical Engineering Journal*, *475*, 146083, https://doi.org/10.1016/J.CEJ.2023.146083.

Pan, M., *et al.* (2013). Model studies of heterogeneous catalytic hydrogenation reactions with gold. *Chemical Society Reviews*, *42*(12), 5002, https://doi.org/10.1039/c3cs35523c.

Pan, M., Pozun, Z. D., Brush, A. J., Henkelman, G., & Mullins, C. B. (2012). Low-Temperature Chemoselective Gold-Surface-Mediated Hydrogenation of Acetone and Propionaldehyde. *ChemCatChem*, *4*(9), 1241–1244, https://doi.org/10.1002/cctc.201200311.

Panlener, R., Blumenthal, R., & Garnier, J. (1975). A thermodynamic study of nonstoichiometric cerium dioxide. *Journal of Physics and Chemistry of Solids*, *36*(11), 1213–1222, https://doi.org/10.1016/0022-3697(75)90192-4.

Patience, G. S. & Bockrath, R. E. (2010). Butane oxidation process development in a circulating fluidized bed. *Applied Catalysis A: General*, *376*(1-2), 4–12, https://doi.org/10.1016/J.APCATA.2009.10.023.

Patrakeev, M. V., Leonidov, I. A., & Kozhevnikov, V. L. (2011). Applications of coulometric titration for studies of oxygen non-stoichiometry in oxides. *Journal of Solid State Electrochemistry*, *15*(5), 931–954, https://doi.org/10.1007/s10008-010-1111-z.

Pena, F. d. l., *et al.* (2017). Electron Microscopy (Big and Small) Data Analysis With the Open Source Software Package HyperSpy. *Microscopy and Microanalysis*, *23*(S1), 214–215, https://doi.org/10.1017/S1431927617001751.

Peña, F. d. l., *et al.* (2022). hyperspy/hyperspy: Release v1.7.3 https://zenodo.org/record/7263263.

Pfaff, I. & Kather, A. (2009). Comparative thermodynamic analysis and integration issues of CCS steam power plants based on oxy-combustion with cryogenic or membrane based air separation. *Energy Procedia*, *1*(1), 495–502, https://doi.org/10.1016/j.egypro.2009.01.066.

Pirola, C., Galli, F., & Patience, G. S. (2018). Experimental methods in chemical engineering: Temperature programmed reduction—TPR. *The Canadian Journal of Chemical Engineering*, *96*(11), 2317–2320, https://doi.org/10.1002/CJCE.23317.

Poling, B. E., Prausnitz, J. M., & O'connell, J. P. (2001). *The Properties of Gases and Liquids*. New York: McGraw Hill, 5th edition.

Preis, W. (2017). Thermodynamic model for perovskite – type lanthanum strontium ferrite (LSF) https://data.mendeley.com/datasets/c4xtzwjncv/1.

Pröll, T., Kolbitsch, P., Bolhàr-Nordenkampf, J., & Hofbauer, H. (2009). A novel dual circulating fluidized bed system for chemical looping processes. *AIChE Journal*, *55*(12), 3255–3266, https://doi.org/10.1002/AIC.11934.

Pu, T., Setiawan, A., Mosevitzky Lis, B., Zhu, M., Ford, M. E., Rangarajan, S., & Wachs, I. E. (2022). Nature and Reactivity of Oxygen Species on/in Silver Catalysts during Ethylene Oxidation. *ACS Catalysis*, *12*(8), 4375–4381, https://doi.org/10.1021/acscatal.1c05939.

Puglia, C., Nilsson, A., Hernnäs, B., Karis, O., Bennich, P., & Mårtensson, N. (1995). Physisorbed, chemisorbed and dissociated O2 on Pt(111) studied by different core level spectroscopy methods. *Surface Science*, *342*(1-3), 119–133, https://doi.org/10.1016/0039-6028(95)00798-9.

Qin, Y., Cui, Y., Tian, Z., Wu, Y., & Li, Y. (2017). Synthesis of AG@AgCl Core–Shell Structure Nanowires and Its Photocatalytic Oxidation of Arsenic (III) Under Visible Light. *Nanoscale Research Letters*, *12*(1), 247, https://doi.org/10.1186/s11671-017-2017-9.

Rabiei, M., Palevicius, A., Dashti, A., Nasiri, S., Monshi, A., Vilkauskas, A., & Janusas, G. (2020). Measurement Modulus of Elasticity Related to the Atomic Density of Planes in Unit Cell of Crystal Lattices. *Materials*, *13*(19), 4380, https://doi.org/10.3390/ma13194380.

Rakshit, S. K., Parida, S. C., Dash, S., Singh, Z., Sen, B. K., & Venugopal, V. (2007). Thermodynamic studies on SrFe12O19(s), SrFe2O4(s), Sr2Fe2O5(s) and Sr3Fe2O6(s). *Journal of Solid State Chemistry*, *180*(2), 523–532, https://doi.org/10.1016/j.jssc.2006.11.012.

Reller, A. (1993). Chemical and physical implications of cationic and anionic modifications in perovskite related metal oxides. *Philosophical Magazine A*, *68*(4), 641–652, https://doi.org/10.1080/01418619308213988.

Reller, A., Emmenegger, R., Padeste, C., & Oswald, H.-R. (1991). Thermochemical Reactivity of Metal Carbonates. *Chimia*, *45*(9), 262, https://doi.org/10.2533/chimia.1991.262.

Renner, H., *et al.* (2001). Silver, Silver Compounds, and Silver Alloys. In *Ullmann's Encyclopedia of Industrial Chemistry*. John Wiley & Sons, Ltd https://onlinelibrary.wiley.com/doi/abs/10.1002/14356007.a24_107.

Rocha, T. C. R., *et al.* (2012). The silver–oxygen system in catalysis: new insights by near ambient pressure X-ray photoelectron spectroscopy. *Physical Chemistry Chemical Physics*, *14*(13), 4554, https://doi.org/10.1039/c2cp22472k.

Rojluechai, S., Chavadej, S., Schwank, J. W., & Meeyoo, V. (2007). Catalytic activity of ethylene oxidation over Au, Ag and Au–Ag catalysts: Support effect. *Catalysis Communications*, *8*(1), 57–64, https://doi.org/10.1016/j.catcom.2006.05.029.

Rueden, C. T., Schindelin, J., Hiner, M. C., DeZonia, B. E., Walter, A. E., Arena, E. T., & Eliceiri, K. W. (2017). ImageJ2: ImageJ for the next generation of scientific image data. *BMC Bioinformatics*, *18*(1), 1–26, https://doi.org/10.1186/s12859-017-1934-z.

Ruiz Puigdollers, A., Schlexer, P., Tosoni, S., & Pacchioni, G. (2017). Increasing Oxide Reducibility: The Role of Metal/Oxide Interfaces in the Formation of Oxygen Vacancies. *ACS Catalysis*, *7*(10), 6493–6513, https://doi.org/10.1021/acscatal.7b01913.

Rupp, G. M., Opitz, A. K., Nenning, A., Limbeck, A., & Fleig, J. (2017). Real-time impedance monitoring of oxygen reduction during surface modification of thin film cathodes. *Nature Materials*, *16*(6), 640–645, https://doi.org/10.1038/nmat4879.

Salmeron, M. & Schlögl, R. (2008). Ambient pressure photoelectron spectroscopy: A new tool for surface science and nanotechnology. *Surface Science Reports*, *63*(4), 169–199, https://doi.org/10.1016/J.SURFREP.2008.01.001.

Sanders, C. E., Verreault, D., Frankel, G. S., & Allen, H. C. (2015). The Role of Sulfur in the Atmospheric Corrosion of Silver. *Journal of The Electrochemical Society*, *162*(12), C630–C637, https://doi.org/10.1149/2.0051512jes.

Savinskaya, O. A., Nemudry, A. P., Nadeev, A. N., & Tsybulya, S. V. (2008). Synthesis and study of the thermal stability of SrFe1 xM xO3 z (M = Mo, W) perovskites. *Solid State Ionics*, *179*(21-26), 1076–1079, https://doi.org/10.1016/J.SSI.2008.02.005.

Savintsev, A. P., Gavasheli, Y. O., Kalazhokov, Z. K., & Kalazhokov, K. K. (2016). X-ray photoelectron spectroscopy studies of the sodium chloride surface after laser exposure. *Journal of Physics: Conference Series*, *774*(1), 012118, https://doi.org/10.1088/1742-6596/774/1/012118.

Scherrer, P. (1918). Nachrichten von der Gesellschaft der Wissenschaften zu Göttingen, Mathematisch-Physikalische Klasse. *Nachrichten von der Gesellschaft der Wissenschaften zu Göttingen, Mathematisch-Physikalische Klasse*, (pp. 98–100).

Schmidt, M. & Campbell, S. (2002). In situ neutron diffraction study (300–1273 K) of non-stoichiometric strontium ferrite SrFeO x. *Journal of Physics and Chemistry of Solids*, *63*(11), 2085–2092, https://doi.org/10.1016/S0022-3697(02)00198-1.

Schmidt, M. & Campbell, S. J. (2001). Crystal and Magnetic Structures of Sr2Fe2O5 at Elevated Temperature. *Journal of Solid State Chemistry*, *156*(2), 292–304, https://doi.org/10.1006/JSSC.2000.8998.

## References


Schön, G. (1973). ESCA Studies of Ag, Ag2O and AgO. *Acta Chemica Scandinavica*, *27*, 2623–2633, https://doi.org/10.3891/acta.chem.scand.27-2623.

Seah, M. P., Gilmore, I. S., & Beamson, G. (1998). XPS: binding energy calibration of electron spectrometers 5?re-evaluation of the reference energies. *Surface and Interface Analysis*, *26*(9), 642–649, https://doi.org/10.1002/(SICI)1096-9918(199808)26:9<642::AID-SIA408>3.0.CO;2-3.

Seubsai, A. & Senkan, S. (2011). The Effects of Cofeeding Chlorinated Hydrocarbons in the Direct Epoxidation of Propylene by Molecular Oxygen. *ChemCatChem*, *3*(11), 1751–1754, https://doi.org/10.1002/cctc.201100178.

Shah, K., Moghtaderi, B., Zanganeh, J., & Wall, T. (2013). Integration options for novel chemical looping air separation (ICLAS) process for oxygen production in oxy-fuel coal fired power plants. *Fuel*, *107*, 356–370, https://doi.org/10.1016/j.fuel.2013.01.007.

Shchukarev, A. V. & Korolkov, D. V. (2004). XPS study of group IA carbonates. *Central European Journal of Chemistry*, *2*(2), 347–362, https://doi.org/10.2478/BF02475578.

Sheridan, P. J. (1989). Determination of experimental and theoretical kASi factors for a 200-kV analytical electron microscope. *Journal of Electron Microscopy Technique*, *11*(1), 41–61, https://doi.org/10.1002/JEMT.1060110107.

Shirley, D. A. (1972). High-Resolution X-Ray Photoemission Spectrum of the Valence Bands of Gold. *Physical Review B*, *5*(12), 4709, https://doi.org/10.1103/PhysRevB.5.4709.

Siddiqui, M. R. H., Adil, S., Assal, M., Ali, R., & A. Al-Warthan, A. (2013). Synthesis and Characterization of Silver Oxide and Silver Chloride Nanoparticles with High Thermal Stability. *Asian Journal of Chemistry*, *25*(6), 3405–3409, https://doi.org/10.14233/ajchem.2013.13874.

Somani, M., Liauw, M. A., & Luss, D. (1996). Hot spot formation on a catalyst. *Chemical Engineering Science*, *51*(18), 4259–4269, https://doi.org/10.1016/0009-2509(96)00009-7.

Song, D., *et al.* (2024a). Unraveling the atomic interdiffusion mechanism of NiFe2O4 oxygen carriers during chemical looping CO2 conversion. *Carbon Energy*, (pp. e493)., https://doi.org/10.1002/CEY2.493.

Song, D., *et al.* (2023). Review on Migration and Transformation of Lattice Oxygen during Chemical Looping Conversion: Advances and Perspectives. *Energy and Fuels*, *37*(8), 5743–5746, https://doi.org/10.1021/ACS.ENERGYFUELS.3C00402.

Song, D., Lin, Y., Zhao, K., Huang, Z., He, F., & Xiong, Y. (2022). Migration Mechanism of Lattice Oxygen: Conversion of CO2 to CO Using NiFe2O4 Spinel Oxygen Carrier in Chemical Looping Reactions. *Catalysts*, *12*(10), 1181, https://doi.org/10.3390/catal12101181.

Song, D., *et al.* (2024b). Micro-structure change and crystal-structure modulated of oxygen carriers for chemical looping: Controlling local chemical environment of lattice oxygen. *Fuel*, *364*, 131087, https://doi.org/10.1016/J.FUEL.2024.131087.

Srnová-Šloufová, I., Vlcková, B., Bastl, Z., & Hasslett, T. L. (2004). Bimetallic (Ag)Au Nanoparticles Prepared by the Seed Growth Method: Two-Dimensional Assembling, Characterization by Energy Dispersive X-ray Analysis, X-ray Photoelectron Spectroscopy, and Surface Enhanced Raman Spectroscopy, and Proposed Mechanism of Gro. *Langmuir*, *20*(8), 3407–3415, https://doi.org/10.1021/la0302605.

Stangl, A., *et al.* (2023). Isotope Exchange Raman Spectroscopy (IERS): A Novel Technique to Probe Physicochemical Processes In Situ. *Advanced Materials*, *35*(33), 2303259, https://doi.org/10.1002/ADMA.202303259.

Starkov, I., Bychkov, S., Matvienko, A., & Nemudry, A. (2014). Oxygen release technique as a method for the determination of "$\delta$–pO 2 –T" diagrams for MIEC oxides. *Physical Chemistry Chemical Physics*, *16*(12), 5527–5535, https://doi.org/10.1039/C3CP52143E.

Steiner, T., *et al.* (2024). Chemical looping of synthetic ilmenite, Part I: Addressing challenges of kinetic TGA measurements with H2. *Fuel*, *368*, 131528, https://doi.org/10.1016/J.FUEL.2024.131528.

Stevie, F. A. & Donley, C. L. (2020). Introduction to x-ray photoelectron spectroscopy. *Journal of Vacuum Science & Technology A: Vacuum, Surfaces, and Films*, *38*(6), 63204, https://doi.org/10.1116/6.0000412/1024200.

Stoerzinger, K. A., Wang, L., Su, H., Lee, K.-J., Crumlin, E. J., & Du, Y. (2020). Influence of strain on SrFeO3-$\delta$ oxidation, reduction, and water dissociation: Insights from ambient pressure X-ray photoelectron spectroscopy. *Applied Surface Science*, *527*, 146919, https://doi.org/10.1016/j.apsusc.2020.146919.

Sumiyama, K. & Nakamura, Y. (1984). High Concentration Fe-Cu and Fe-Ag Alloys Produced by Vapor Quenching. *physica status solidi (a)*, *81*(2), K109–K112, https://doi.org/10.1002/PSSA.2210810244.

Sun, Z., *et al.* (2023). Chemical looping-based energy transformation via lattice oxygen modulated selective oxidation. *Progress in Energy and Combustion Science*, *96*, 101045, https://doi.org/10.1016/J.PECS.2022.101045.

Suo, Z., Jin, M., Lu, J., Wei, Z., & Li, C. (2008). Direct gas-phase epoxidation of propylene to propylene oxide using air as oxidant on supported gold catalyst. *Journal of Natural Gas Chemistry*, *17*(2), 184–190, https://doi.org/10.1016/s1003-9953(08)60049-3.

Tan, H., Verbeeck, J., Abakumov, A., & Van Tendeloo, G. (2012). Oxidation state and chemical shift investigation in transition metal oxides by EELS. *Ultramicroscopy*, *116*, 24–33, https://doi.org/10.1016/j.ultramic.2012.03.002.

Taylor, D. D., Schreiber, N. J., Levitas, B. D., Xu, W., Whitfield, P. S., & Rodriguez, E. E. (2016). Oxygen Storage Properties of La 1– x Sr x FeO 3$\delta$ for Chemical-Looping Reactions—An In Situ Neutron and Synchrotron X-ray Study. *Chemistry of Materials*, *28*(11), 3951–3960, https://doi.org/10.1021/acs.chemmater.6b01274.

Teržan, J., Huš, M., Likozar, B., & Djinović, P. (2020). Propylene Epoxidation using Molecular Oxygen over Copper- and Silver-Based Catalysts: A Review. *ACS Catalysis*, *10*(22), 13415–13436, https://doi.org/10.1021/acscatal.0c03340.

Thalinger, R., Gocyla, M., Heggen, M., Klötzer, B., & Penner, S. (2015). Exsolution of Fe and SrO Nanorods and Nanoparticles from Lanthanum Strontium Ferrite La0.6Sr0.4FeO3-$\delta$ Materials by Hydrogen Reduction. *Journal of Physical Chemistry C*, *119*(38), 22050–22056, https://doi.org/10.1021/acs.jpcc.5b06014.

Thrane, J., Mentzel, U. V., Thorhauge, M., Høj, M., & Jensen, A. D. (2021). A review and experimental revisit of alternative catalysts for selective oxidation of methanol to formaldehyde. *Catalysts*, *11*(11), 1329, https://doi.org/10.3390/CATAL11111329.

Tian, X., Zheng, C., & Zhao, H. (2022a). Ce-modified SrFeO3-$\delta$ for ethane oxidative dehydrogenation coupled with CO2 splitting via a chemical looping scheme. *Applied Catalysis B: Environmental*, *303*, 120894, https://doi.org/10.1016/J.APCATB.2021.120894.

Tian, Y., Luongo, G., Donat, F., Müller, C. R., Larring, Y., Westmoreland, P. R., & Li, F. (2022b). Oxygen Nonstoichiometry and Defect Models of Brownmillerite-Structured Ca2MnAlO5+$\delta$for Chemical Looping Air Separation. *ACS Sustainable Chemistry and Engineering*, *10*(31), 10393–10402, https://doi.org/10.1021/ACSSUSCHEMENG.2C03485.

Toole, F. J. & Johnson, F. M. (1933). The solubility of oxygen in gold and in certain silver-gold alloys. *Journal of Physical Chemistry*, *37*(3), 331–346, https://doi.org/10.1021/j150345a005.

Trent, D. (2000). Propylene oxide. *Kirk-Othmer Encyclopedia of Chemical Technology*, https://doi.org/10.1002/0471238961.1618151620180514.a01.

Van Aken, P. A. & Liebscher, B. (2002). Quantification of ferrous/ferric ratios in minerals: New evaluation schemes of Fe L23 electron energy-loss near-edge spectra. *Physics and Chemistry of Minerals*, *29*(3), 188–200, https://doi.org/10.1007/S00269-001-0222-6.

Vannice, M. (2005). *Kinetics of Catalytic Reactions*. Boston, MA: Springer US.

Vieten, J., *et al.* (2019). Materials design of perovskite solid solutions for thermochemical applications. *Energy and Environmental Science*, *12*(4), 1369–1384, https://doi.org/10.1039/c9ee00085b.

Vieten, J., Bulfin, B., Senholdt, M., Roeb, M., Sattler, C., & Schmücker, M. (2017). Redox thermodynamics and phase composition in the system SrFeO3 $\delta$ — SrMnO3 $\delta$. *Solid State Ionics*, *308*, 149–155, https://doi.org/10.1016/J.SSI.2017.06.014.

Villars, P. & Cenzual, K. (2012). SrFeO3 Crystal Structure: Datasheet from "PAULING FILE Multinaries Edition – 2012" https://materials.springer.com/isp/crystallographic/docs/sd_1503839.

Vyazovkin, S. (2020). Kissinger Method in Kinetics of Materials: Things to Beware and Be Aware of. *Molecules*, *25*(12), 2813, https://doi.org/10.3390/MOLECULES25122813.

Vyazovkin, S. (2021). Determining preexponential factor in model-free kinetic methods: How and why? *Molecules*, *26*(11), 3077, https://doi.org/10.3390/molecules26113077.

Wack, S., Lunca Popa, P., Adjeroud, N., Guillot, J., Pistillo, B. R., & Leturcq, R. (2019). Large-Scale Deposition and Growth Mechanism of Silver Nanoparticles by Plasma-Enhanced Atomic Layer Deposition. *The Journal of Physical Chemistry C*, *123*(44), 27196–27206, https://doi.org/10.1021/acs.jpcc.9b06473.

Wakao, N. & Funazkri, T. (1978). Effect of fluid dispersion coefficients on particle-to-fluid mass transfer coefficients in packed beds: Correlation of sherwood numbers. *Chemical Engineering Science*, *33*(10), 1375–1384, https://doi.org/10.1016/0009-2509(78)85120-3.

Wang, B. & Shen, L. (2022). Recent Advances in NH 3 Synthesis with Chemical Looping Technology. *Industrial & Engineering Chemistry Research*, *61*(50), 18215–18231, https://doi.org/10.1021/acs.iecr.2c02926.

Wang, C. B., Deo, G., & Wachs, I. E. (1999). Interaction of Polycrystalline Silver with Oxygen, Water, Carbon Dioxide, Ethylene, and Methanol: In Situ Raman and Catalytic Studies. *Journal of Physical Chemistry B*, *103*(27), 5645–5656, https://doi.org/10.1021/JP984363L.

Wang, F., Egerton, R., & Malac, M. (2009). Fourier-ratio deconvolution techniques for electron energy-loss spectroscopy (EELS). *Ultramicroscopy*, *109*(10), 1245–1249, https://doi.org/10.1016/J.ULTRAMIC.2009.05.011.

Wang, H., *et al.* (2017). Activation and deactivation of Ag/CeO2 during soot oxidation: influences of interfacial ceria reduction. *Catalysis Science & Technology*, *7*(10), 2129–2139, https://doi.org/10.1039/C7CY00450H.

Wang, J., Lai, X., Zhang, H., Zhou, X., Lin, T., Wang, J., & Chen, Y. (2023). Low-temperature toluene oxidation on Ag/CexZr1-xO2 monolithic catalysts: Synergistic catalysis of silver and ceria-zirconia. *Combustion and Flame*, *248*, 112577, https://doi.org/10.1016/j.combustflame.2022.112577.

Wang, Q., Gu, Y., Zhu, W., Han, L., Pan, F., & Song, C. (2021). Noble-Metal-Assisted Fast Interfacial Oxygen Migration with Topotactic Phase Transition in Perovskite Oxides. *Advanced Functional Materials*, *31*(50), 2106765, https://doi.org/10.1002/adfm.202106765.

Wang, X., *et al.* (2022a). High-throughput oxygen chemical potential engineering of perovskite oxides for chemical looping applications. *Energy & Environmental Science*, *15*(4), 1512–1528, https://doi.org/10.1039/D1EE02889H.

Wang, X., Yang, L., Ji, X., Gao, Y., Li, F., Zhang, J., & Wei, J. (2022b). Reduction kinetics of SrFeO3$\delta$/CaO · MnO nanocomposite as effective oxygen carrier for chemical looping partial oxidation of methane. *Frontiers of Chemical Science and Engineering*, *16*, 1726–1734, https://doi.org/10.1007/S11705-022-2188-5.

Wei, Y., Wang, H., & Li, K. (2010). Ce-Fe-O mixed oxide as oxygen carrier for the direct partial oxidation of methane to syngas. *Journal of Rare Earths*, *28*(4), 560–565, https://doi.org/10.1016/S1002-0721(09)60154-X.

Wilson, S. A. & Muhich, C. L. (2024). A Bayesian method for selecting data points for thermodynamic modeling of off-stoichiometric metal oxides. *Journal of Materials Chemistry A*, https://doi.org/10.1039/D3TA06627D.

Wilson, S. A., Stechel, E. B., & Muhich, C. L. (2023). Overcoming significant challenges in extracting off-stoichiometric thermodynamics using the compound energy formalism through complementary use of experimental and first principles data: A case study of Ba1-xSrxFeO3-$\delta$. *Solid State Ionics*, *390*, 116115, https://doi.org/10.1016/j.ssi.2022.116115.

Winayu, B. N. R., Tseng, T. K., & Chu, H. (2023). Chemical Looping Strategy in Various Types of Carbon Capture Technologies. *Processes*, *11*(11), 3164, https://doi.org/10.3390/PR11113164.

Xing, Y., *et al.* (2022). Atomic-scale operando observation of oxygen diffusion during topotactic phase transition of a perovskite oxide. *Matter*, *5*(9), 3009–3022, https://doi.org/10.1016/j.matt.2022.06.013.

Xing, Y. L., *et al.* (2019). In situ Negative Cs HRTEM Imaging of Topotactic Phase Transformation from Perovskite SrFeO3 to Brownmillerite SrFeO2.5. *Microscopy and Microanalysis*, *25*(S2), 1482–1483, https://doi.org/10.1017/S1431927619008146.

Xu, M., Wu, H. C., Lin, Y. S., & Deng, S. (2018). Simulation and optimization of pressure swing adsorption process for high-temperature air separation by perovskite sorbents. *Chemical Engineering Journal*, *354*, 62–74, https://doi.org/10.1016/J.CEJ.2018.07.080.

Yoo, J., Verma, A., Wang, S., & Jacobson, A. J. (2005). Oxygen Transport Kinetics in SrFeO[sub 3$\delta$], La[sub 0.5]Sr[sub 0.5]FeO[sub 3$\delta$], and La[sub 0.2]Sr[sub 0.8]Cr[sub 0.2]Fe[sub 0.8]O[sub 3$\delta$] Measured by Electrical Conductivity Relaxation. *Journal of The Electrochemical Society*, *152*(3), A497, https://doi.org/10.1149/1.1854617.

Zambelli, T., Barth, J. V., & Wintterlin, J. (2002). Thermal dissociation of chemisorbed oxygen molecules on Ag(110): an investigation by scanning tunnelling microscopy. *Journal of Physics: Condensed Matter*, *14*(16), 4241–4250, https://doi.org/10.1088/0953-8984/14/16/314.

Zhang, X., Pei, C., Zhao, Z. J., & Gong, J. (2024). Towards green and efficient chemical looping ammonia synthesis: design principles and advanced redox catalysts. *Energy & Environmental Science*, *17*(7), 2381–2405, https://doi.org/10.1039/D4EE00037D.

Zhao, Z. & Carpenter, M. A. (2013). Support-Free Bimodal Distribution of Plasmonically Active Ag/AgO x Nanoparticle Catalysts: Attributes and Plasmon Enhanced Surface Chemistry. *The Journal of Physical Chemistry C*, *117*(21), 11124–11132, https://doi.org/10.1021/jp400837r.

Zhong, M., Wang, C., Xu, J., Cai, Y., Xiao, B., Xu, T., & Wang, X. (2024). Composite xNiFe2O4/(1-x)SrFe12O19 oxygen carriers for chemical looping reforming of bioethanol coupled with water splitting to coproduce syngas and hydrogen. *Journal of the Energy Institute*, *117*, 101780, https://doi.org/10.1016/J.JOEI.2024.101780.

Zhou, H. D. & Goodenough, J. B. (2005). Electronic behavior of three oxygen nonstoichiometric Fe4+/Fe3+ oxoperovskites. *Journal of Solid State Chemistry*, *178*(12), 3679–3685, https://doi.org/10.1016/J.JSSC.2005.09.020.

Zhou, Y., *et al.* (2023). Ruddlesden-Popper-type perovskite Sr3Fe2O7$\delta$ for enhanced thermochemical energy storage. *EcoMat*, *5*(7), e12347, https://doi.org/10.1002/EOM2.12347.

Zhu, A., Li, D., Zhu, T., & Zhu, X. (2024). Tailored SrFeO3-$\delta$ for chemical looping dry reforming of methane. *Green Chemical Engineering*, https://doi.org/10.1016/J.GCE.2024.04.003.

Zhu, C., Hou, S., Hou, L., & Xie, K. (2018). Perovskite SrFeO3$\delta$ decorated with Ni nanoparticles for high temperature carbon dioxide electrolysis. *International Journal of Hydrogen Energy*, *43*(36), 17040–17047, https://doi.org/10.1016/j.ijhydene.2018.07.148.

Zhu, X., Imtiaz, Q., Donat, F., Müller, C. R., & Li, F. (2020). Chemical looping beyond combustion – a perspective. *Energy & Environmental Science*, *13*(3), 772–804, https://doi.org/10.1039/c9ee03793d.

# Appendix A

# Supplementary material for Chapter 2

## A.1 Parameters for fitting XRD patterns

Table A.1 ICSD collection codes for reference patterns used for phase refinement from XRD measurements

| Phase | ICSD Collection Code |
|---|---|
| $SrFeO_3$ | 91062 |
| SrO | 163625 |
| $Sr_3Fe_2O_7$ | 74437 |
| $SrCO_3$ | 15195 |
| $SrFeO_{2.5}$ | 51318 |
| $\alpha$-$Fe_2O_3$ | 56372 |
| $CeO_2$ | 24887 |
| Ag | 53759 |
| $\alpha$-$Al_2O_3$ | 10425 |
| $NaNO_3$ | 15332 |
| $Na_2CO_3$ | 60311 |
| Au | 52249 |
| AgCl | 56538 |
| AgAu | 604769 |

## A.2 Determination of Raman spot size

The effective spot size of the laser beam used to collect Raman spectra was determined by collecting scans of photosensitive $Ag_2CO_3$, which upon exposure to light undergoes photocorrosion to form Ag and release $CO_2$ (Dai *et al.*, 2012). After *c.* 30 s exposure to the laser beam, dark spots corresponding to beam damage of approximate diameter 20 $\mu$m were observed, with representative examples shown in Fig. A.1.

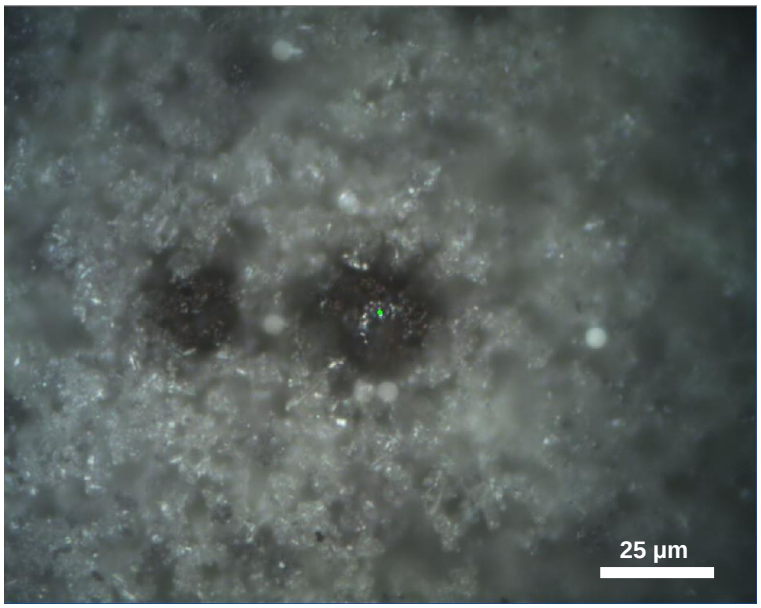


Fig. A.1 Beam damage to light-sensitive $Ag_2CO_3$ from Raman laser (white = $Ag_2CO_3$, black = Ag).

# A.3 Measurements of exhaust gas from TGA

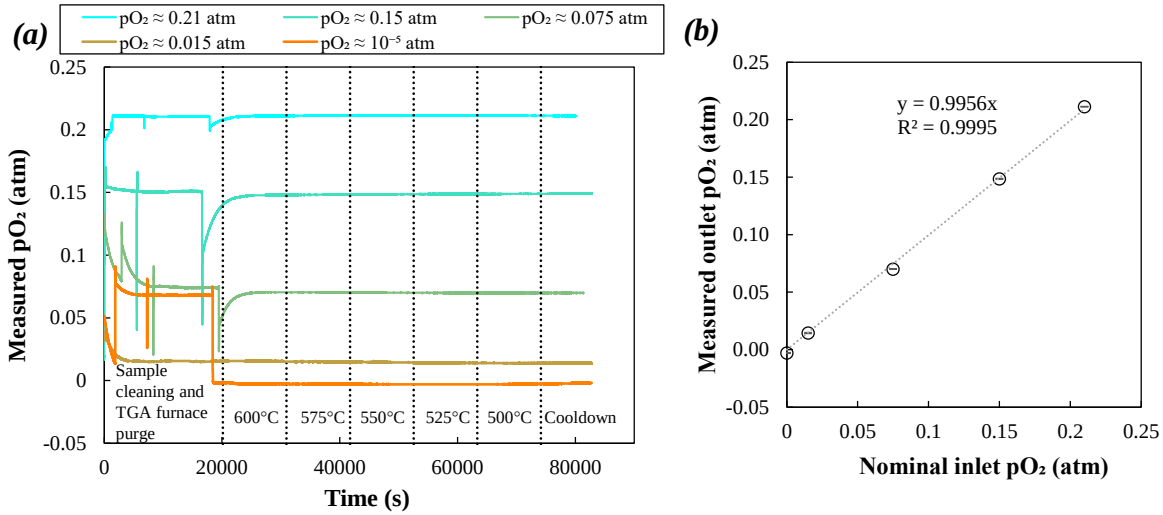


Fig. A.2 (a) Measured $pO_2$ at the outlet of the TGA over the course of experiments with varied inlet $pO_2$ values, showing minimal variation over time, (b) average $pO_2$ measured at the TGA outlet compared with nominal inlet concentration (error bars show standard deviation over 15 h of measurements after cleaning the sample and purging the TGA furnace with blended gas).

# A.4 Calibration mixtures for gas chromatography

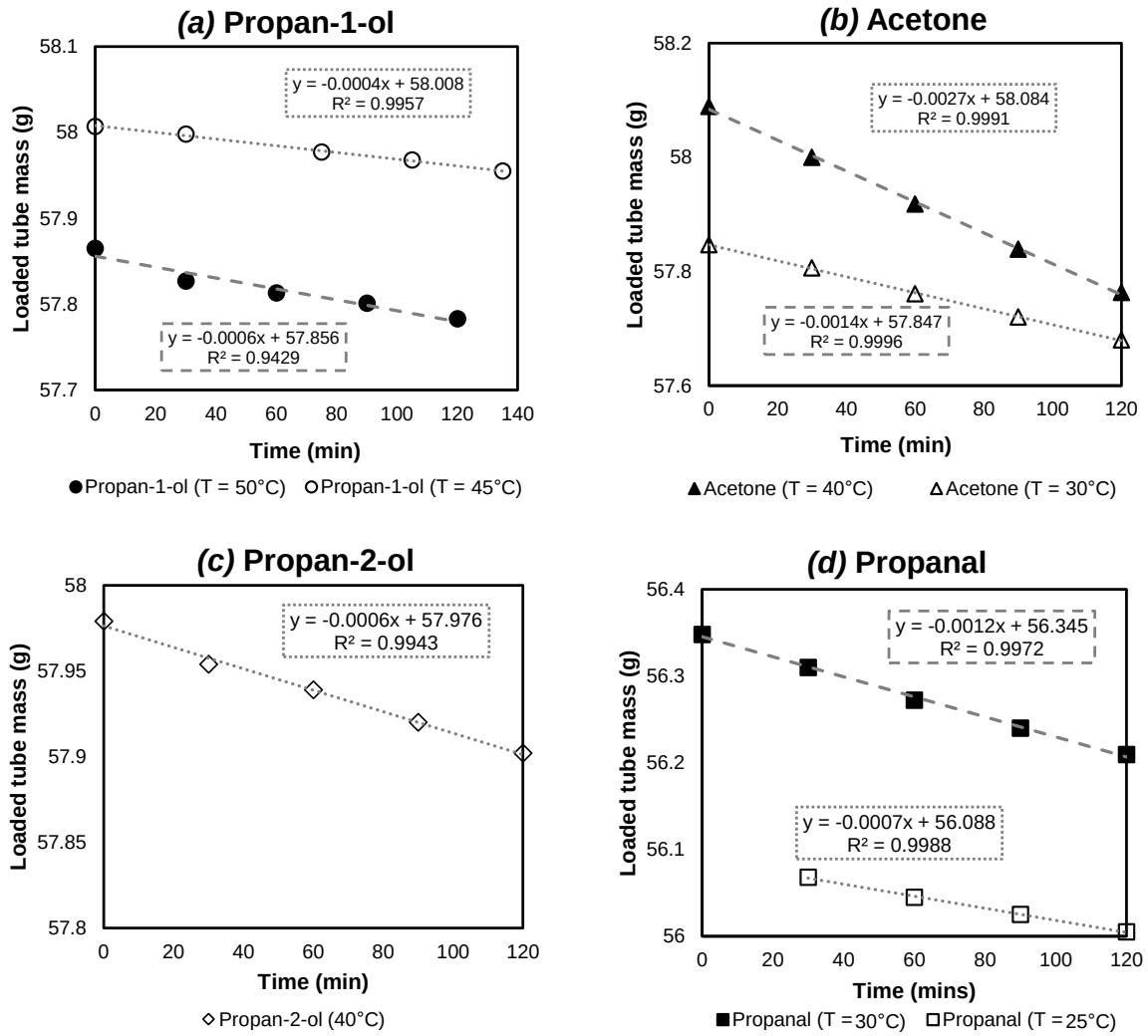


Fig. A.3 Total mass (diffusion tube plus analyte liquid mass) as a function of time for (a) propan-1-ol, (b) acetone, (c) propan-2-ol, and (d) propanal. Linear gradient implies approximately constant outlet analyte concentration.

# Appendix B

# Supplementary material for Chapter 3

## B.1 Additional thermogravimetric analysis

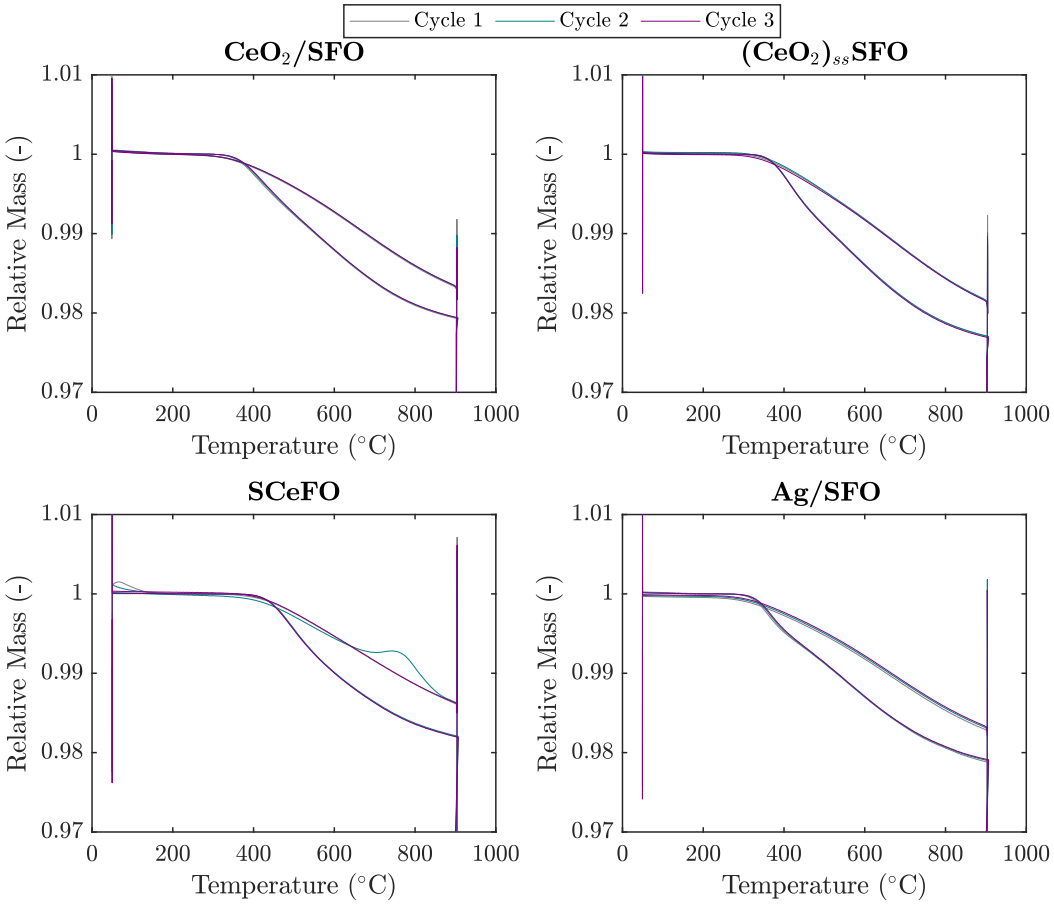


Fig. B.1 Temperature ramping cycles with reduction in $N_2$ and oxidation in air for $CeO_2$/SFO, $(CeO_2)_{ss}$SFO, SCeFO, and Ag/SFO showing minimal difference in mass change between successive cycles for each sample. The deviation observed in cycle 2 for SCeFO at around 800°C was attributed to a fluctuation in TGA coolant temperature, rather than a genuine change in sample mass.

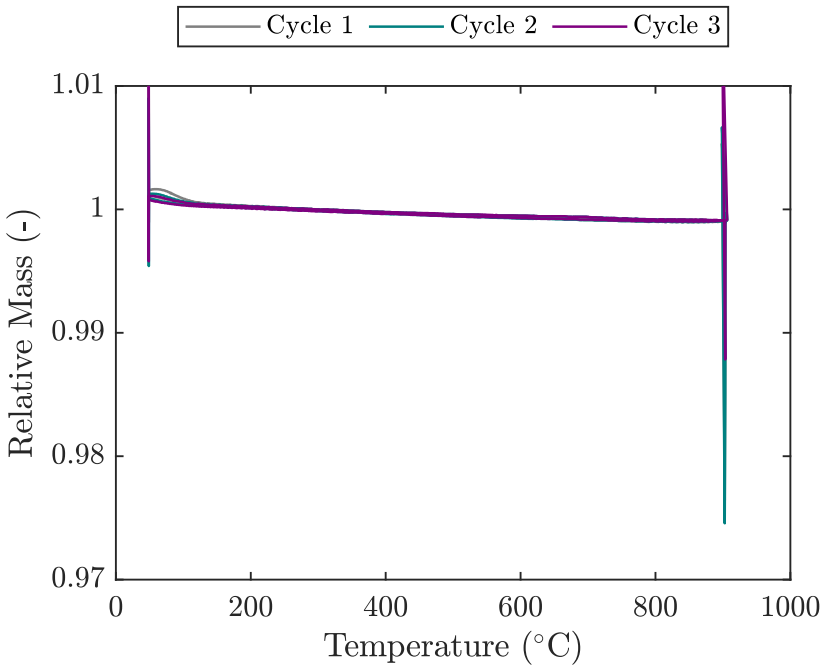


Fig. B.2 Temperature ramping cycles with reduction in $N_2$ and oxidation in air for particles of $CeO_2$, showing a relative mass change of less than 0.01.

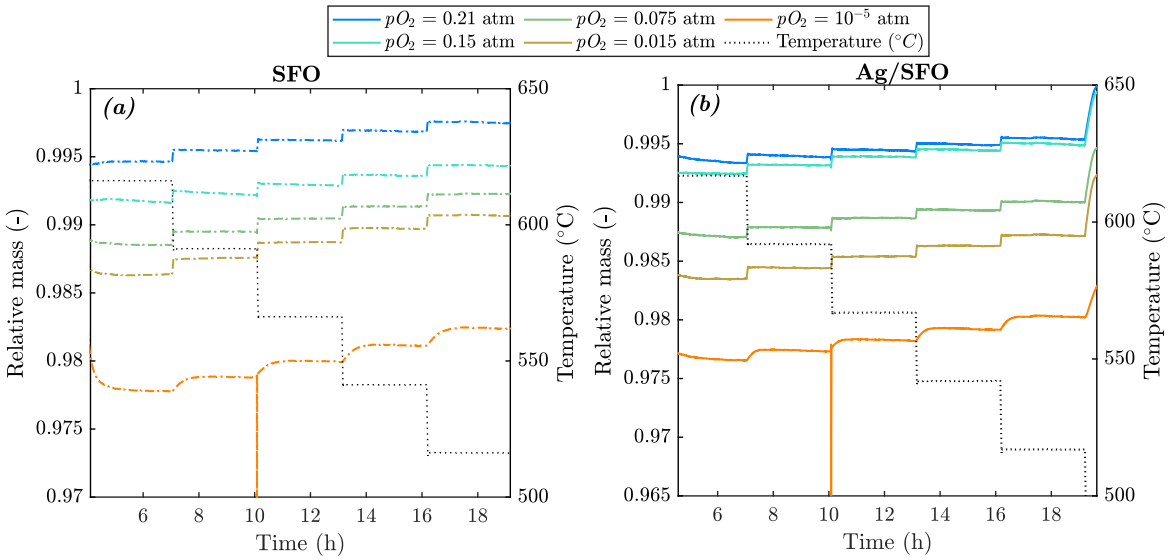


Fig. B.3 TGA curves for **(a)** SFO (dash-dot lines) and **(b)** Ag/SFO (solid lines), brought to equilibrium over the temperature range 500-600°C in varied $pO_2$ atmospheres

## B.2 Comparison of linear and non-linear regression to determine kinetic parameters

Measurements of oxygen release using the packed-bed reactor were fitted over the temperature range 500-575°C for SFO, and over the range 475-575°C for all other samples. Given that each measured temperature point consisted of multiple repeated cycles, results from all cycles were included when fitting regression parameters. Representative non-linear and linear fits are shown in Fig. B.4. The extracted values of $E_a$ and $A$ *via* non-linear and linear regression are summarised in Table B.1.

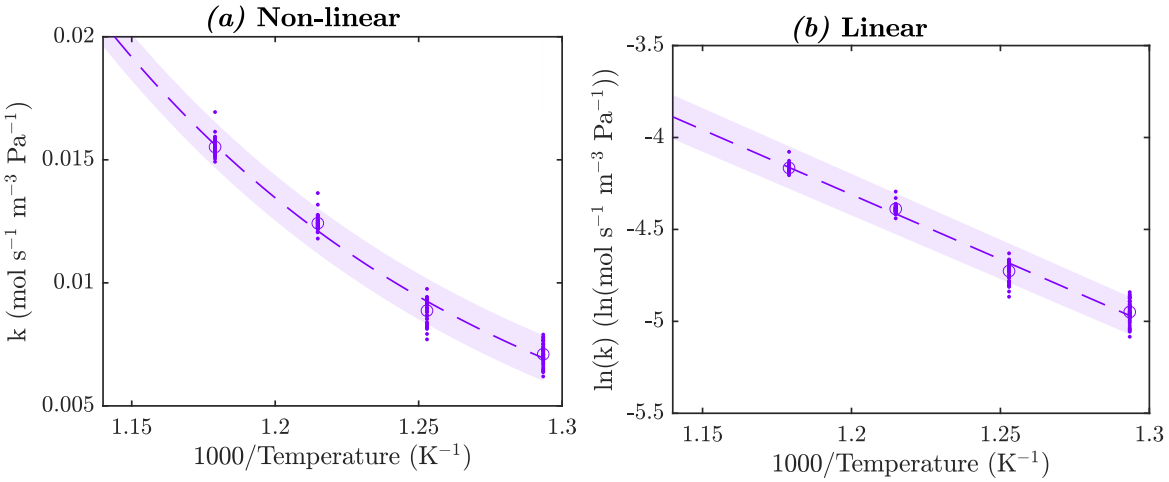


Fig. B.4 **(a)** Non-linear and **(b)** linear fit for oxygen release from Ag/SFO. Points indicate experimental measurements, circles indicate average value at each temperature point, dashed line indicates fitted curve, shaded area indicates 95% prediction band for fitted parameters.

Table B.1 Extracted kinetic parameters from linear and non-linear regression of experimental measurements in the packed bed. Bracketed values indicate estimated 95% confidence intervals for each fitted parameter.

| Sample | $E_a$ (kJ mol$^{-1}$) (Linear) | $A$ (mol$_{O_2}$s$^{-1}$m$^{-3}$Pa$^{-1}$) (Linear) | $R^2$ (Linear) | $E_a$ (kJ mol$^{-1}$) (Non-linear) | $A$ (mol$_{O_2}$s$^{-1}$m$^{-3}$Pa$^{-1}$) (Non-linear) | $R^2$ (Non-linear) |
|---|---|---|---|---|---|---|
| SFO | 109.3 (104.9; 113.6) | 66170 (32860; 120600) | 0.99 | 102.3 (97.9; 106.7) | 22030 (8103; 36320) | 0.99 |
| $CeO_2$/SFO | 51.5 (48.5; 54.6) | 16.9 (10.6; 26.9) | 0.83 | 66.3 (63.1; 69.5) | 152 (81.0; 223) | 0.90 |
| $(CeO_2)_{ss}$SFO | 77.9 (75.8; 80.0) | 862 (625; 1187) | 0.95 | 75.7 (73.9; 77.5) | 623 (459; 788) | 0.98 |
| SCeFO | 26.8 (25.1; 28.6) | 0.54 (0.41; 0.70) | 0.81 | 29.9 (26.7; 33.2) | 0.88 (0.46; 1.30) | 0.89 |
| Ag/SFO | 68.4 (66.6; 70.2) | 267.1 (203.5; 350.6) | 0.96 | 69.0 (66.0; 71.9) | 278 (158; 398) | 0.99 |

# Appendix C

# Supplementary material for Chapter 4

## C.1 Additional *in-situ* XRD characterisation

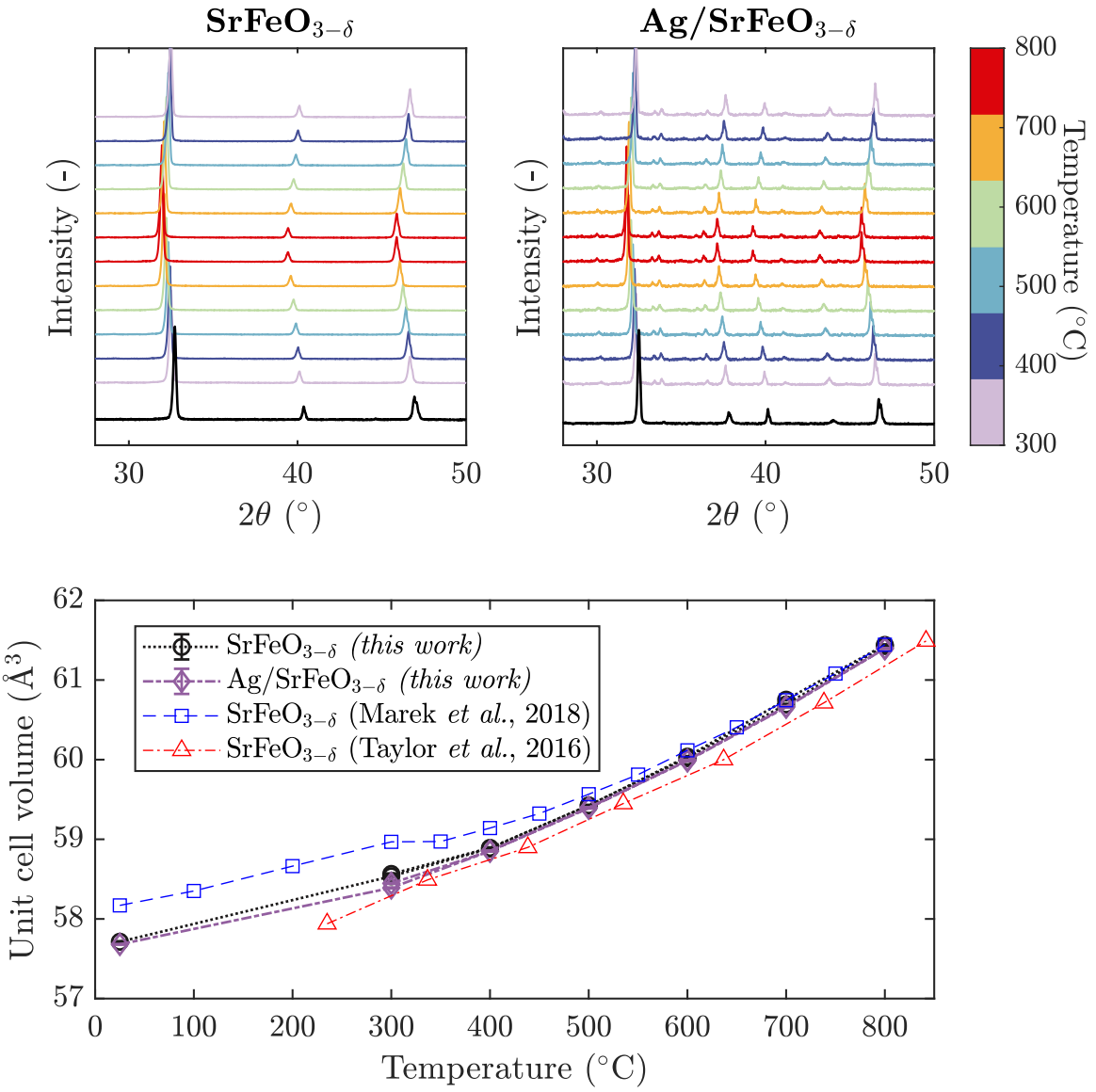


Fig. C.1 *In-situ* XRD patterns during heating and cooling of $SrFeO_{3-\delta}$ and $Ag/SrFeO_{3-\delta}$ in air, and corresponding estimated unit cell volume of $SrFeO_3$ phase, as compared to results reported by Marek *et al.* (2018a) and Taylor *et al.* (2016).

## C.2 XPS fitting parameters and additional scans

Table C.1 Binding energy (BE) and peak full width at half maximum (FWHM) constraints for fitting peaks to O1s XPS spectra, with peak assignments and references.

| Peak | BE constraint | FWHM constraint | Assignment |
|---|---|---|---|
| A | 529.0 ± 1 eV | ≤2 eV | $SrFeO_{3-\delta}$ lattice oxygen |
| B | A + 1.2 eV (fixed offset) | Equal to A | SrO termination oxygen |
| C | A + 2.5 ± 0.75 eV | ≤1.75 eV | Surface oxygen |
| D | C + 1 ± 0.50 eV | ≤2 eV | Ag-$O_x$ species |
| E | 533.0 ± 0.50 eV | ≤2 eV | Impurities |
| F | 539.0 ± 0.50 eV | ≤1 eV | $O_2$ (physisorbed) |
| G | 539.5 ± 0.50 eV | ≤1 eV | $O_2$ (gas) |

| Peak | Reference(s) |
|---|---|
| A | Crumlin *et al.* (2012); Stoerzinger *et al.* (2020); Zhou *et al.* (2023) |
| B | Crumlin *et al.* (2012); Stoerzinger *et al.* (2020) |
| C | Crumlin *et al.* (2012); Stoerzinger *et al.* (2020); Zhou *et al.* (2023) |
| D | Pu *et al.* (2022); Schön (1973) |
| E | Abd El-Naser *et al.* (2021); Falcón *et al.* (2002) |
| F | Puglia *et al.* (1995) |
| G | Avval *et al.* (2019) |

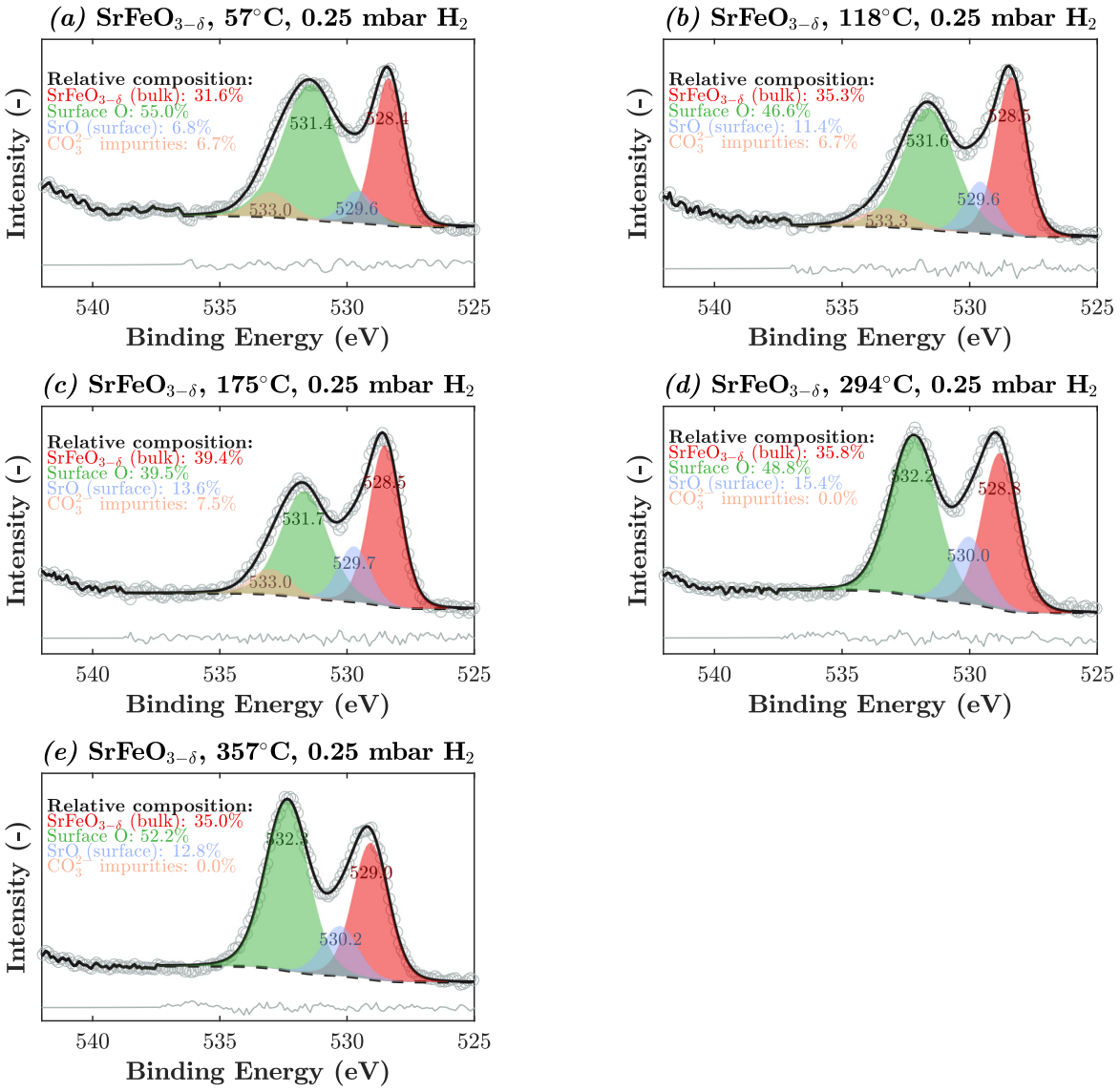


Fig. C.2 Additional NAP-XPS O1s spectra of $SrFeO_{3-\delta}$ under 0.25 mbar $H_2$. Circles indicate experimental measurements, solid black lines indicate overall fitted curve, shaded areas correspond to individual fitted peaks, dashed lines correspond to fitted baseline, and solid grey lines correspond to difference between fitted curve and measurements. Percentage areas estimated for each peak are given, corresponding to the approximate proportion (at%) of each species at the surface.

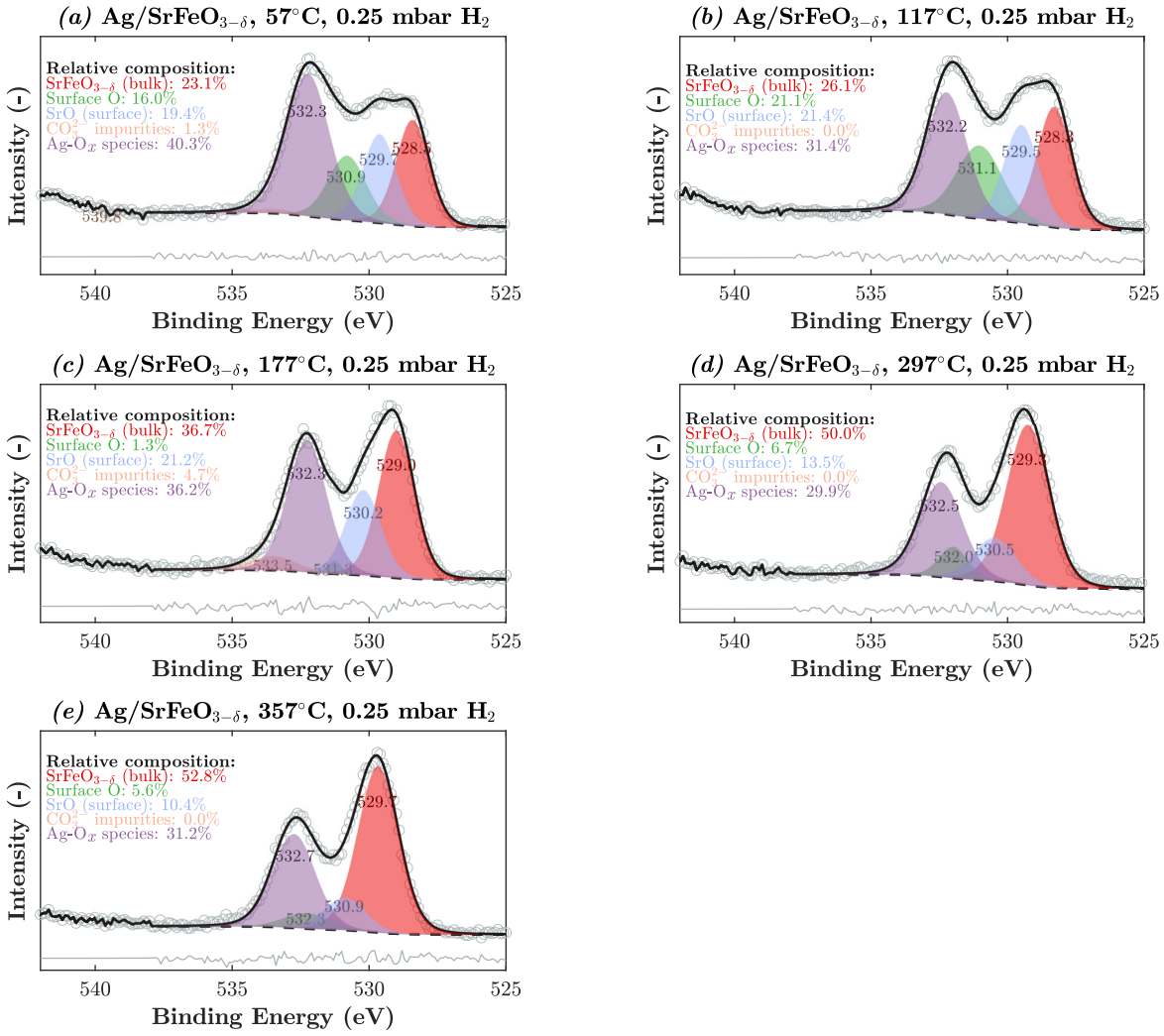


Fig. C.3 Additional NAP-XPS O1s spectra of $Ag/SrFeO_{3-\delta}$ under 0.25 mbar $H_2$. Circles indicate experimental measurements, solid black lines indicate overall fitted curve, shaded areas correspond to individual fitted peaks, dashed lines correspond to fitted baseline, and solid grey lines correspond to difference between fitted curve and measurements. Percentage areas estimated for each peak are given, corresponding to the approximate proportion (at%) of each species at the surface.

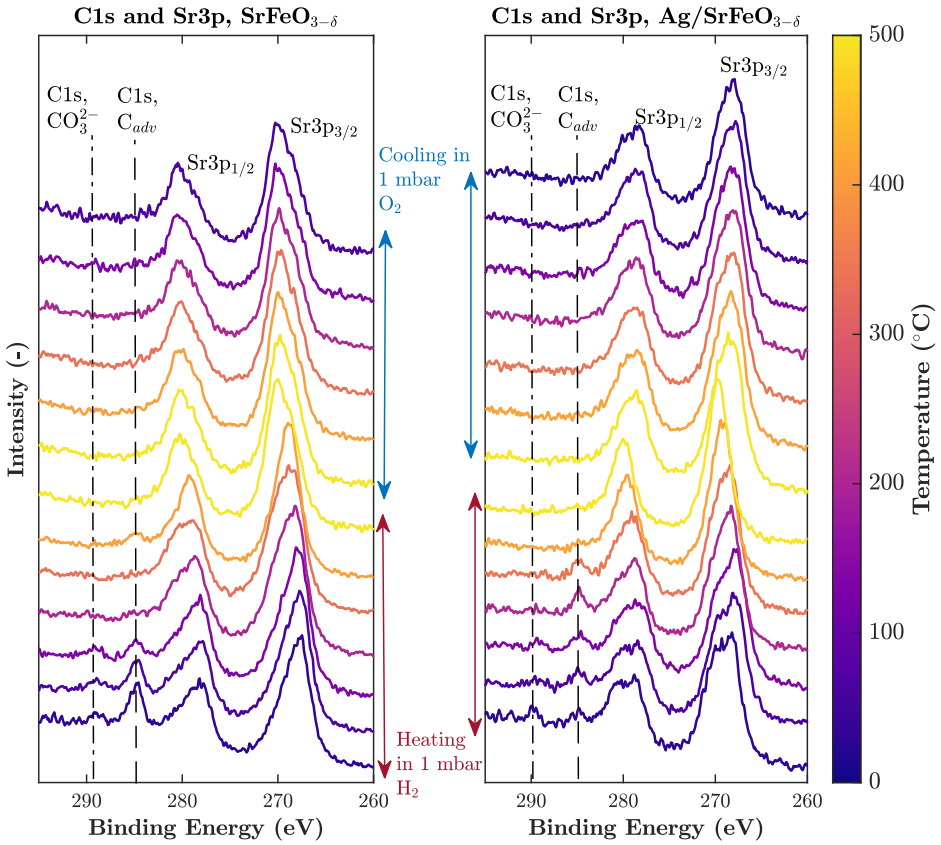


Fig. C.4 NAP-XPS C1s and Sr3p spectra of $SrFeO_{3-\delta}$ and $Ag/SrFeO_{3-\delta}$ under 0.25 mbar $H_2$ and 1 mbar $O_2$, with peaks corresponding to adventitious carbon ($C_{adv}$) and carbonate impurities ($CO_3^{2-}$) labelled.

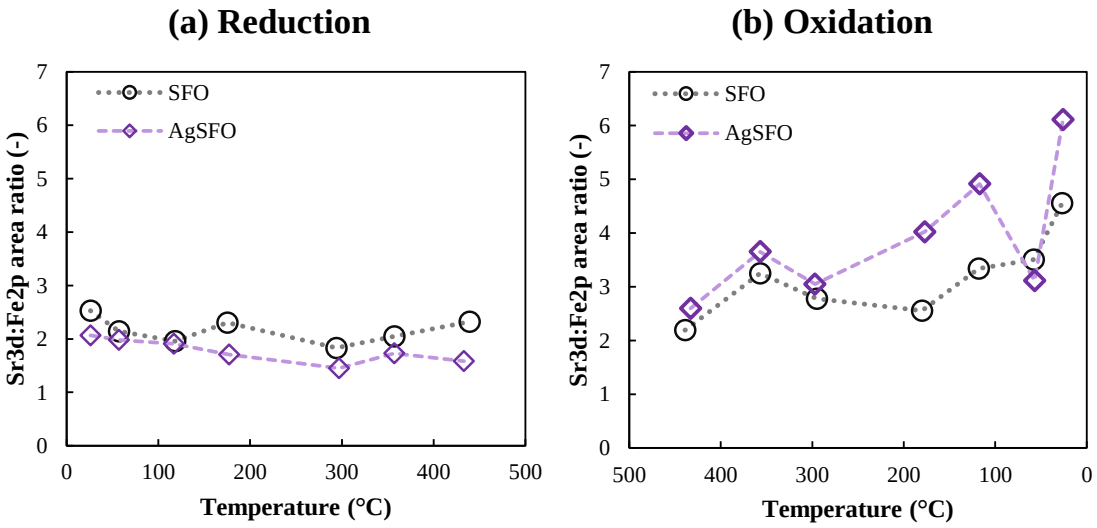


Fig. C.5 Ratio of peak areas from NAP-XPS measurements of Sr3d and Fe2p regions for $SrFeO_{3-\delta}$ and $Ag/SrFeO_{3-\delta}$ during **(a)** reduction in 0.25 mbar $H_2$ and **(b)** oxidation in 1 mbar $O_2$.

## C.3 Comparison with $H_2$-TPR measurements from literature

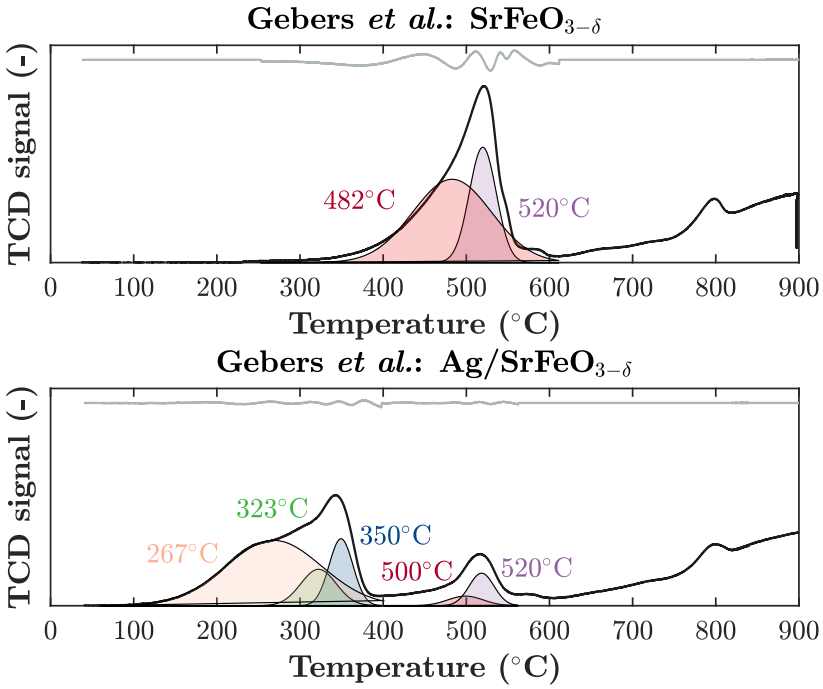


Fig. C.6 Temperature-programmed reduction of SFO and Ag/SFO in 5 vol% $H_2$, with total hydrogen consumption represented by each feature indicated. Figure reproduced based on published measurements from Gebers *et al.* (2023). Shaded curves added based on Gaussian fits with peak centres labelled, and grey line above TCD signal indicating difference between measured values and fitted curves.

## C.4 Proposed structure of $AgSO_x$ surface species

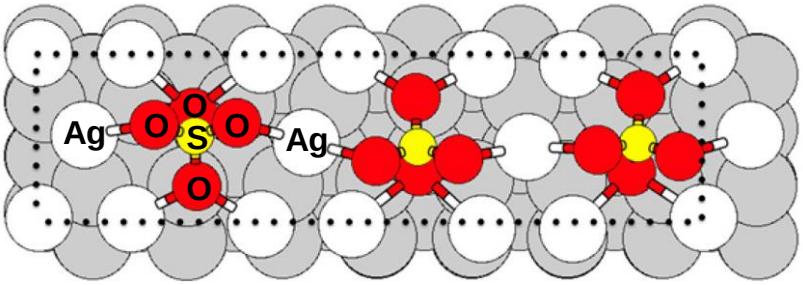


Fig. C.7 Proposed structure of $AgSO_x$ surface species, suggested to be selective for epoxidation of alkenes over Ag. Figure reproduced from Jones *et al.* (2018)

# Appendix D

# Supplementary material for Chapter 5

## D.1 X-ray diffraction patterns

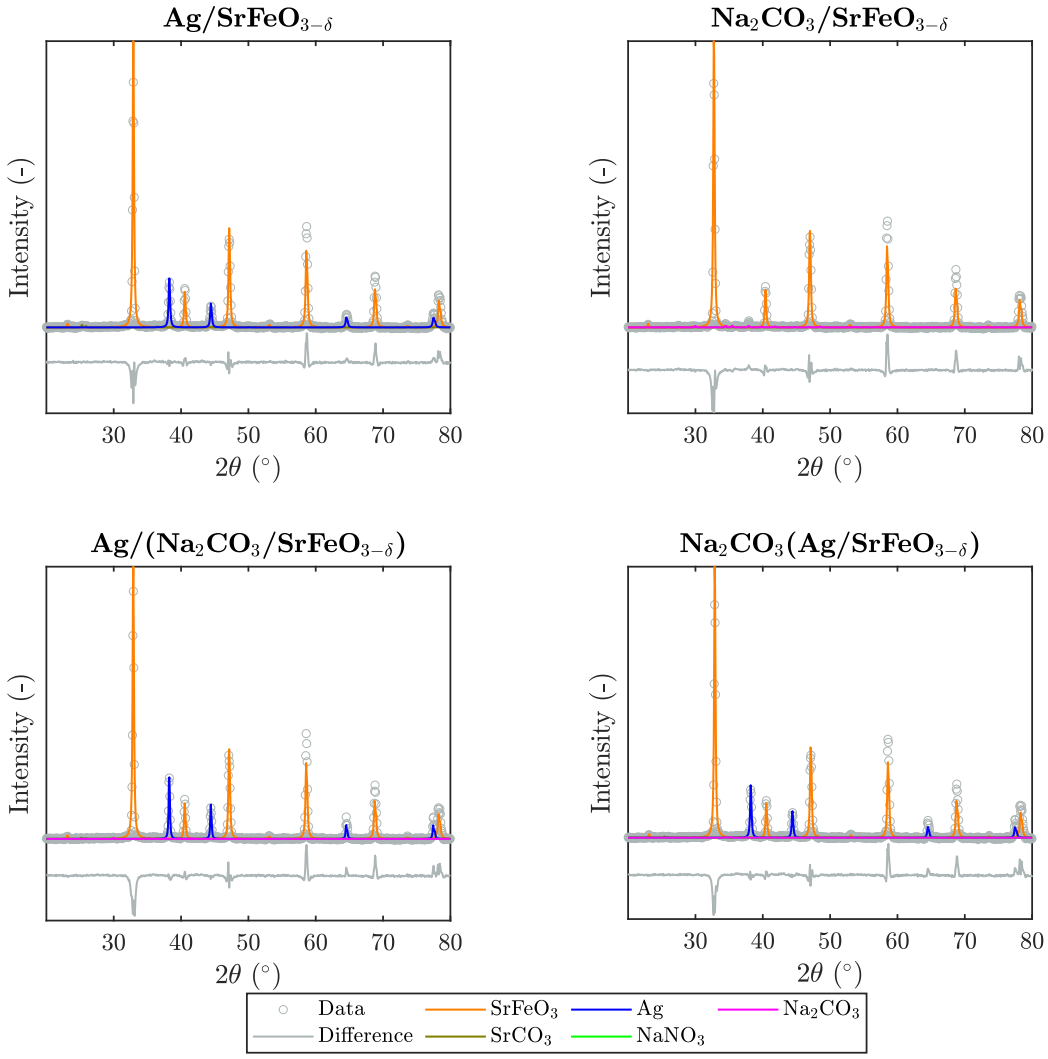


Fig. D.1 Sections of XRD patterns for Ag/SFO, NCO/SFO, Ag(NCO/SFO), and NCO(Ag/SFO). Circles indicate experimental measurements; lines indicate fitted model using reference patterns.

## D.2 XPS fitting parameters and additional scans

Table D.1 Binding energy (BE) and peak full width at half maximum (FWHM) constraints for fitting peaks to XPS spectra, with peak assignments and references.

| Peak | BE constraint (eV) | FWHM constraint (eV) | Assignment |
|---|---|---|---|
| Na1s-A | 1071.6 ± 0.25 | 2 | $Na_2CO_3$ |
| Na1s-B | 1072.9 ± 0.1 | 2 | $Na_2O$ or NaOH |
| O1s-A | 528.5 ± 0.5 | 2 | $SrFeO_3$ lattice oxygen |
| O1s-B | O1s-A + 1.2 (Fixed offset) | Equal to O1s-A | SrO lattice oxygen |
| O1s-C | 531.5 ± 0.5 | 2.5 | $CO_3^{2-}$ and Surface O |
| O1s-D | 533.75 ± 0.25 | 2 | Hydroxide impurities |
| NaKLL | 536.0 ± 0.25 | 3 | Na Auger Peak |
| $Ag3d_{5/2}$-A | 368.5 ± 0.25 | 1.5 | Metallic Ag |
| $Ag3d_{3/2}$-B | $Ag3d_{5/2}$-A + 6 (Fixed offset) | Equal to $Ag3d_{5/2}$-A | Metallic Ag |
| $Ag3d_{5/2}$-C | 369.25 ± 0.25 | 2 | Metallic Ag |
| $Ag3d_{3/2}$-D | $Ag3d_{5/2}$-C + 6 (Fixed offset) | Equal to $Ag3d_{5/2}$-C | Metallic Ag |
| $Ag3d_{5/2}$-E | 367.5 ± 0.25 | 2 | Metallic Ag |
| $Ag3d_{3/2}$-F | $Ag3d_{5/2}$-E + 6 (Fixed offset) | Equal to $Ag3d_{5/2}$-E | Metallic Ag |
| C1s-A | 284.8 ± 0.05 | 1.75 | Adventitious carbon |
| C1s-B | 289.0 ± 0.25 | 2 | $Na_2CO_3$ |

| Peak | Reference(s) |
|---|---|
| Na1s-A | (Hammond *et al.*, 1981) |
| Na1s-B | (Barrie and Street, 1975; Citrin, 1973; Savintsev *et al.*, 2016) |
| O1s-A | (Crumlin *et al.*, 2012; Stoerzinger *et al.*, 2020; Zhou *et al.*, 2023) |
| O1s-B | (Crumlin *et al.*, 2012; Stoerzinger *et al.*, 2020; Zhou *et al.*, 2023) |
| O1s-C | (Abd El-Naser *et al.*, 2021; Falcón *et al.*, 2002; Pu *et al.*, 2022; Schön, 1973) |
| O1s-D | (Barrie and Street, 1975) |
| NaKLL | (Shchukarev and Korolkov, 2004) |
| $Ag3d_{5/2}$-A | (Seah *et al.*, 1998) |
| $Ag3d_{3/2}$-B | |
| $Ag3d_{5/2}$-C | |
| $Ag3d_{3/2}$-D | |
| $Ag3d_{5/2}$-E | |
| $Ag3d_{3/2}$-F | |
| C1s-A | (Biesinger, 2022) |
| C1s-B | (Hammond *et al.*, 1981) |

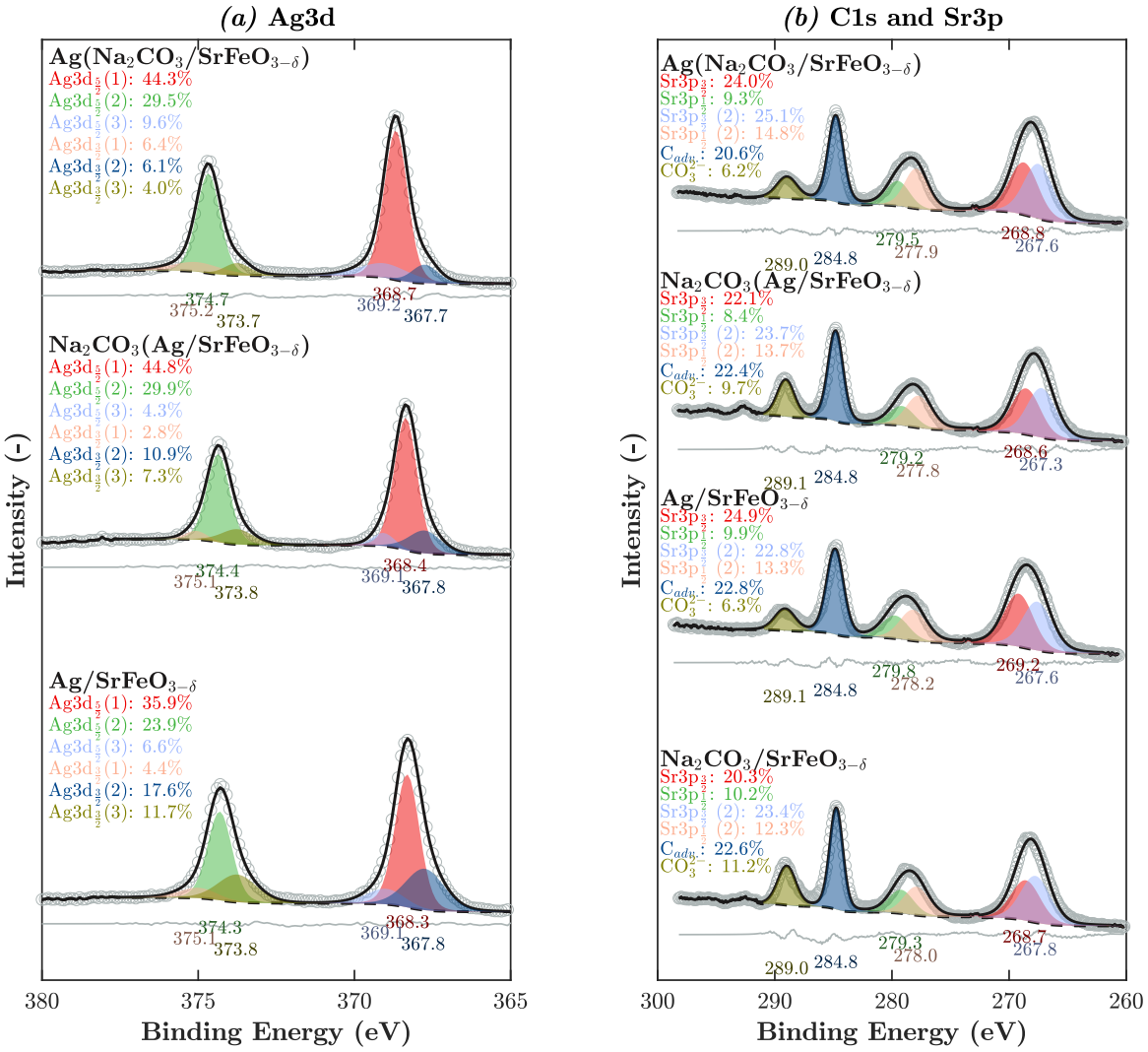


Fig. D.2 Additional XPS spectra corresponding to the **(a)** Ag3d and **(b)** C1s and Sr3p binding energy regions. Circles indicate normalised experimental measurements, solid black lines indicate overall fitted curve, shaded areas correspond to individual fitted peaks, dashed lines correspond to fitted baseline, and grey solid lines correspond to difference between fitted curve and measurements. Percentage areas estimated for each peak are given, corresponding to the approximate proportion (at%) of each species at the surface.

## D.3 Additional measurements from experiments in packed bed reactor

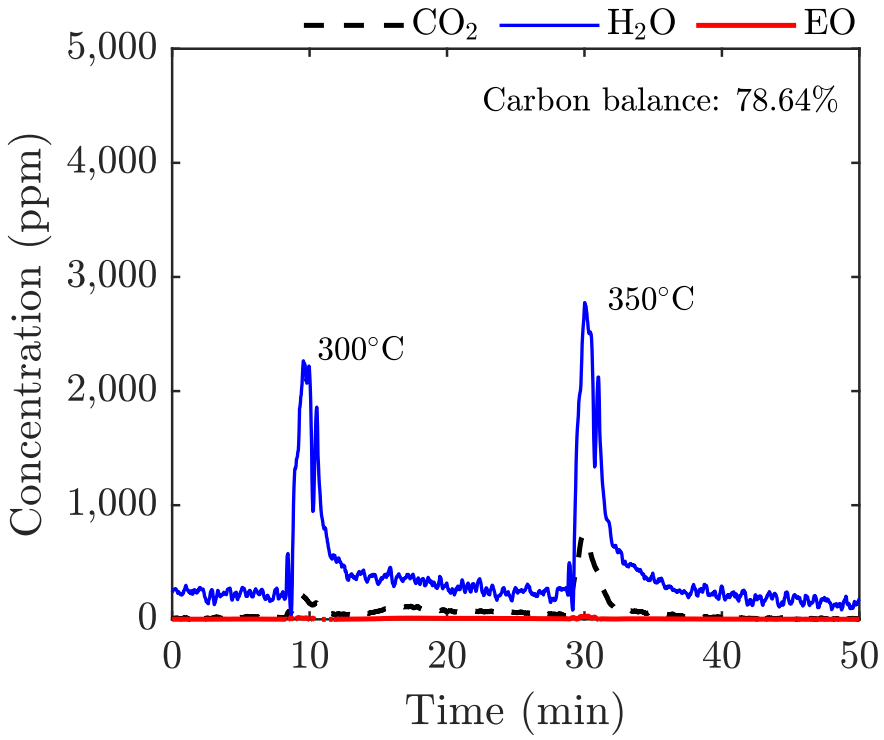


Fig. D.3 Concentration of products during two chemical looping cycles over NCO(Ag/SFO) at 300°C and 350°C.

# Appendix E

# Supplementary material for Chapter 6

## E.1 Additional characterisation measurements

Table E.1 Mean crystallite sizes (nm) of Ag, AgCl, Au, and AgAu in impregnated samples, estimated from broadening of three XRD peaks for each phase.

| Crystallite size (nm) | Ag/SFO | AgCl/SFO | Au-D/SFO | 5AgCl/5Au-D/SFO |
|---|---|---|---|---|
| Ag | 50.2 ± 6.6 | 79.9 ± 15.9 | - | - |
| AgCl | - | 30.0 ± 3.2 | - | 31.9 ± 2.1 |
| AgAu | - | - | - | 75.5 ± 4.3 |
| Au | - | - | 68.0 ± 3.4 | - |

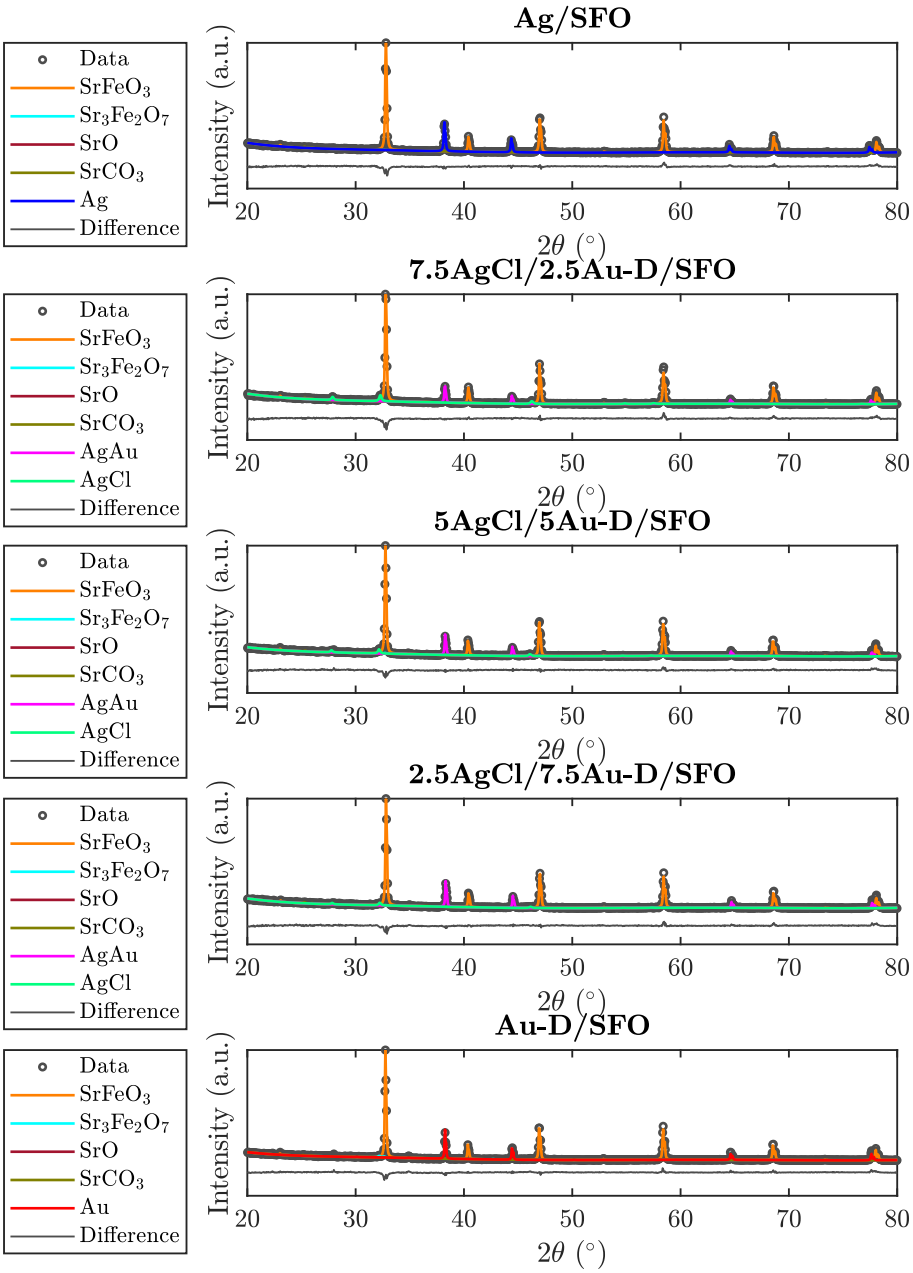


Fig. E.1 XRD patterns for Ag/SFO, Au/SFO, and $x$Ag/(10-$x$)Au-D/SFO materials, with peaks identified.

Table E.2 Peak positions for fitted peaks to XPS spectra, with peak assignments and references.

| Region | Sample | Peak | Peak Position (eV) |
|---|---|---|---|
| $Ag3d_{5/2}$ | Ag foil | Ag3d-A | 368.2 |
| | AgCl powder | Ag3d-B | 367.9 |
| | Ag/SFO | Ag3d-C | 368.2 |
| | AgCl/SFO | Ag3d-D | 367.8 |
| | AgCl/SFO | Ag3d-E | 369.0 |
| | 5AgCl/5Au-D/SFO | Ag3d-F | 367.5 |
| | 5AgCl/5Au-D/SFO | Ag3d-H | 368.6 |
| $Au4f_{7/2}$ | Au foil | Au4f-A | 84.0 (fixed) |
| | 5AgCl/5Au-D/SFO | Au4f-B | 84.5 |
| | 5AgCl/5Au-D/SFO | Au4f-C | 85.5 |
| O1s | All | O1s-A | 528.25 ± 0.25 |
| | All | O1s-B | $SrFeO_3$ peak + 1.2 eV |
| | All | O1s-C | 530.75 ± 0.25 |
| $Cl2p_{3/2}$ | AgCl powder | Cl2p-A | 198.8 |
| | AgCl/SFO | Cl2p-B | 197.3 |
| | 5AgCl/5Au-D/SFO | Cl2p-C | 199.1 |

| Peak | Assignment | Reference(s) |
|---|---|---|
| Ag3d-A | Metallic Ag | (Seah *et al.*, 1998) |
| Ag3d-B | AgCl | (Gaarenstroom and Winograd, 1977) |
| Ag3d-C | Metallic Ag | (Seah *et al.*, 1998) |
| Ag3d-D | AgCl | (Gaarenstroom and Winograd, 1977) |
| Ag3d-E | Strongly oxidised Ag | (Lu *et al.*, 2002) |
| Ag3d-F | AgCl | (Gaarenstroom and Winograd, 1977) |
| Ag3d-H | AgAu alloy | (Chimentão *et al.*, 2006)<br>(Malathi *et al.*, 2014) |
| Au4f-A | Metallic Au | (Seah *et al.*, 1998) |
| Au4f-B | Metallic Au | (Seah *et al.*, 1998) |
| Au4f-C | AgAu alloy | (Chimentão *et al.*, 2006)<br>(Malathi *et al.*, 2014)<br>(Kariuki *et al.*, 2004)<br>(Srnová-Šloufová *et al.*, 2004) |
| O1s-A | $SrFeO_3$ lattice oxygen | (Crumlin *et al.*, 2012)<br>(Stoerzinger *et al.*, 2020)<br>(Zhou *et al.*, 2023) |
| O1s-B | SrO lattice oxygen | (Crumlin *et al.*, 2012)<br>(Stoerzinger *et al.*, 2020)<br>(Zhou *et al.*, 2023) |
| O1s-C | Surface O, $CO_3^{2-}$ impurities | (Abd El-Naser *et al.*, 2021)<br>(Falcón *et al.*, 2002)<br>(Schön, 1973) |
| Cl2p-A | AgCl | (Kaushik, 1991) |
| Cl2p-B | AgCl | (Kaushik, 1991)<br>(Qin *et al.*, 2017) |
| Cl2p-C | AgCl | (Kaushik, 1991) |

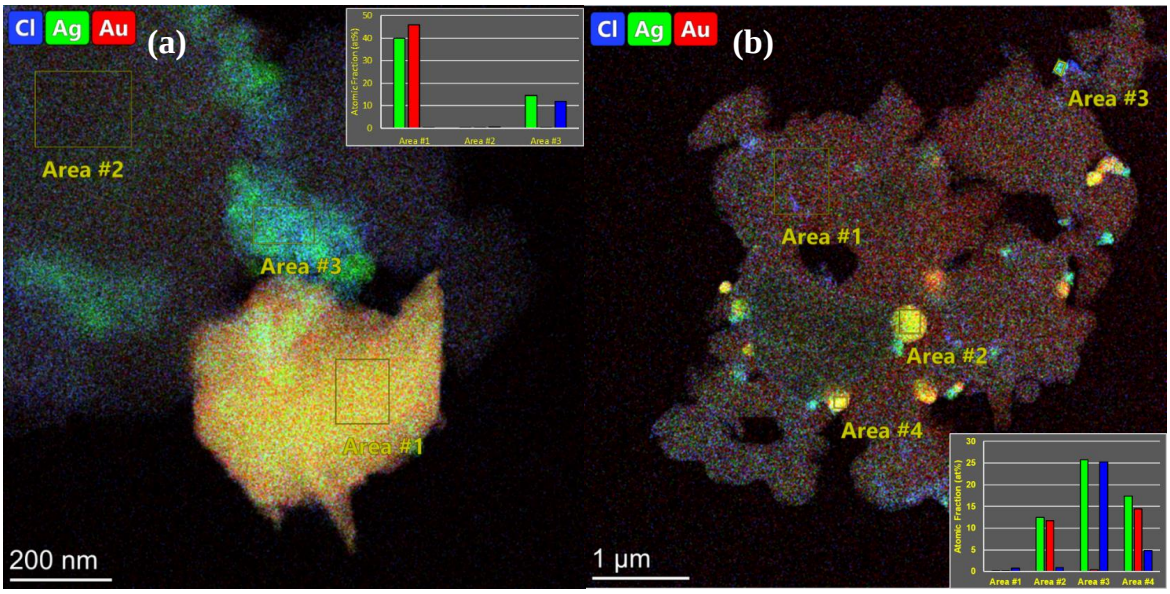


Fig. E.2 STEM-EDS surface maps of 5AgCl/5Au-D/SFO sample, with elemental composition of areas of interest given in inlay. In **(a)**, particles of AgCl (areas 3 and 4) show an Ag:Cl ratio of around 2, suggesting the presence of metallic Ag within the particles, whereas the AgCl particles in **(b)** (area 3) show a ratio of approximately 1, corresponding to a pure AgCl phase.

## E.2 Calculation of available oxygen from AgCl/Au-D/SFO materials

Extended reduction was performed over 2.5AgCl/7.5Au-D/SFO and 7.5AgCl/2.5Au-D/SFO materials by passing 5.13% propylene over the active bed for 100 min, taking a gas sample from the outlet stream every 20 min. The gradient of the cumulative oxygen release curve corresponds to the rate of oxygen relase from the SFO support. For 2.5AgCl/7.5Au-D/SFO (Fig. E.3a), the gradient was approximately constant, indicating a constant rate of oxygen release. For 7.5AgCl/2.5Au-D/SFO (Fig. E.3b), the cumulative oxygen release reached a plateau with increasing time, corresponding to a decrease in the rate of oxygen release.

The maximum possible oxygen available from silver oxides (shown as a dash-dot line in Fig. E.3), in the hypothetical case that all Ag was present as $Ag_2O$, was estimated from Eq. E.1, where $n_{oxygen}$ is the amount of oxygen available (mol), $m_{bed}$ is the mass of the active bed (*i.e.* 1.5 g for all experiments), $\lambda_m$ is the nominal mass fraction of surface Ag, and $M_r(Ag)$ is the molar mass of silver (g mol$^{-1}$). The factor of 2 in the denominator accounts for the 2:1 ratio of Ag to O in $Ag_2O$.

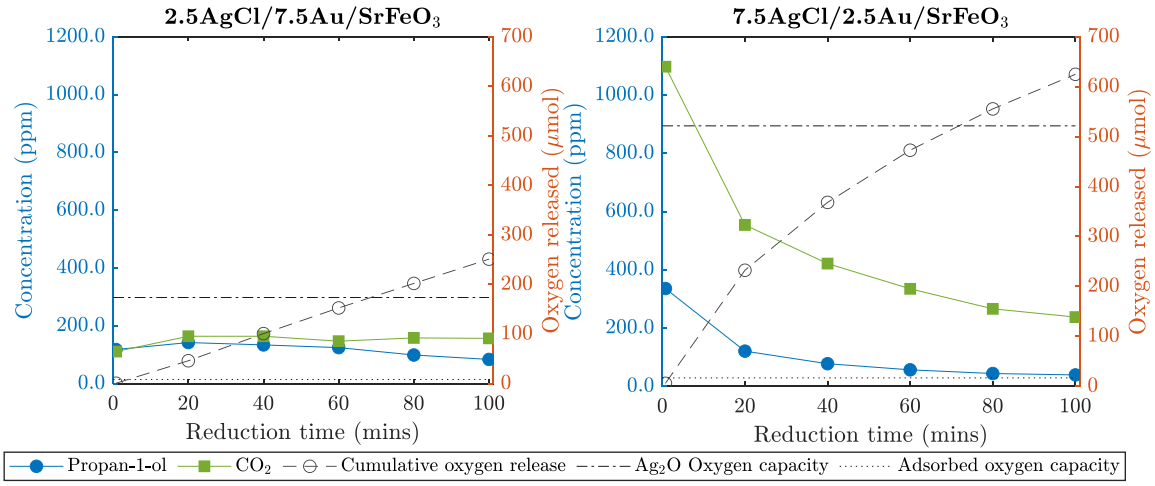


Fig. E.3 Outlet gas composition for extended reduction of **(a)** 2.5AgCl/7.5Au-D/SFO and **(b)** 7.5AgCl/2.5Au-D/SFO in 5.13 vol% propylene at 280°C. Horizontal lines indicate calculated oxygen availability from $Ag_2O$ if all Ag were present as $Ag_2O$, and available oxygen from adsorption of O at the surface of the AgCl and Au catalyst.

$$n_{oxygen} = \frac{m_{bed}\lambda_m}{2M_r(Ag)} \tag{E.1}$$

The maximum theoretical adsorbed oxygen at the surface of AgCl (shown as a dotted line in Fig. E.3) was estimated by assuming a Sauter mean diameter, $d_{3,2}$, of 135.3 nm (as estimated from SEM images), and assuming approximately spherical particles of AgCl. Oxygen was assumed to adsorb as $(O_2)_a$ at surface Ag sites on AgCl (Kim *et al.*, 2018), with one adsorbed $O_2$ molecule *per* four Ag surface sites; oxygen adsorption on AgAu was assumed to be minimal (Geenen *et al.*, 1982; Rojluechai *et al.*, 2007).

The dispersion of AgCl, Đ, was estimated from Eq. E.2, where $\rho_s = 7.03 \times 10^{19}$ m$^{-2}$ is the surface atomic density of AgCl averaged over the (100), (110), and (111) planes, and $\rho_b = 4.47 \times 10^{28}$ m$^{-3}$ is the bulk atomic density for a lattice parameter of 5.546 Å (Gebers *et al.*, 2022; Rabiei *et al.*, 2020).

$$Đ = \frac{\rho_s \pi d_{3,2}^2}{\rho_b \frac{\pi d_{3,2}^3}{6}} = \frac{6\rho_s}{\rho_b d_{3,2}} \tag{E.2}$$

The number of moles of adsorbed oxygen atoms on AgCl, $n_{oxygen,ads}$, was then estimated from Eq. E.3, where $\lambda$ is the measured AgCl loading (as given in Table 6.2), and $M_r(AgCl)$ is the molar mass of AgCl.

$$n_{oxygen,ads} = \frac{Đ\lambda m_{bed}}{2M_r(AgCl)} \tag{E.3}$$

The maximum amount of adsorbed oxygen available was estimated to be around 8 $\mu$mol for 2.5AgCl/7.5Au-D/SFO, and 17 $\mu$mol for 7.5AgCl/2.5Au-D/SFO. For 7.5AgCl/2.5Au-D/SFO, the maximum theoretical oxygen available from adsorbed oxygen was of the order of the amount of oxygen detected in products after 1 min of reduction. As appreciable activity was detected after >20 min of reduction (shown in Fig. E.3), the contribution of adsorbed oxygen was taken to be minimal, and so oxygen provided from the SFO support was assumed to be the primary source of oxygen in products.

The amount of oxygen soluble in AgCl was approximated by taking the specific molar solubility of oxygen in AgCl to be around 16 $\mu$mol g$^{-1}$ (Jayaraman and Yang, 2005). The maximum amount of oxygen that could be dissolved in AgCl for the 7.5AgCl/2.5Au-D/SFO sample was estimated to be of the order *c.*1.6 $\mu$mol, which was an order of magnitude less than the amount of oxygen detected in products after 1.5 min of reduction, and so was neglected.

The total absorption and dissolution of oxygen in Au, $n_{tot,Au}$ was estimated using Eq. E.4 where $\Phi_{v,Au}$ is the estimated volumetric oxygen solubility ($m^3_{O_2}/m^3_{AgAu}$) (Toole and Johnson, 1933), $m_{Au}$ is the mass of gold present, estimated from XRD measurements, and $\rho_{Au}$ is the density of gold (kg m$^{-3}$) (Kraut and Stern, 2000).

$$n_{tot,Au} = \Phi_{v,Au} \cdot \frac{m_{Au}}{\rho_{Au}} \cdot \frac{P}{RT} \tag{E.4}$$

The sample with maximum gold loading was Au-D/SrFeO3, with 7.3 wt% Au loading. The maximum amount of oxygen that could be absorbed by Au in Au-D/SFO, was estimated to be of the order 1 nmol, *i.e.* several orders of magnitude less than the amount of oxygen detected in reaction products. Therefore, the oxygen absorbed by gold was assumed to be negligible for all other samples with lower gold loading.

The maximum amount of oxygen soluble in bulk Ag, $n_{dis,Ag}$ was estimated using Eq. E.5 where $\Phi_{m,Ag}$ is the molar solubility of oxygen in Ag (taken to be $\Phi = 10^{-6}$ $mol_O/mol_{Ag}$ from Lu *et al.* (2005)), $m_{Ag}$ is the mass of Ag, and $M_r(Ag)$ is the molar mass of Ag. For the sample with the highest Ag loading, Ag/SFO, with 11.8 wt% Ag loading, the maximum oxygen soluble was estimated to be of the order 16 nmol. As this was at least two orders of magnitude less than the amount of oxygen detected

in reaction products, the contribution of oxygen dissolved in Ag to the reacton was assumed to be negligible for all other samples with lower silver loading.

$$n_{dis,Ag} = \Phi_{m,Ag} \cdot \frac{m_{Ag}}{M_r(Ag)} \tag{E.5}$$

## E.3 Reaction of propylene over control samples

To verify the postulated chemical looping mechanism, cycling experiments were performed over various control samples. Co-feeding propylene and air (2.5 mol% propylene, 10.5 mol% $O_2$) over SFO resulted in formation of $CO_2$ only, with a decrease in activity from *c.* 1.9% to 0.5% for the overall propylene conversion after 1 h on stream (shown in Fig. E.4a). Additionally, co-feeding over Ag/SFO (10 wt% Ag) was also performed, giving $CO_2$ as the only reaction product, in line with previous work on direct propylene oxidation over Ag (Khatib and Oyama, 2015). The substantial increase in the amount of $CO_2$ formed between unimpregnated SFO and Ag/SFO was attributed to the reaction of propylene with $O_a$ on Ag, stripping the hydrogen atom bonded to the $\gamma$-carbon in propylene to form an unstable allyl radical, aiding the complete combustion reaction.

In Fig. E.4b, $CO_2$ was the only reaction product for looping over unimpregnated SFO. Therefore, the SFO support was inactive towards selective oxidation, and so $C_3$ oxygenate products detected formed at the AgCl/Au catalysts.

Samples of Ag and AgCl/Au-D catalysts impregnated on particles of $\alpha$-$Al_2O_3$ (180-355 $\mu$m, Alfa Aesar) were prepared by incipient wetness impregnation as described in Sections 2.1.2 and 6.2. Reaction of propylene over Ag/$Al_2O_3$ and 5AgCl/5Au-D/$Al_2O_3$ under looping conditions was investigated, as shown in Fig. E.4c. For both samples, $CO_2$ was detected as the only reaction product, indicating that reactions between propylene and adsorbed surface oxygen, or trace $Ag_2O$ and AgO phases, were not selective in the absence of the SFO oxygen carrier support.The decrease in $CO_2$ concentration for Ag/$Al_2O_3$ over successive cycles was attributed to the depletion of unstable $AgO_x$ phases, which were not subsequently regenerated during the re-oxidation step.

Chemical looping reaction of propylene over AgCl supported on $Al_2O_3$ yielded no oxygen-containing products above 5 ppm, including $CO_2$, showing that for reaction over AgCl/SFO, all the oxygen in products was provided from the SFO support.

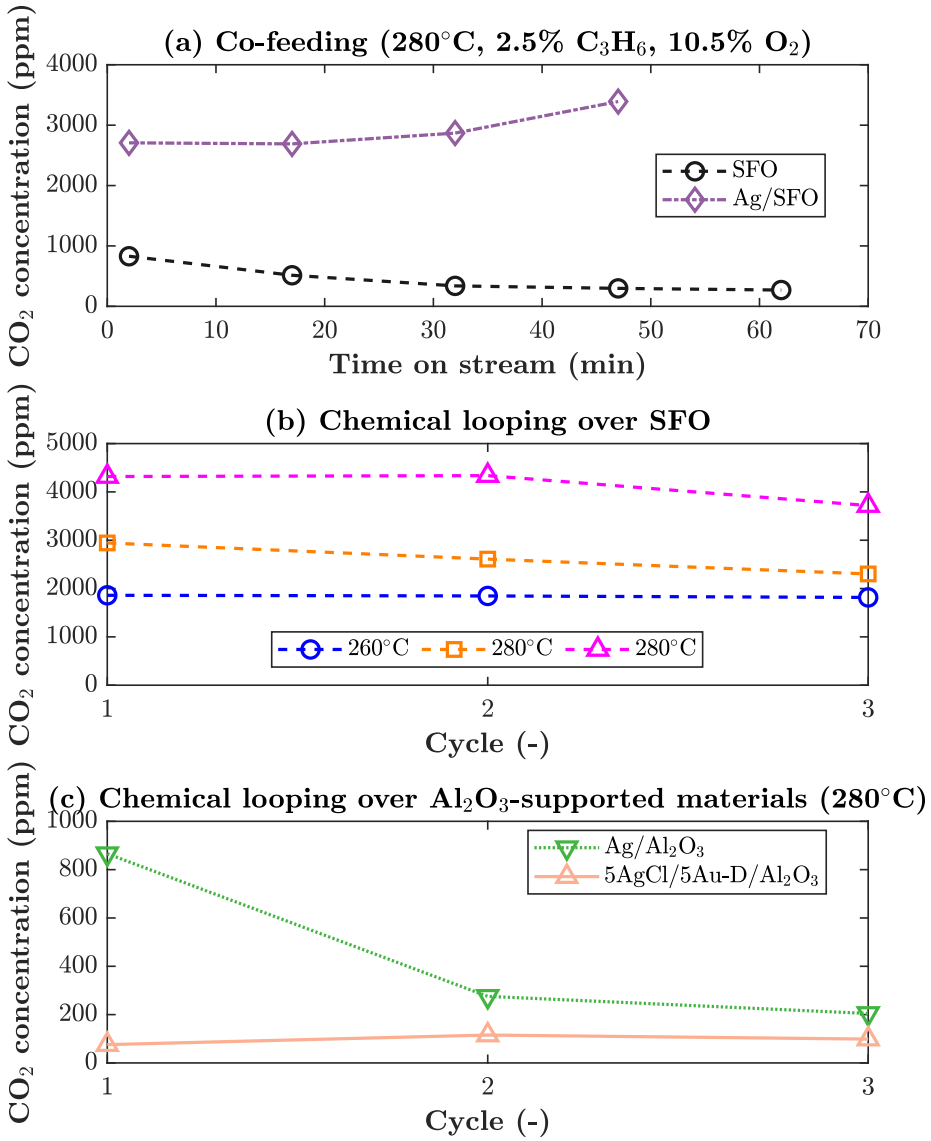


Fig. E.4 Product compositions in reactor outlet during **(a)** co-feeding and **(b)** chemical looping over SFO, and **(c)** chemical looping over $Ag/Al_2O_3$ and $5AgCl/5Au\text{-}D/Al_2O_3$. No other reaction products above 5 ppm were detected.